

TRIBOLOGICAL BEHAVIOR OF Al-B₄C METAL MATRIX NANOCOMPOSITES

Thesis submitted

By

DEEPAK MANOHARRAO SHINDE

Doctor of Philosophy

(Engineering)

**DEPARTMENT OF MECHANICAL ENGINEERING
FACULTY COUNCIL OF ENGINEERING & TECHNOLOGY
JADAVPUR UNIVERSITY**

2022

Tribological Behavior of Al-B₄C Metal Matrix Nanocomposites

Thesis submitted by

DEEPAK MANOHARRAO SHINDE

**Doctor of Philosophy
(Engineering)**

**DEPARTMENT OF MECHANICAL ENGINEERING
FACULTY COUNCIL OF ENGINEERING & TECHNOLOGY
JADAVPUR UNIVERSITY
KOLKATA, INDIA**

2022

**JADAVPUR UNIVERSITY
KOLKATA-700032, INDIA**

INDEX NO. 68/19/E

1. Title of Thesis:

Tribological behavior of Al-B₄C metal matrix nanocomposites

2. Name, Designation & Institution of the Supervisor:

Prof. Prasanta Sahoo

Professor, Mechanical Engineering Department,

Jadavpur University, Kolkata-700032

3. List of Publications (Referred Journals):

1. Shinde D. M., Sahoo P. (2022). Nanoindentation, scratch and corrosion studies of aluminum composites reinforced with submicron B₄C particles. *International Journal of Metalcasting*. 16 (3), 1363-1387. [SCIE]
2. Shinde D. M., Sahoo P. (2022). Influence of speed and sliding distance on the tribological performance of submicron particulate reinforced Al-12Si/1.5 wt% B₄C composite. *International Journal of Metalcasting*. 16 (2), 739-758. [SCIE]
3. Shinde D. M., Poria S., Sahoo P. (2020). High temperature tribology of A413/B₄C nanocomposites under dry sliding contact. *Materials Performance and Characterization*. 9 (1), 477-496. [ESCI].
4. Shinde D. M., Poria S., Sahoo P. (2020). Dry sliding wear behavior of ultrasonic stir cast boron carbide reinforced aluminum nanocomposites. *Surface Topography: Metrology and Properties*. 8, 025033. [SCIE].
5. Shinde D. M., Sahoo P., Davim J. P. (2020). Tribological characterization of particulate-reinforced aluminum metal matrix nanocomposites: A review. *Advanced Composites Letters*. 29, 1-28. [SCIE]

6. Shinde D. M., Poria S., Sahoo P. (2019). Synthesis and characterization of Al-B₄C nano composites. *Materials Today: Proceedings*. 19, 170-176. [SCOPUS].

4. List of Patents: Nil

5. List of Presentations in International Conferences:

1. Shinde D. M., Poria S., Sahoo P. (2020). Tribological performance of 1.5 wt% B₄C particulate reinforced Al-12Si alloy nanocomposite fabricated by ultrasonic stir casting. *International Conference on Advances in Material Science and Mechanical Engineering (ICAMSME-2020)*. 07th - 09th February, *NBKR Institute of Science and Technology, Vidyanaagar, Nellore, India*.
2. Shinde D. M., Poria S., Sahoo P. (2019). Dry sliding wear behavior of ultrasonic stir cast boron carbide reinforced aluminum nanocomposites. *10th International Conference on Industrial Tribology (IndiaTrib-2019)*. 01st - 04th December, *Indian Institute of Science, Bangalore, India*.
3. Shinde D. M., Poria S., Sahoo P. (2019). Synthesis and characterization of Al-B₄C nano composites. *1st International Conference on Manufacturing, Material Science and Engineering (ICMMSE-2019)*, 16th - 17th August, *CMR Institute of Technology, Hyderabad, India*.

6. List of Book Chapters:

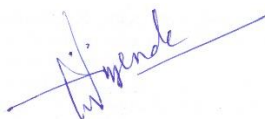
1. Shinde D. M., Sahoo P. "Fabrication of aluminium metal matrix nanocomposites: an overview." In S. Sahoo (Ed.), *Recent advances in layered materials and structures*, Material horizons: From nature to nanomaterials, (2021):107-132. Springer Nature Singapore Pte Ltd.

STATEMENT OF ORIGINALITY

I, **Deepak Manoharrao Shinde** registered on **30.04.2019** do hereby declare that this thesis entitled “**Tribological Behavior of Al-B₄C Metal Matrix Nanocomposites**” contains literature survey and original research work done by the undersigned candidate as part of Doctoral studies.

All information in this thesis have been obtained and presented in accordance with existing academic rules and ethical conduct. I declare that, as required by these rules and conduct, I have fully cited and referred all materials and results that are not original to this work.

I also declare that I have checked this thesis as per the “Policy on Anti Plagiarism, Jadavpur University, 2019”, and the level of similarity as checked by iThenticate software is **4 %**.



15/07/22

Signature of Candidate: _____

(Deepak Manoharrao Shinde)

Date:

Certified by Supervisor:  15/7/2022

(Signature with date, seal) **(Prasanta Sahoo)**

“This page is left intentionally blank”

CERTIFICATE FROM THE SUPERVISOR

This is to certify that the thesis entitled “*Tribological Behavior of Al-B₄C Metal Matrix Nanocomposites*” submitted by *Deepak Manoharrao Shinde*, who got his name registered on **30.04.2019** for the award of Ph.D. (Engineering) degree of Jadavpur University is absolutely based upon his own work under the supervision of *Prof. Prasanta Sahoo* and that neither his thesis nor any part of the thesis has been submitted for any degree/diploma or any other academic award anywhere before.

Prasanta Sahoo

15/7/2022

(Prof. Prasanta Sahoo)

Signature of the Supervisor
and date with Office Seal

“This page is left intentionally blank”

Abstract

The present thesis deals with the tribological behavior of Al-B₄C metal matrix nanocomposite and establishes the composite matrix as a potential tribo material. Aluminum has several favourable factors like low-cost availability, low density, better strength, corrosion resistance, near-infinite recyclability, and casting ease. Aluminium alloys for wear applications are generally based on Al-Si alloy system. Accordingly AlSi12 alloy is used as a base matrix. Boron carbide (B₄C) nanoparticle is selected as reinforcement material as it has better interfacial bonding with aluminium. Besides, it has superior properties like low density (2.52 g/cc), high melting point (2450°C), high elastic modulus (460 GPa), thermal & chemical stability, extremely high hardness (30 GPa), good wear and impact resistance, low thermal expansion coefficient ($5 \times 10^{-6}/^\circ\text{C}$), low thermal conductivity (40 W/mk) etc. Al-B₄C nanocomposites are fabricated using a combination of mechanical stirring and ultrasonic vibration assisted stir casting methods. Initially the fabricated specimens are tested for density and porosity to ensure defect free castings. Microhardness values of the composites are determined and compared with the base matrix. Afterwards the cast specimens are characterized using optical microscopy, scanning electron microscopy, and energy dispersive spectroscopy analysis. Wear and friction properties of the nanocomposites are investigated by considering several parameters like reinforcement content, applied loads, speeds, sliding distances, and the elevated operating temperatures. Tribochemical interactions occur in the sliding surfaces which are studied using worn surface micrographs and elemental analysis. Nanoindentation and elastic modulus of the fabricated composites are determined by nanoindentation tests. Scratch behavior is studied using a single point scratch test. Finally corrosion behavior of the composites is studied in 3.5% NaCl solution. Corroded surfaces and the degradation mechanisms are examined using FESEM images and EDX spectra.

Microstructural characterization of Al-B₄C composites revealed that the particles are homogeneously distributed in the composite structure with good interfacial bonding. Micro hardness of the alloy is enhanced with increasing B₄C content. Presence of hot hard ceramic particles significantly improved the tribological properties of Al alloy tested

under different parametric conditions. Increased strength of alloy, delay in thermal softening and lubricative transfer layers formed in the sliding interface were found crucial for this enhanced performance. Significant increase in nanohardness and scratch resistance is observed with the increasing content of ceramic particles. Corrosion resistance of alloy is improved for the small incorporation (0.5 wt %) of B₄C particles. However further increase in the reinforcement content degraded the corrosion behavior. It is expected that the results presented in the thesis will be of significant interest, both from the academic and industrial viewpoint.

About the Author

The author Shri **Deepak Manoharrao Shinde** was born in Latur, a district place of Maharashtra state in the year 1975. He spent his childhood days and completed 10+2 education from the same place. He graduated in Production Engineering (BE) in 1998 from Shivaji University Kolhapur. He completed Master of Engineering (ME) in Mechanical-CAD/CAM from Shri Ramanand Teerth Marathwada University, Nanded in 2006. After graduation he started his career as a teaching faculty in an engineering diploma institute and then switched over to degree institute in private sector. In 2011, he is selected for Maharashtra State Polytechnic Teachers Services Group A by public service commission. He is deputed by state government for pursuing PhD (Engg.) at Jadavpur University Kolkata, under QIP (POLY) scheme of AICTE, Government of India. He is currently employed as Sr. Lecturer in Mechanical Engineering at Government Polytechnic Ratnagiri.

“This page is left intentionally blank”

Acknowledgement

The present thesis is the result of the research work carried out in the last three years. During this period, a number of people have supported me for the successful completion of the research work. Thus it is my humble duty to convey my sincere thanks to all who were directly or indirectly associated with this research work.

Firstly, I would like to pay my heartfelt gratitude to my respected thesis supervisor, Prof. Prasanta Sahoo sir, without whom this research work wouldn't have been possible. Coming from a work culture having no space for research activities initially made things a little difficult for me. But the methodical and visionary guidance from sir helped me a lot in enriching myself during the period of work. His continuous help and motivation during all these days made things simpler. His approach towards life and work is a lifetime learning experience for me.

I would like to thank AICTE for running a scheme [QIP (Poly)] for polytechnic teachers to pursue Ph.D and granting me an opportunity. The financial assistance (scholarship) received from the scheme was encouraging, which helped me complete the costly material characterization work. At this juncture, I must appreciate the support received from the technical staff at IEST Shibpur, MMMF lab and NanoIndenter lab at IIT Mumbai for carrying out the FESEM, Optical and nanoindentation work. Moreover, I would like to thank all the past researchers in this field whose published literatures have greatly helped me in getting an insight towards the research work done.

Most of the research work time is spent in the lab and as such fruitful interactions take place and light moments are shared with the lab mates. I am thankful to all the lab mates of machine elements laboratory and Smart foundry lab of Jadavpur University. Firstly I would like to thank Dr. Suswagato Poria and Dr. Sudip Banerjee for all their help and support. My special thanks goes to Tamonash and Deviprasanaa whose helping hand made a homely environment for me. I cannot forget the time spent in lab with Dr. Brajesh, Sushanta, Abhijit, Manik, Avinash for all the useful discussions, witty comments and fun that relieved me from the stress of work. I should also mention my friends, Mr.

Suresh Kadam, Anup Pardey, Manoj Gajbhiye, and Rahul Meshram from Maharashtra doing PhD work in other departments of JU in the same period. Their support and daily trips to canteen for a cup of tea refreshed me all the time.

I would like to convey my thanks to the Head of the Department, the Laboratory-in-Charge, Machine Elements Laboratory and all the academic and technical staffs of Mechanical Engineering Department, Jadavpur University, Kolkata.

Finally, last but certainly not the least, I thank my beloved family members, well-wishers and friends for their patience and constant support without which this work couldn't have been completed.

DEEPAK MANAOHARRAO SHINDE

To,

Family, friends and all the teachers who
influenced my life a lot

“This page is intentionally left blank”

Table of Contents

	Page No
Thesis title and list of publications	i
Statement of originality	iii
Certificate from the supervisors	v
Abstract	vii
About the author	ix
Acknowledgement	xi
Dedication	xiii
Table of contents	xv
List of figures	xix
List of tables'	xxv
Chapter 1: Basic considerations and literature review	1-25
1.1 Introduction	1
1.2 Motivation for the work	3
1.3 Aluminium metal matrix composites	5
1.4 Processing of Al nanocomposites: an overview	7
1.5 Tribological characterization of Al nanocomposites: a review	15
1.6 Corrosion behavior of AMMCs	21
1.7 Scope of the work	23
1.8 Outline of the thesis	25
1.9 Closure	25
Chapter 2: Materials and methods	27-49
2.1 Fabrication of Al-B ₄ C nanocomposites by ultrasonic stir casting	27
2.2 Density and porosity measurement	31
2.3 Microhardness testing	32
2.4 Microstructural examination	34
2.4.1 Metallographic sample preparation	35
2.4.2 Optical, FESEM-EDX study	35

2.5	Dry sliding tribological testing	37
2.5.1	Pin-on-disk wear and friction monitor	38
2.5.2	High temperature tribology tester	39
2.6	Nanoindentation testing	40
2.7	Single point scratch test	43
2.8	Corrosion measurement	44
2.8.1	Potentiodynamic polarization test	45
2.8.2	Electrochemical impedance spectroscopy test	47
2.9	Closure	49
Chapter 3: Characterization of fabricated composites		51-60
3.1	Characterization of B ₄ C	51
3.2	Density and porosity	52
3.3	Micro-indentation hardness	53
3.4	Microstructure	54
3.4.1	Optical microscopy of samples	55
3.4.2	FESEM-EDX analysis of fabricated materials	57
3.5	Closure	60
Chapter 4: Tribological performance of Al-B₄C nanocomposites at room temperature		61-102
4.1	Introduction	61
4.2	Plan of experiments	62
4.3	Results and discussion	63
4.3.1	Wear behavior	63
4.3.1.1	Effect of reinforcement content	63
4.3.1.2	Effect of applied contact pressure	64
4.3.1.3	Effect of sliding speed	72
4.3.1.4	Effect of sliding distance	74
4.3.2	Friction behavior	76
4.3.3	Tribological performance of 1.5 wt% B ₄ C composite	79
4.3.3.1	Influence of speed	80
4.3.3.2	Influence of distance	88
4.3.4	Wear debris analysis	98

4.4	Closure	101
Chapter 5: High temperature tribology of Al-B₄C nanocomposites		103-123
5.1	Introduction	103
5.2	Experimental conditions	105
5.3	Results and discussion	106
5.3.1	Wear behavior	106
5.3.2	Friction behavior	119
5.4	Closure	122
Chapter 6: Nanoindentation, scratch, and corrosion behavior of Al-B₄C nanocomposites		125-152
6.1	Introduction	125
6.2	Experimental details	127
6.3	Results and discussion	129
6.3.1	Nanohardness and elastic modulus	129
6.3.2	Wear resistance under scratch loads	134
6.3.3	Scratch hardness	136
6.3.4	Friction characteristics	137
6.3.5	Morphology of scratch grooves	139
6.3.6	Potentiodynamic polarization study	141
6.3.7	Electrochemical impedance spectroscopy study	143
6.3.8	Corroded surfaces and degradation mechanisms	145
6.4	Closure	151
Chapter 7: Final remarks		153-155
7.1	Conclusions	153
7.2	Future scope	154
Bibliography		157-168
Publications from the thesis		169-176

“This page is left intentionally blank”

List of Figures

	Page No.
Figure 1.1 Different methods of fabricating Al metal matrix nanocomposites	7
Figure 2.1 Ultrasonic stir casting (a) Process schematic; (b) Mechanism of particle deagglomeration	28
Figure 2.2 (a) Ultrasonic vibrator, (b) stir casting unit, (c) melt pouring arrangement, (d) die drawing, disassembled die and fabricated cast specimen	28
Figure 2.3 (a) Typical sample for density measurement, (b) weighing machine	32
Figure 2.4 Vicker's indentation and diagonals of the impression	33
Figure 2.5 (a) LECO Microhardness Tester, LM248AT; (b) display of hardness (HV)	34
Figure 2.6 Equipments used for microstructure examination in this study	37
Figure 2.7 Pin-on-disk tribotester (TR-208-M2, DUCOM India)	38
Figure 2.8 Elevated temperature POD tribotester (TR-20-M60, DUCOM)	39
Figure 2.9 (a) Typical nanoindentation sample, (b) indentation array pattern, (c) optical image of the test surface along with its roughness (Ra) and scanned surface profiles.	41
Figure 2.10 Instruments used for micro tribology tests (a) Nanoindenter, Hysitron Inc Minneapolis USA, TI900, (b) Scratch tester, TR-101-IAS, Sr. no. 921 DUCOM	41
Figure 2.11 Load versus displacement curve	42
Figure 2.12 (a) geometry of scratch indenter (b) typical images of scratches (c) scratch width measurement	44
Figure 2.13 A typical polarization plot (ASTM Standard G3-89 2010)	46
Figure 2.14 Randles circuit model to fit EIS data (McCafferty, 2010)	47
Figure 2.15 Nyquist plot for Randle's circuit	48

Figure 2.16	Corrosion measurement setup (Gill AC, ACM instrument)	49
Figure 3.1	Characterization of boron carbide: a) FESEM image. b) As received powder, c) FESEM-EDS spectrum, d) XRD pattern	52
Figure 3.2	Variation of microhardness with % B ₄ C content	54
Figure 3.3	Optical micrographs: a Al alloy, b 0.5 wt% B ₄ C, c 1.0 wt% B ₄ C, d 1.5 wt% B ₄ C, e 2.0 wt% B ₄ C	56
Figure 3.4	SEM-EDX spectrums: a AlSi alloy, b 0.5 % B ₄ C, c 1.0 wt% B ₄ C, d 1.5 wt% B ₄ C, e 2.0% B ₄ C	57
Figure 3.5	Microstructure and elemental mapping: (a) Al-Si alloy, (b) Al 2.0 wt% B ₄ C composite	58
Figure 3.6	(a) B ₄ C particles in the composite matrix; (b) Small area EDS of particle 3	59
Figure 4.1	Mass loss as a function of B ₄ C wt %	64
Figure 4.2	Effect of applied pressure on (a) wear rate and (b) specific wear rate	66
Figure 4.3	Worn surfaces of a) Base alloy, b) 1wt% B ₄ C, c) 2 wt% B ₄ C (at 0.354 MPa); d) Base alloy, e) 1wt% B ₄ C, f) 2 wt% B ₄ C (at 1.412 MPa).	67
Figure 4.4	EDS for 1.061 MPa (at 0.49 m/s): a base, b 1% B ₄ C, c 2% B ₄ C	68
Figure 4.5	EDS of 1.0 wt % nB ₄ C composite for a 0.354 MPa, b 1.412 MPa (at 0.66 m/s)	69
Figure 4.6	Surface roughness for 0.66 m/s: (a) Alloy, (b) 2 wt% composite (at 0.354 MPa); (c) Alloy, (d) 2 wt% composite (at 1.412 MPa)	70
Figure 4.7	Wear rate Vs sliding speed at 1.412 MPa	73
Figure 4.8	EDS of 2.0 wt % nB ₄ C composite at 1.412 MPa for speed variation: (a) 0.16 m/s, (b) 0.66 m/s.	74
Figure 4.9	Wear rate of fabricated materials as a function of sliding distance	75
Figure 4.10	Worn surface profiles obtained at 400, 1600 m sliding distance: (a), (b) base alloy; (c), (d) Al-1.5 wt% B ₄ C	76

Figure 4.11	COF variations with (a) applied pressure and (b) sliding speed	77
Figure 4.12	COF profiles for 1.5 wt% B ₄ C at different applied loads at 0.16 m/s speed	79
Figure 4.13	Effect of sliding speed on: (a) wear rate (b) coefficient of friction	81
Figure 4.14	Worn surfaces obtained at sliding speed of 0.25, 0.5 and 1.25 m/s: Base alloy (a, b, c), Al-B ₄ C composite (d, e, f)	83
Figure 4.15	EDX analysis of worn surfaces obtained at different speeds 0.25, 0.5, 1.25 m/s: Base alloy a, b, c ; Al-B ₄ C composite d, e, f	85
Figure 4.16	Friction profile against sliding duration at different speeds: (a) Base alloy (b) Al-B ₄ C composite	87
Figure 4.17	Wear rate variation with sliding distance at 0.5 m/s	88
Figure 4.18	Worn surfaces obtained at 0.5 m/s for 20, 30, 40 min of sliding duration (600, 900, 1200 m distance): Base alloy (a, b, c), Al-B ₄ C composite (d, e, f)	90
Figure 4.19	EDS spectrums obtained at 0.707 MPa, 0.5 m/s, 30 min of sliding: (a) Al-Si alloy (b) magnified view at square 'A' of (a) showing compacted MML with cracks, (c) Al-B ₄ C composite	92
Figure 4.20	Friction profile against sliding duration and/or distance at 0.5 m/s	93
Figure 4.21	Wear rate variation with sliding distance at 1.25 m/s	94
Figure 4.22	Worn surfaces for 750, 2250, 3000 m of sliding distance (10, 30, 40 min duration) obtained at 1.25m/s: Al alloy (a, b, c), Al-B ₄ C (d, e, f)	96
Figure 4.23	EDX analysis of worn surfaces obtained at 1.25 m/s for 10, 40 min of sliding duration Al alloy (a), (b); Al-B ₄ C (c), (d)	97
Figure 4.24	Friction profile against sliding duration and/or distance at 1.25 m/s	98
Figure 4.25	Wear debris; a base alloy, b 2wt% B ₄ C nanocomposite at 0.354 MPa and 0.66 m/s	98
Figure 4.26	Wear debris morphology obtained at 0.49 m/s and 10, 40 min of sliding: Al alloy (a), (b); Al-1.5 wt% B ₄ C (c), (d)	99

Figure 4.27	(a) wear debris of 1.5 wt% B ₄ C composite at 0.49 m/s, 40 min; (b) elemental map	100
Figure 5.1	Variation of wear rate vs. temperature at 20 N applied load	106
Figure 5.2	Worn out surface FESEM micrographs of Al alloy pin tested at 20 N load and temperature of: a 50°C; b 200°C	107
Figure 5.3	Variation of wear rate vs. temperature at 60 N applied load.	109
Figure 5.4	Worn out surface FESEM micrographs of Al alloy pin tested at 60N load and temperature of: a 50°C; b 200°C.	110
Figure 5.5	Worn out surfaces at 60N: (a) 100°C (b) 150°C (alloy); (c) 100°C (d) 150°C (1.0 wt% composite)	111
Figure 5.6	Worn out surface FESEM micrographs of Al-2wt% B ₄ C nanocomposite pin tested at 60N load and temperature of: a 50°C; b 100°C; c 150°C; d 200°C	112
Figure 5.7	FESEM image of MML obtained at 2000X magnification for 0.5 wt% composite at 20 N, 100°C	113
Figure 5.8	FESEM image of MML obtained at different test conditions: (a) 1 wt% composite, 60 N, 50°C (b) 2 wt% composite, 20 N, 150°C	114
Figure 5.9	3D topography and roughness of worn out surfaces obtained at different operating temperatures (50-200 °C) and 60 N load: (a) Base alloy (b) 2 wt% B ₄ C nanocomposite	115
Figure 5.10	FESEM images of wear tracks obtained at 60N and temperature of 150°C for: a Al alloy, b 0.5 wt% B ₄ C, c 1.0 wt% B ₄ C, d 1.5 wt% B ₄ C, e 2.0 wt% B ₄ C	118
Figure 5.11	Variation of friction coefficient vs. temperature at 20 N applied load	119
Figure 5.12	Variation of friction coefficient vs. temperature at 60 N applied load	120
Figure 5.13	COF of base alloy during entire sliding duration at 60 N	121
Figure 5.14	COF of 2 wt% B ₄ C composite during entire sliding duration at 60 N	122
Figure 6.1	Nanoindentation load-displacement profiles: (a) AlSi alloy, (b) 0.5 wt% B ₄ C, (c) 1.0 wt% B ₄ C, (d) 1.5 wt% B ₄ C, (e) 2.0 wt%	132

B₄C

Figure 6.2	Magnified partial views of loading curves showing difference in slopes: (a) Base alloy, (b) 2 wt% composite	133
Figure 6.3	Variation of scratch width against applied load	134
Figure 6.4	Macroscopic image showing load dependence on scratch width	135
Figure 6.5	Variation of wear volume against wt% of B ₄ C	136
Figure 6.6	Profile of friction coefficient with scratch duration: (a) Al alloy (b) Al-2wt% B ₄ C composite	138
Figure 6.7	Groove topography and magnified ridges at 5 N: (a), (b) Al alloy; (c), (d) Al/2wt% B ₄ C	139
Figure 6.8	Groove topography and magnified ridges at 20 N: (a), (b) Al alloy; (c), (d) Al/2wt% B ₄ C	141
Figure 6.9	PDP curves for Al alloy and Al/B ₄ C composites	142
Figure 6.10	Nyquist plots of Al alloy and Al-B ₄ C composites	144
Figure 6.11	Al-Si alloy: (a), (b) Micrographs of corroded surface at different magnifications; (c) EDX analysis; (d) Oxide product at high magnification (3 KX) with EDX spectrum	146
Figure 6.12	SEM images of corroded composites: (a), (b) 0.5 wt% B ₄ C; (c), (d) 1.0 wt% B ₄ C; (e), (f) 1.5 wt% B ₄ C; (g), (h) 2.0 wt% B ₄ C	149
Figure 6.13	EDX analysis of the corroded surfaces at 200X magnification: (a) 0.5 wt% B ₄ C, (b) 1.5 wt% B ₄ C, (c) 2.0 wt% B ₄ C; (d) 2.0 wt% B ₄ C at 3000X magnification	151

“This page is left intentionally blank”

List of Tables

		Page No.
Table 1.1	Al nanocomposites produced by solid state processing methods	8
Table 1.2	Al nanocomposites produced by semi-solid and liquid state processing methods	11
Table 1.3	Different parameters investigated for tribological characterization of Al nanocomposites by various researchers.	20
Table 2.1	Properties of Al alloy and B ₄ C reinforcement.	29
Table 2.2	Composition of Al-12Si alloy	29
Table 2.3	Parameters used during fabrication	31
Table 3.1	B ₄ C powder details	51
Table 3.2	Results of density and porosity measurement	53
Table 3.3	EDX analysis (Wt. %) of particles shown in micrograph Figure 3.6 a	60
Table 5.1	Constituents obtained in EDS spectrums of the whole area of worn surfaces shown in FESEM micrographs	108
Table 5.2	Surface profile roughness (Ra) values of worn surfaces obtained at different operating temperatures, loads and measured in 3D optical profilometer	116
Table 6.1	Scratch test parameters	128
Table 6.2	Average values of 15 indents each for Al alloy and Al/B ₄ C composites	132
Table 6.3	Scratch hardness values of fabricated materials	136
Table 6.4	Average friction coefficients at different applied loads in scratch test	138
Table 6.5	Electrochemical parameters obtained from Tafel plot	143

Table 6.6 Electrochemical parameters obtained from EIS plots through circle fitting method

145

Chapter 1

Basic considerations and literature review

1.1 Introduction

Fuel economy, reduced emission, safety, styling options, and luxury features at competitive cost are the challenges before the automotive and aerospace industries nowadays. It has prompted continuous research on developing lightweight materials with desired and tailored properties. European automotive industry is using new design concepts like body in white (BIW) and super light car (SLC) which focus on producing light weight vehicles for space and economy. Mostly light metals such as aluminum, magnesium, titanium and corresponding alloys have received commercial recognition due to their relatively low cost and easy processing. However pure metals or their alloys cannot always individually satisfy the needs of modern engineering applications. For example, pure magnesium or magnesium alloys shows low ductility, poor tribological properties and as such cannot be used for making sliding components. The need of different property combinations such as high specific strength and ductility for aerospace and automobile field, low coefficient of thermal expansion and high thermal stability for elevated temperature applications, high wear resistance, high specific stiffness and corrosion resistance for defense sector can be fulfilled by metal matrix composites (MMCs). It is because metals and ceramics have vastly different physical, thermal, electrical and mechanical properties making it possible to obtain desired property combinations. Metal matrix composites have gained popularity in industrial applications. Matrix and reinforcements are carefully selected based on criteria like density, elastic modulus, hardness, thermal stability, coefficient of thermal expansion, etc. Compatibility with matrix (wettability, reaction with matrix), size, morphology, availability and cost are other deciding factors for making composites of desired properties. Most of the commercially produced metal matrix composites were consumed by the ground transportation sector, almost 62% in 1999. The first major commercial utilization of metal matrix composite is dated back to 1983 when automobile giant Toyota incorporated

alumina reinforced aluminum composite piston in their diesel engine. Later on in 1990 Honda started using Al/Al₂O₃ composites for engine blocks. Brake system components such as discs, rotors, calipers, pads made of Al-Mg/Al₂O₃ and Al/SiC composites are manufactured by Lotus Elise and Volkswagen. Automotive racing market is a leading consumer of high performance brake components, calipers and push rods. Chevrolet S-10 and GMC pick-up trucks have utilized drive shafts and engine cradles made of Al/SiC particulate composites. Al/TiC particulate connecting rod and pistons are produced by Martin Marietta. Nissan used Al/SiC for connecting rod while Duralcan used it for making propeller shafts. Altezza 2.0L L4 engine used intake and exhaust valves made of composites. These are some of the key applications already been explored by the progressive auto industry worldwide. Thus use of metal matrix composites for automobile parts is now a proven technology. MMCs are now commercially made available and used on increasing scale. Utilization of MMCs has reached several sectors beyond automobile such as electronics, military, sports, infrastructure, marine, aerospace, etc. as well.

Component surfaces in sliding or rolling contact is a common feature in every engineering system. It is not always possible to lubricate such pairs in moving contact due to system constraints. Hence the dry contact wear behavior of these components is significant for their extended life with reliable performance. As heavy iron parts are being replaced by lightweight materials like aluminum, their friction and wear behavior is required to be enhanced and so has become an area of major research focus. Tribology is a science and technology that deals with the investigation of interacting surfaces in relative contact. It involves the study of wear, friction and lubrication. Wear is a progressive loss of material from the contacting surfaces in relative motion under load. Improved understanding of different types of wears like sliding, abrasive, corrosive and fatigue can develop better wear reduction technologies. Hardness is the most important mechanical property that controls wear. Frictional response depends upon the instantaneous condition of the asperities in the real areas of contact between surfaces. Control of friction is essential for the desired functioning of component parts during their estimated life span. Complex microscopic interactions take place in the interface of contact surfaces which are influenced by their mechanical, physiochemical and geometrical aspects. Measurement of tribological characteristics (wear and friction) in steady state conditions determines the long term properties / performance of the system.

Besides, examination of surface damages and understanding the undergoing wear mechanisms is essential. It is because failure of a tribological system is not always caused by the loss of material from the tribosurfaces. A series of events take place which changes the character of the contact surface. For instance sometimes the cutting performance of a tool is lost not by wearing of the cutting edge but because of the local plastic deformation, edge fractures, etc. Structural modification of the surfaces, plastic deformation, surface cracking, material transfer between surfaces, and corrosion assisted wear are some of the surface damages observed in tribological systems. Tribological properties are measured by scientifically designed tests. The purpose of tribotesting is to understand how a material behaves in tribological applications. Tribological tests are classified according to the level of their realism i.e. how closely they mimic with real world conditions as: 1. field test, 2. bench test, 3. subsystem test, 4. component test, 5 model test. Test equipment designed to evaluate friction and wear is termed as ‘tribometer’. Sliding wear tests in laboratory are performed with different geometrical configurations like block-on-ring, pin-on-disk, sphere-on-disk, block-on-cylinder, crossed cylinders. After tribo tests the worn surfaces of the test samples are examined. For understanding microstructural changes, subsurface deformation and wear mechanisms, optical microscopy, scanning electron microscopy, field emission scanning electron microscopy (FESEM), transmission electron microscopy (TEM) are used as routine tools. Energy dispersive spectroscopy (EDS) and X-ray diffraction (XRD) are used to investigate chemical elements and phase compositions quantitatively in the material samples on regular basis.

1.2 Motivation for the work

Silicon carbide (SiC) and Aluminum oxide (Al_2O_3) are the two most often used reinforcements for research studies undertaken in the area of metal matrix composites. Boron carbide possess superior properties like less density, high melting point (2450°C), high elastic modulus (460 GPa), thermal & chemical stability, extremely high hardness (30 GPa), good wear & impact resistance, low thermal expansion coefficient (CTE), low thermal conductivity (40 W/mk), neutron absorption capacity etc. (Poovazhagan et al. 2016; Thevenot 1990). Also it has better interfacial bonding with aluminum than Al_2O_3 and SiC (Shubhajit et al., 2018). CTE of Al alloy ($20 \times 10^{-6} \text{ }^\circ\text{C}$) is four times higher than that of boron carbide. Mismatch of CTE between particles and matrix generate

geometrically necessary dislocations (GND). These GNDs contribute to the rise in yield strength of the material. Density of B_4C is 2.52 g/cc whereas the density of solid aluminum is 2.7 g/cc (2.37 g/cc in liquid state). Less density difference with aluminum make its incorporation easier through liquid metallurgy route. Moreover boron carbide is the third hardest element and better than silicon carbide and alumina in wear resistant applications. Despite this it has not been given due attention for producing aluminum composites. Moreover, negligible attempts of the tribological investigation of aluminum matrix reinforced with submicron or nano B_4C particle are seen in the published literature, possibly due to high cost of B_4C nano powder. Dry condition sliding wear behavior of Al/ B_4C nanocomposites produced by mechanical milling and hot pressing (Sharifi et al., 2011), milling and hot extrusion (Alizadeh and Taheri-Nassaj, 2011; Abdollahi et al., 2014), friction stir processing (Yuvaraj et al., 2015), stir casting (Siddesh Kumar et al., 2016) and ultrasonic assisted stir casting (Harichandran and Selvakumar, 2016; Poovazhagan et al., 2016) are the few but promising studies reported. Nanocomposites with 5-15 wt% nB_4C reinforcement after subjecting to 20 N load and 0.08 m/s speed for the sliding distance of 500 m were found to exhibit enhanced wear resistance than base alloy (Sharifi et al., 2011). It is due to formation of tribolayer on the worn surfaces. Alizadeh and Taheri-Nassaj, (2011) also revealed positive friction and wear properties of Al-2wt% Cu alloy reinforced with nano B_4C particles. Abdollahi et al. (2014) compared dry sliding wear response of coarse grained Al2024 alloy, nanostructured Al2024 alloy and Al2024-5wt% B_4C nanocomposites. They observed significant rise in the hardness of base alloy from 87 HBN to 173 HBN. Also considerable decrease in the wear rate of alloy is observed due to mechanical milling and addition of nano boron carbide particles. Friction stir processed Al5083- B_4C surface nanocomposite after three passes exhibited hardness of 124.8 Hv and wear rate of 0.27 g/m as compared to the base alloy hardness of 82 Hv and wear rate of 5.7 g/m (Yuvaraj et al., 2015). In another work significant increase in the wear resistance of nanocomposite specimens is found at all the tested loads (20 - 60N) and speeds (3.14 - 5.64 m/s) (Siddesh Kumar et al., 2016). It has been reported recently that tremendous improvement in mechanical, thermal, electrical and structural properties of aluminum matrix can be obtained by very fine size B_4C particles (Isfahani et al., 2019; Ubaid et al., 2017).

Al-Si cast alloys are crucial for the transportation sector. Among different cast and wrought Al compositions, Al-Si alloys are particularly important for their wear resistant property (Baker et al., 2010) and majorly associated to sliding and abrasive wear in industrial applications. These alloys are preferred for applications like piston, cylinder block, clutches and others subjected to tribological interactions. Hence it would be beneficial to extend their wear resistance by ceramics like B_4C . Friction and wear study of AlSi12- B_4C nanocomposites produced by ultrasonic stir casting is missing in the literature. The presented experimental work will fill this void. This work is aimed to comprehensively investigate the suitability of Al-n B_4C as a tribo material

1.3 Aluminum metal matrix composites

Aluminum and its alloys are preferred for engineering applications due to low-cost availability, low density, good strength, corrosion resistance, near-infinite recyclability, and casting ease. Aluminum alloys of 2xxx, 5xxx, 6xxx, 7xxx series designation are in large usage due to high strength formability, damage tolerance, fatigue resistance, energy absorption and excellent crash characteristics. Successful automotive applications of Al include transmission components, brake elements, structural parts like chassis, suspension, body parts, including bumpers, doors, and interiors (Hirsch, 2014). However, properties of pure Al and Al alloys are not sufficient to support the high performance applications. For instance, the use of aluminum and its alloys is restricted due to poor resistance to wear, seizure and galling (Prasada and Asthana, 2004). Different methods of improving hardness and wear, scuffing resistance of Al alloys include solid solution strengthening, dispersion strengthening and precipitation hardening. Dispersion strengthening involves reinforcing the soft matrix with either hard particles or combination of hard (increases abrasive resistance) and/or soft particles (yield less friction). Interaction of dislocations with particles is found to strengthen the material matrix to significant extent (Prasada and Rohatgi, 1987). In general properties of aluminum are improved by reinforcing them with ceramic phase to produce so-called aluminum metal matrix composites (AMMCs). Especially particulate reinforced Al based MMCs are of interest and account for majority of the annual MMC produced and utilized on volume and mass basis (Zhang et al., 2018). Aluminum composites have attracted researchers due to properties like high strength and stiffness, increased resistance to wear

and corrosion, and improved high-temperature performance (Allison and Cole, 1993; Prasada and Asthana, 2004). Aluminum-based micro composites have been successfully utilized in different sectors like ground transportation, aerospace, electronics, recreational goods industries for structural and wear resistance applications. It has been reported that different composites mostly Al based now constitute more than 50% of the Boeing 787 aircrafts and 25% of Airbus A380. Aluminum-based composites have shown performance improvements in various applications requiring good wear resistance, low friction, and improved corrosion properties. Different reinforcement particles such as borides (TiB_2 , ZrB_2 , MoB , CrB , and WB), carbides (B_4C , CrC , SiC , TaC , TiC , WC , ZrC), nitrides (AlN , BN , CrN , Si_3N_4 , TiN , WN , ZrN) and oxides (Al_2O_3 , B_2O_3 , CuO , Fe_3O_4 , MgO , SiO_2 , TiO_2 , WO_3 , Y_2O_3 , ZnO , ZrO_2) are employed to produce Al metal matrix composites.

It is to be noted that all of the commercial Al composites are made using micron size reinforcements. Practical utilization of aluminum metal matrix nanocomposite (AMMNC) is not reported in the published literature yet. However, it is also clearly demonstrated in several lab scale studies in the recent past that nanoparticle reinforced composites outperform micro composites in many respects. For instance, the compressive strength performance of A356 alloy composites reinforced with 20 μm and 50 nm size Al_2O_3 particles were compared (Sajjadi et al., 2011); and found 610 MPa strength for 3.0 wt% alumina nanocomposite, as compared to 453 MPa measured for 10 wt% alumina micro composite. Enhanced dislocation density, grain refinement, Orowan mechanism are the strengthening effects identified in case of nanocomposites. Aluminum nanocomposites are strengthened more by indirect mechanisms wherein particles transfer their load bearing capacity to matrix. It is achieved through improved mechanical properties induced by microstructure refinement more than by direct strengthening. In case of refined microstructure, the load is borne by particles either by shear lag theory or by homogenization concept in which stress developed gets shared by particles and matrix on the volume average basis. Aluminum nanocomposites have tremendous potential and are required to be produced on industrial scale. But the critical issue in producing MMNCs is the uniform dispersion of nanoparticles in the metal matrix. Due to large surface area, they tend to form clusters under the influence of Van der Waals's force of attraction. During conventional liquid processing, due to limited wettability ceramic particles get pushed to the solidification front. It leads to particle agglomeration near the

grain boundaries. Also, the formation of pores/voids seriously affects properties diminishing the beneficial effects of nanoparticles. Aluminum composites are still facing the challenges of inferior ductility, low fracture toughness, poor machinability and weldability, and precise control of distribution of different micro/nano constituents during processing. Besides, tribological behavior is to be evaluated before considering them for the related applications. So current research activities are focused on improving their mechanical properties, reliability, reduction in manufacturing costs, prevention of corrosion, fretting wear, fatigue in the quest for developing next-generation materials (Ma et al., 2017).

1.4 Processing of Al nanocomposites: an overview

Fabrication of nanocomposite is relatively complex due to fine size particles, which are difficult to handle and introduce uniformly into the matrix. Researchers are continuously trying to promote suitable methods for low-cost defect-free production of nanocomposites with possible industrial scalability. But still, most of these efforts are of laboratory scale.

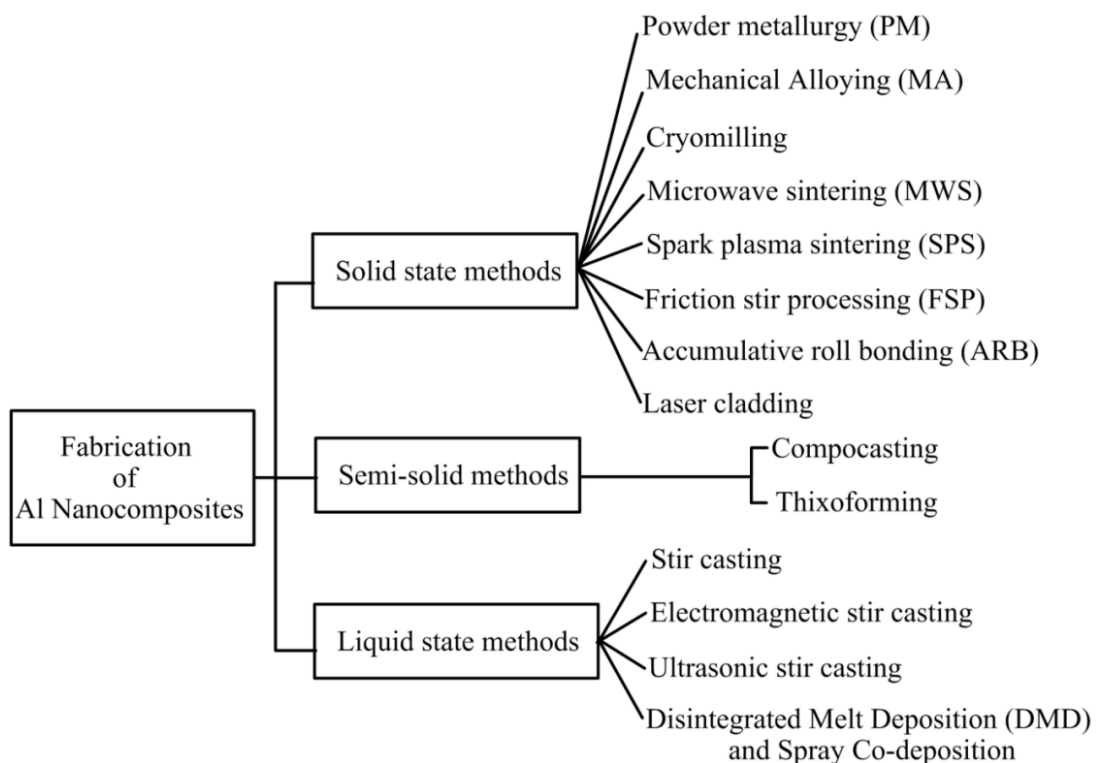


Figure 1.1: Different methods of fabricating Al metal matrix nanocomposites

Most of the existing methods of fabricating MMNCs are similar to MMCs but are modified to tackle added challenges posed by nanoparticles. An overview on the published work of Al composite fabrication methods is conducted so as to select the best one for the current work. Different methods employed for fabricating aluminum metal matrix nanocomposites can be divided into three major groups: 1. solid-state processing, 2. semi-solid state processing, and 3. liquid state processing. Some attempts have also been made to combine the above principal methods for availing their benefits and are termed as hybrid methods. Solid and liquid state processes are either Ex-situ or In-situ types depending upon whether the reinforcement particles are generated during the fabrication process or are available for incorporation beforehand respectively. A general classification of Al nanocomposite fabrication methods is presented in Figure 1.1.

Table 1.1: Al nanocomposites produced by solid state processing methods

Fabrication technique	Al nanocomposites	Researchers
Solid state processing		
Powder metallurgy	Al-MWCNT, Al-Si ₃ N ₄ , Al-SiC Al-Al ₂ O ₃	Simoes et al., 2014; Ma et al., 1996; Kang and Chan, 2004; Mahmoud et al., 2012.
Mechanical Alloying	Al-ZrO ₂ , Al-TiC Al-AlN, Al-SiC, Al-Al ₂ O ₃ , Al-BN Al-TiB ₂ , Al-Al ₃ Mg ₂	Dutkiewicz et. al., 2009; Wan-li, 2006; El-Daly, 2013; Tazari, 2017; Prabhu et. al., 2006; Poirier, 2010.
Cryomilling	Al-B ₄ C	Ye et al., 2006
Microwave Sintering	Al-SiC, Al-Al ₃ N ₄	Reddy et al., 2017; Mattli et al., 2019
Spark Plasma Sintering	Al-Al ₂ O ₃ , Al-SiO ₂ , Al-SiC, Al-AlB ₂ , Al-MgB ₂ , Al-CNT,	Dash et al., 2013; Cavalierea et al., 2018; Bathula et al., 2012; Kubota et al., 2008; Najimi and Shahverdi, 2017
Friction stir processing	Al-Al ₂ O ₃ , Al-Al ₃ Ti, Al-TiB ₂ , Al-SiC	Sharifitabar et al., 2011; Hsu et al., 2006; Maa et al., 2014; Mazaheri et al., 2011
Accumulative Roll Bonding	Al-SiC, Al-TiO ₂ , Al-B ₄ C	Alizadeh and Paydar, 2010; Soltania et al., 2012; Wagih et al., 2018; Yazdani and Salahinejad, 2011
Laser Cladding	Al-Al ₂ O ₃ , Al-SiC, Al-TiB ₂ , Al-TiO ₂ /B ₄ C	Han et al., 2017; Changjun et al., 2008; Xu and Liu, 2006; Masanta et al., 2009

Solid-state processing techniques are typically based on the conventional powder metallurgy route and its modified versions regarding powder size modification, compaction techniques, sintering methodologies, and secondary processes utilized for microstructure refinement. Material processing takes place below solidus temperature, and hence it reduces undesirable reactions between the matrix and reinforcements. In the conventional PM method, fine metallic powder and reinforcement particles in the desired proportion are mixed in a mechanical mixture. The mixed powder is then compacted using uniaxial/isostatic cold or hot compaction. Green compacts are then sintered, usually in an inert atmosphere for obtaining dense microstructure. Compacted specimens may require secondary processes such as extrusion, rolling, heat treatment for microstructure refinement, and uniform distribution of reinforcement particles. Powder metallurgy has benefits which include capability of producing near net shaped parts, possibility of incorporation of large volume reinforcement content and ability to manufacture parts in large batches. However it suffers from the limitation on the size of part, industrial scalability, flexibility in tailoring properties, complexity as well as relative cost of manufacturing and high porosity. Mechanical alloying (MA) improves compaction and has unique features such as forming nanometer-size mixtures of immiscible elements, uniform dispersion of intermetallic phases, solid solutions, and alloys. The process involves high-energy ball milling responsible for repetitive cold welding, plastic deformation-induced fracture, and rewelding of powder particles. Mechanical attrition in the presence of nanoparticles accelerates the fracture and welding process, and on reaching equilibrium, produces equiaxed, fine particles with random orientation. The powder is then compacted and sintered to produce bulk parts. It is a promising technique of nanocomposite fabrication that involves mechanochemical milling of various combinations of oxides, metals, and especially carbides. It gets influenced by processing parameters like miller type, ball-powder ratio, speed, time, process control agent (PCA), and milling environment. In conventional milling of the powder mixture, frictional temperatures induce severe recovery and recrystallization of microstructures. Low-temperature processing suppresses such an effect in cryomilling which is usually carried out in a cryogenic medium like liquid nitrogen. So cryomilling is beneficial in obtaining refined nanocrystalline grain structure more rapidly besides avoiding undesirable chemical reactions between reinforcements and matrix material (Ye et al., 2006).

Microwave sintering (MWS) is considered a unique technique that involves instantaneous conversion of electromagnetic energy into thermal energy for efficient volumetric heating of powder compact. It avoids variation of microstructure along with the thickness of the specimen as observed in any differential heating. Microwaves penetrate deep into powder compact, and the generated heat radiate outwards. MWS is found better for fabricating nanocomposites with enhanced properties due to merits like high heating rate, short processing time, and homogeneous microstructure. Spark plasma sintering (SPS), a novel technique is used for consolidating powders to relatively high density with fine crystalline structure by generating plasma spark between gaps of compacted powders via electric DC pulse discharge. The process is known popularly for low processing temperature, self-purification of the particle surface, and short sintering time compared to conventional PM. Effective consolidation of nanostructured Al alloy composites by SPS is done by optimizing process parameters like temperature, applied pressure, heating/cooling rate, and cyclic pulse duration. Friction stir processing (FSP), a relatively new process under developmental stage is employed for fabricating surface nanocomposites. Arora et al. (2012) published an exhaustive review paper on FSP. At first, a groove of the desired size is made in the composite. Later it is filled with the required amount of reinforcement particles. A blunt pin less non-consumable rotating tool is plunged into the work piece to close the groove encapsulating reinforcements inside. Later on, a rotating tool with a pin is pushed inside the surface and moved along the groove length to spread particles by intense stir action. The pin can be moved several times along the groove to improve the particle distribution. Successful fabrication of surface composite by FSP depends on processing parameters like tool size, speed, number of passes, etc. In accumulative roll bonding (ARB) process, metallic sheets are cleaned and then stacked with uniformly spread reinforcement particles in between. Later the sheets are rolled together to reduce the stacked thickness by up to 50% in a single rolling cycle. The roll bonded sheets are then cut into two pieces and stacked again for rolling to reduce the thickness by half. This process is continued several times and examined periodically to obtain uniformly dispersed particles embedded inside the bulk material. Laser cladding process is a relatively recent method of producing nanocomposites. In this effective method, the nanocomposite is developed by additively depositing a new layer onto the substrate by laser melting blown reinforcement powders or already preplaced powder bed. Rapid

heating and cooling experienced by deposited powder and substrate develop strong metallurgical bond between them forming cladded nanocomposite. It does not change the initial composition and properties of added materials. Different combinations of powder mixtures can be deposited on the substrate to develop a tailored surface with desired properties like improved strength, hardness, thermal stability, corrosion, and wear resistance. Selection of optimized process parameters such as laser power, speed, and the beam diameter is required to avoid melting of nanoparticles (Zhong et al., 2014). This process is in the developmental stage and issues like nanoparticle powder handling and delivery, agglomeration, particle dissolution, health hazards, fabricating 3D parts etc. are being addressed.

Table 1.2: Al nanocomposites produced by semi-solid and liquid state processing methods

Fabrication technique	Al nanocomposites	Researchers
Semi-solid state processing		
Compocasting	Al-Al ₂ O ₃ , Al-SiC	El-Mahallawi et al., 2012; Hoziefa et al., 2016; Jiang and Wang, 2015
Thixoforming	Al-SiC, Al-TiB ₂	Kandemir et al., 2014
Liquid state processing		
Stir casting	Al-Al ₂ O ₃ , Al-SiC	Hashim and Looney, 1999; Surappa, 2003; Zhang et al., 2015.
Electromagnetic Stir Casting	Al-SiC, Al/Al ₂ O ₃	Yu, 2010; Li et al., 2013
Ultrasonic Stir Casting	Al-SiC, Al-Al ₂ O ₃ , Al-B ₄ C, Al-TiB ₂ , Al-SiO ₂ , Al-GNP, Al-hBN	Dehnavi et al., 2014; Liu et al., 2014; Estruga et al., 2013; Mula et al., 2012; Salehi et al., 2015
Liquid Infiltration	Al-CNT, Al-SiC, Al-CuO	Zhou et al., 2007; Uozumia et al., 2008; Zhang et al., 2006; Ferguson et al., 2014
Disintegrated Melt Deposition and Spray Co-deposition	Al-ZrO ₂	Hemanth, 2009

Semi-solid method consists of processing the metallic systems in between solidus and liquidus temperatures, wherein the partial solid slurry contains nearly globular grains with 20 to 60% solid fractions. Due to semisolid conditions and low processing temperatures, it is possible to produce castings having less shrinkage pores and less thermochemical degradation to reinforcements. Two types of semisolid processing methods viz compocasting and thixoforming are seen for fabricating metal matrix nanocomposites. Compocasting, also termed as rheocasting involves producing semisolid slurry by lowering the molten metal temperature during the casting process itself to reach between liquidus and solidus line. In this condition, the required amount of preheated reinforcements are added into the slurry and stirred vigorously for uniform incorporation. Compocasting is found suitable for producing aluminum nanocomposite with improved mechanical properties due to refinement of grains. In thixoforming process, a solid feedstock or slug is reheated to a semisolid state and formed to shape in partially melted condition with liquid fraction between 30 & 50%. It can produce complex near net-shaped components using the thixotropic behavior of materials in semisolid conditions. It saves manufacturing costs. The thixoforming process outperforms traditional casting regarding reduced porosity because the semisolid metal flow is not turbulent but laminar.

In the liquid metallurgy route, the matrix material of composite is heated well above its melting point and then solid reinforcement particles are added from outside into it or created inside the melt by effecting thermochemical reactions between composite constituents. Nanoparticles are dispersed inside the melt by employing techniques like mechanical stirring, electromagnetic stirring, or ultrasonic vibrations. Liquid infiltration, disintegrated melt deposition are other liquid processing methods of composite fabrication. Although liquid processing is widely studied due to its relative simplicity and flexibility, it has some critical issues, especially in fabricating nanocomposites. As nanoparticles provide a large surface area, Van der Waals's force of attraction induces them to agglomerate near the grain boundaries and fail to disperse uniformly in the matrix, which effectively reduces their strengthening potential. It has been found that the aggregation rate of 20 nm size particles is four orders of magnitude higher than that of 1 μm size particles. Nanoparticles on account of large surface area increase the interfacial reactions manifold, producing reaction products that may be undesirable and spoil composite properties. Ceramics have limited wettability with liquid aluminum, which can

create poor interfacial bonding between particles and matrix. There is a critical size of nanoparticles below which, if added to the matrix deteriorates material properties due to the negative Hall-Petch effect. Also, there is a limit for the addition of nanoparticles in the liquid melt above which if added forms clusters reducing the effectiveness of dislocation hindrance and thereby lowers the mechanical strength. However researchers have shown that the homogeneous addition of nanoparticles into the matrix can dramatically improve the mechanical properties of alloys. Stir casting is a widely used liquid state processing method for simplicity and low cost. In the process, metal alloy ingots are heated for complete liquefaction inside the furnace crucible. The reinforcement particles are then dropped manually over the surface of melt which is then stirred for spreading the particles inside. A mechanical rod carrying impeller blades at the bottom is used for stirring the melt after particle addition. Stirring action creates a vortex inside the melt which helps to suck in particles due to differential pressure gradient. However, as mentioned earlier, it is usually difficult to distribute particles uniformly inside the melt because of their low wettability and tendency to cluster (Hashim & Looney, 1999; Surappa, 2003) while the situation aggravates further for nanoparticles due to the increased surface area. The large density difference between particles and alloy can make the situation even more challenging as the particle can start moving to float or sink the moment stirring is stopped. To tackle these issues, different ways and means have been tried like preheating the particles, coating or pre-treating them to enhance wettability, modified stirring (Hamedan & Shahmiri, 2012) introducing particles with the help of master alloy powder (Valibeygloo et al., 2013), the addition of Mg (Schultz et al., 2011) and K_2TiF_6 salt flux, etc. with some reported success. For better densification efforts like the use of melt degassing tablet, particle addition using argon gas-assisted injection, continuous supply of inert gas inside the furnace, bottom pouring, and vacuum-assisted casting, etc. are employed. Electromagnetic stirring, a novel method also known as induction heating, is used for grain refinement and homogeneous addition of nanoparticles into the metallic melts using an external magnetic field. In this process, electric current is passed through induction coils fixed around the crucible. It creates an alternating magnetic field introducing Lorentz forces in the melt. These forces generate vortex-type flow patterns and intense stirring action to disperse nanoparticles by breaking their clusters. The process parameters like stirring time, electromagnetic frequency,

temperature, and current intensity are to be controlled for best results. Ultrasonic stir casting is observed as the most effective method for uniform distribution of very fine particles by breaking their clusters in the melt, refined microstructure and improvement in wettability especially of ceramics in aluminum (Ma et al., 1995; Li et al., 2004; Xuan & Nastac, 2018). This process is employed for fabricating several aluminum based nanocomposites reinforced with SiC, Al₂O₃, B₄C, TiB₂, SiO₂, GNPs, h-BN etc. Researchers have reported superior particle incorporation, wettability, improved densification, grain refinement and mechanical properties, for instance 92% rise in hardness for just 2% Al₂O₃ (Mula et al., 2012) and 134% enhancement in tensile strength for just 5 vol% GNP (Alipour & Eslami-Farsani, 2017) incorporation. Ultrasonic processing produce sound castings on account of excellent degassing effect. In this process effective deagglomeration of nano size particles is accomplished by two effects such as acoustic streaming and ultrasonic vibrations. Because of these benefits ultrasonic stir casting is used in this experimental work. The basic details of the process and the fabrication procedure are discussed in chapter 2, section 2.1. This promising technique, however, suffers from the fact that a very large volume of the melt cannot be treated because of the need for a corresponding high ultrasonic power source which limits its industrial scalability. Ultrasonic treatment of continuously flowing liquid can be seen as a possible solution for scaling up. In liquid infiltration method, liquid metal is incorporated into the preformed porous solid of reinforcement under either the influence of applied pressure or allowed to seep in with time without external pressure. The slurry consisting of reinforcements and liquid binder carrier is formed to the required shape under pressure. Thereafter preform is heat treated and dried for its dimensional stability. During liquid infiltration process, preform is placed into die and liquid metal is poured over it. Melt is then forced to infiltrate the preform by applying ram pressure. Liquid infiltration process is also referred as squeeze casting and may take the form wherein the composite slurry of metal and reinforcements is squeezed into the die under pressure. Contact angle between melt and nanoparticle is required to be less than 90° to ensure wetting. In disintegrated melt deposition (DMD) process, the superheated and stirred mixture of metal and reinforcement is allowed to fall under gravity from crucible through small nozzle into a chamber filled with inert gas. The falling slurry is disintegrated by two argon gas jets arranged normal to the metal flow which then solidifies on a metallic substrate. Although

suitable for both Al and Mg alloys, it is specifically adopted for fabricating Mg based composites. It is because Mg is highly oxidisable and DMD process reduces formation of oxides in the casting. The cast specimen obtained by this process is usually extruded in order to reduce porosity. Spray co-deposition is a method close to DMD process. In this technique molten metal stream is allowed to fall into inert chamber and is incorporated with reinforcement particles sprayed onto it through jets of argon gas while simultaneously disintegrating the falling mass. Layers of fallen metal droplets on substrate create composite material after solidification. Various Al nanocomposites fabricated by different processing routes are presented in tables 1.1 and 1.2.

1.5 Tribological characterization of Al nanocomposites: a review

Comprehensive reviews on the dry sliding wear of discontinuously reinforced microcomposites are available in the published literature (Sannino and Rack, 1995; Deus et al., 1997) but none on the tribological behavior of aluminum matrix nanocomposites (AMNCs). It is commonly observed that the use of ultrafine and nanosized reinforcements for the metal matrix improves its mechanical properties especially strength to a great extent. A detailed review on the tribological investigations of the Al metal matrix nanocomposites indicated that wear and friction are influenced by many different interacting parameters. Extrinsic factors include externally applied load, speed, contact distance, dynamically modifying tribolayer on sliding surface, temperature etc. Intrinsic factors like process and processing parameters, reinforcement type, size, content, microstructure composition, heat treatment etc. decide tribological performance. Table 2.3 presents different parameters investigated by researchers for their impact on the tribological behavior of Al nanocomposites. Most of the studies have used laboratory scale wear test machines mostly of pin on disc configuration wherein the pin with flat, conical or hemispherical end made of the composite material is slid against steel counterface.

It is generally understood that the incorporation of reinforcement particles (ceramics, oxides, carbides; nitrides etc.) into the aluminum matrix improves its mechanical and tribological properties. Hence various researchers have incorporated increasing amount of hard or soft reinforcements into different Al alloys looking for its likely effect. Nemati et al. (2011) revealed decreasing wear rate of Al-4.5wt% Cu-TiC nanocomposites as the

nTiC content is increased up to 5 wt% with slight reduction for 7% at both (10, 20 N) loads. The significant improvement in wear resistance as compared to base alloy is attributed to the increased hardness due to uniform dispersion of hard carbide particles which act as load supporting elements protecting the surface against destructive action of abrasives, similarly as found with Al-TiO₂ (Nassar and Nassar, 2017) and Al-ZrO₂ (Ramachandra et al., 2015) nanocomposites. Effect of varying concentration of submicron alumina particulate in Al6061 alloy by Al-Qutub et al. (2006) revealed increase in wear resistance of 10%, 20%, 30% reinforced composites by 45%, 113% & 145% respectively. Whereas with just 3 vol. % reinforcement Moseleh-shirazi et al. (2016) observed Al6061/SiC nanocomposite to exhibit almost six times rise in hardness and reduction in volume loss by approximately 77% as compared to base alloy. Zaolriasatein et al. (2013) found that as the reinforcement content in Al-Al₃Mg₂ nanocomposite is increased from 0 to 5wt% and 5 to 10 wt%, wear coefficient get decreased by 47% and 11% respectively. Tavoosi et al. (2010) also reported reducing wear rate for Al-Al₂O₃ nanocomposites as the reinforcement content is increased from 4 to 16 wt%. Moazami and Akhlaghi (2016) found that increasing SiC reinforcement content from 2.5 to 5 wt% in Al5252 alloy provided thermal stability to the matrix, increasing its hardness and wear resistance but further reinforcement of 7 wt% decreased the hardness and increased wear rate which is attributed to the agglomeration of particles. Donthamsetty and Babu (2017) reported that with just 0.5 wt% SiC reinforcement, A356 alloy displayed increase in wear resistance by 53% and 47% when tested at 30 N and 40 N loads respectively with constant velocity of 4.187 m/s and sliding distance of 2000 m against EN32 counterface. Overall it is observed that investigators have tried incorporation of nanoparticles up to 30% and most have a common consensus on the trend of decreasing wear rate as the hard reinforcement content is increased in the aluminum matrix. But content beyond critical limit especially in the composites processed by liquid metallurgy route show deterioration of wear performance. It is due to the problems of agglomeration, porosity and weakening of particle matrix bonding. Several authors have investigated the reinforcement size effect on the tribological properties. Hosseini et al. (2010) reported significant effect of micro to nano size variation of alumina particle (60 μm, 1 μm, 30 nm) on the increased density and hardness of Al 6061-Al₂O₃ bulk composite which consequently decreased the wear rate. Durai et al. (2007)

also mentioned that decrease in the inter-particle distance due to the reduced size of the uniformly distributed particles increases hardness and wear resistance. Particle size significance on the abrasive wear behavior AA5083 alloy reinforced with equal volume fraction but varying sizes of boron carbide particles in the micron, submicron and nano scale range is evaluated by Nieto et al. (2017). It is stated that nanoparticles because of strong interfacial bonding require almost 11 times more force for their pullout from matrix as compared to micro particles having same volume fraction. Wear and friction behavior is significantly governed by the type of reinforcement used in the metal matrix. Except the mostly preferred silicon carbide and alumina, several other reinforcements from the carbide, boride, nitride and oxide categories are used for reinforcing aluminum matrix. Compatibility of reinforcement with the alloy matrix is an important issue of consideration. Especially in liquid metallurgy route there is the challenge of agglomeration and poor wettability of ceramic nanoparticles with molten alloy. The situation aggravates further when the difference between densities of ceramic particle and the base alloy becomes large. Particles either sink or float in the liquid metal and are pushed towards grain boundaries during solidification. Akbari et al. (2015) used two different type of nanoparticles, TiO_2 (4.23 g/cc) and TiB_2 (1.52 g/cc) to reinforce A356 (2.7 g/cc) matrix using stir casting process in order to study the nanoparticle capture during solidification and its effect on wear behavior. The van der Waals energy of composite systems for both TiO_2 and TiB_2 nanoparticles was found to be positive resulting in a tendency of particle rejection. But the force of nanoparticle rejection in Al- TiO_2 was found to be much higher than Al- TiB_2 composite system as the Hamaker constant of TiB_2 particle is close to that of liquid aluminum resulting in the favorable condition of TiB_2 particle capture. Only 2.1 vol% TiO_2 particles could be incorporated into alloy melt while 3.3 vol% TiB_2 out of 5 vol% were introduced, the remaining got rejected to the surface of molten composite. They also reported that under same test conditions, the wear resistance of Al- TiB_2 specimen was more than Al- TiO_2 specimen. Hybrid composites are designed to obtain application specific desired properties and as such their performance is governed by the relative amount and characteristics of the involved reinforcements. With an aim to use hybrid composite in braking system of automobile, Muley et al. (2015) reinforced LM6 alloy with SiC and Al_2O_3 nanoparticles in equal ratio. They found that better wettability with aluminum and high hardness make

SiC more effective than Al_2O_3 to resist wear. In another work Al-7075- Al_2O_3 -SiC hybrid composite is found to be more wear resistant than single reinforced Al7075- Al_2O_3 nanocomposite due to additional hard SiC phase (Kannan et al., 2018). Solid lubricants like graphite, MOS_2 , hBN have been used by researchers to bring in self-lubricating effect for reducing wear rate of MMCs both as single reinforcement and hybrid constituent. Ravindran et al. (2013) compared wear behavior of Al2024-5 wt% SiC nanocomposite with hybrid Al2024-SiC-Gr hybrid nanocomposites as well as base alloy. It is observed that wear loss of silicon carbide reinforced nanocomposite increased at all loads but was drastically reduced beyond load of 20 N when incorporated with graphite particles. In another work, Reddy et al. (2019) demonstrated that wear rate of Al6061T6-SiC-Gr hybrid nanocomposite is reduced by 73% due to addition of just 2 wt% nano graphite particles in the base alloy.

Processing method is also found to influence the mechanical and tribological characteristics of the metallic composites. Qu et al. (2011) found that friction stir processing developed a hard layer of more than 1 mm thickness on the substrate. It improved the wear resistance of Al- Al_2O_3 and Al-SiC nanocomposites by one order of magnitude and reduced friction by 40% without affecting ductility and conductivity in the substrate. Effectiveness of spark plasma sintering (SPS) technique for compacting mechanically milled mixture of Al5083 and SiC powder to the near theoretical density is demonstrated by Bathula et al. (2012). Nanostructured Al5083 alloy and Al5083/SiC nanocomposite displayed microhardness of 148 HV and 280 HV respectively with significant enhancement in wear behavior due to the uniformly dispersed ceramic particles, dense compaction and good interface between SiC and Al matrix. Accumulated roll bonding process employed by Darmiani et al. (2013) for fabricating Al1050/SiC nanocomposite also revealed homogeneously distributed and refined SiC particles in the matrix at the end of tenth ARB cycle that enhanced hardness of alloy by three times. Evolution of nanocomposite microstructure with strong particle-matrix bonding and interface integrity has found to be crucial in its tribological performance. Hosseini et al. (2012) also reported mechanical milling and hot pressing (MP) induced crystallization that witnessed reduction of aluminum grains from 45 nm to 38 nm as the reinforcement of n Al_2O_3 increased from 1 to 5 vol%. Evolution of microstructure with uniform particle dispersion as a function of stirring time was investigated by Akbari et al. (2013) for

A356-Al₂O₃ composite. EM micrographs displayed grain size reduction by more than half when melt was stirred for 4 minutes causing maximum hardness and wear resistance.

Load applied in the contact interface is one of the most important external parameters because severity of the tribological condition is signified by the product of load and velocity i.e. PV factor. Wear rate is found to increase with increasing loads (Al-Qutub et al., 2006; Durai et al., 2007; Abbass and Fouad, 2014) applied in 5 – 35 N range. Pal et al. (2018) and Manivannan et al. (2017) have reported decrease in the wear rate of nanocomposites when the load is increased from 10 to 40 N. Fale et al. (2015) identified load to be a strong factor deciding wear behavior for Al-AlN nanocomposites. In general, nanocomposites are found to sustain much higher loads before they start to exhibit severe wear. In the low load range they show abrasion wear behavior while at certain higher load transition to severe wear is seen witnessing material removal by delamination process. But this happens at much higher load as compared to the unreinforced alloys extending the realm of oxidational wear regime. Wear behavior as a function of sliding velocities (0.6 - 1.2 m/s) for AA6061 reinforced with TiC, Al₂O₃ and hybrid (TiC + Al₂O₃) nanocomposites was studied by Jeyasimman et al. (2014). All the nanocomposites indicated almost same wear rate at all the increasing sliding velocities for low load of 5 N. However considering higher loads (7, 10 N) monolithic composites displayed higher wear rates as compared to hybrid nanocomposite and were highest for the speed of 1.2 m/s. Worn surface examination carried out for all nanocomposites by scanning electron microscopy revealed different wear mechanisms as abrasion, delamination and oxidation with increasing sliding speed. Sliding distance is also studied as an influencing tribological parameter among other prominent parameters in several investigations. Siddesh kumar et al. (2016) observed sharp rise in wear rate of AA2219 alloy for sliding distance above 2000 m at all the tested parameters and attributed this behavior to the third body wear by loose debris trapped in the tribo couple. On the other hand nanocomposite indicated only a marginal rise in the wear rate with sliding distance. In another study specific wear rate of SiC reinforced A2219 alloy is found to increase linearly from 0.15×10^{-3} to 0.35×10^{-3} mm³/Nm with increasing distance up to 4000 m tested at constant speed 0.733 m/s and load 5 N (Murthy et al., 2016).

Table 1.3: Different parameters investigated for tribological characterization of Al nanocomposites by various researchers.

Parameter	Researchers
Reinforcement (type / size / content)	Akbari et al., 2015; Muley et al., 2015; Ravindran et al., 2013; Fallahdoost et al., 2016; Poovazhagan et al., 2016; Kannan et al., 2018; Reddy et al., 2019; Moazami and Akhilaghi, 2016; Hosseini et al., 2010; Nieto et al., 2017; Al-Qutub et al., 2006; Nemati et al., 2011; Zolriasatein et al., 2013; Ramchandra et al., 2015; Moslehshirazi et al., 2016; Alizadeh et al., 2017.
Processing method and its parameters	Kumar A. et al., 2017; Yuvaraj et al., 2015; Moghadam et al., 2016; Darmiani et al., 2013; Bathula et al., 2012; Sharifi and Karimzadeh, 2011
Microstructure / composition	Abdollahi et al., 2014; Lekatou et al., 2015; Akbari et al., 2013; Alizadeh and Nassaj, 2012; Hosseini et al., 2012
Applied load	Pal et al., 2018; Manivannan et al., 2017; Harichandran and Selvakumar, 2016; Siddesh Kumar et al., 2016; Fale et al., 2015; Amarnath and Sharma, 2013; Tavoosi et al., 2010; Durai et al., 2007
Sliding speed	Liu et al., 2010; Jeyasimman et al., 2014
Sliding distance	Zhou et al., 2007; Uozumia et al., 2008; Zhang et al., 2006; Ferguson et al., 2014
Temperature	Nemati et al., 2016
Heat treatment	Al-Qutub, 2009; Sameezadeh et al., 2011; Sahu et al., 2015
Wear products	Sharifi et al., 2011; Kalashnikov et al., 2015

Effect of heat treatment on wear behavior of nanocomposites is reported in few studies. Al-Qutub (2009) observed in a dry sliding wear test that the transition of wear mechanism of Al6061-Al₂O₃ nanocomposite from mild to severe wear is increased from 0.53 MPa to 0.71 MPa, an increase of about 30% due to a solution heat treatment. Sahu et al. (2015) on using same heat treatment cycle for Al-Al₂O₃ nanocomposites revealed increasing wear rates with increasing loads and speeds with similar trends for both heat treated and

non-heat treated samples. However, worn surfaces of heat treated samples revealed narrow grooves of less width indicating superior wear resistance. Qu et al. (2011) also found 30% rise in the wear resistance of post-FSP heat treated Al6061-Al₂O₃ surface nanocomposite in the ball on flat sliding test. Role of wear products generated in the sliding interface of a tribo couple to influence wear behavior is investigated in a couple of studies. Sharifi et al. (2011) observed formation of hard and characteristic dark transfer layers containing oxides of Al and Fe on the worn surfaces of nanocomposites. These oxides were said to act as an effective insulation avoiding direct metal to metal contact which resulted in the reduced wear rate. The authors concluded that the MML formed because of the process of mechanical mixing /oxidation was the key factor controlling wear mechanism for all nanocomposites.

Relative importance and percentage contribution of different wear test parameters on the wear behavior of composites is useful for designing products and operational settings to improve their life when subjected to tribological interactions. As such some researchers have used soft tools and techniques like Taguchi, ANOVA, central composite design (CCD), response surface methodology (RSM) etc. for optimizing the wear performance (Ambigai and Prabhu, 2017; Singh et al., 2018; Siddesh kumar et al., 2018; Ekka et al., 2015).

1.6 Corrosion of AMMCs

Corrosion is the process by which materials on exposure to certain environments develop reaction products on the surface which deteriorates and adversely affect their properties. Rusting of steel is common example wherein steel develops Fe₂O₃.H₂O on the surface when exposed to industrial atmosphere. Corrosion is undesirable as material gets consumed in corrosive environments leading to loss of performance and premature failure of component.

Aluminum, in general, is better at corrosion resistance due to the formation of corrosion-protective, self-healing oxide layer. But when alloyed or reinforced with the second phase, it becomes prone to corrosion attack due to heterogeneities created in the structure. Heterogeneities can exist both at microscopic and macroscopic levels. Corrosion depends on the synergistic effect of several factors like intermetallics, matrix-reinforcement

system (bonding, interfacial reactions/stresses, galvanic properties, etc.), reinforcement volume, grain boundaries, fabrication process, heat treatment, environment, etc. Although a large volume of research work is available on the mechanical and tribological behavior of Al composites (Bhoi et al., 2020), the same is not for corrosion performance. Most of the corrosion studies of Al composites are related to SiC and Al₂O₃ reinforcements (Verma et al., 2015; Rohatgi et al., 2018). Murthy et al. (2013) studied the corrosion response of Al6061/TiN (2 - 6 wt %) composites in NaCl media and found them more corrosion resistant than the matrix alloy. They reported that interfacial corrosion products decoupled TiN particles from the matrix, which eliminated the micro-galvanic effect. TiN particles acted as physical barriers to the process of pitting corrosion. Nie et al. (2019) saw improvement in the corrosion resistance of Al-TiB₂/TiC cast composite when the thickness of composite is reduced by 20 % through the hot rolling process. They attributed it to the enhanced particle-matrix bonding, uniform particle dispersion, less porosity, and grain refinement. But with further rolling reduction (40% to 90%), corrosion resistance decreased due to increased dislocation density and the concentrated internal stresses. However, even 90 % rolled composite plate reflected better corrosion resistance than the unrolled cast alloy. El-Aziz et al. (2015) observed significant improvement in the corrosion resistance of Al-Si alloy for the addition of Al₂O₃ particles up 20% but not for further addition. However, when the composites were heat-treated, their corrosion resistance further improved with a striking reduction in the pitting behavior. They linked this improvement to the uniform particle spread and the formation of corrosion protective layers such as Al hydroxide (Al(OH)₃), bayerite (Al₂O₃.3H₂O), and boehmite (Al₂O₃.H₂O) on the composite surface. Recently Dinesh Kumar et al. (2021) investigated the influence of ZrB₂ (5 to 15 wt. %) on the corrosion response of Al7178 matrix in 3.5 wt% NaCl. Corrosion resistance improved as ZrB₂ particles reduced the reactivity of the Al matrix. The formation of the β phase at the grain boundaries was also held responsible besides the positive effect of strong particle-matrix bonding. They observed decrement in the corrosion pits and cracks with increasing ZrB₂ content. Gurrappa and Prasad (2006) observed degradation in corrosion behavior of Al-4Cu-1Mg/SiC composites with increasing SiC (5-35 vol%) content in the simulated marine environment. SiC/Al interfaces identified as the preferential sites for pitting corrosion due to the galvanic effect. They detected bigger pits for base alloy, while composite surfaces

revealed a large number of smaller but shallow pits. On the contrary, Kiourtsidis and Skolianos (1998) found no galvanic effect between SiC (8-24 vol. %) and squeeze cast Al2024 alloy in the aerated 3.5% NaCl solution. Further, they revealed a relatively more number of pits in base alloy while pits in the composites were of less depth. They described corrosion by two anodic reactions viz corrosion of α solution near Al_2Cu region and pitting of dendritic cores. SiC content did not affect the corrosion performance of the base alloy. Recently, in another research, Sharma et al. (2019) found intergranular corrosion for both cast and friction stir processed (FSPed) Al-TiB₂ composites in NaCl corrosive. Composites were less susceptible to intergranular corrosion than the alloy matrix. But they did not find pitting corrosion behavior in the cast as well as FSPed samples. Thus it implies that corrosion studies of Al micro composites have produced contradictory results with no particular consensus (Loto and Babalola, 2019). Hence more studies are required for better understanding of corrosion behavior, and the area is still wide open.

1.7 Scope of the work

Automotive and aerospace industries are facing the challenges of pollution norms, fuel economy, and increased safety. Besides, more advanced features of comfort and luxury are desired by passengers at competitive cost. Hence there is continuous research on developing novel light-weight materials with desired and tailored properties. Existing literature indicate that metallic composites with ceramic reinforcements can satisfy the growing demand of varying functional requirement of materials. Judicious selection of matrix, reinforcement and careful processing is found to effect exciting improvement in the properties of metal matrix composites. Aluminum alloys have become a popular pick among different light weight metals for use as matrix material. It is because of the several desirable properties like low weight, good strength, corrosion resistance, infinite recyclability, casting ease and low cost availability. Different compatible particles among various carbides, borides, nitrides and oxides are used for reinforcing the aluminum matrix. Aluminum matrix nanocomposites (AMNCs) are reported to exhibit exceedingly better properties than micro composites and unreinforced monolithic alloys. Although microcomposites are now being commercially made available and used on increasing scale, the development of metallic nanocomposites is still in its infancy. Nanocomposites

have become one of the rapidly growing areas of material research due to the parallel progress in nanotechnology. The properties targeted for improvement in Al composites are: tensile and compressive strength, ductility, fatigue, creep strength, high temperature mechanical properties, thermal shock resistance, wear and friction behavior, scratch resistance, machinability, and corrosion resistance. Several publications have revealed that the tribological performance of Al alloy gets improved due to ceramic reinforcements. Friction and wear properties are governed by several extrinsic and intrinsic operating parameters like load, speed, temperature, tribolayer, reinforcement, fabrication process, microstructure, etc. However nanocomposite fabrication is a relatively complex issue. Due to large surface area lighter nanoparticles tend to form clusters near grain boundaries under the influence of Van der Waals force of attraction. Limited ceramic wettability with Al and possibility of the detrimental reaction products are other issues to be tackled carefully. Hence after fabrication the nanocomposites are first examined for particle distribution, material composition, and the overall microstructural integrity. Once the compatibility of the selected reinforcement with the Al matrix is established, then the composite is characterized for properties like microhardness, nanohardness, density, porosity, elasticity, etc. Mechanical behavior for different loading conditions viz tensile, compressive, fatigue and creep, etc. is also studied. Tests under adverse conditions like corrosive environment, high temperature are also performed later. Al composite is designed and aimed to be used in applications like engine block, brake system components, transmission parts, etc. So it is greatly required to evaluate its suitability as tribo material in various operating conditions. Tribological studies are essential to extend the service life and reliable performance of components as well as to reduce their maintenance costs.

In the present study, boron carbide (B_4C) is used as reinforcement for AlSi12 (LM6) alloy. Ultrasonic vibration assisted stir casting is used for fabricating the composites. Composites are initially characterized for density, porosity, microhardness and microstructural stability for ensuring particle inclusion and distribution. Metallurgical examination is performed and the observations are compared with the published results on similar materials for validating the fabrication process. Later on a detailed investigation of the tribological performance is carried out by considering several parameters (reinforcement content, load, speed and sliding distance) at room temperature

and elevated temperatures. The results obtained are compared with the base alloy. Nanoindentation and scratch tests are performed in detail to understand the micro scale behavior. Finally corrosion response is evaluated in 3.5% NaCl solution because metal/ceramic composites generally are prone to degradation in corrosive environments.

1.8 Outline of the thesis

The present thesis contains seven (07) chapters. The first chapter introduces the topic, describes aluminum matrix composites and presents literature reviews on the fabrication and tribological performance of aluminum metal matrix nanocomposites (AMMNCs). Fabrication of the Al/B₄C nanocomposite is detailed in second chapter along with different tools and techniques used for the characterization purpose. In third chapter results of the microstructural examination and basic properties like density, microhardness are presented and discussed. Detailed investigation on the tribological behavior of the fabricated composites, base alloy at room and elevated temperatures are respectively presented in chapter 4 and chapter 5. Nanoindentation, scratch and corrosion behavior of the developed nanocomposites is discussed in chapter 6. Finally in chapter 7, the conclusions of the present work are mentioned and the future scope is projected.

1.9 Closure

In the first chapter introduction to metal matrix composites and the need for tribological assessment is emphasized. Extensive literature reviews on the fabrication and tribological characterization aspects of Al metal matrix nanocomposites are presented. Past work on the corrosion behavior of Al composites is also given. Finally the scope of the present work and the structure of the thesis are presented.

“This page is left intentionally blank”

Materials and methods

2.1 Fabrication of Al-B₄C nanocomposites by ultrasonic stir casting

Metallic composites can be manufactured by several different methods as described in detail in chapter 1, section 1.4. Among those all ultrasonic stir casting process is better especially for nanocomposites due to many distinct advantages. After first successful attempt of this process in 2004 for fabricating Al nanocomposite, only in recent times the fabrication attempts are increased in detectable number (Yang et al., 2004; Liu et al., 2014; Vishwanatha et al., 2017; Srivastava and Choudhari, 2016, 2018). Researchers have a common consensus on the benefits of this process such as grain refinement, uniform particle dispersion, improved ceramic wettability, least porosity, great improvement in mechanical properties etc. Ultrasonic stir casting involves treating nanocomposite melt by ultrasonic waves with an approximate frequency of 20 kHz using high power density ultrasound (100 W/cm²). A typical schematic of the ultrasonic stir casting process is shown in Figure 2.1(a). Sonotrode made of titanium or niobium alloy on account of high-temperature stability is dipped in the melt to pass in high-frequency ultrasonic waves. It gives rise to two principal effects in the melt called cavitation and acoustic streaming. During the negative part of the ultrasonic wave, air bubbles are created in the melt under tensile stress. Under a positive cycle, bubbles shrink under the compressive stress of waves. Air entrapped in voids of clusters is believed to provide nucleation sites for bubble growth. On reaching critical size bubbles burst to create local microsites of very high temperatures (5000°C) and pressures (1000 atm) called hot spots. This effect of formation and collapse of transient hot spots is called as cavitation effect which can clean the particle surface for improved wettability. Due to the high-pressure gradient in several small places in the bulk melt, a strong macroscopic flow circulation effect is created called acoustic streaming which helps in dispersing loose particles as shown in Figure 2.1(b). Moreover, as the melt is not agitated hence air entrapment is diminished.

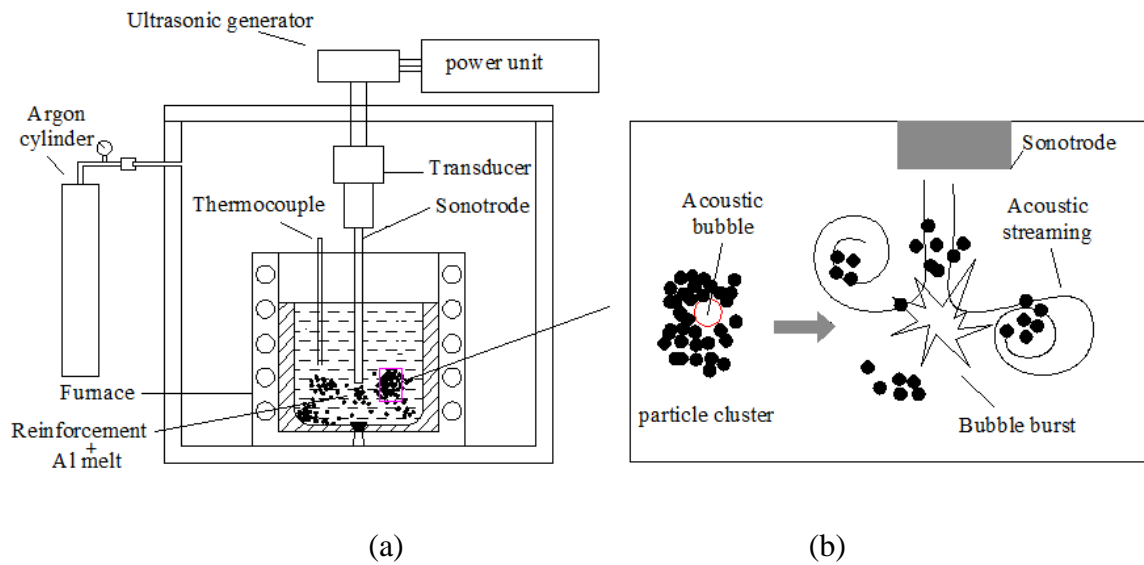


Figure 2.1: Ultrasonic stir casting (a) Process schematic; (b) Mechanism of particle deagglomeration

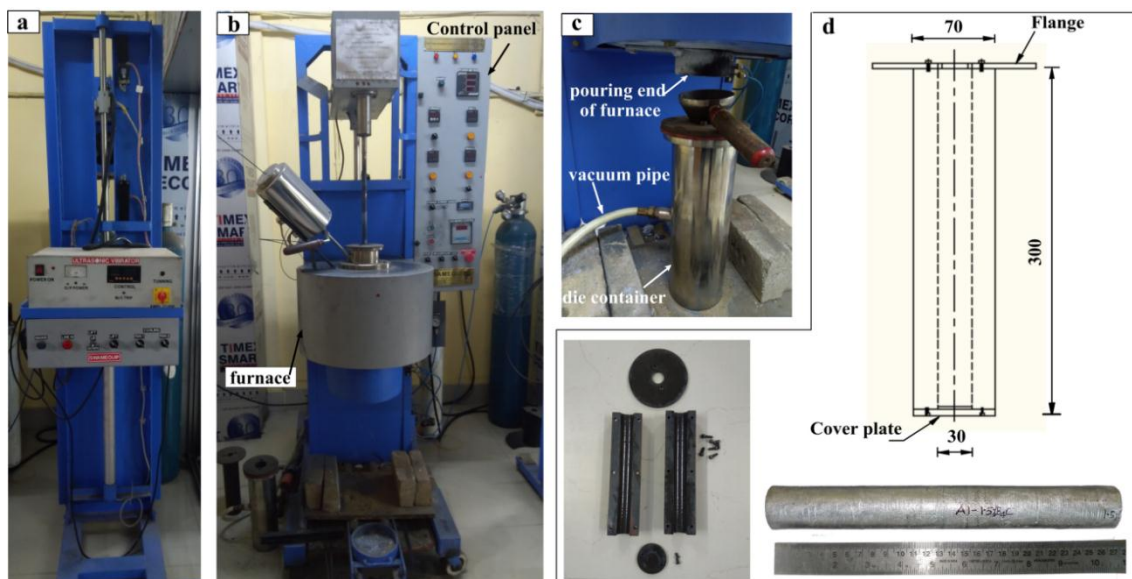


Figure 2.2: (a) Ultrasonic vibrator, (b) stir casting unit, (c) melt pouring arrangement, (d) die drawing, disassembled die and fabricated cast specimen

Fabrication of Al-B₄C nano-composites is carried out using bottom pouring type stir casting furnace (developed by SWAMEQIP, India) with ultrasonic vibrator and vacuum

casting set up. A combination of mechanical stirring and ultrasonic vibration is employed to produce Al-B₄C composites. Different properties of the contributing materials i.e. base (AlSi12) and reinforcement (B₄C) used are listed in Table 2.1. Commercial Al-12Si aluminum alloy is used because of its good casting characteristics and better wear resistance. Chemical composition of the AlSi alloy is shown in Table 2.2.

Table 2.1: Properties of Al alloy and B₄C reinforcement

Material	Al-Si12 [BS 1490:1988]	B ₄ C (Thevenot, 1990)
Density (g/cc)	2.7	2.52
Hardness	68 (H _{V0.1})*	30 GPa
Elastic modulus (GPa)	71	450
Melting point (°C)	575	2445
Thermal expansion coefficient (/ °C)	20 x 10 ⁻⁶	5 x 10 ⁻⁶
Thermal conductivity at 25° C (W/m.K)	142	30 - 42

*experimental determination in this work

Table 2.2: Composition of Al-Si12 alloy

Element	Si	Fe	Mn	Mg	Ni	Others	Al
Wt. %	12	0.6	0.4	0.1	0.1	0.65	Balance

Figure 2.2 shows the ultrasonic stir casting setup and a fabricated sample nanocomposite. The limiting operating temperature of this furnace is 1000°C. Initially the purchased Aluminum alloy (LM6) ingots are cut and pieces weighing 500 grams are placed inside the furnace for melting. Melting temperature of the furnace is kept constant at 750°C. This melting temperature is selected to maintain better melt fluidity and to minimize undesirable reaction products as per Al-B₄C reaction chemistry (Fyzik & Beaman 1995; Viala & Bouix 1997). Boron carbide powder in proportionate amount (2.5 grams for 0.5wt% composite) is weighed by digital weighing machine and placed inside the particle pre-heating furnace. Preheating of particles is essential to remove moisture and it

improves their wettability with the molten Al alloy. Preheating of nB_4C particles is done at $300^\circ C$. When the metal became molten, mechanical stirrer is introduced to create vortex in the melt which is continued for 05 min. Stirring speed was maintained constant at 350 rpm. Thereafter preheated particles are introduced into the melt near vortex. Mechanical stirring is again started and continued for 15 min at 350 rpm. Then mechanical stirring is discontinued and ultrasonic sonotrode is placed inside the melt pool at $2/3$ rd depth of crucible. Ultrasonic power supply generated very high frequency electric energy of 20 kHz on receiving the conventional 230 V, 50 Hz input power. High frequency energy was then converted to near about 70 micron vibrations at the end of sonotrode horn for ultrasonic melt processing. Composite melt is thus subjected to ultrasonic stirring for 05 min. Meanwhile a cleaned split die is placed inside a chamber connected to vacuum pump. Die preheating is done at $300^\circ C$. Die heating is done to avoid particle segregation near die wall due to chilling effect. Die surface from inside was coated with liquid graphite so as to protect it from erosion and eventual wear. Temperatures in the furnace and preheating die are monitored by k-type thermocouple. At the end of ultrasonic cavitation assisted stirring, the split die is placed at the bottom of furnace. The vacuum pump started, plug at the bottom of the furnace is removed and the molten metal is allowed to fall under gravity to fill the split die. To remove gases from the cast, 10^{-2} mbar vacuum condition is generated using vacuum pump. Die is allowed to cool in air and then the fabricated cylindrical composite specimen is taken out.

By varying the reinforcement content, the other three variants (1.0 wt%, 1.5 wt% and 2.0 wt %) of the composite specimens are produced following the identical procedure. Base alloy is also developed by the same process so as to have its identical effect on the microstructure. Different parameters used in the fabrication process are based on the previous experiences (Poria S et al., 2018; Pal A. et.al. 2018), and various studies reported in the literature on Al-ceramic composites (Li J. et. al., 2018; Srivastava & Choudhari 2016; Raj & Thakur 2016; Toptan et. al., 2010). These utilized parameters are listed in the Table 2.3.

Table 2.3: Parameters used during fabrication

Parameters	Value
Melting temperature inside furnace	750° C
Particle preheating temperature	300° C
Die preheating temperature	300° C
Thermocouple	K type
Material of mechanical stirrer	Stainless steel
Stir blade angle	45°
Stirring speed	350 rpm
Mechanical stirring time	05 – 15 min
Ultrasonic horn	Titanium alloy
Vibrations at horn tip	70 microns
Ultrasonic stirring	5 min
Die	Cast Iron, (ø50 X 300 mm), split type
Die vacuum	10 ⁻² mbar

2.2 Density and porosity measurement

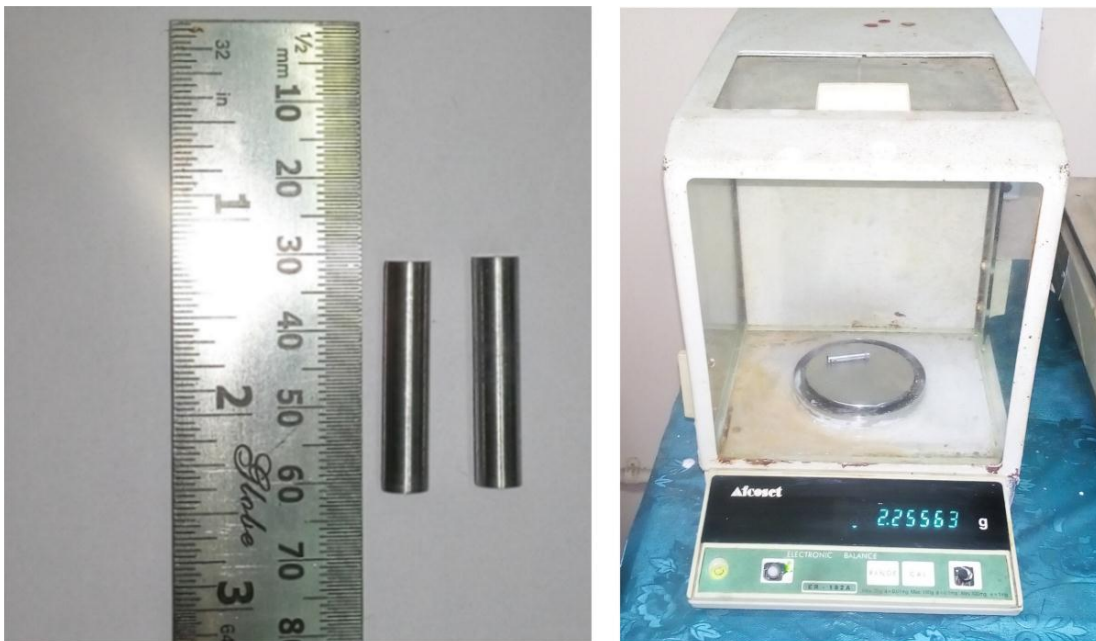
Cast specimens may suffer with defects like bow holes, subsurface cracks, etc., if the processing conditions are not optimum or the material combinations do not have requisite compatibility. So it is necessary to check the soundness or quality of the fabricated composite specimens. The first obvious test is density and porosity measurement and hence taken up in this study. Fabricated cast bars are machined to produce samples of 6 mm diameter and 30 mm lengths as shown in Figure 2.3 (a), and are taken for density and porosity measurement. Experimental density of cast composites is measured by Archimedes principle. To cross confirm, it is also measured by weighing 10 samples of each variant of the composite and averaging the results. Mass of the specimens is measured by a sensitive electronic balance Afcoset ER-182 A (Figure 2.3 b). Volume of the cylindrical pin comes out to be 0.8482 cm³. Using mass volume relation, the experimental density of each composite material is determined. Theoretical density of aluminum (LM6) base matrix and boron carbide particle is taken as 2.7 g/cc (Muley A.

V., 2015) and 2.52 g/cc respectively. Theoretical densities of composites are measured by using the rule of mixtures.

$$\text{Rule of mixtures: } \rho_c = \rho_m w_m + \rho_r w_r. \quad (2.1)$$

Symbols ρ & w in above relation indicate density and weight fraction of the phases involved while subscripts c , m & r refer to the composite, matrix and reinforcement respectively. Based on the experimental and theoretical densities, the porosity of fabricated samples is determined using following relation,

$$\% \text{ Porosity} = [(\text{Density}_{\text{Theoretical}} - \text{Density}_{\text{Experimental}}) / \text{Density}_{\text{Theoretical}}] * 100 \quad (2.2)$$



(a)

(b)

Figure 2.3: (a) Typical sample for density measurement, (b) weighing machine

2.3 Microhardness testing

Hardness of the material is its ability to resist scratch or indentation. Material hardness is of high and critical significance especially in applications involving surface contact and relative motion of the component parts. Hardness influences the surface wear, performance and life of tribological units and systems. Hence every material aimed for

tribological applications is required to be evaluated for the desired hardness. Metal matrix composites are becoming popular due to light weight and enhanced hardness. These materials are expected to reflect uniform hardness but that gets influenced by the distribution of hard particles in soft matrix. Hence hardness of metallic composites is evaluated by applying very low loads in microhardness testers. Bulk hardness of material is generally differentiated into three types based on the indentation depth (d) such as nano-hardness ($d < 1 \mu\text{m}$), micro-hardness ($d = 1\text{-}50 \mu\text{m}$), and macro-hardness ($d > 50 \mu\text{m}$). Suitable load is selected to reach the corresponding indentation depth based on the material being tested. Being easier to perform, Vickers hardness test is popular among researchers. Also the hardness measured by this test is independent of the size of the indenter and the applied load. Further the same indenter can be used for different materials irrespective of their hardness. In this method, a square based pyramidal diamond indenter (as in Figure 2.4) is forced into the test surface, and after its removal, the lengths of the two diagonals of the projected area of indentation are measured to determine the Vickers hardness number. The applied force in Vickers test varies between 1 gf to 120 kgf while the indentation time is limited to 10 to 15 secs.

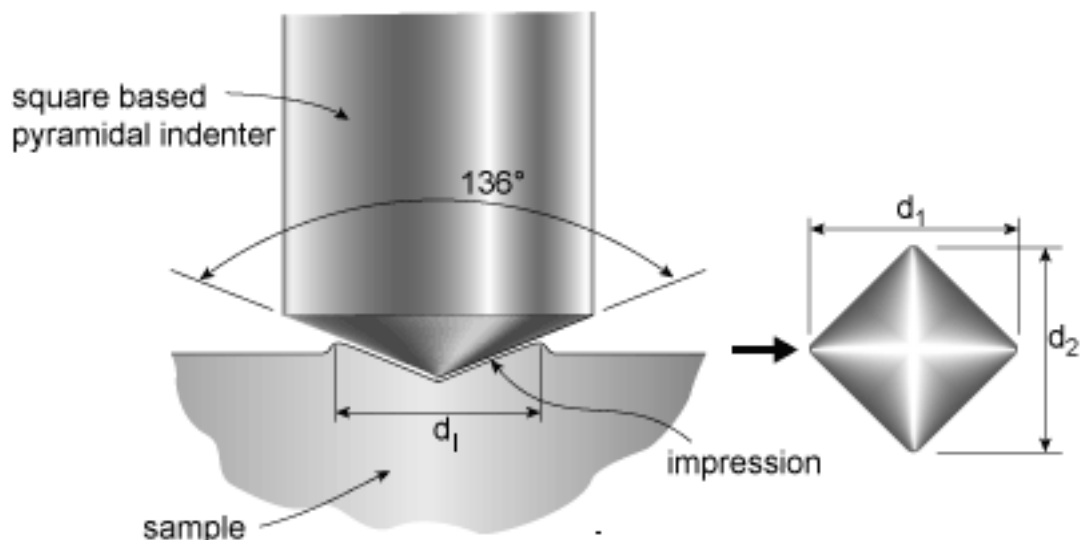


Figure 2.4: Vicker's indentation and diagonals of the impression

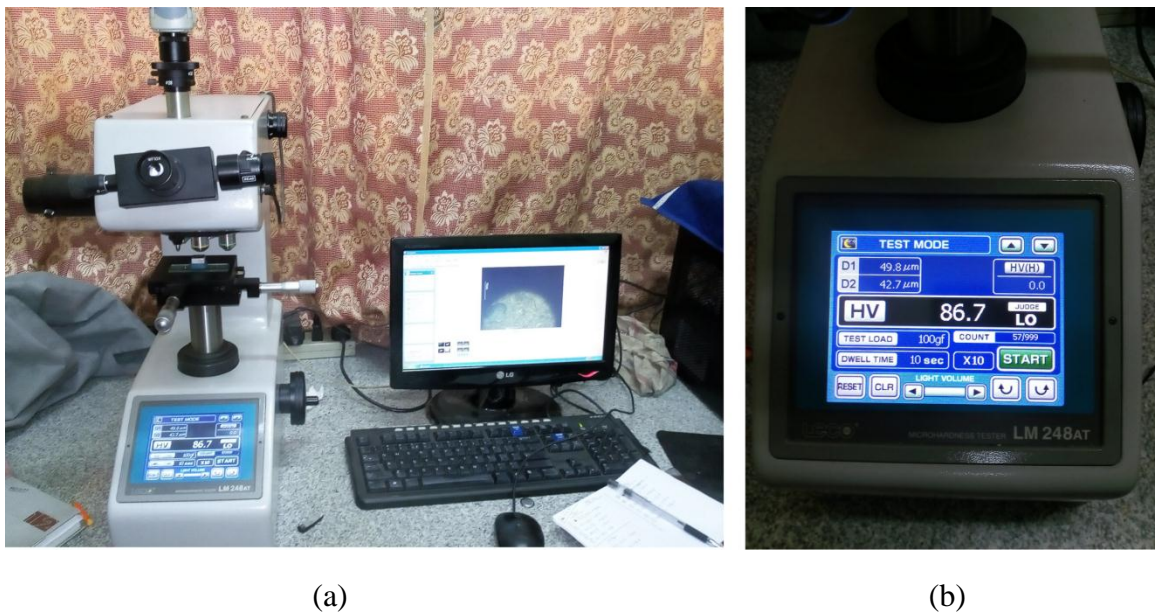


Figure 2.5: (a) LECO Microhardness Tester, LM248AT; (b) display of hardness (HV)

In the present study, Vickers Microhardness is measured by using LECO Microhardness Tester LM248AT (Figure 2.5a) as per ASTM E384-17 standard. 100gf load is applied with dwell time of 10 seconds at five random places on the composite. Prior to tests the test surfaces of the samples are polished using SiC grit papers and then subjected to machine polishing. Diagonal ends of the indentation impression are selectively marked using precision micrometer by looking through the eyepiece. Dedicated software installed on the computer connected to the microhardness tester digitally displayed the hardness value. Displayed hardness values are analytically cross-examined. Vickers Micro indentation hardness is calculated using indentation test forces in grams-force and average length of indentation diagonals in micrometers by following relation:

$$HV = 1854.4 * [F / (dv)^2] \quad (2.3)$$

Where F = indentation force (gf), dv = mean diagonal length of indentation impression (μm). Average of five readings is reported as the bulk hardness of the composite sample.

2.4 Microstructural examination

After knowing that the fabricated materials are sound with no manufacturing defects, the next important step was to investigate the microstructural details. Material

characterization is essential to verify that the chemical composition, grain size, structure and distribution of the phase elements are as similar as desired. Further it helps to understand the material properties, behavior and performance to certain extent. Microscopic techniques are hugely popular in this regard. These are useful to quickly determine the relation between material structure and the properties. In the field of material research microscopic techniques are at the forefront wherein newer combinations of material properties are examined and developed. Test samples are carefully prepared by standard metallography. Different tools like optical microscope, scanning electron microscope, X-ray diffraction, Raman spectroscopy, atomic force microscopy etc. are available for microstructure evaluation. The objective of the present microstructural study is to examine the distribution of reinforcement particles, grain structure, and identification of phase elements in the fabricated composite structures.

2.4.1 Metallographic sample preparation

Samples for microstructural characterization are prepared by following ASTM standard E3-11. First the fabricated cast materials are cut carefully to get the test samples of required size. Samples are obtained from various places of the cylindrical castings so that the test surfaces do not reveal biased information about the particle distribution. Samples are then cleaned, mounted and subjected to polishing. Machine polishing is done using diamond slurry on Struers Tegramin-25 machine. Finally, etching of the polished test surfaces is done. In general Keller's reagent is found suitable for observing surface structures of Al alloys and cast aluminum specimens (Tarn and Walker, 1991). Researchers have tried different etchants without specifying a particular one for Al/Ceramic composites. However, especially for Al-12Si/B₄C composites, Hemanth J. (2005) has tried several etchants and found that Keller's reagent (2 ml HF, 3 ml HCL, 5 ml HNO₃ and 190 ml distilled water) is the best among all, hence used in this study.

2.4.2 Optical, FESEM-EDX Study

Optical Microscope is used to observe the general distribution of phase elements in the microstructure. It is useful to understand the modification of material structure due to incorporation of a different phase. But due to magnification limits, optical microscope is

not suitable to detect very fine particles in the submicron range although it can easily detect micro scale particle clusters or agglomerations. In this study microstructural examination of images up to 1000X magnification is done using optical microscope Leica DM2700 M. Scanning electron microscopy is an effective tool for observing the microstructure at great details with a resolution around 1 nm at high magnification (50 KX). In this a beam of electrons is allowed to incident on the sample surface coated with a thin conductive material. As a result, signals in terms of the reflected secondary/backscattered electrons or characteristic x-rays are developed. These signals representing surface structures are captured by detectors to produce images on the computer screen. Light elements (atomic number < 9) are difficult to detect in the most common SEM machines, especially when heavy elements are present in the material composition. In this regard, SEM machines having field emission gun (FEG) called as field emission scanning electron microscope are better suited. These machines are capable of detecting light elements (using low accelerating voltages) in a variety of materials and provide excellent resolution imaging with different contrasting methods. Hence for detecting B₄C (light elements B & C) FESEM is used in this study. Apart from imaging, FESEM is superior for compositional analysis of material using an energy dispersive spectroscopy attachment. In EDS, when X-ray photon hits the semiconductor detector to knock out electron, some energy is consumed. By measuring the current produced, the original energy of photon is measured and as it is element specific, the corresponding element is identified. Thus the X-rays produced by heating the beam of electrons on the material surface are element specific and called as characteristic X-rays. Typically EDX spectrum is displayed as a plot between X-ray counts and energy (in keV). Besides the graph of elemental peaks, the % of various elements is obtained in EDX analysis. Further, in EDS elemental mapping is possible which shows distribution of X-ray counts in the acquisition by unique colors. It helps to identify the position and spatial arrangement of different elements in the sample. Thus both qualitative and quantitative evaluation of microstructure can be effectively done in FESEM. The elemental compositions in the tested surfaces are also examined through FESEM. The roughness of worn out test surfaces are examined for topographic details using 3D optical profiler. Different equipments used for the microstructural studies are presented in Figure 2.6.



(a) Optical microscope (Leica DM 2700 M) (b) FESEM (JEOL JSM-7610F)



(c) FESEM (ZEISS GeminiSEM 300)

(d) 3D surface profiler
(Bruker, ContourGT-K 3D)

Figure 2.6: Equipments used for microstructure examination in this study

2.5 Dry sliding tribological testing

The main focus of the present experimental research work is to study the wear and friction behaviour of the fabricated composites and Al matrix alloy under dry sliding conditions. Two bodies kept under continuous sliding contact encounter frictional resistance. The frictional forces in the interface are influenced by several working parameters like load, speed, contact duration etc. and decides the wearing of sliding bodies. Wear is an important aspect that decides the functionality and life of the

components in use. Hence careful evaluation of the impact of such factors on the tribological behavior of the newly developed composite materials is essential. Several laboratory experimental methods are in use for checking the sliding wear. Important aspects in a tribological test are: materials of the trio pair, contact geometries, applied contact pressure, speed, and environment. Different geometries used in a sliding tribo test are: pin-on-disc, block-on-ring, pin-on-reciprocating flat, ring-on-ring, twin disc etc. A dedicated instrument used for such experimental test is called as tribometer or tribotester. Two types of tribotesters are used in this study to evaluate the tribological behavior of cast composites.



Figure 2.7: Pin-on-disk tribotester (TR-208-M2, DUCOM)

2.5.1 Pin-on-disk wear and friction monitor

For room temperature dry sliding wear test pin on disk tribotester (TR-208-M2) is used. The test unit is shown in Figure 2.7. The test is conducted according to ASTM G99-05

standard. The work sample of cylindrical shape is held normal against the rotary counter disc made of EN31 material (Hardness 63 HRC). Hardness of the counterface is much higher than the general hardness of the test material. Loads are applied manually by putting dead weights on the pan attached to the loading lever. Speed and the duration of test are set by the control unit attached to the interfaced computer through dedicated software. Frictional force is measured by using a beam type load cell (range of 0 - 100 N) with accuracy of $0.1 \pm 2\%$ N. The installed software continuously displayed the real time variation trend of the test material friction coefficient. The data recorded during the entire test is utilized to plot the graph by the installed software. After each test the mass loss of the specimen is measured by a sensitive digital balance. Wear rate is then determined by dividing mass loss by sliding distance.

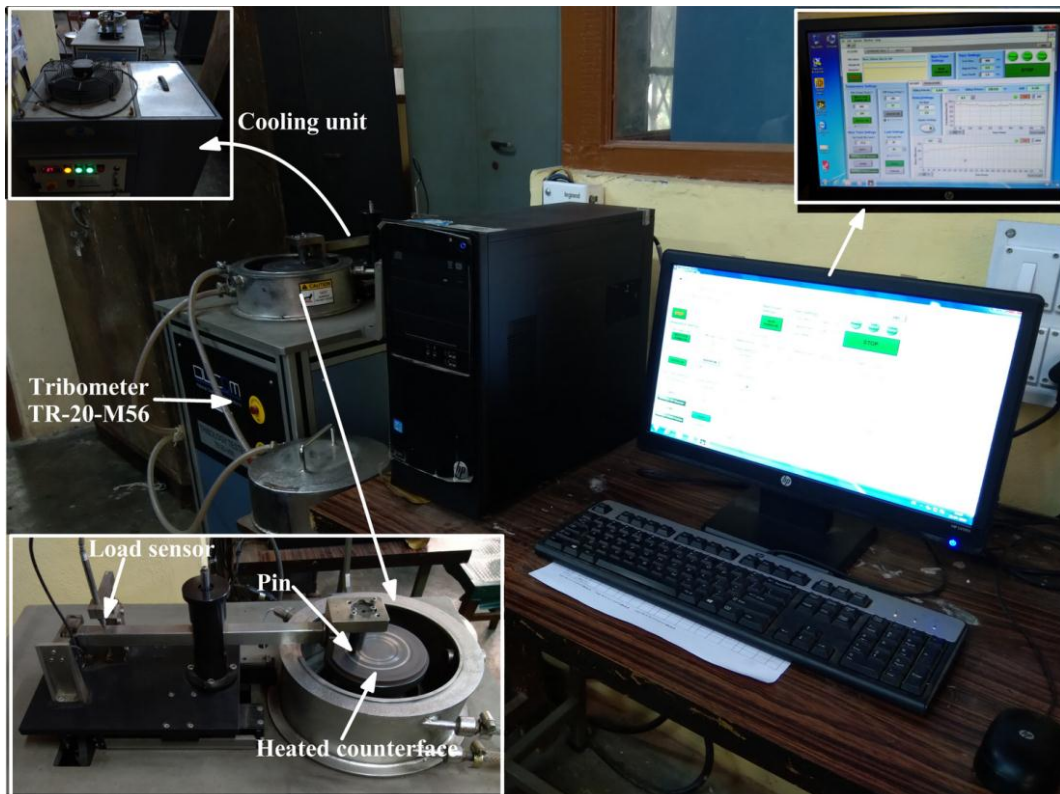


Figure 2.8: Elevated temperature POD tribotester (TR-20-M60, DUCOM)

2.5.2 High temperature tribology tester

Another set of tribological tests at high working temperatures are performed using a different tribotester setup (TR-20-M60 DUCOM, India) as per ASTM G99-05 standard.

The equipment is presented in Figure 2.8. The general working of this tribotester is similar to the pin-on-disc set up explained earlier. The major difference here is that either the pin sample or the counter face disc can be heated to the desired temperature to simulate the high temperature sliding environment. For this purpose an induction heater of beryllium copper coil having 15 kVA heating capacity is incorporated in the set up. Maximum temperature that can be reached is $975^{\circ}\text{C} \pm 1^{\circ}\text{C}$ and it is measured by a non-contact type pyrometer. The desired temperature can be set and maintained throughout the test period. In this study counter face disc is heated at different temperatures. Once the disc is set to desired temperature the test pin sample is brought in conformal surface contact against it. Thereafter the load is applied and the test is performed by setting speed and sliding duration. Force of friction is measured by a button type load cell of 10 kg capacity. Software installed on the interfaced computer is used to plot friction coefficient against sliding time. Wear rate is calculated by mass loss method.

2.6 Nanoindentation testing

Nanoindentation is a popular technique used to determine properties like hardness, modulus, fracture toughness, creep resistance, etc., at nano/micro-scale in the bulk matrix and thin films. In this method, imaging of the indent is not necessary and the contact area is obtained indirectly from the penetration depth. As indentation depths are small, the surface roughness (variation of asperity height) becomes crucial and may introduce errors in measuring hardness and modulus. For reducing the uncertainty of measuring contact area below 5%, indentation depth has to be 20 times greater than the roughness of the test surface (Fischer-Cripps, 2011). So after trial indents, a higher load of 50 mN was selected for indentation in this study. Secondly, the test surfaces of around 100 nm roughness were prepared by standard metallography. Surface profiles and roughness values were examined with ContourGT-K 3D (Bruker) microscope. Figure 2.9a-b shows a typical test sample and the indentation pattern. A sample measurement of test surface profile along with corresponding roughness (Ra) value is presented in Figure 2.9c. Measurement of nano hardness and elastic modulus was done using a nanoindentation tester (Hysitron Inc Minneapolis USA, TI900) equipped with Berkovich diamond indenter (Figure 2.10a). The instrument is capable of dynamic measurement of modulus/hardness of thin films and bulk, multiphase, nanostructured materials. It can work in low load range up to 9.5 mN

and high load range up to 500 mN. Before commencing tests, the equipment was calibrated with a standard procedure using a quartz sample.

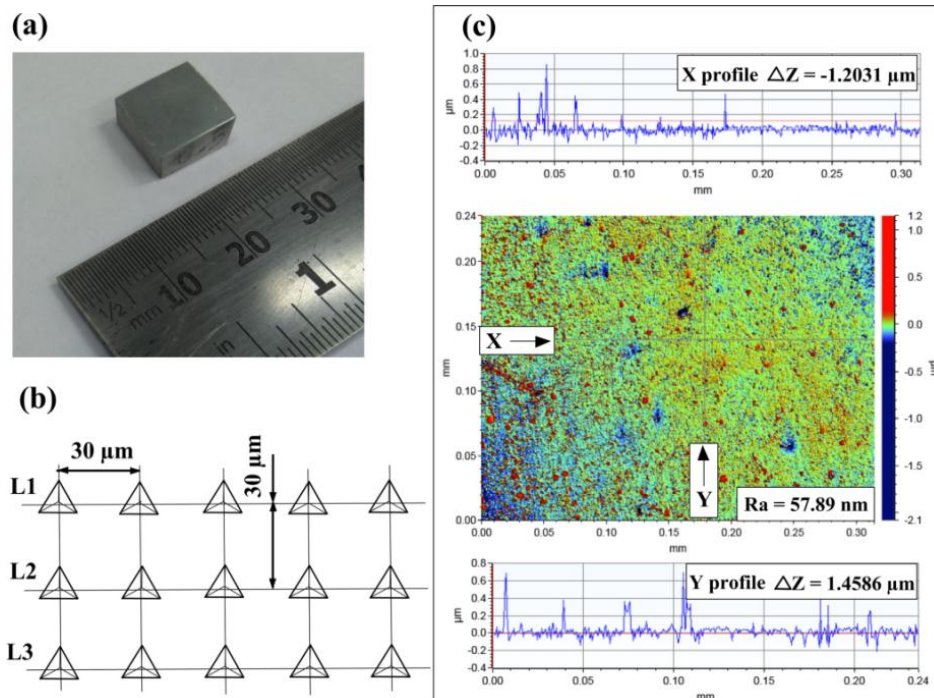


Figure 2.9: (a) Typical nanoindentation sample, (b) indentation array pattern, (c) optical image of the test surface along with its roughness (Ra) and scanned surface profiles.

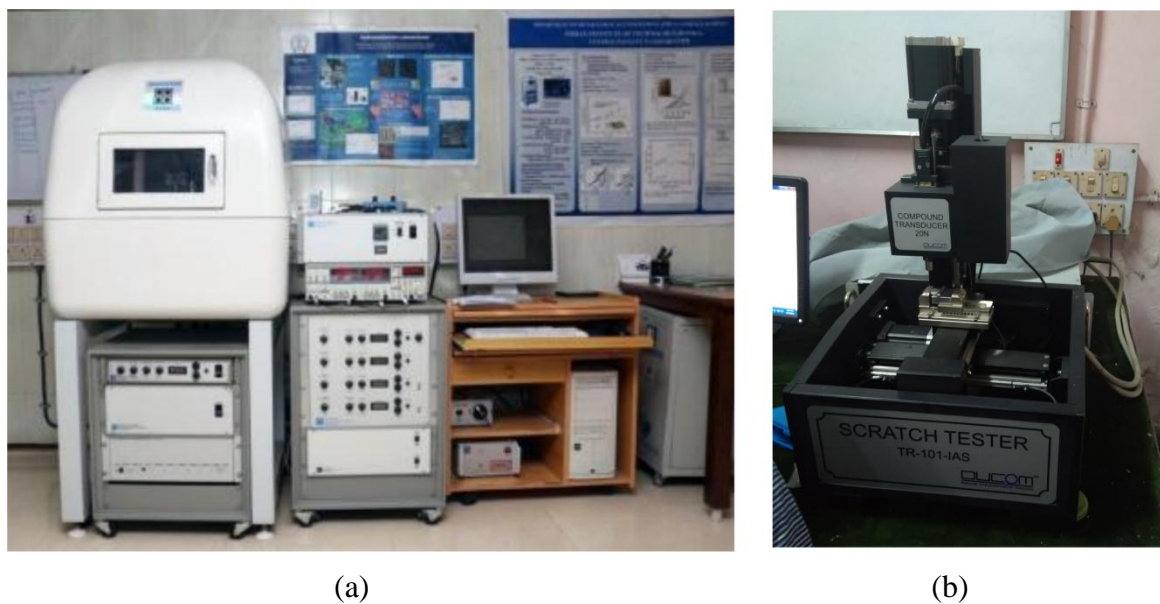


Figure 2.10: Instruments used for micro tribology tests (a) Nanoindenter, Hysitron Inc Minneapolis USA, TI900, (b) Scratch tester, TR-101-IAS, Sr. no. 921 DUCOM

Oliver and Pharr's method was followed to get material properties as briefed below. The typical load-displacement profile generated in a nanoindentation test (Oliver and Pharr, 2004) is shown in Figure 2.11.

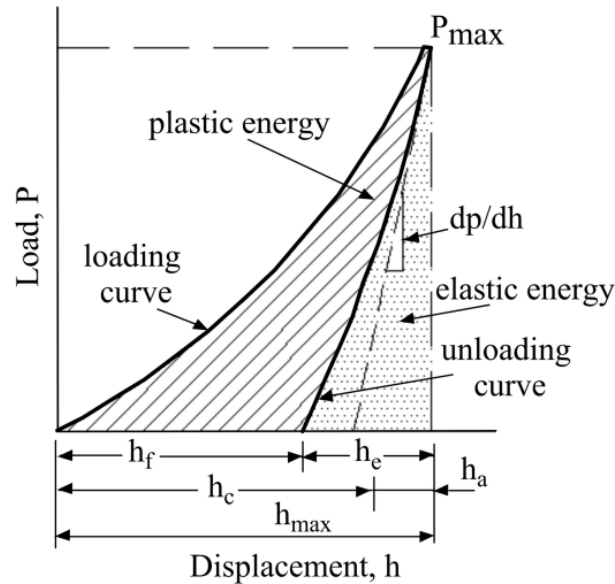


Figure 2.11: Load versus displacement curve.

h_f is depth of residual impression, h_e is depth of elastic displacement, h_c is depth of edge of contact circle with specimen measured from maximum depth, h_a is the distance moved by indenter contact with specimen surface upon elastic reloading.

$$\text{We have, } h_{max} = h_c + h_a \quad (2.4)$$

$$\text{Also for Berkovich indenter, } h_a = \left(\frac{\pi-2}{2}\right) h_e \quad (2.5)$$

Once the depth of contact h_c is found, the projected contact area is determined as,

$$A = 24.5 (h_c)^2 \quad (2.6)$$

Nanohardness (H) is then calculated with following equation,

$$H = \frac{P_{max}}{A} \quad (2.7)$$

Where, P_{max} is applied peak load and A is the projected contact area.

Further, the reduced modulus (combined modulus of indenter tip and test material) E^* is evaluated using contact stiffness (S) and the projected area of contact (A) as,

$$E^* = \frac{\sqrt{\pi} S}{2\beta \sqrt{A}} \quad (2.8)$$

Where β having a value of 1.034 is an indenter geometry correction factor.

Finally, the elastic modulus (E) of test material is calculated by the following equation using values viz indenter modulus ($E_i=1140$ GPa), Poisson's ratio for test specimen ($V_s=0.34$), Poisson's ratio for indenter ($V_i=0.07$) and the reduced modulus (E^*).

$$\frac{1}{E^*} = \frac{(1-V_s^2)}{E} + \frac{(1-V_i^2)}{E_i} \quad (2.9)$$

2.7 Single point scratch test

A Single point scratch test was performed to measure the damage resistance of a material to permanent deformation against moving indenter. Evaluation of scratch hardness of composites and the base alloy was done using a scratch tester (TR-101-IAS, Sr. no. 921 DUCOM India). The scratch tester is shown in figure 2.10b. A conical diamond indenter, Rockwell C with the hemispherical end (nose radius 200 μm , flank angle 120°) was used for scratch indentation test. The scratch tester is equipped with an image acquisition system with a 5-megapixel camera, using which scratches were viewed and captured for analysis. Scratch tester is interfaced with a computer through winducom 2010 software to input test parameters and visualize outputs. Scar View 2016 software was used to measure the scar widths. The geometry of the scratch indenter, the typical scratches captured by the scratch tester, and the width measurement procedure are presented schematically in Figure 2.12. The average width of scratch and the applied load were used to determine scratch hardness (GPa) according to the ASTM G171-03 standard (Sinha et al., 2006). It is expressed in terms of the scratch hardness number given as Scratch hardness (H_s) = 24.98 (m / x^2), where 'm' is applied load in grams and 'x' is the scratch width in μm . Scratch depth was calculated considering indenter geometry and the generated scratch width. Wear volume was then determined based on projected scratch area and stroke length. Traction force was acquired continuously by the compound load cell over the entire stroke length. The coefficient of friction was determined from the average traction load and the applied normal load. Data of traction force was used to

obtain profiles of varying friction coefficients. Scratches were observed under scanning electron microscopy (ZEISS EVO LS 10) to reveal scratch wear mechanisms.

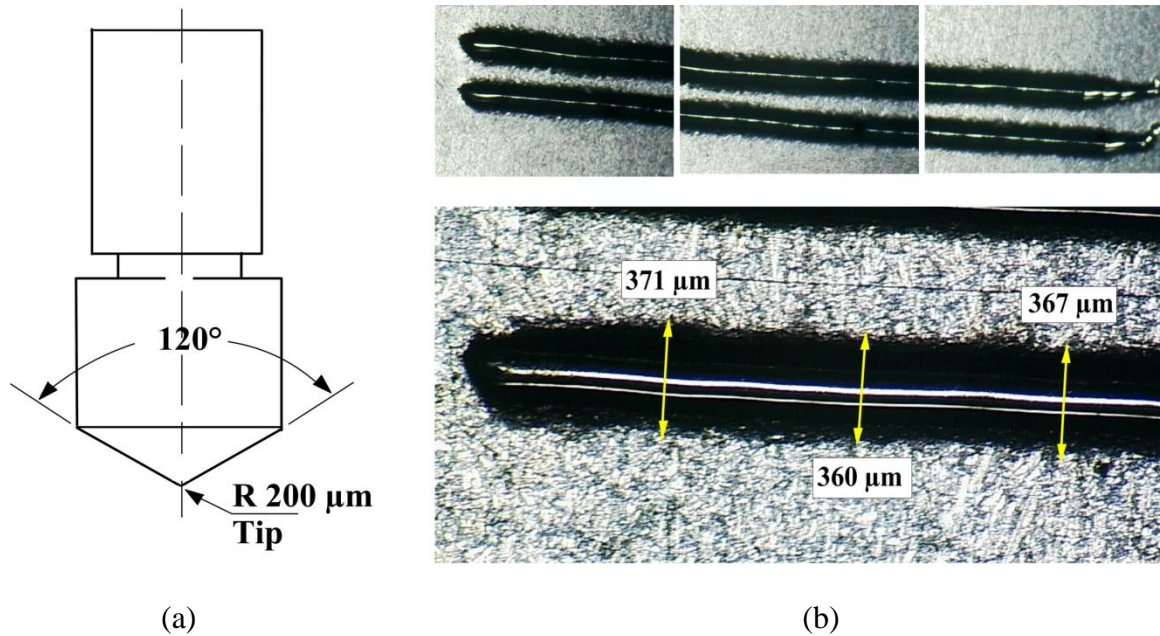


Figure 2.12: (a) geometry of scratch indenter (b) typical images of scratches (c) scratch width measurement

2.8 Corrosion measurement

Measurement of corrosion is essential for understanding the response of material to different corrosive mediums. It helps to plan and implement protective measures for restoring useful properties of the component. Different standardized test methods employed for measuring the corrosion of aluminum and its alloys are mentioned below.

- (a) Visual and microscopic examination
- (b) Gravimetric determination of mass loss
- (c) Chemical analysis of corroded surface or corrosion product
- (d) Scale thickness measurement
- (e) Gasometric method (when one of the reaction product is gas)
- (f) Scanning reference electrode technique (Electrode probes)
- (g) Electrochemical techniques

Among different methods listed above the electrochemical technique is best in providing useful insights about the corrosion mechanism. Besides it provides an opportunity to

mitigate corrosion by controlling the electrode potential. Direct current polarization and electrical impedance spectroscopy are most popular methods among electrochemical techniques. Potentiostat is an instrument that controls the voltage across work electrode-counter electrode pair and also maintains the potential difference between work-reference electrode pair according to the function generator defined program. Potentiostat supplies required current through the working electrode for maintaining desired potential all the time.

2.8.1 Potentiodynamic polarization test

It is a technique wherein the work electrode potential is polarized (shifted from open circuit potential) at desired scan rate and the respective current is measured as a function of time or potential. Open circuit potential (E_{OCP}) of metal is its corrosion potential, dissolution potential or equilibrium potential. Potential-time relation reflects the formation and breakdown of protective films on metal surface in corrosive media, as respectively indicated by increase and decrease of corrosion potential. With suitable scan rate the potential is varied from cathodic region to open circuit potential and then to anodic region while continuously monitoring the output current. The method uses an electrochemical cell having three electrodes placed in a suitable container filled with corrosive media. It has working electrode (test sample), reference electrode and the counter electrode, all connected to the potentiostat. The test potential is measured against the standard potential of reference electrode while counter electrode just transfers electrons to the solution in order to complete the circuit. The current flows into the working electrode via counter electrode as potentiostat varies the potential at steady state between two pre-set potentials. Experimental values of potential, current etc. are stored in the connected computer with the help of dedicated software. Recorded data is utilised to plot different graphs like the typical Tafel plot shown below in Figure 2.13. It presents polarization data on a semi-logarithmic plot between applied volts and current density. Tafel extrapolation technique is used to get different corrosion parameters like corrosion potential (E_{corr}), corrosion current density (I_{corr}), corrosion rate etc. once the interpolation data is obtained and plotted graphically. Nonlinearity of the plot near zero overvoltage signifies the fact that half-cell reactions still exists contributing the total current (McCafferty, 2005). With increasing potential the graph gradually becomes linear

and achieves full linearity at high overvoltage. Linear part of the graph is termed as Tafel region wherein the potential change and reaction rate develops a relation expressed by Tafel equation:

$$\eta = B \log \frac{i}{i_0} \quad (2.10)$$

Where η = over potential = $E_{\text{applied}} - E_{\text{ocp}}$, B = Tafel slope (determined from linear regions of anodic and cathodic branches), ' i ' = applied current density and ' i_0 ' = exchange current density. The lines representing Tafel regions on the cathodic and anodic sides are extrapolated back to intersect at zero overvoltage line. The current and voltage corresponding to that point are respectively called as corrosion current density (i_{corr}) and corrosion potential (E_{corr}). Ideally the accuracy of Tafel extrapolation method is equivalent to that of weight loss method. The process is rapid and accurate. Besides, a continuous monitoring of the extremely low corrosion rate is possible by this method.

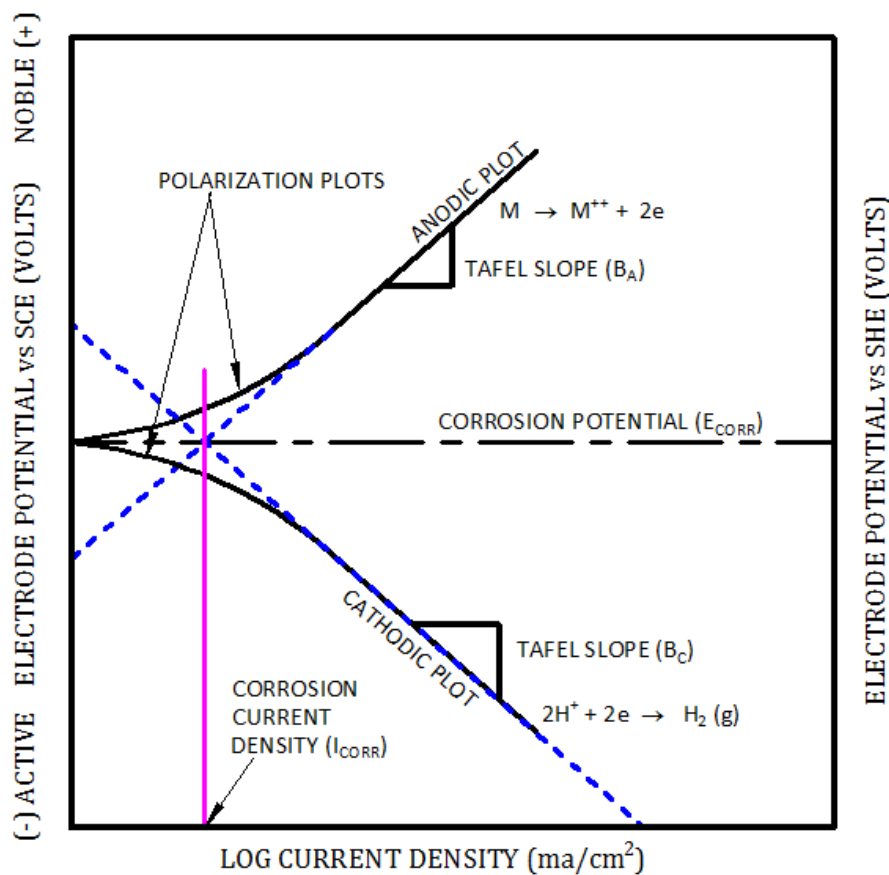


Figure 2.13: A typical polarization plot (ASTM Standard G3-89 2010)

2.8.2 Electrochemical impedance spectroscopy test

In this method electrode impedance is plotted against frequency. Impedance implies alternating current equivalent of direct current resistance, a complex resistance witnessed when current passes through a circuit having capacitors, resistors, inductors or a combination thereof. Aim of impedance measurement is to establish a relation between resistance and capacitance on account of phenomena such as charge transfer, diffusion, adsorption etc. occurring at the solid-liquid interface. It is a useful tool for studying the corrosion behavior of metallic composites. In this method a very small voltage signal (virtually non-destructive) is applied to the corroding metal and the resulting current is measured. Examination of electrochemical systems is done by using their equivalent circuits. For instance, a popular Randles circuit as shown in Figure 2.14 is commonly used in EIS to evaluate the impedance data. In this figure, ' R_s ' means the solution resistance between working electrode and reference electrode. ' R_{ct} ' is charge transfer resistance or polarization resistance at the interface between solution and electrode. ' C_{dl} ' is double layer capacitance at metal substrate interface. The experimental setup used for polarization test can be used for impedance measurements. The instrument is capable of measuring phase angle as well as current induced in the sample. The impedance data measured by potentiostat cum frequency analyser is stored and plotted using the linked computer. Both real and imaginary parts of the impedance are represented by a Nyquist plot.

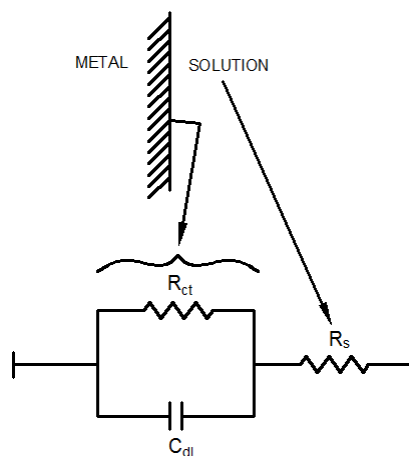


Figure 2.14: Randles circuit model to fit EIS data (McCafferty, 2010)

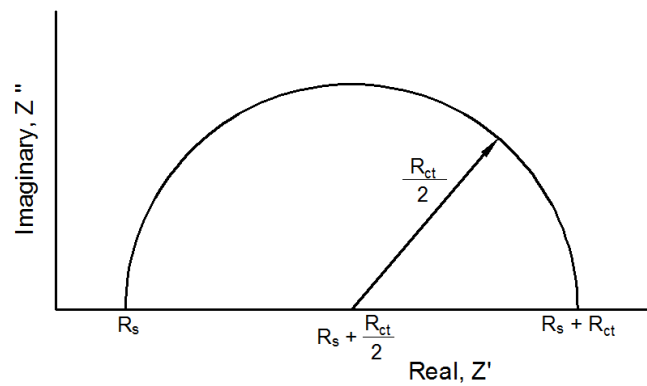


Figure 2.15: Nyquist plot for Randle's circuit

The perfect semicircle shown in figure 2.15 is a Nyquist plot for the circuit shown in figure 2.14. Electrochemical impedance plots often contain many semicircles or even partial ones representing relevant electrochemical behavior. Desired corrosion parameters are obtained by curve fitting these semicircles obtained by testing corrosion samples.

In the present study, a potentiostat (Gill AC, ACM instruments) was employed to conduct PDP and EIS tests on the fabricated composites to reveal their corrosion behavior. Tests were performed at ambient conditions with seawater, a popular corrosive media. An electrochemical cell with three electrodes inserted in glass cylinder filled with NaCl solution as shown in the Figure 2.16 is employed. Work specimen is used as a working electrode. Saturated calomel electrode (SCE) was used as a reference electrode while a platinum electrode was selected as an auxiliary electrode. Output data of the test was utilized and the polarization curves were plotted through installed software. Corrosion potential (E_{corr}) and corrosion current (I_{corr}) were obtained by extrapolating cathodic and anodic branches of the Tafel plot. Electrochemical impedance spectroscopy was employed for studying the corrosion behavior of fabricated materials in terms of corrosion parameters like R_{ct} , C_{dl} , R_s . These parameters were extracted from the Nyquist plot by semicircle fitting technique using the installed software. Corrosion rate (mm/year) and corrosion resistance (Ω/m^2) were calculated as given by:

$$Corrosion\ rate = \frac{Metal\ factor \times I_{corr}}{1000} \quad (2.11)$$

Where, I_{corr} is current density in A/m^2 and Metal factor = 1083 (for base alloy, determined from ACM software).

$$\text{Corrosion resistance} = \frac{\beta_a \times \beta_c}{2.3 \times I_{\text{corr}} \times (\beta_a + \beta_c)} \quad (2.12)$$

Where, β_a and β_c are anodic and cathodic slopes in volts and I_{corr} in A/m^2 .

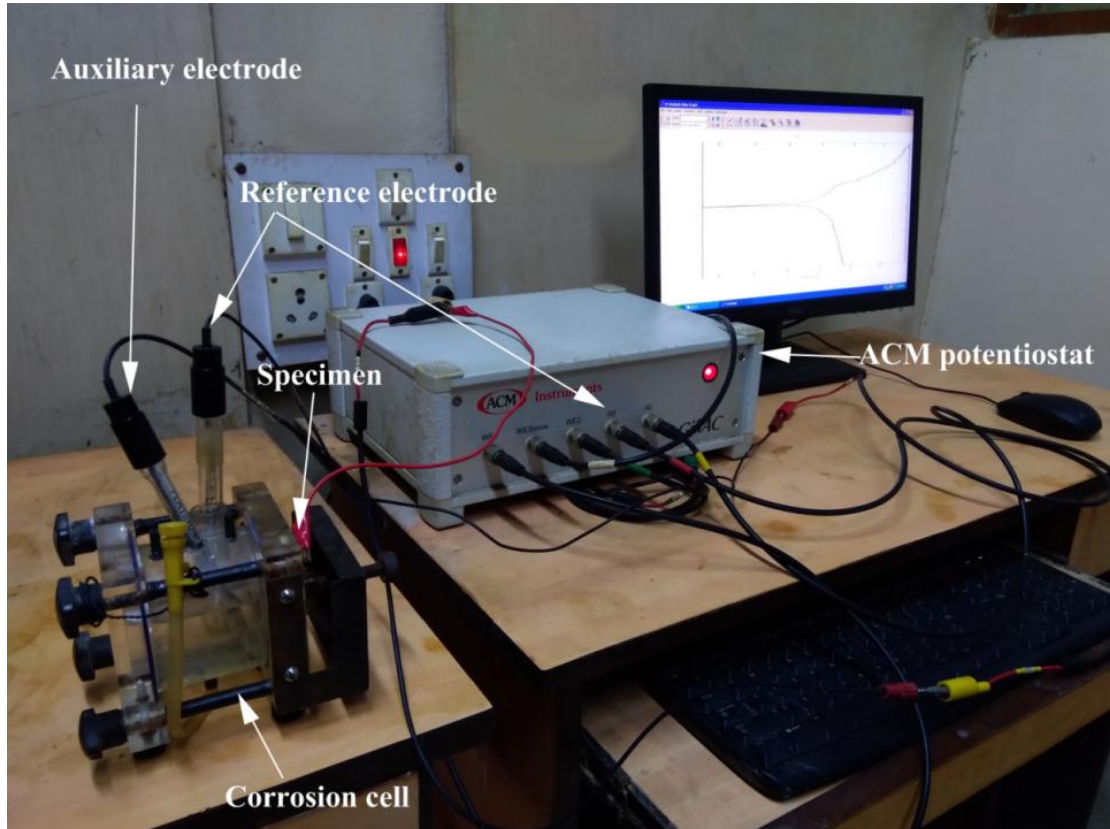


Figure 2.16: Corrosion measurement setup (Gill AC, ACM instrument)

2.9 Closure

In this chapter details about the experimental procedures are presented along with the test equipments used. Initially the process of fabricating cast composites is discussed. Then the basic material characterization methods including density, porosity, and hardness measurement is explained. It is followed by discussion of test set ups used for the metallurgical characterization, tribological characterization, micro scale behavior tests (nanoindentation and scratch), and the corrosion performance analysis. Experimental parameters of various tests are presented in the next relevant chapters that follow.

“This page is left intentionally blank”

Characterization of fabricated nanocomposites

In this study, Al-B₄C nanocomposites with four different weight percentages of nB₄C particulates, i.e. 0.5 %, 1.0 %, 1.5 % and 2.0 % are fabricated. In order to produce sound Al-B₄C composites, the particle content was restricted up to 2 wt%. Because literature indicates that higher incorporation leads to the deterioration of material properties on account of particle agglomeration. Fabrication procedure is detailed earlier in chapter 2, section 2.1. After fabrication the cast bar are cut into samples of required size for material characterization and wear tests.

3.1 Characterization of B₄C

B₄C particles of APS 500 nm (Product code: K520) bought from Hongwu International Group China are used for reinforcement. Details of B₄C powder as provided by the supplier are shown in Table 3.1.

Table 3.1: B₄C powder details

Product	Color	Purity	Crystal structure	Particle size	Composition
B ₄ C	Dark grey	99%	Rhombohedral	500 nm	B - 77.48%, C - 21.52%

Before utilization, the purchased B₄C powder is characterized for morphology and chemical composition. Figure 3.1 (a) shows field emission scanning electron microscopy image of boron carbide powder obtained at 20000X magnification. Irregular shaped B₄C powder particles of size ranging around 500 nm are clearly visible in the structural image. As received B₄C powder of greyish black color is shown in Figure 3.1 (b). The peaks related only to boron and carbons are seen in the EDS elemental image (Figure 3.2 c) confirming purity of B₄C powder. The amount of carbon is seen to be relatively large. It may be due to the fact that B₄C powder was placed on the adhesive carbon tape for examination. Figure 3.2 (d) shows XRD image of B₄C powder. Although all the peaks in

XRD pattern are related to boron carbide phase, the intense one is seen at 37.757° diffraction angle (hkl: 021).

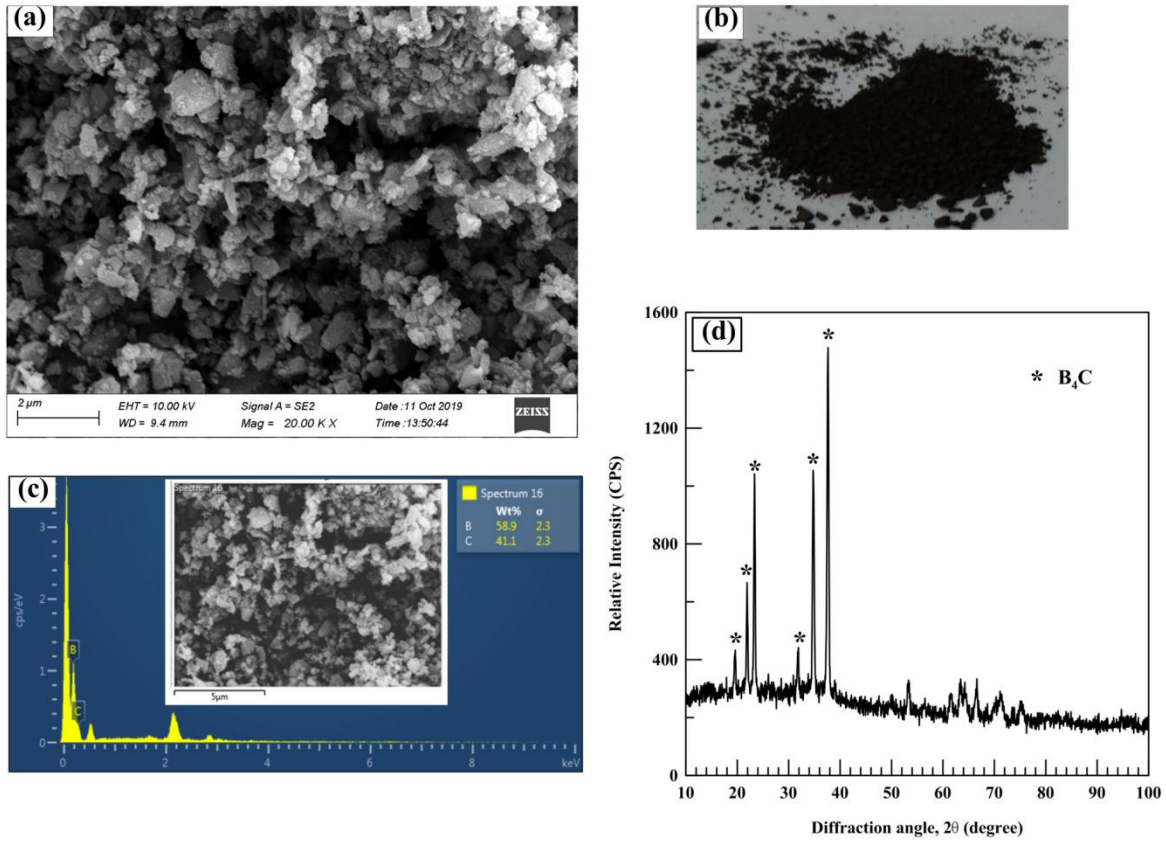


Figure 3.1 Characterization of boron carbide: (a) FESEM image. (b) As received powder, (c) FESEM-EDS spectrum, (d) XRD pattern

3.2 Density and porosity

Table 3.2 shows theoretical and experimental densities of the base alloy and fabricated composite specimens. The samples used for the analysis are presented earlier in Figure 2.3(b) (chapter 2, section 2.2). Densities of the nanocomposites are found to decrease with increasing amount of reinforcements as density of boron carbide is less than Aluminum alloy. This decreasing trend of densities is cross confirmed using water displacement method and these values are found to be close to those obtained by rule of mixtures. The density values obtained are very close to each other which indicate consistency in the density. The specimens used in this study are cut randomly from the stir cast rods and hence close density values confirm uniform dispersion of reinforcement

particles in the alloy matrix. The low value of porosity means better densification of the composite samples. Considering the isothermal melt processing above liquidus temperature at 750°C and small volume of melt (0.5 kg) ultrasonication for 5 min is thus found to be sufficient to degas the melt (Xua et al., 2004). It is to be noted that although by marginal amount, the porosity of nanocomposites is found to increase with increasing amount of nanoparticles in the base alloy.

Table 3.2: Results of density and porosity measurement

Sr. No	Material	Experimental Density (g/cc)	Theoretical Density (g/cc)	Porosity (%)
1	Al alloy	2.6637	2.7	1.334
2	Al/0.5% nB ₄ C	2.6966	2.6991	0.093
3	Al/1.0% nB ₄ C	2.6687	2.6982	1.093
4	Al/1.5% nB ₄ C	2.6596	2.6973	1.397
5	Al/2.0% nB ₄ C	2.6583	2.6964	1.413

3.3 Micro-indentation hardness

Figure 3.2 shows variation of microhardness of nanocomposites as a function of boron carbide reinforcement. Vickers microhardness is found to increase almost linearly with increasing reinforcement content in the base alloy. Hardness of nanocomposite is found to be higher than LM6 base alloy. This happened because of the incorporation of B₄C particles having high hardness relative to that of the matrix alloy. These nanoparticles act as obstacle to the dislocation movements under the action of applied load resulting in the reduced depth of penetration. The variation in the measured hardness value of base alloy is found to be 68 ± 5 while that in 2 wt% reinforced composite is 87 ± 4.5 . Rest of the composites showed marginal variation of 2-3 units around the mean value. These variations are shown in the figure by error bars. The indentations are taken at different locations on the sample and so this reflects that hard particles are uniformly distributed in the soft matrix. The improvement in material hardness is caused by increase in the dislocation density obtained due to elastic modulus mismatch and large difference in the

coefficient of thermal expansion of the constituent materials of the composite. Similar hardness improvement results are obtained by Muley A.V. et al. (2015) by reinforcing LM6 with 2 wt% nanoparticles (SiC & Al₂O₃, 1 wt% each).

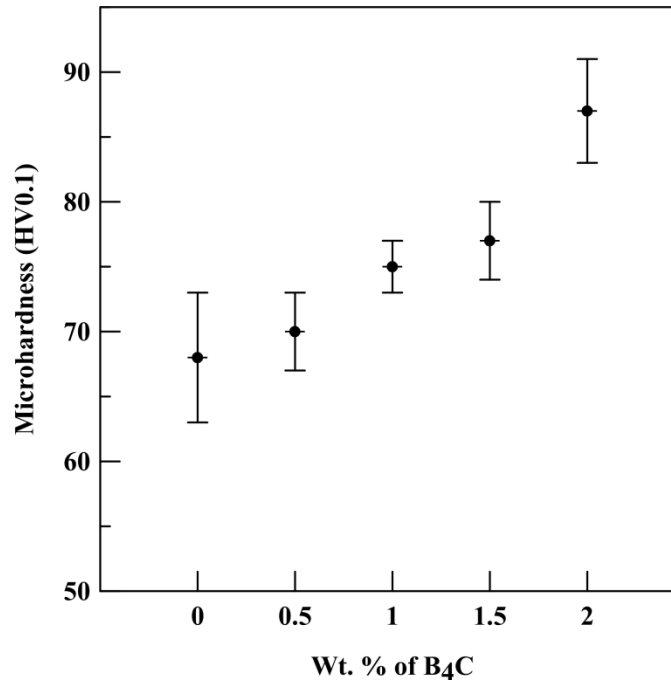


Figure 3.2 Variation of microhardness with % B₄C content

3.4 Microstructure

After fabricating different variants of Al/B₄C nanocomposites, the test specimens required for material characterization are prepared by standard metallography as mentioned in earlier chapter. The sizes of the specimens are prepared as per the requirement of various characterization units utilized for the purpose. It is necessary to see whether the boron carbide particles introduced in the alloy melt are incorporated properly and proportionately in the cast specimens. It is also required to examine the dispersion of B₄C particles in the alloy matrix because uniform dispersion is essential for improving material properties. Besides, development of possible intermetallics due to reaction between boron carbide and alloy matrix is to be checked. Generally for the microstructural investigations several tools such as optical microscopy, scanning electron microscope, x-ray diffraction, etc. are utilized. Details of these tools and techniques used

for the present study are discussed previously in chapter 2. The results of the microstructural examination are discussed below.

3.4.1 Optical microscopy of samples

Microstructure of Al alloy and Al-B₄C composites observed at 200X magnification under optical microscope is shown in Figure 3.3. Optical image of Al-12Si alloy in Figure 3.3a shows discrete distribution of needle shaped and randomly oriented eutectic silicon particles. Few irregular shaped primary silicon particles are also present in the aluminum matrix. Microstructures of Al/B₄C composites (Figure 3.3b-e) appear to be modified. Reduction in size of eutectic silicon particles is observed with relative increase in primary silicon particles. Refined microstructure devoid of particle micro-clusters is clearly visible in the optical micrographs of composite materials. As both alloy and composite samples are fabricated by the same process, the microstructure modifications can be attributed to the inclusion and uniform dispersion of B₄C nanoparticles. Dehnavi et al. (2014) reported similar observation using optical microscopy images about grain size reduction and refinement of Al413/SiC microstructure due ultrasonically dispersed nanoparticles. It is worthwhile to note that ultrasonication effect alone can transformation the microstructure of Al-Si alloys from dendritic to globular morphology (Kandemir et al., 2014; Jia et al., 2016). Further refinement of microstructure can occur due to dispersed nanoparticles as they provide multiple heterogeneous nucleation sites for grain growth in the solidifying melt (Srivastava and Choudhari, 2016; Akbari et al., 2015). Moreover, in alloy system of metal matrix with fine particulates, the interaction between grain boundaries and particles restrict grain growth leading to grain refinement called Zener pinning effect. The optical images of the fabricated materials obtained at 1000 X are placed as inserts in their corresponding images in Figure 3.3. These magnified inserts are useful to visualise the morphological changes with more clarity. Silicon crystals are showing platelet structure with sharp and clear edges in base alloy. These edges are seen rough and broken in the composite matrix. Apart from main constituent phases (Al, Si), many light grey patches and small size incorporations are seen distributed in the entire composite microstructure. These can be reaction products. Trace elements present in the base alloy can produce intermetallic phases. Also boron is known to react with

Aluminum and can produce AlB_2 and marginal amount of Al_4BC at the operating temperature of $750^\circ C$ (Fyzik and Beaman, 1995).

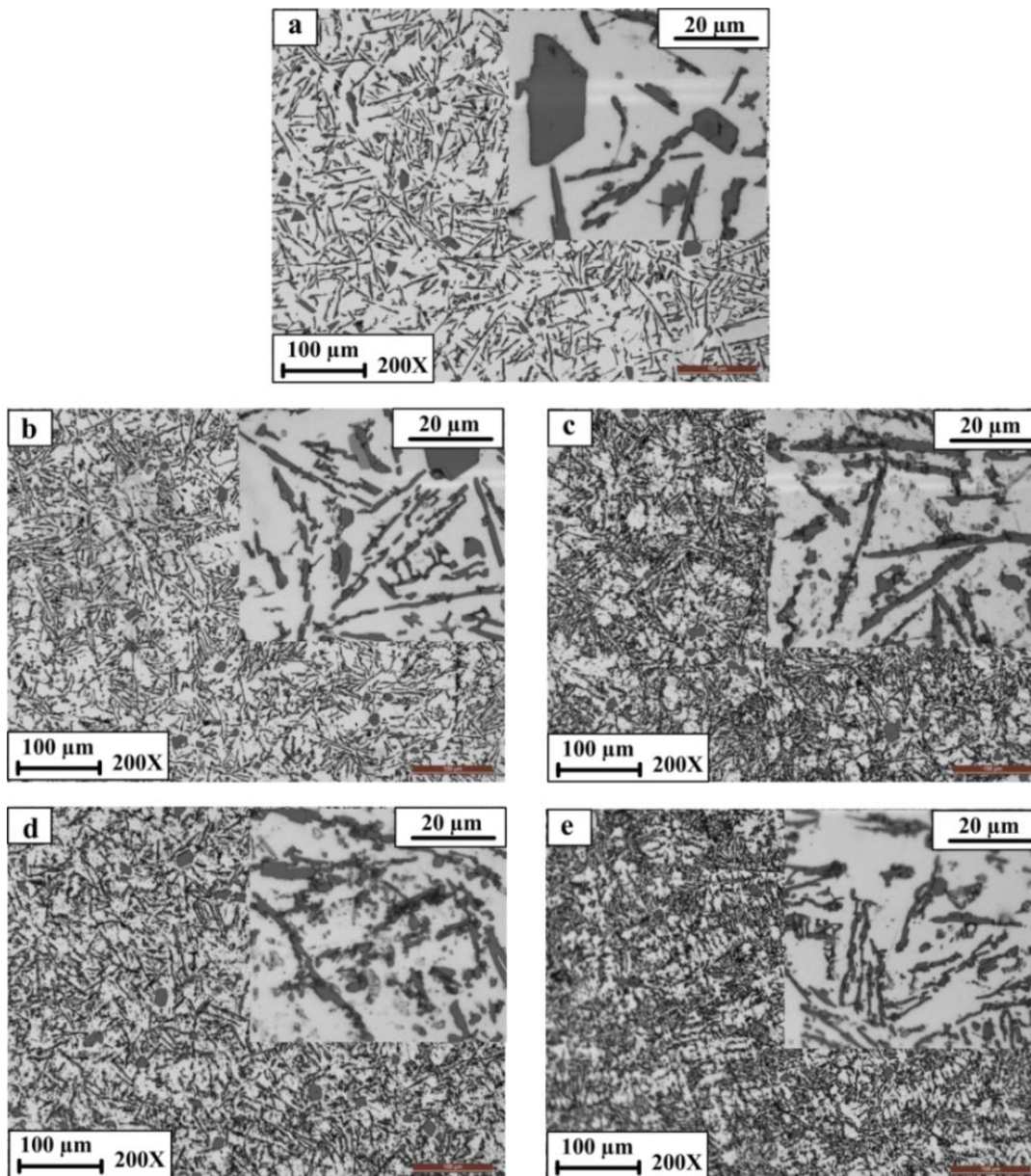


Figure 3.3: Optical micrographs: **a** Al alloy, **b** 0.5 wt% B_4C , **c** 1.0 wt% B_4C ,
d 1.5 wt% B_4C , **e** 2.0 wt% B_4C

Magnified optical images have also revealed no evidence of porosity and are useful to understand that the particles are not agglomerated. Based on rule of mixture and density measurements we have found quite marginal porosity of 1.413 % even for 2 wt% B_4C composite. Density decreased with increasing reinforcement while hardness is improved

by about 20%. This clearly indicates that the castings are produced without defects. It could be due to ultrasonic treatment. Li et al. (2018) have reported that ultrasonic vibration treatment effectively reduces porosity by degassing effect.

3.4.2 FESEM-EDX analysis of fabricated materials

It is difficult to resolve boron carbide particles among small entities visible in optical microscopy. Hence electron microscopy is utilized to confirm the particle incorporation and the overall material composition. Figure 3.4 a-e shows scanning electron micrographs of base alloy and Al/B₄C nanocomposites along with corresponding EDX spectrums.

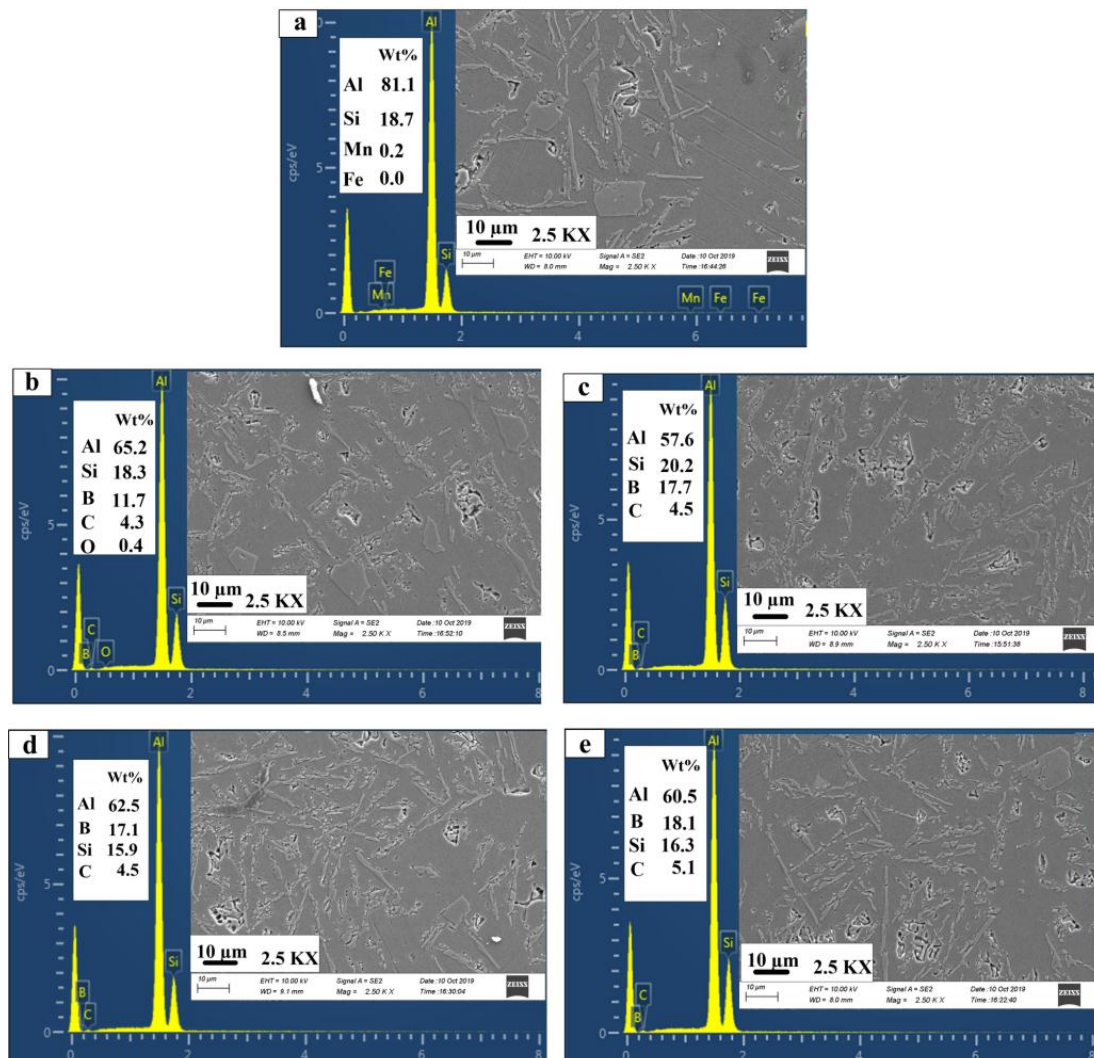


Figure 3.4 SEM-EDX spectra: **a** AlSi alloy, **b** 0.5 % B₄C, **c** 1.0 wt% B₄C, **d** 1.5 wt% B₄C, **e** 2.0% B₄C

Silicon crystals are bigger in terms of length and width in base matrix. On the other hand, few elongated plate like while most broken silicon crystals are seen distributed in the composite matrix as shown in the high magnification (2.5 KX) image. Xuan and Nastac, (2018) have identified that presence of nanoparticles is a responsible factor for the modification of eutectic silicon phase. Dendrite fragmentation resulting into globular grain morphologies was however stated to be the result of ultrasonic treatment. The images are showing few small cavities. These are created due to removal of protruding silicon particles from material surfaces under the action of machine polishing. Al and Si are the main elements detected in EDX of base alloy along with marginal traces of manganese and iron, which confirms it to be a eutectic alloy. EDX of composite clearly reveals the presence of Al, Si, B and C elements. Boron carbide is found in all variants of the composite material, although not exactly in a linear manner. It may be because of the smaller amount of incorporation and the small area of examination. Again, EDX is said to be unreliable for quantity analysis although it is useful for qualitative investigation.

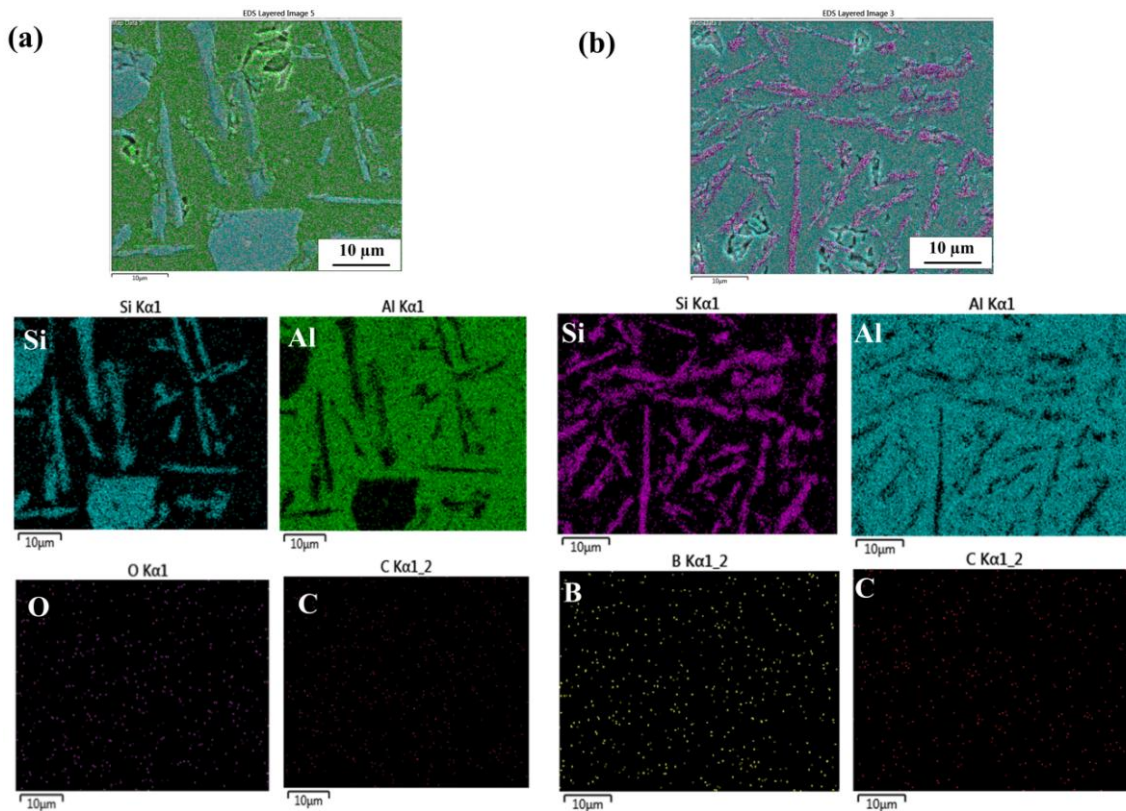


Figure 3.5: Microstructure and elemental mapping: (a) Al-Si alloy, (b) Al-2.0 wt% B_4C composite

In the composite microstructures, many small dots like structures are visible. However, it is difficult to differentiate all those as B_4C particles among many small rounded silicon particles. Hence EDX elemental mapping is carried out to see the distribution of different constituent elements of the material matrix. As an example, elemental mapping of the base alloy and 2.0 wt% B_4C composite is presented in Figure 3.5. Other variants of the composite material shows similar elemental distribution pattern. Elemental mapping image not only confirmed the incorporation of boron carbide particles but also revealed their uniform distribution in the microstructure. Other researchers have also used elemental mapping technique to confirm deagglomeration of fine particles in Aluminum-ceramic composites (Poovazhagan et al., 2014; Jia et al., 2016; Vishwanatha et al., 2017). In order to detect B_4C particles in the alloy matrix a high magnification (30 KX) image is taken at such tiny entities as presented in Figure 3.6a. A small area EDX analysis done at point 3 is shown in Figure 3.6b which indicates it to be a B_4C particle.

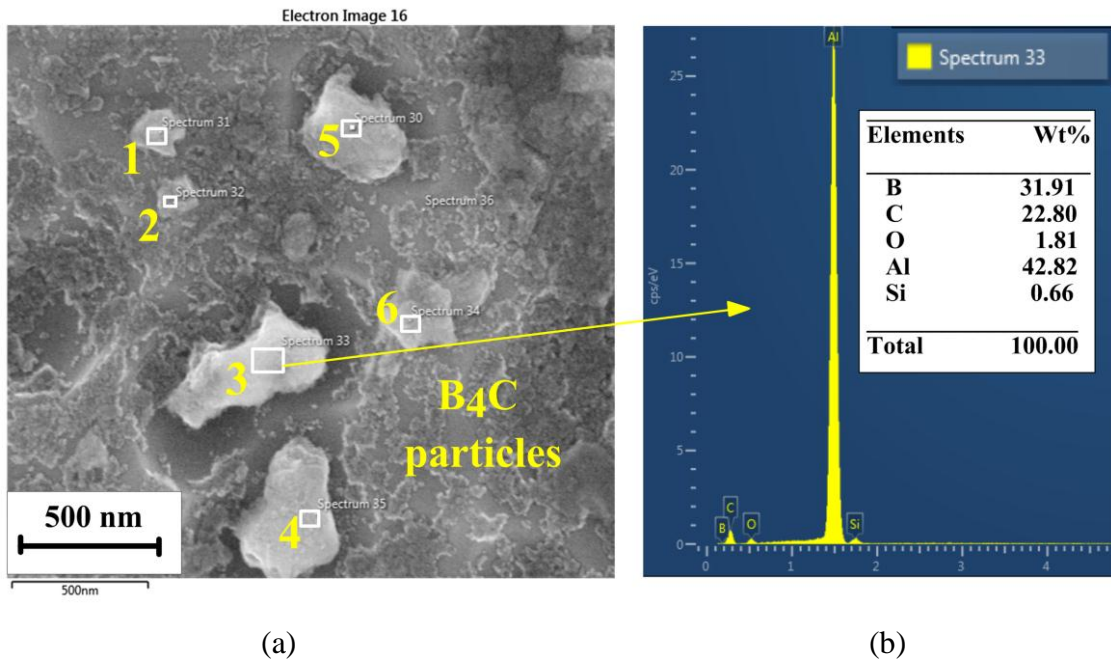


Figure 3.6: (a) B_4C particles in the composite matrix; (b) Small area EDS of particle 3

Elements found in the EDX analysis at different small entities in the image are shown in Table 3.3. It can be noted that negligible amount of silicon while appreciable amounts of boron and carbon are detected at each particle site. Hence these particles can be confirmed as B_4C . Further these particles appear to have clear interface with the matrix

suggesting good interfacial bonding. Larger particles (3 and 4) with somewhat rough edges are surrounded by thin, distinct layer and it could be a reaction interface. Ceramics are known to create mechanical and /or chemical bonding with matrix through interface. Strong interfaces are useful for load transfer. Thus by the use of optical and scanning electron microscopy the successful incorporation of B₄C particles in Al alloy matrix is ascertained.

Table 3.3: EDX analysis (Wt. %) of particles shown in micrograph Figure 3.6 a

Particle / area	Wt. %				
	B	C	O	Al	Si
1	27.89	25.41	2.86	43.10	0.74
2	29.53	22.55	1.69	45.51	0.72
4	29.62	27.23	2.07	40.44	0.64
5	30.14	23.13	1.47	43.89	1.37
6	30.22	27.77	1.95	39.24	0.82

3.5 Closure

In the present chapter initially the details about the contributing materials used for fabricating composites are presented along with the processing parameters. Next the examination of the fabricated composites for density and porosity attainment is discussed and the results are compared to those of the base matrix. Later on the microhardness variation with the reinforcement content is presented. Finally the microstructural examination conducted by using optical and field emission scanning electron microscopy is explained. Density of the fabricated composites decreased with increasing reinforcement content due to the effect of ultrasonic degassing. Microhardness of alloy is increased due to hard B₄C content. B₄C particles are uniformly distributed in the alloy matrix with no cast defects. Energy dispersive spectroscopy images and the elemental table confirm the inclusion of boron carbide in the alloy matrix. Composite microstructures are refined with increasing reinforcement due to the Zener pinning effect of nanoparticles and the ultrasonication treatment given to the melt. Silicon appearance is changed from long needle and plate like form to more spherical one.

Tribological performance of Al-B₄C nanocomposites at room temperature

4.1 Introduction

Despite several attractive properties, the use of Aluminum and its alloys is limited to some extent due to their poor resistance to wear, seizure and galling (Prasada and Asthana, 2004; Ma et al., 2017). Researchers are continuously trying to incorporate different types of ceramics into variety of the Aluminum alloys in the pursuit to improve their wear resistance. Efforts are also directed towards developing self-lubricating Aluminum composites. It is observed that wear and friction behavior of Aluminum composites depend upon several intrinsic and extrinsic parameters (Deuis et al., 1997). Extrinsic factors include applied load, sliding speed, operating temperature, environment etc. Intrinsic factors include reinforcement (content, type, and size), microstructure, processing method and heat treatment. Micro particles are stated to act as load bearing elements thereby protect the soft alloy matrix against wear loss. But under high loads these micro particles get crushed to smaller size fragments and can play the role of abrasives to deteriorate the wear performance. Nanoparticles on the other hand are observed to strengthen the metal matrix by Zener pinning and Orowan strengthening mechanisms which improve properties of the base alloy. Better transfer of load takes place between particles and matrix. Strongly bonded nanoparticles prevent wear loss by restricting subsurface crack propagation. As such nanocomposites are seen to display properties remarkably enhanced over their micro counterparts during several lab scale investigations. Recently Moseleh-shirazi et al. (2016) produced Al6061/SiC nanocomposite by PM process followed by extrusion and observed that with just 2 wt% SiC reinforcement, hardness of the base alloy increased by six times while volume loss in wear test was reduced by 77%. It was due to the restriction offered by SiC particles to the metal flow during sliding. Friction coefficient was also reduced from 0.55 to 0.33 with

increasing reinforcement up to 3 wt%. Significant effect of micro to nano size variation of alumina particle (60 μm , 1 μm , 30 nm) on the increased density and hardness of Al 6061- Al_2O_3 bulk composite is reported by Hosseini et al. (2010). Durai et al. (2007) found that reduced inter particle distance between uniformly distributed fine size reinforcement particles improved hardness and wear resistance of Aluminum alloy. Ravindran et al. (2013) while working with Al2024-5 wt% SiC and Al2024-SiC-Gr nanocomposites revealed that increasing wear rate of monolithic composites at all loads is drastically reduced beyond 20N when incorporated with graphite particles. Detachment of soft graphite particles from matrix and mixing with wear debris created lubricating tribolayer to reduce wear rate. Jiang et al. (2018) found that wear resistance of Al2024 alloy improved for Al_2O_3 particle content up to 7 vol% but decreased with further addition. It was due to the agglomeration of particles which set off the benefit of improved hardness on wear resistance. Decrease in the wear rate of Al6061/1.2 wt% SiC nanocomposite produced by ultrasonic stir casting is reported recently by Manivannan et al. (2017). The mechanical mixed tribolayer, rich in oxygen and iron was found responsible for the increased wear resistance of the composite at all loads. Very few but promising reports are available on tribological assessment of Al/ B_4C nanocomposites; mentioned in chapter 1, section 1.2.1.

Aluminum-silicon alloy is a popular material choice for wear resistant applications as silicon phase is believed to act like hard reinforcement. Al-Si alloy of near eutectic composition is found to be best from the view point of wear resistance (Clarke J., Sarkar, 1979) and possess better foundry characteristics. It has been widely investigated for wear performance. Hence in the present work eutectic binary Al alloy (LM6) is reinforced with B_4C particles using ultrasonic stir casting process to study its dry sliding wear performance under different operating parameters. Such combination of work is missing in the published literature and so is carried out to fill the gap.

4.2 Plan of experiments

The procedure employed for the room temperature tribological tests and the equipment used for it are described earlier in chapter 2, section 2.5.1. The tests are performed at ambient conditions of 33-35°C temperature and relative humidity of 65-70%. Samples of diameter 6 mm and height 30 mm machined from cast bar are used as pin specimens. Flat

end of pin is manually polished using SiC papers of 400, 800, 1200, 1600 and 2000 grade and cleaned with acetone to ensure its conformal contact with the counter body. Stationary pin is held normal against the rotating counterface disc made of EN31 material (Hardness 63 HRC). Counterface is also cleaned by acetone before each test. Wear tests are conducted by applying loads in the range of 10 - 40N creating four nominal contact pressures of 0.354, 0.707, 1.061, 1.412 MPa. Four different sliding speeds of 0.16 m/s, 0.33 m/s, 0.49 m/s and 0.66 m/s are employed. Each tribological test for studying the effect of load and speed is conducted for the fixed sliding time of 15 min. The loading lever is arranged to create the sliding track of 55 mm diameter. Weight of the pin before and after the wear test is measured with sensitive electronic balance of 0.01 mg least count. Mass loss (kg) is divided by sliding distance (m) and applied load (N) to get specific wear rates. Effect of sliding distance on the wear response of fabricated materials is investigated by varying sliding duration at fixed speed-load conditions. Test duration is varied between 10 to 40 minutes in steps of 10 min so as to create minimum and maximum sliding distance of 100 m and 1600 m respectively. All the selected test parameters are literature based and thoughtfully selected so that our results could be correlated and compared with the previous reported studies. Wear debris generated on the wear track is collected for tribochemical analysis. Images of worn surfaces and wear debris are analyzed to understand the wear mechanisms. 3D optical profiles of worn surfaces and their roughness values are obtained to relate wear performance.

4.3 Results and discussion

4.3.1 Wear behavior

Wear performance of Al Alloy and Al-nB₄C composites is studied by considering several parameters like reinforcement content, applied load, sliding speed, sliding distance and is presented as below.

4.3.1.1 Effect of reinforcement content

From Figure 4.1 it is observed that mass loss of Al-B₄C nanocomposites is less than the base alloy and is decreased with increasing wt% of nB₄C particles in the matrix at all loads. Similar trend is found at all the other sliding speed of 0.33, 0.49 and 0.66 m/s. Incorporation of B₄C nano particulates has increased the hardness of alloy. Although not

solely responsible, hardness is considered as crucial factor for reducing the indentation and volume loss of material as signified by Archard's wear law. Large difference in coefficient of thermal expansion and elastic modulus between boron carbide and Aluminum is useful to increase the dislocation density in material matrix. Refined microstructure effected by the uniformly dispersed boron carbide particles and their better bonding with matrix resulted in the increased hardness and strength of alloy. These modifications should have enhanced the ability of composite matrix to protect its mass against hard asperities of the sliding steel counterface. Such observations are in line with those reported earlier (Durai et al., 2007; Alizadeh et al., 2017).

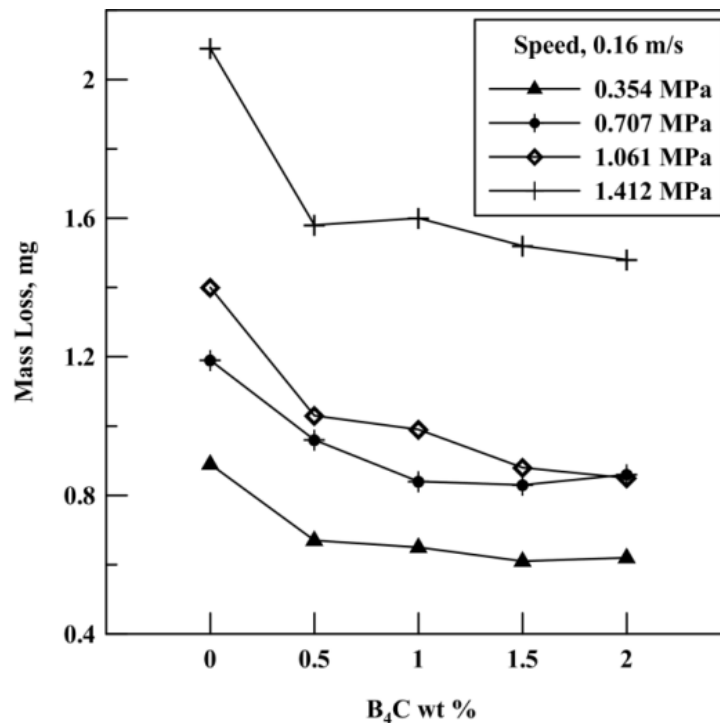
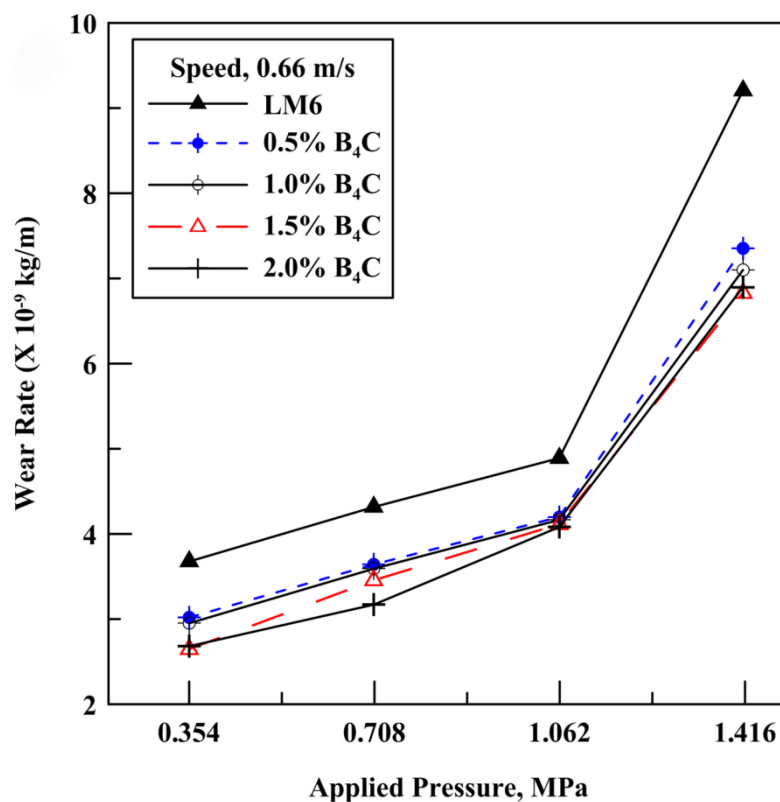


Figure 4.1: Mass loss as a function of B₄C wt %

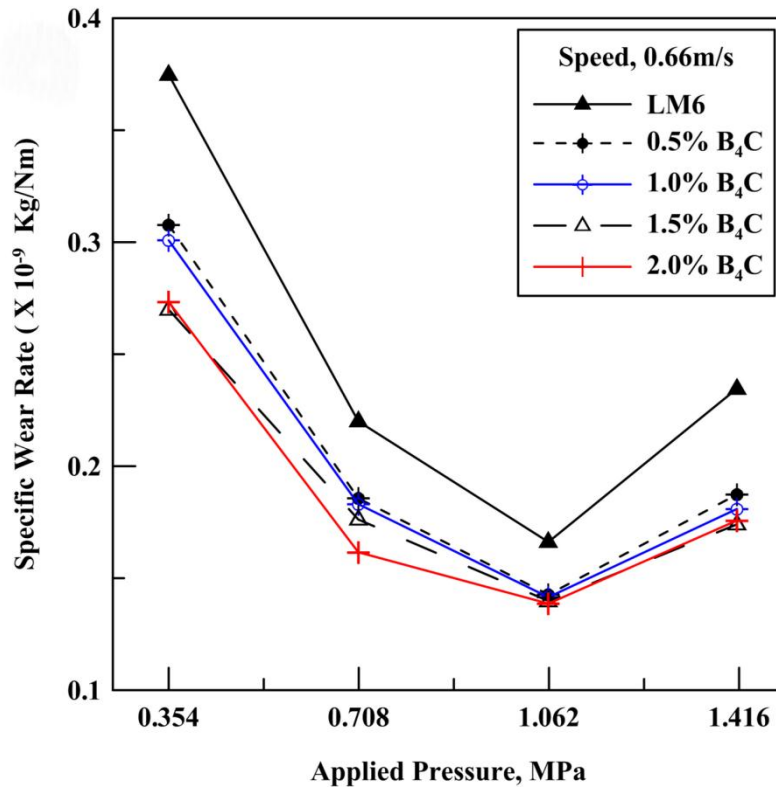
4.3.1.2 Effect of applied contact pressure

Pin on disc wear tests are carried out with an aim to explore the effectiveness of B₄C reinforcement on Al-Si alloy under four different loads and speeds. Figure 4.2a shows that the wear rates of all the materials at 0.66 m/s increase gradually with increasing applied nominal pressure up to 1.062 MPa but a sharp rise is seen thereafter. Nanocomposites have relatively close wear rate variations but they are found to perform exceedingly better than the base alloy especially at high speed-load condition. Similar

nonlinear wear rise is observed under the influence of varying pressure at all the lower fixed speeds but without a sharp change. This signifies that severe wear is initiated beyond 1 MPa pressure at higher speed. Load is the most influencing parameter which increases deformation and surface damage and is generally found to increase wear rate as advocated by Archard's law. Increased metallic intimacy due to deformation led rise in contact area is seen at lower loads. Whereas tendency to break protective oxide and transfer layer is observed to increase wear rate at higher loads. Such behavior of Al-Si alloys under dry sliding conditions is mentioned by Dwivedi (2010) in his comprehensive review article. However the load specific wear rate is found to decrease as shown in Figure 4.2b. This enhanced wear resistance could be due to the improved load bearing capacity offered by B₄C reinforcement. Boron carbide offers thermal stability to the matrix. Hence despite microthermal softening caused by the rising interface temperature, composite alloys displayed lesser wear loss in proportion to the increasing applied pressure. For the similar tribological conditions such behavior is reported for Al/SiC (Manivannan et al., 2017) and Al-WC (Pal et al., 2018) nanocomposites recently.



(a)



(b)

Figure 4.2: Effect of applied pressure on (a) wear rate and (b) specific wear rate.

FESEM images are examined to reveal the undergoing wear mechanisms. Worn surface of LM6 alloy (Figure 4.3a) reveals formation of cavities with some delaminated areas and long scratch lines. It implies that base alloy is subjected to mild adhesion-delamination wear at the applied pressure of 0.354 MPa. But when subjected to 1.412 MPa pressure, base alloy surface underwent heavy plastic deformation revealing severe wear as can be seen in Figure 4.3d. Worn surface of nanocomposites at low contact pressure has developed long grooves possibly created by abrading action of steel counterface. It is also seen that loose wear debris particles are spread on the wear tracks as shown in Figure 4.3 b and c. At higher pressure of 1.412MPa, the nanocomposite surfaces are seen covered with mechanically mixed layers and wear debris. The tribolayer is even found firmly adhered and compacted to the surface of composite and receiving abrasive grooves on it as can be seen in Figure 4.3 e and f.

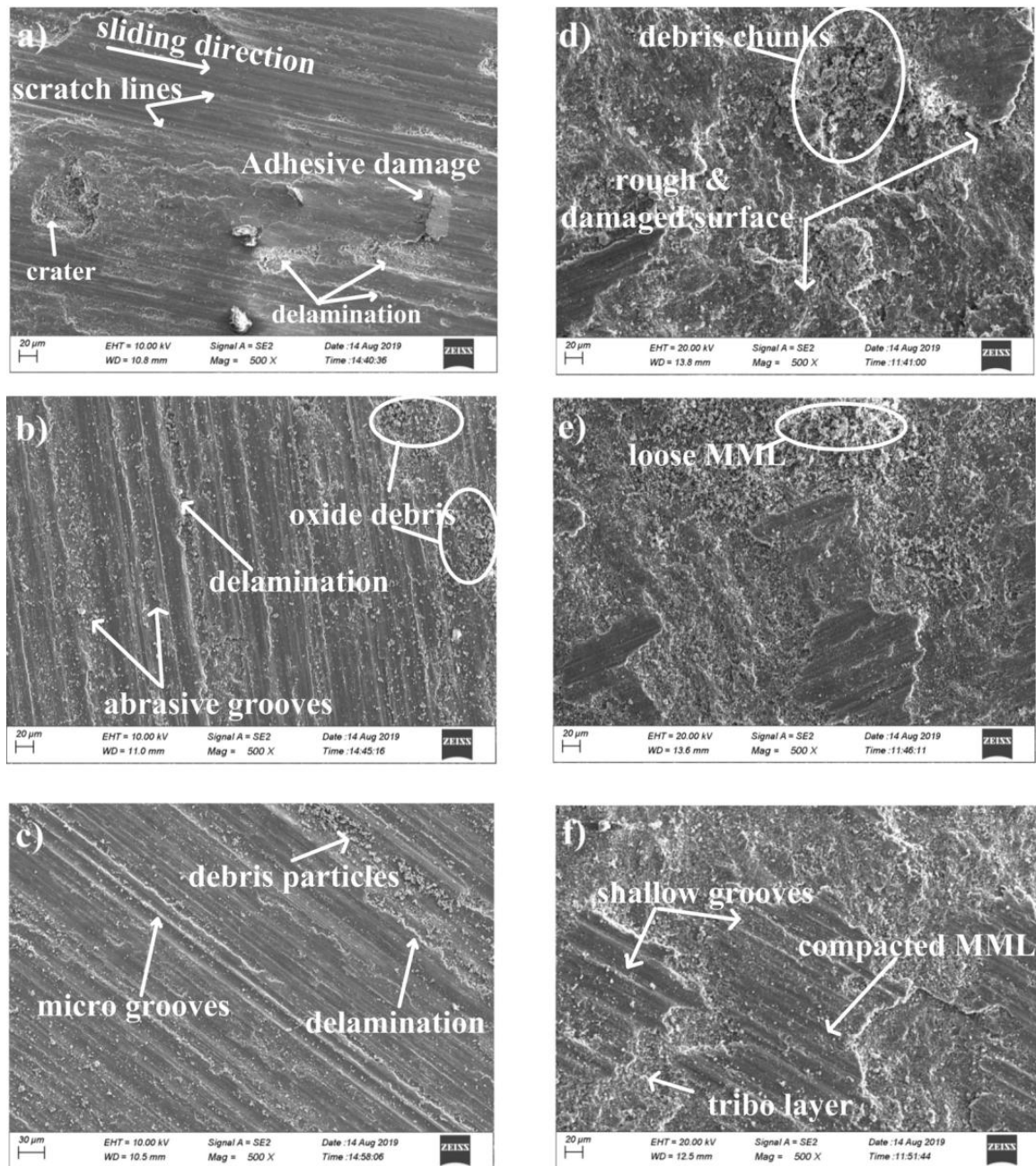


Figure 4.3: Worn surfaces of **a)** Base alloy, **b)** 1 wt% B₄C, **c)** 2 wt% B₄C (at 0.354 MPa); **d)** Base alloy, **e)** 1 wt% B₄C, **f)** 2 wt% B₄C (at 1.412 MPa).

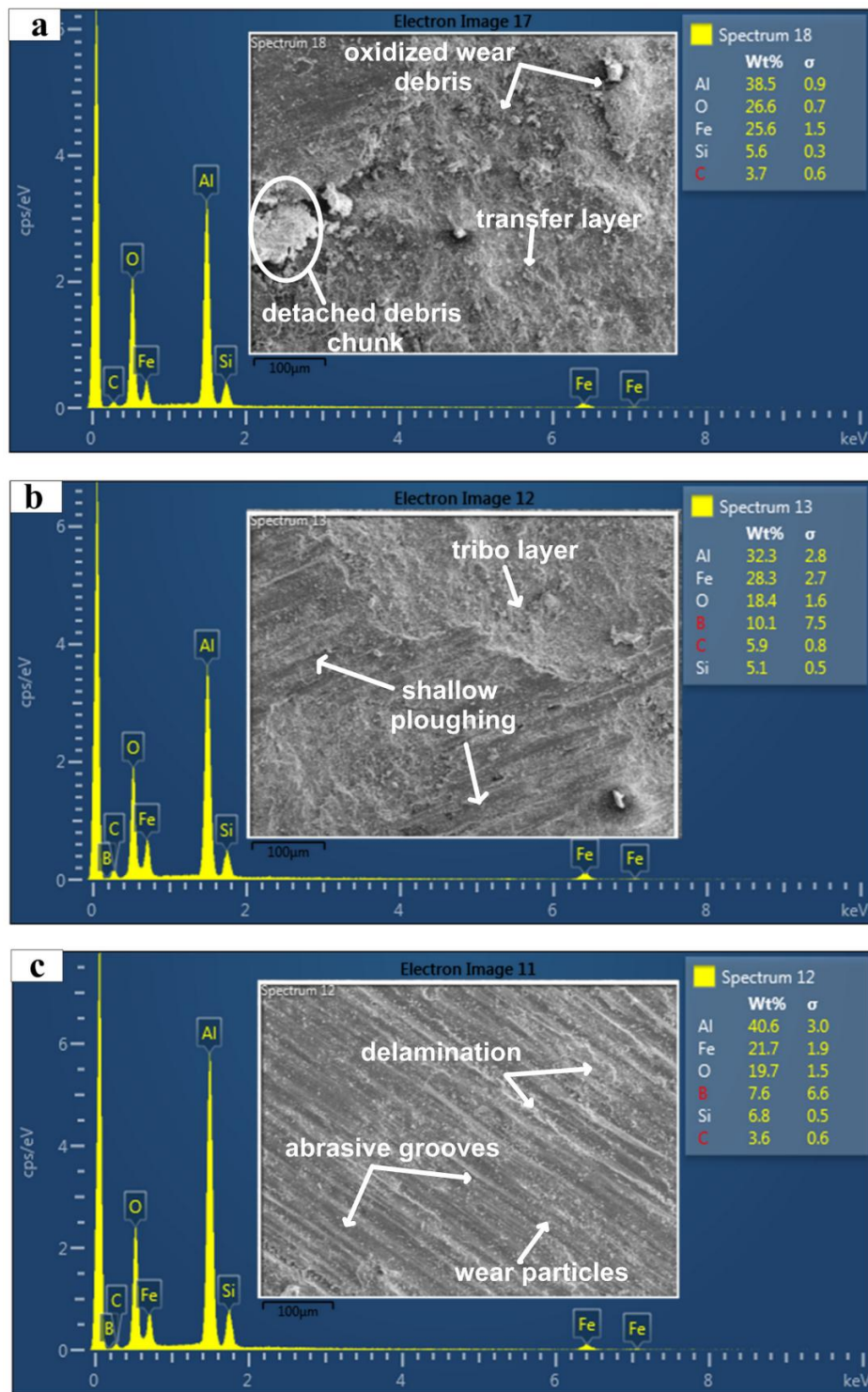


Figure 4.4 EDS for 1.061 MPa (at 0.49 m/s): **a** base, **b** 1% B₄C, **c** 2% B₄C.

Energy dispersive x-ray (EDAX) spectrums are observed to understand the tribochemical interactions occurring in the sliding surfaces. Figure 4.4 shows the EDAX results of base

alloy and composites wear tested at 0.49 m/s and 1.061 MPa. The corresponding worn surfaces are also shown as inset which can be helpful for observing the effect of reinforcement content. Heavy plastic deformation and surface damage of base alloy can be revealed from Figure 4.4 a, whereas Figure 4.4 c shows parallel grooves and delamination on the surface. Peaks of Al, Si, O and Fe are seen for base alloy while additional peaks of B and C are seen for the composites. Maximum iron content is seen for the base alloy which is seen to decrease for the composites with increasing reinforcement. It can be due to the reduced wear of counterface on account of wear protective layers formed on the composite. Oxygen and iron peaks along with peaks related to the elements of material matrix confirm oxidation and presence of mechanically mixed transfer layers. Wear debris elements are possibly generated because of the cracking and delamination of the transfer layers.

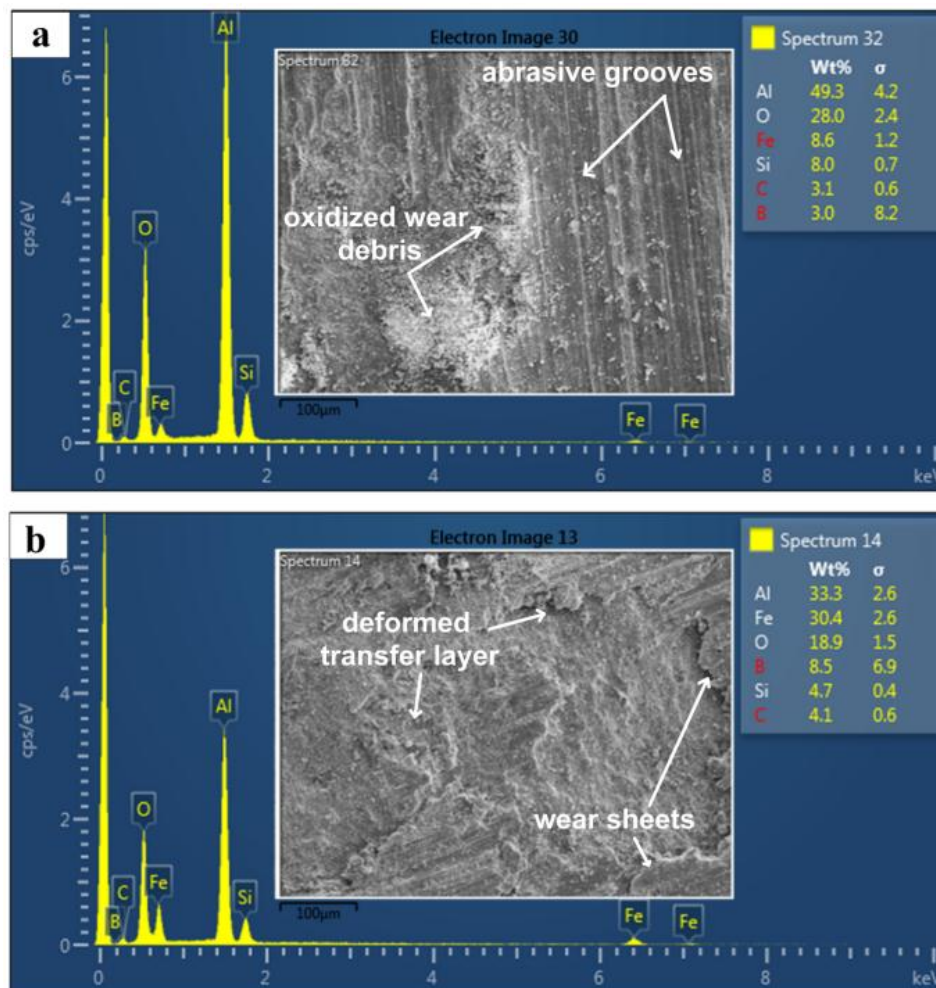


Figure 4.5 EDS of 1.0 wt % nB₄C composite for **a** 0.354 MPa, **b** 1.412 MPa (at 0.66 m/s).

Figure 4.5 displays the EDAX spectrums of 1 wt% composite tested at 0.66 m/s when the nominal pressure is varied from 0.354 MPa to 1.412 MPa. It reflects heavy rise in the iron content on the worn surface when the applied pressure is maximized. As the base alloy has marginal iron content in its composition it is obvious that more iron is drawn from the counterface steel disc under the action of highly stressful metallic sliding contact.

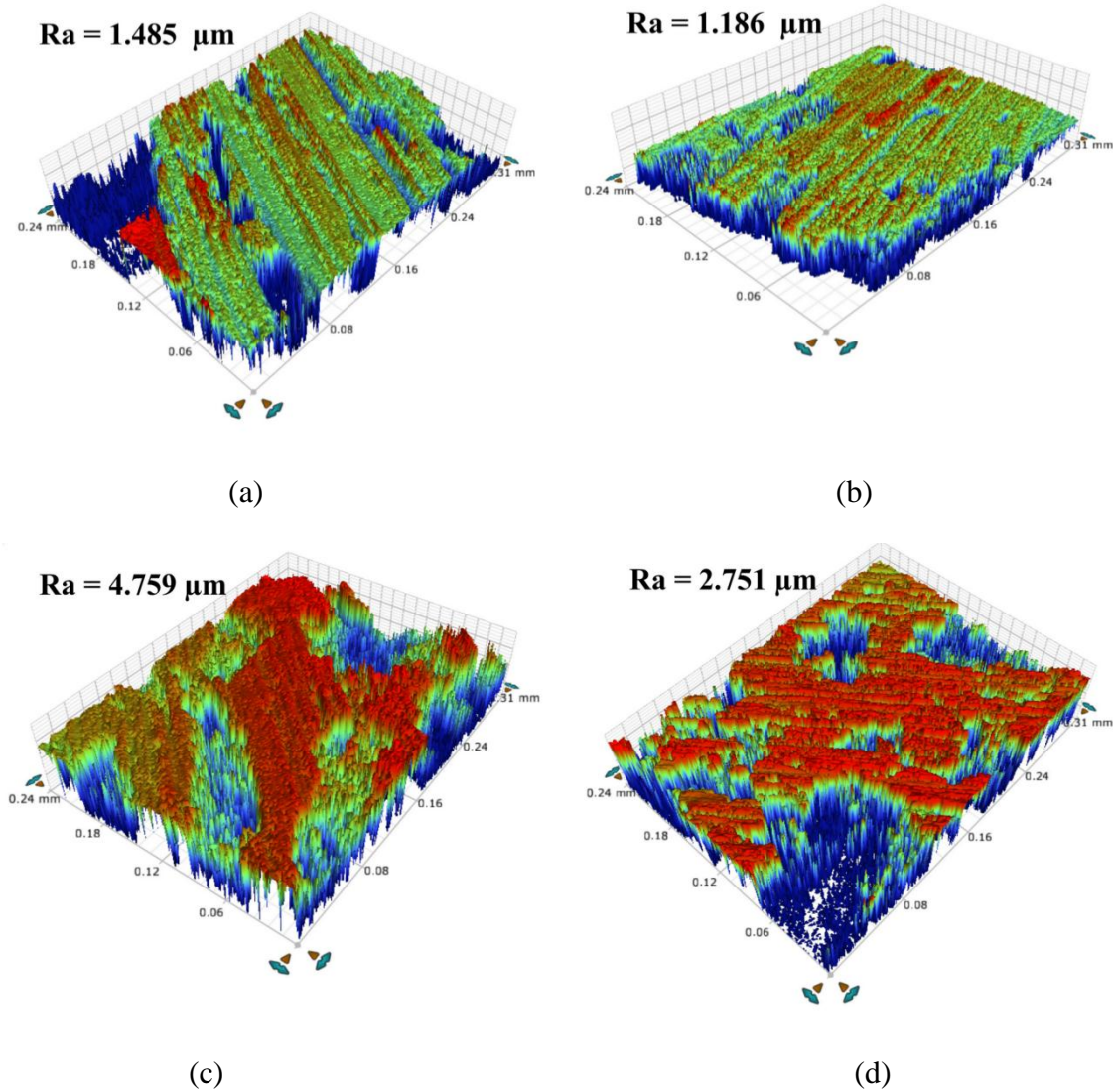


Figure 4.6: Surface roughness at 0.66 m/s: (a) Alloy, (b) 2 wt% composite (at 0.354 MPa); (c) Alloy, (d) 2 wt% composite (at 1.412 MPa)

Figure 4.6 shows 3D optical profiles of the worn surfaces of base alloy and 2wt% composite when the minimum and maximum load-speed (PV factor) conditions are

employed. It can be visualized that surface roughness values of both alloy and composite are increased when subjected to higher load. Relatively wider and deeper grooves can be seen for base alloy at low pressure. At high pressure less cavities and more uniform top land of debris layer is observed for the worn surface of composite. These topographical features are in correlation with the wear rates observed.

Considering the wear loss results obtained in pin on disc test, worn surface morphologies and their EDAX spectrums, the possible wear mechanisms for the tribo pair under investigation are described as follows. During initial conformal sliding contact hard asperities from either surface started scratching each other. Silicon being hard phase (1450 Hv) can easily scratch steel counterface (approx. 900 Hv) although the overall hardness of LM6 is just about 70 HV (Sarkar and Clarke, 1980). Hence even at low load condition iron is detected on the worn surfaces of alloy and all composites. At the same time silicon is susceptible to cracking under such situation. It is because silicon-matrix interface being stress raiser can easily provide crack propagation site under low sliding temperatures. Therefore some of the silicon particles are removed from the sliding surface and detected in the dispersive X-ray analysis. Whereas at high load silicon particles get pushed inside the thermally softened Aluminum matrix and as such less amount of silicon is detected in EDAX spectrums. Besides adhesive friction created asperity welds and their breakage resulted in transfer and back transfer of elements between the sliding surfaces. But this occurred for very early period of the sliding contact. As sliding is continued more debris particles are generated and simultaneously get compacted with increasing loads which gave rise to transfer layers. Rising temperature in the interface with increasing load oxidized the wearing material which is intensified with load. Depth of surface damage heightened and severe transition of wear rates are observed beyond 1 MPa pressure. Removal of wear debris from wearing surfaces is increased in the process. However the presence of oxidized debris is seen prevalent on the highly deformed worn surfaces. It suggests that the oxidation and adhesive delamination wear mechanisms are still prevalent. No evidence of gross metallic wear is observed in the entire load range employed for all the fabricated materials. Abrasive wear dominated the wear behavior of composites at low loads as evidenced by parallel abrasive groove lines caused by hard steel asperities. Improved hardness of composites due to reinforcement prevented large indentation in the composite matrix. Due to which adhesion is eliminated and the entire

surface is covered with numerous debris particles. Few shallow delamination patches are also seen to have been filled with loose wear particles. As the load is increased these debris are accumulated to form mechanically mixed tribo layers. Stability of these layers improved with thermally insulative boron carbide particles. These layers being hard yet lubricative can be attributed to the reduced wear rate of Al-nB₄C composites relative to base alloy. Thickness of the tribo layers increased with sliding and on reaching a critical size developed subsurface microcracks. At higher applied pressure these work hardened layers started getting delaminated leading to the formation of shallow craters. Thus for the nanocomposites under test, mechanical mixed layer (MML) and oxidized debris are found to be the key factors governing wear rates. At low loads abrasives grooves with relatively smooth surfaces are observed (Figure 4.3 b, c) while at high loads damaged transfer layers are seen as shown in Figure 4.3 e-f. These observations are in line with those reported earlier (Manivannan et al., 2017; Harichandran and Selvakumar, 2016; Li and Tandon, 1999; Rosenberger et al., 2005; Tavoosi et al., 2010).

4.3.1.3 Effect of sliding speed

Figure 4.7 exhibits variation of wear rate of all fabricated materials with increasing speed at fixed contact pressure of 1.412 MPa. It is observed that wear rate decreases rapidly when the speed is changed from 0.16 m/s to 0.33 m/s. A moderate fall in wear rate is seen for composites than alloy in between 0.33 to 0.49 m/s speed variation. Thereafter a transition in wear rate is seen for the further rise in sliding speed. At this low load initially in the absence of protective tribo layer, more metallic contact resulted in the adhesive surface damage. Higher wear rate in such situation can be due to transfer deposition of pin material on to the counterface. As the speed is increased, more material transfer occurs between sliding bodies which lead to the formation of oxide film on pin surface under increased interface temperature. Stain rate is also seen to increase the flow strength and hardness of Al-12Si alloy with increasing sliding speed and reduce the wear rate as a result (Subramanian, 1991). But at the same time there is every possibility of losing debris particles from the sliding interface due to increased sliding speed. Loss of material and fresh metallic contacts is probably the reason for the rise in wear rate at the transition speed of 0.49 m/s. Another possibility is that interface temperatures get increased with increasing sliding speed and more so at high loads. Increased heating leads to thermal

softening of the matrix and in turn can result in higher wear rate. Nanocomposites are seen to perform better than alloy due to increased hardness, strength and thermal stability on account of B₄C nanoparticles. EDAX spectrum and corresponding worn surfaces (Figure 4.8) for 2 wt% composite obtained at two extreme speeds reveal this behavior. Relatively smooth worn surface obtained at high speed is an evidence of less wear.

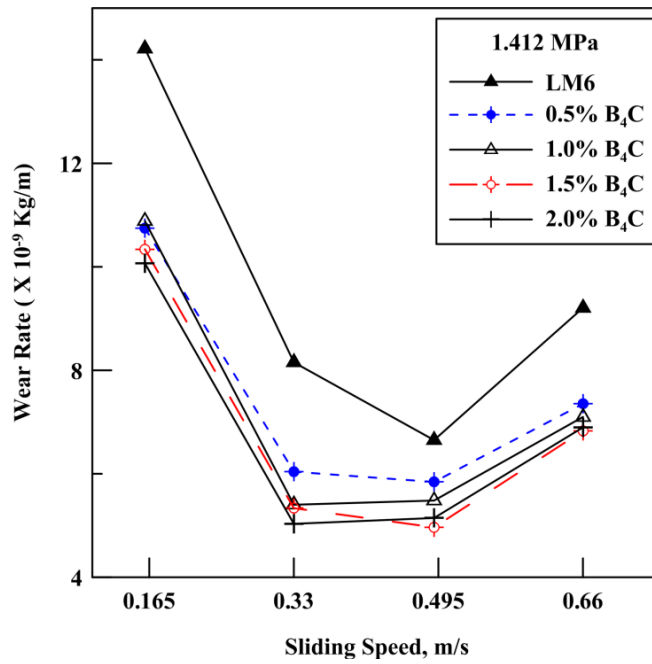
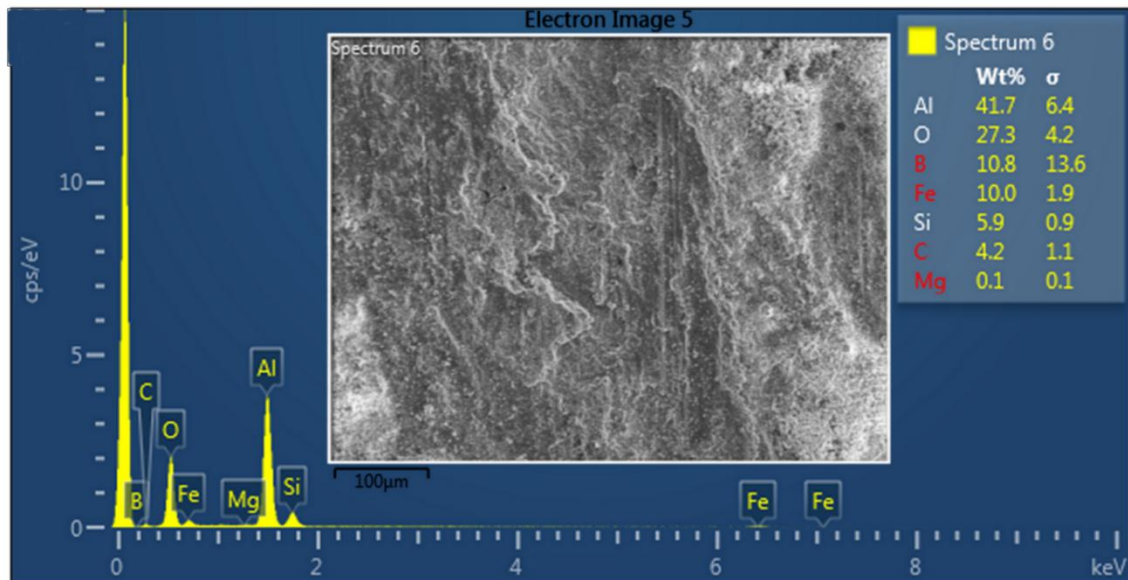
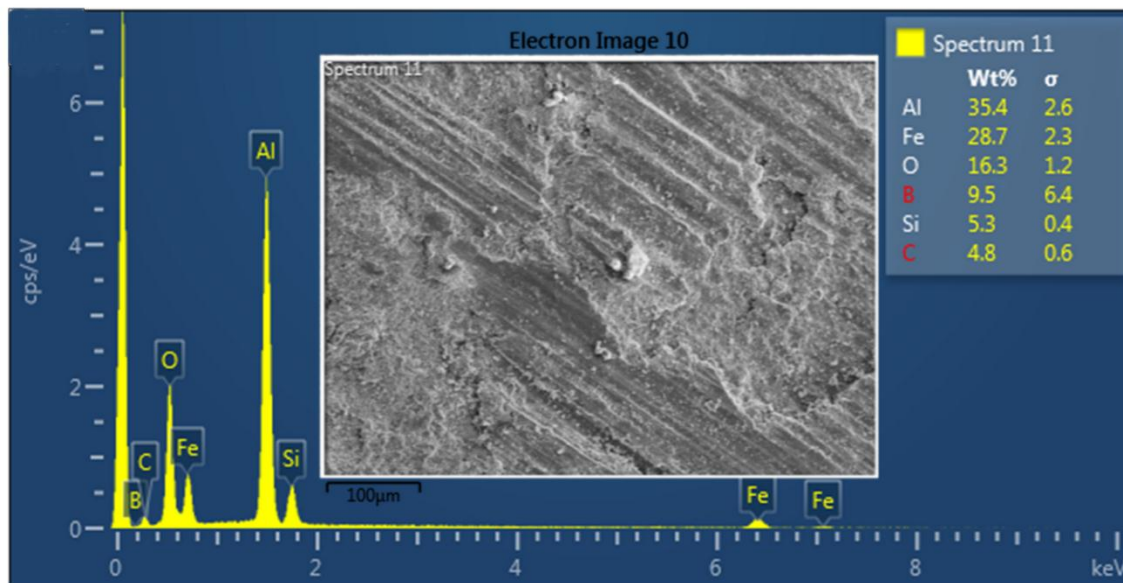


Figure 4.7 Wear rate Vs sliding speed at 1.412 MPa



(a)



(b)

. Figure 4.8: EDS of 2.0 wt % nB₄C composite at 1.412 MPa for speed variation:

(a) 0.16 m/s, (b) 0.66 m/s.

4.3.1.4 Effect of sliding distance

Wear rate variation of all the fabricated materials as a function of sliding distance at fixed nominal pressure (1.412 MPa) and speed (0.66 m/s) is shown in Figure 4.9. Wear rate of all materials remained almost steady during initial 800 m of sliding distance but thereafter base alloy exhibits excessive wear relative to the B₄C composites. Increased temperature in the sliding interface generated on account of prolonged contact under high load cause thermal softening of the matrix. It leads to increased plastic deformation and hence increased wear volume. Weakened top layer under high load and third body wear caused by the trapped wear debris possibly could have led to the high wear rate of base alloy. Ultra-fine B₄C particles however hold the matrix and prevent deformation of sliding surface due particle induced dislocation strengthening. Therefore composites have shown better wear resistance with increasing reinforcement content over the entire sliding distance. Delay in thermal softening on account of hot-hard B₄C particles is another possible reason for their improved wear performance. However wear mass loss is found to increase with increasing sliding distance for all materials at all the applied contact pressures. But at loads of 10 and 20 N, wear rate of fabricated materials have shown

decreasing trend in the initial period of sliding distance say up to maximum of 1200 m especially at low speed of 0.16 m/s after which a sharp increase is detected. Accumulation of wear protective transfer layers and oxidized debris in the early period and their removal from interface after prolonged sliding can be the reason for such behavior.

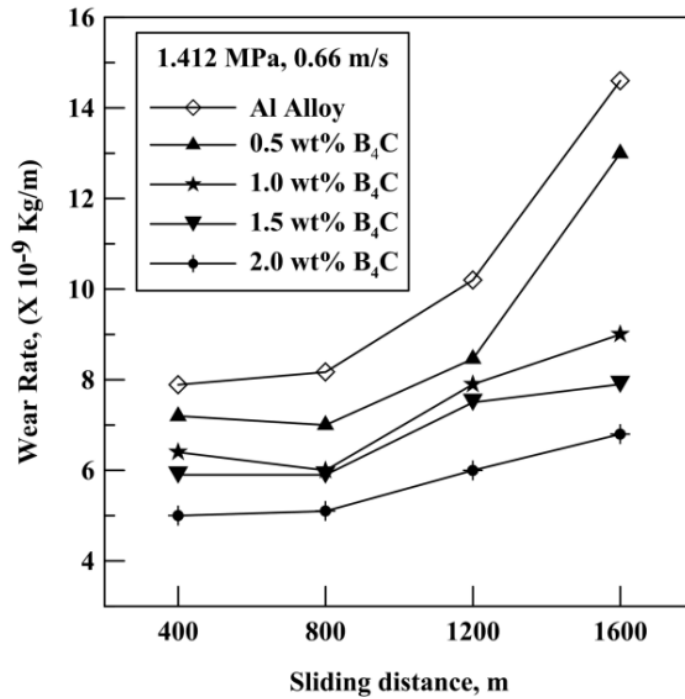
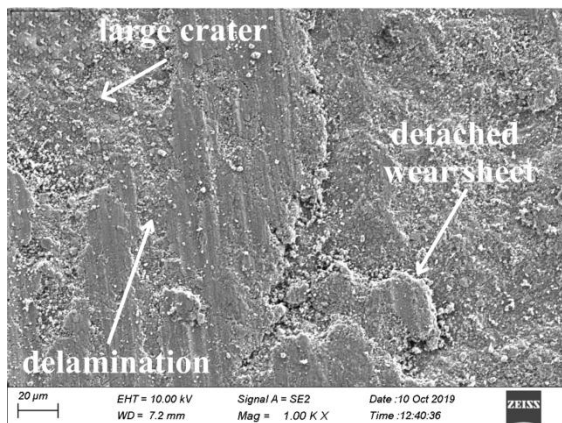
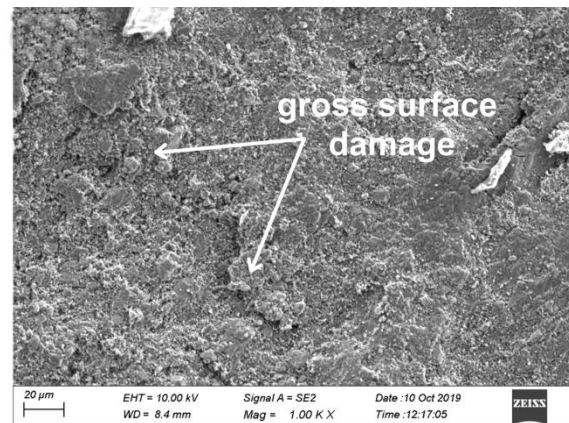


Figure 4.9: Wear rate of fabricated materials as a function of sliding distance



(a)



(b)

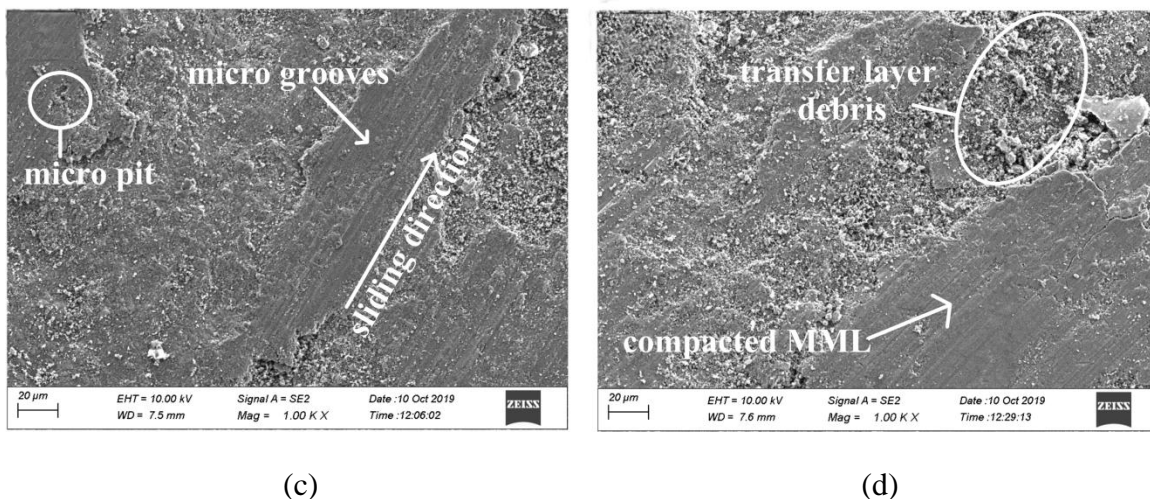


Figure 4.10: Worn surface profiles obtained at 400, 1600 m sliding distance:

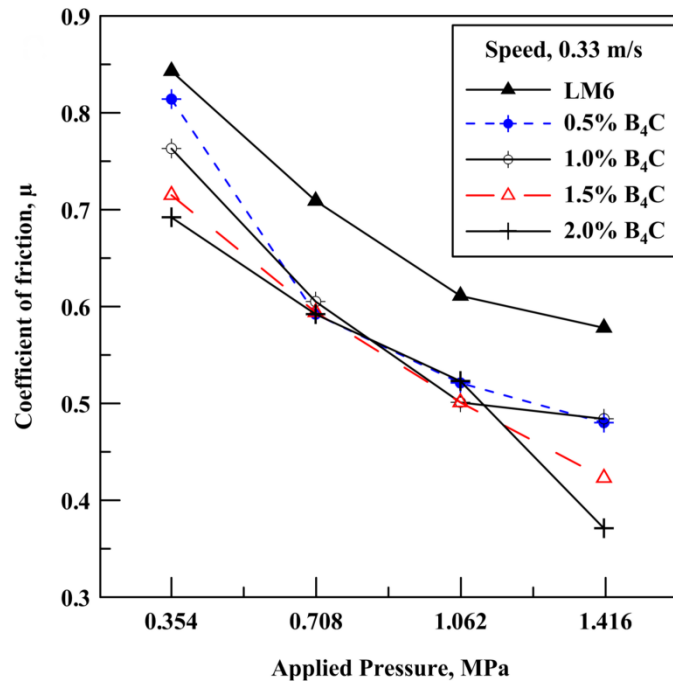
(a), (b) base alloy; (c), (d) Al-1.5 wt% B₄C

Figure 4.10 shows worn surfaces of base alloy and 1.5 wt% B₄C composite captured in FESEM at high magnification (1KX). Gross surface damage is observed for base alloy at 1600 m sliding distance while wear protective compacted mechanically mixed layers are seen for the composites. These images are in accordance with the wear rates measured and shown in Figure 4.9. Well dispersed hard reinforcement particles extended the abrasive delamination wear mode of composites.

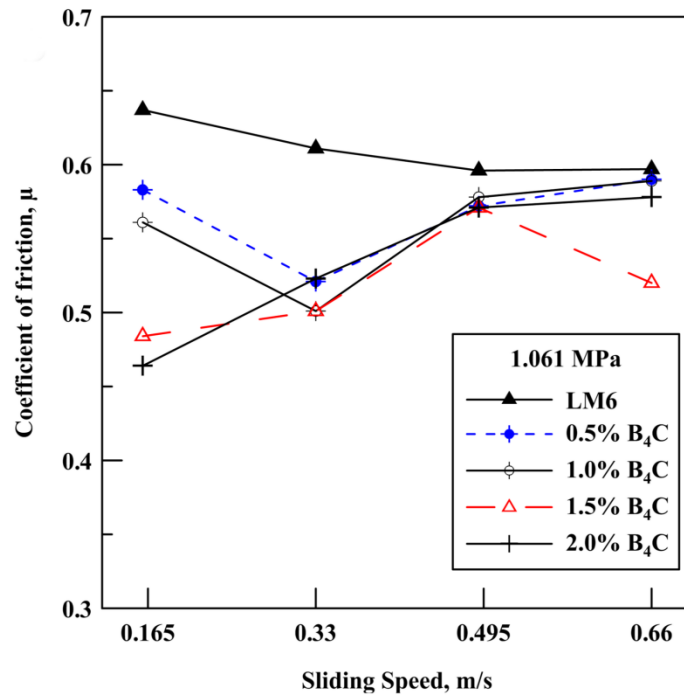
4.3.2 Friction behavior

Influence of applied pressure and sliding speed on the friction coefficient of base matrix and composites is presented in Figure 4.11. Friction coefficient is found to reduce drastically with increasing contact pressure at every fixed sliding speed. With increasing pressure, mechanically mixed layer (MML) gets more accumulation of transfer elements from both sliding components. Moreover because of the increased frictional heating their oxidation is accelerated in the contact interface. Presence of compacted transfer layer reduced direct metal to metal contact and its lubricative nature reduced friction coefficient. It is also found that incorporation of increasing amount of B₄C particles have lowered the frictional resistance of alloy. B₄C particles are thermally stable and for being extremely hard can draw more iron from the steel counter disc. Iron oxides are found to be lubricative in nature. Oxidation of boron carbide takes place at 250°C in humid environment whereas more stable glassy layer of boron oxide (B₂O₃) forms quickly on

B₄C in dry air at temperature around 650°C (Litz and Mercuri, 1963). However Mahesh et al. (2011) recently have found the formation of boron oxide in dry air at 300°C.



(a)



(b)

Figure 4.11: COF variations with (a) applied pressure and (b) sliding speed

Temperatures in the real areas of contact are considerably higher than the average surface temperature in the sliding interface. Hence it is possible that high temperatures at the contact plateaus of transfer layer containing boron carbide will oxidize it. Kumaran and Uthayakumar (2014) have reported formation of B_2O_3 under similar tribological conditions. Boron oxide being lubricious can considerably reduce the dry sliding friction. Hence for high contact pressure of 1.416 MPa probably we have seen such a drop of friction coefficient from 0.692 to 0.371. However further investigations in this regard can provide more insights. Some researchers have seen reduction in frictional force of Aluminum composites due to uniformly dispersed ceramic nanoparticles. They attributed this behavior to the increased hardness and particles supporting the load which reduced contact area (Nemati et al., 2011; Hosseini et al., 2012). We however believe that nanoparticles being too small can share applied load with the matrix on having strong matrix particle interfaces. Also lubricious tribolayer is comparatively more significant in reducing friction than the improved hardness and refined microstructure on account of reinforcement content as observed by Moghadam et al. (2016). On the other hand smooth surface of AlSi12 (hardest amongst the Al alloys) sliding in contact with smooth iron counterface can generate high friction due to adhesive interaction especially at low loads. However, with higher loads and prolonged contact the friction of base alloy can reduce due to the oxidized wear debris. Another observation (Figure 4.6) noted here is that more damaged surface (increased roughness) at high loads has not increased frictional force of the fabricated materials against steel. Among the deformed surface entities such as cavities, grooves and craters the raised portions (with transfer layers) largely decided the contact conditions favoring reduced friction. It has also been observed earlier that a high degree of surface damage does not ensure high friction coefficient (Sarkar and Clarke, 1980). Figure 4.12 shows friction coefficient profiles for 1.5 wt% B_4C nanocomposite which are similar to those seen for other composites and even base alloy. At low load coupled with less speed the adhesive factor of friction is found crucial to increase frictional force. Moreover wild fluctuation with periodic high amplitude is seen for the entire test duration for loads up to 20N. Presence of partially oxidized loose wear debris particles on hard surface and continuously varying asperity contact conditions could be responsible for this quick reversal of frictional resistance. However for the applied load of 40N much smoother friction profile is observed which indicates steadiness in the contact

conditions governed by transfer layer interface. Despite fluctuating and partially overlapping profiles, the average friction coefficient values are seen spaced noticeably for varying loads. For instance average COF values observed for the case in Figure 4.12 are 0.758, 0.628, 0.485 and 0.452. Figure 4.11b shows marginal decrease in the friction coefficient of base alloy with increasing sliding speed. Nanocomposites displayed lower COF values than the alloy but clear behavioral trend is not seen among them for the entire speed range. The range of speed considered may not be sufficient for these composites to create major difference in the frictional conditions for establishing predictive trend. Oscillations in the COF values with speed can be attributed to the varying presence (accumulation and elimination) of debris on the wearing surfaces. So we observe that applied load is the most influencing parameter varying frictional contact resistance under the tested experimental conditions,

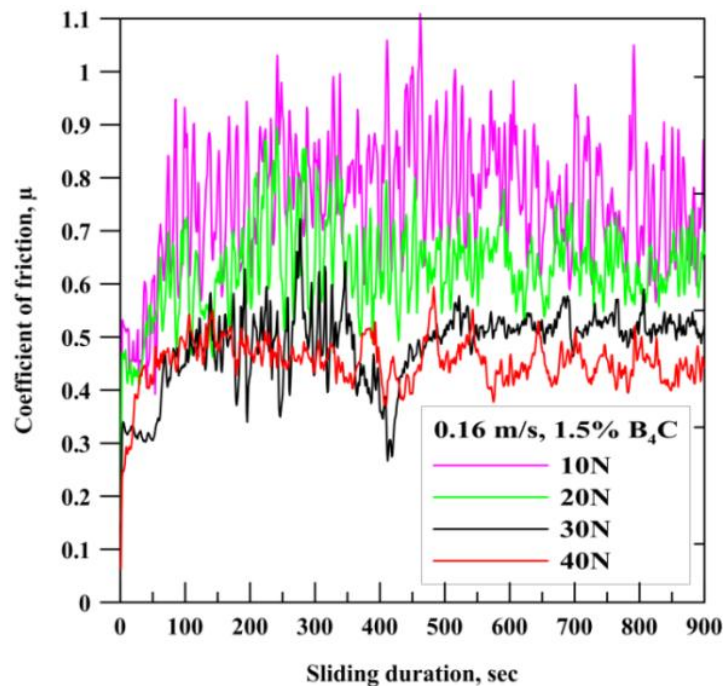


Figure 4.12: COF profiles for 1.5 wt% B₄C at different applied loads at 0.16 m/s speed

4.3.3 Tribological performance of 1.5 wt% B₄C composite

Literature suggests that in most tribological studies, effect of applied load is investigated more than other extrinsic parameters. Components designed to be in continuous tribological contact for extended time however requires detailed investigation for their

tribological behavior as a function of speed or distance. There can be applications wherein the tribo-couple is subjected to relatively fixed PV factor but made to slide for different sliding durations ranging from small to prolonged one. For instance the wear of piston and cylinder liner depend more on sliding duration and speed as the contact stresses are relatively low. Ambigai and Prabhu (2017) in their optimization study have identified sliding distance to be the most dominant factor among other dry wear test parameters. Liu et al. (2010) studied the influence of speed range 0.01- 0.08 m/s and 30 min of sliding on the tribological response of Al composite. They reported that tribo layer thickness increased and hence sharp decrease in wear rate is observed up to 0.04 m/s speed. But for further rise in speed, tribo layer depleted and wear rate decreased only marginally. These studies indicate that speed and distance are influential parameters and as such many more such efforts are required to study their tribological impact.

In the earlier set of experiments the speed range was insufficient to have clear trends on friction variation. Also the maximum sliding distance was 596 m. Hence to understand in detail the influence of speed and sliding distance, a new set of experiments are designed wherein the pressure is kept low (20N). The effect of speed is studied by rotating the disc at different speeds from 0.25 to 1.25 m/s so as to cover a fixed sliding distance of 500 m. The effect of varying distance is studied at two different PV factors of 10 Nm/s and 25 Nm/s. These factors are realized by employing a constant load of 20 N and two sliding speeds of 0.5 m/s and 1.25 m/s which create maximum sliding distances of 1200 m and 3000 m respectively. Duration of the test is set as 40 min and the wear loss is measured after every 10 minutes of sliding duration. One of the fabricated composites (1.5 wt% B₄C) is selected for investigation and its performance is compared with that of base alloy.

4.3.3.1 Influence of speed

Figure 4.13(a) displays the wear rate variation of Al alloy and Al-B₄C composite with increasing speed. Base alloy displayed decreasing wear while composite material exhibited only marginal drop in the wear rate up to the transition speed of 0.5 m/s. But for further increase in sliding speed, sharp rise in wear rate is observed, more so for the base alloy. Compared to the base alloy, Al-B₄C composite has shown significant reduction in the wear rate at all speeds. In general the improved wear resistance of composite matrix is attributed to the enhanced strength and hardness imparted by hard B₄C phase. Composite

has performed much better especially for speeds above 0.75m/s. It can be due to the increased thermal stability and hot hardness offered by B₄C particles. Wear trend of base alloy is found consistent with that published earlier by Subramanian (1991). For the alloy of same composition he found 1 m/s as the critical transition speed for 0.5 MPa applied pressure whereas we found it at 0.5 m/s for 0.707 MPa. He proposed two phenomena to act simultaneously in such situation. First, increased speeds increases strain rate which increases the flow strength of sliding surface. Increased flow strength reduces true contact area and eventually reduces the wear rate. Second, increased speed softens the surface due to frictional heating. It in turn increases the true contact area and hence increases the wear rate. The strain rate effect dominates temperature effect before transition speed while the opposite take place after the critical speed.

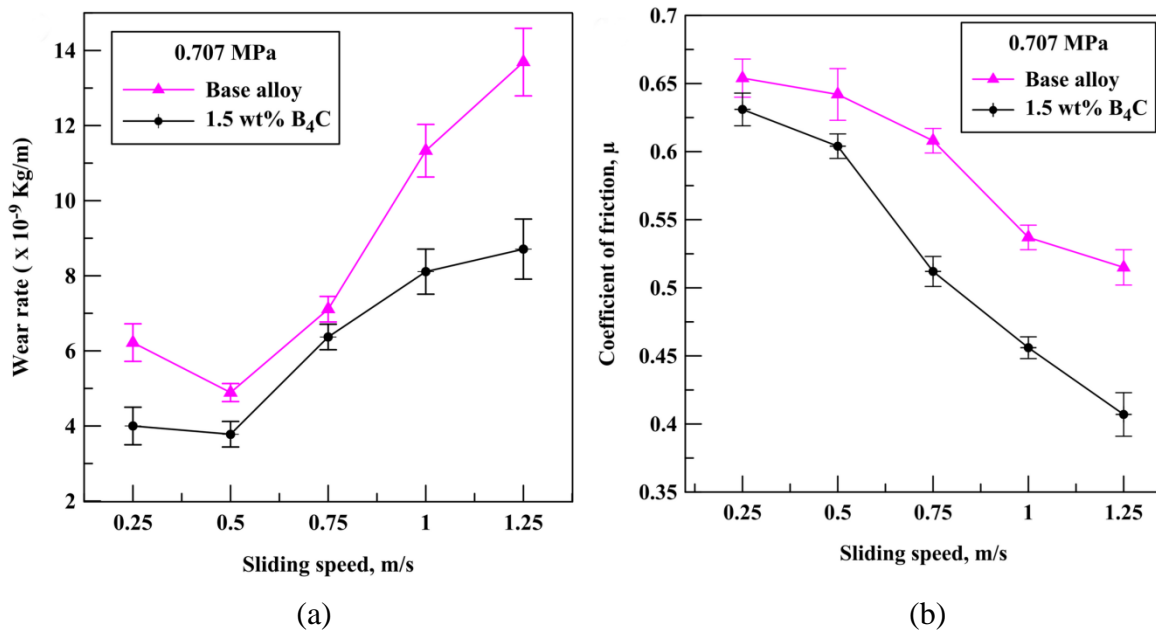


Figure 4.13: Effect of sliding speed on: (a) wear rate (b) coefficient of friction

For understanding wear mechanisms, we examined worn surfaces obtained at various (0.25, 0.5, 1.25 m/s) speeds which are presented in Figure 4.14. Worn surface of base alloy in Figure 4.14a shows two distinct features such as craters and relatively smooth area with fine debris particles. Formation of these features is explained as follows. Wear test started with the conformal contact between mating surfaces. And at lowest speed (0.25 m/s), it took almost 33 min to cover the fixed sliding distance of 500 m. During the early period of sliding metallic contact, hard asperities of counterface removed soft

Aluminum phase surrounding silicon particles. The exposed silicon particles being harder than steel disc started scratching it to draw some iron particles in to the interface. At the same time, under the applied contact pressure, some of the silicon particles fragmented to form part of wear debris. As sliding continued further, these trapped debris particles are crushed to finer sizes. Compaction of debris particles induced formation of smooth debris layer on the wearing surface. Prolonged sliding contact induced thermal softening which increased real areas of contact. This in turn favoured formation and breakage of micro welds at the contact plateaus. Thus adhesive wear mechanism became dominant and therefore cavities and craters are formed on the otherwise smooth sliding surface at low sliding speed. EDX analysis of the worn surface of base alloy obtained at 0.25 m/s is shown in Figure 4.15a. Significant amount of iron is detected which justifies the tribological interaction discussed above. Oxygen peak and its amount clearly indicate that debris particles are oxidised under the operating tribo conditions. At next higher speed of 0.5 m/s, the sliding duration is reduced to about 17 min. At double the previous speed, large amount of debris particles are created in the interface due to transfer and back transfer of materials between sliding bodies. These particles are oxidised and pulverised to finer sizes. They are observed to fill the shallow cavities formed on the surface beforehand as shown in Figure 4.14b. Direct metal to metal contact is reduced due to barrier created by oxidised debris particles. Hence the wear rate is reduced further on account of decreased adhesion. Microcutting lines are also visible in the micrograph. Worn surface thus indicates that combination of abrasion, oxidation and mild delamination is prevailed at this sliding speed. EDX spectrum in Figure 4.15b also justifies oxidation of wear particles. With further increase in sliding speed more and more debris is generated in the interface. But at higher speeds, substantial part of the wear debris is removed from the wearing surface. Hence due to possible occurrence of more metallic contact, higher temperatures are generated in the interface even in relatively short sliding time. Therefore weakening of subsurface region took place resulting into the plastic deformation of the sliding surface. Worn surface obtained in about 7 min of sliding at 1.25 m/s (Figure 4.14c) demonstrates this behavior. It exhibits plastically deformed areas, formed due to severe delamination leading to much higher wear rate. EDX spectrum shown in Figure 4.15c reveals reduction in oxygen and iron content. It further adds to the understanding that wear particles are not oxidised and compacted to

great extent due to reduced sliding time. On the other hand, worn surface of Al-B₄C composite is covered with smaller and equiaxed debris particles at 0.25 m/s as shown in Figure 4.14d. It also shows the evidence of mild delamination and micro cutting action. Increased hardness of composite surface covered with fragmented debris particles can diminish adhesive action (Hemanth, 2005).

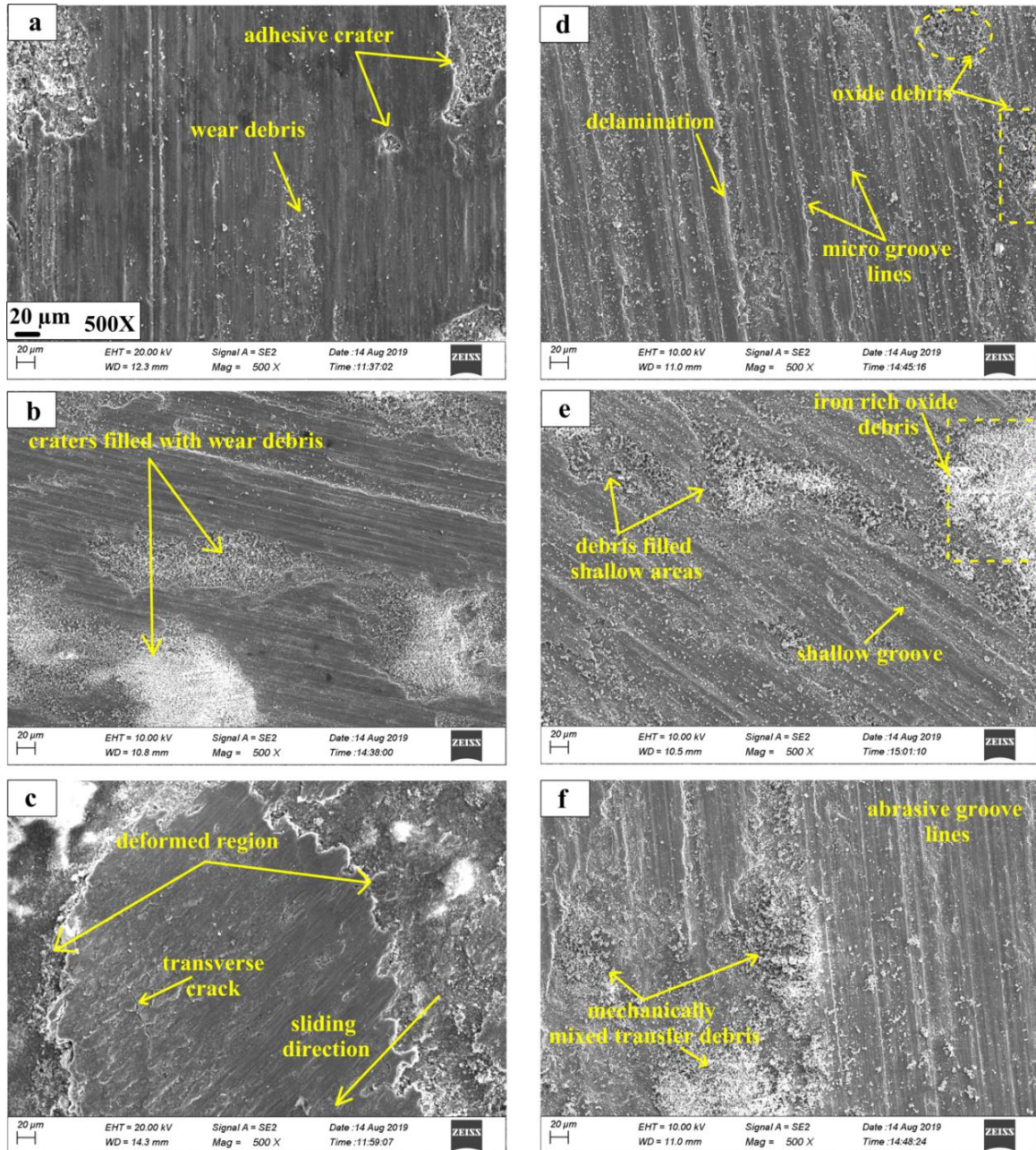
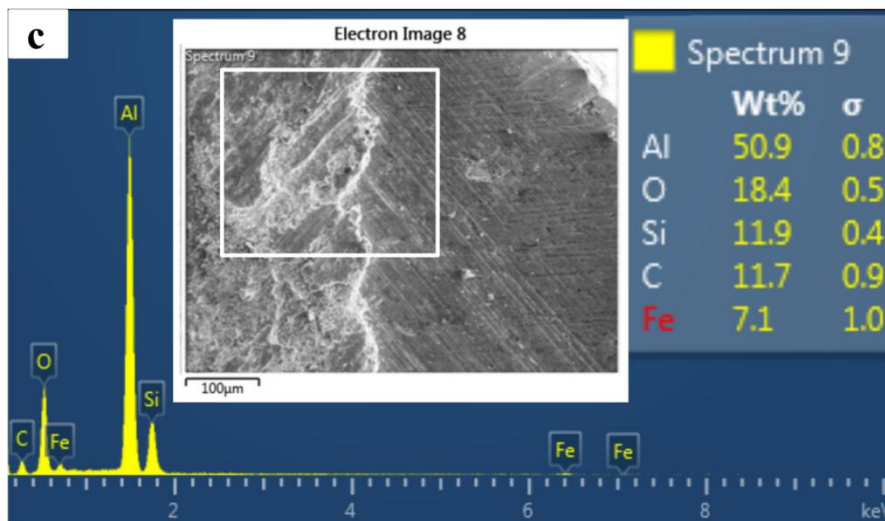
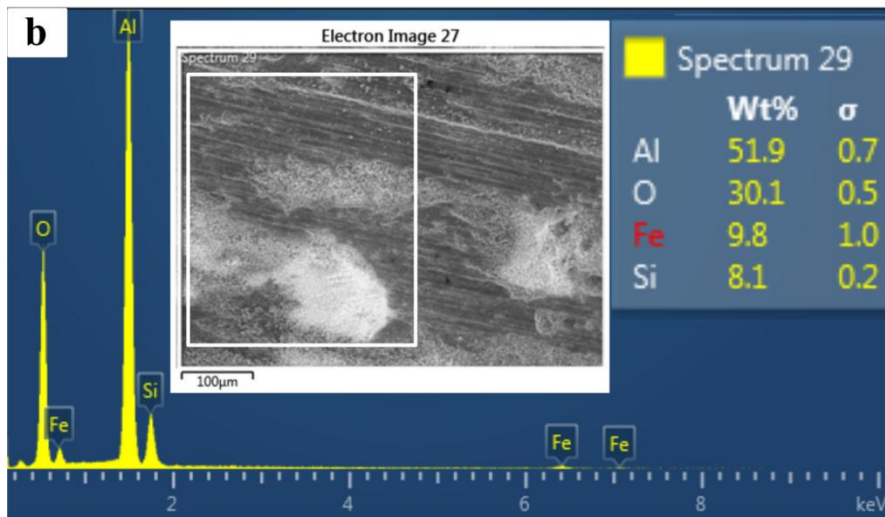
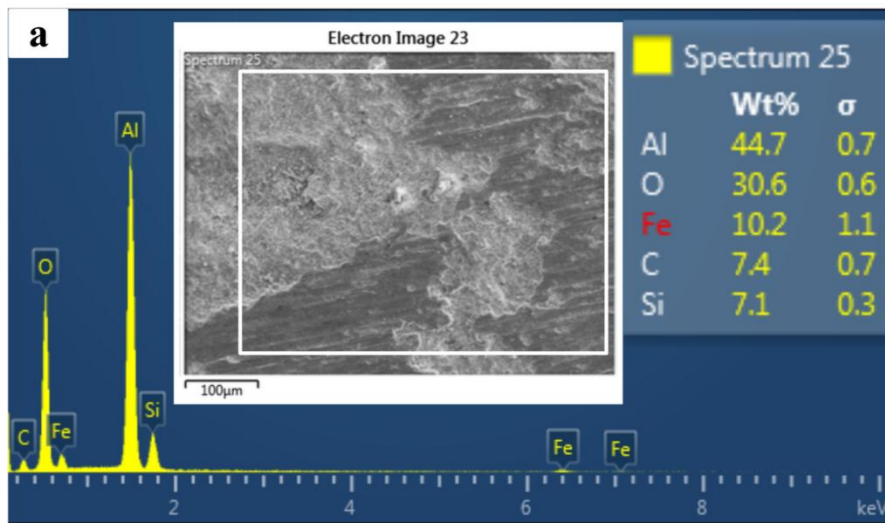


Figure 4.14: Worn surfaces obtained at sliding speed of 0.25, 0.5 and 1.25 m/s: Base alloy (a, b, c), Al-B₄C composite (d, e, f)



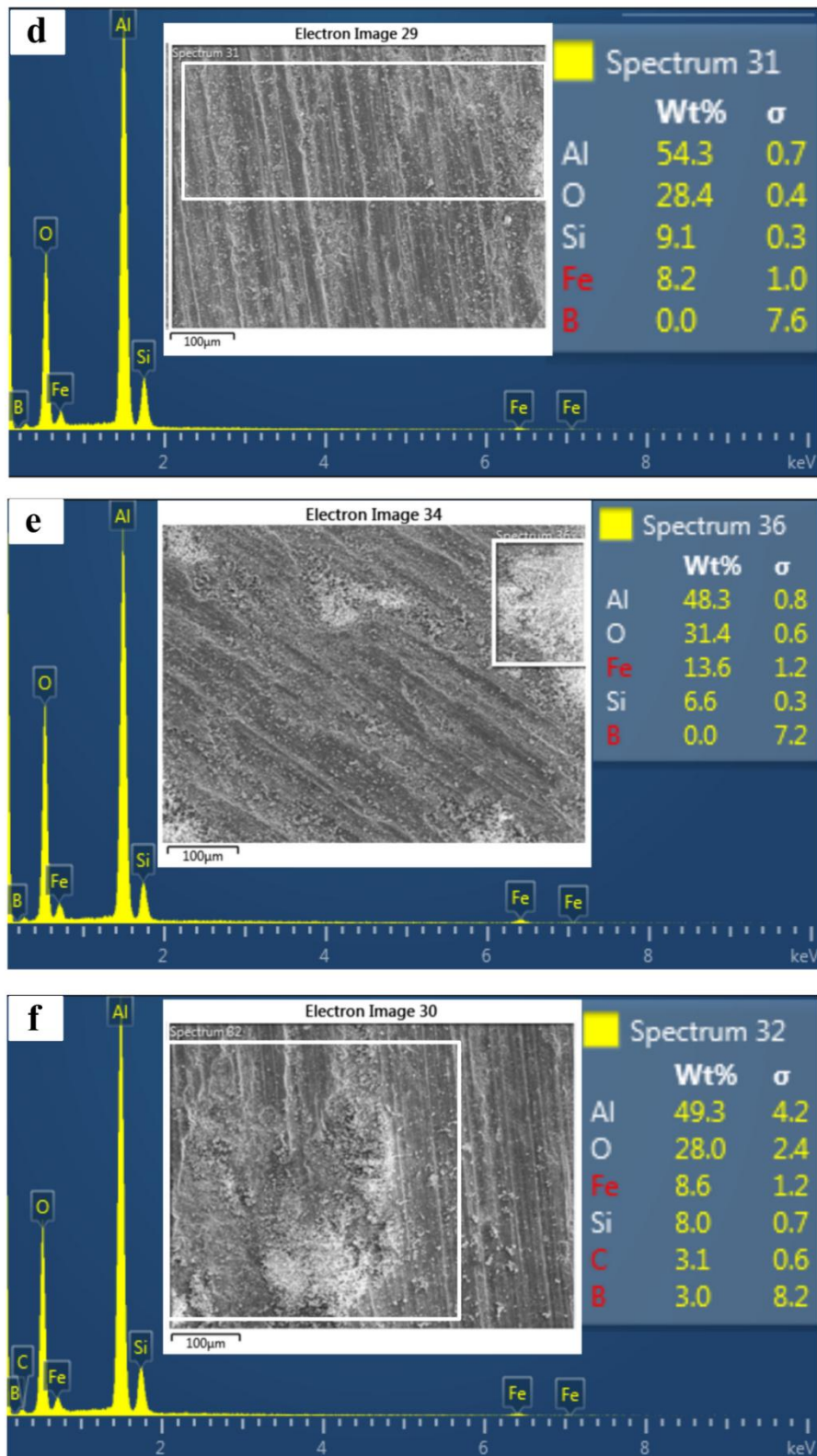
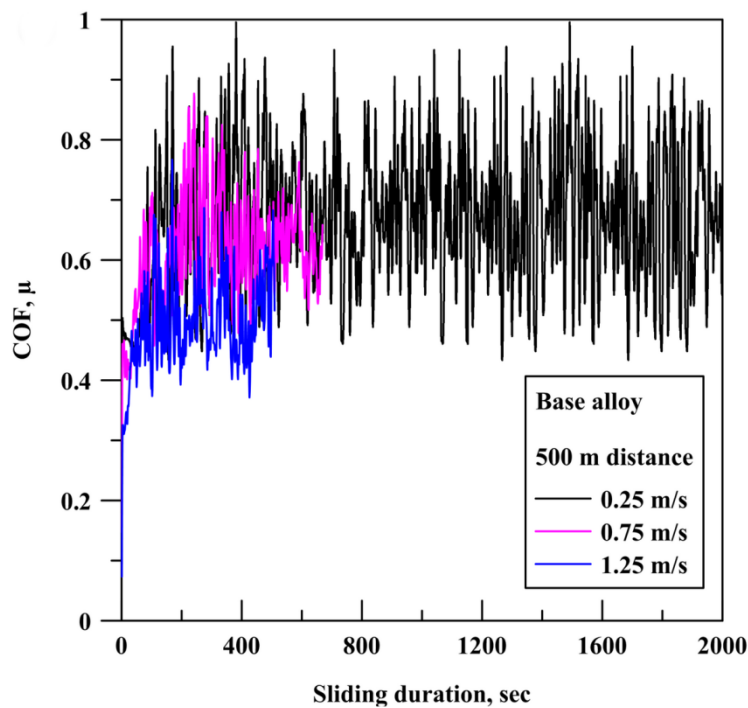
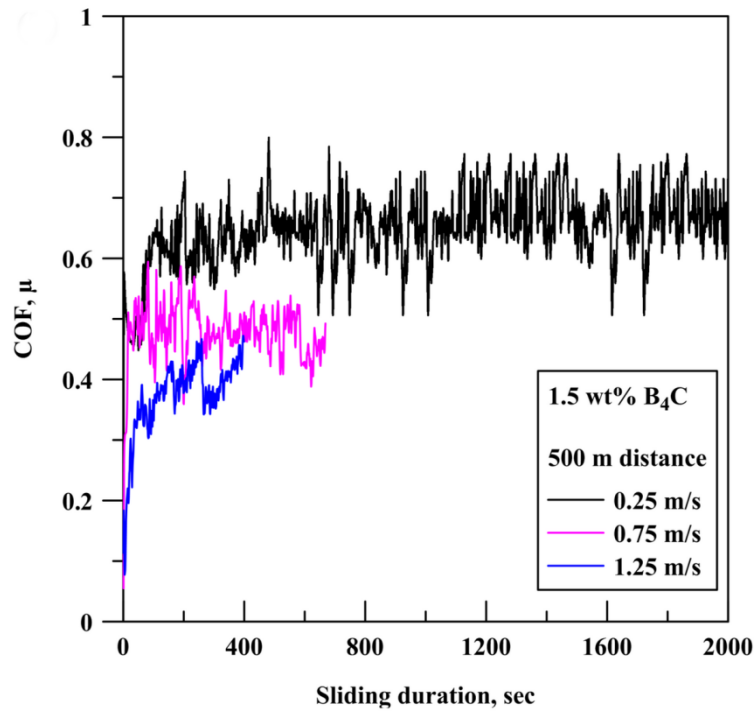


Figure 4.15: EDX analysis of worn surfaces obtained at different speeds 0.25, 0.5, 1.25 m/s: Base alloy (a, b, c); Al-B₄C composite (d, e, f)

EDX data in Figure 4.15d proves that oxidative abrasion wear played dominant role to reduce wear rate. At 0.5 m/s, wearing surface is characterized by shallow grooves and micro craters with large amount of debris as shown in Figure 4.14e. From the EDX analysis of this surface (Figure 4.15e) it can be concluded that iron rich oxide debris are created on the sliding surface. Composite has exhibited least wear rate because of this mechanically mixed oxide debris. Even at the highest sliding speed of 1.25 m/s composite specimen displayed relatively less surface damage. Abrasive wear mechanism continued to play the dominant role due to B_4C strengthened aluminum matrix. Boron carbide particles on detachment from the matrix have become part of the wear protective transfer layer as is obvious from the EDX spectrum shown in Figure 4.15f. The above discussion of wear mechanism reveals that incorporation of B_4C particles has changed adhesion-delamination wear mechanism of base alloy to mostly abrasive mode for composite. Formation of oxidized wear debris to influence wear rate is found common for both the fabricated materials at various speeds. Similar observations are reported by other researchers for aluminum-ceramic composites (Daouda et al., 2004; Lashgari et al., 2010).



(a)



(b)

Figure 4.16: Friction profile against sliding duration at different speeds:

(a) Base alloy (b) Al-B₄C composite

Figure 4.13(b) shows that friction coefficients are decreased with increasing sliding speed. Accelerated oxidation of wear debris, softened wearing surface and diminished adhesion could have reduced the frictional resistance between sliding surfaces at higher speeds. Friction coefficient of base alloy varied between 0.66 and 0.52. Composite matrix displayed lower friction values than those of base alloy and varied between 0.66 and 0.37. It is due to the lubricating effect provided by B₄C particles and the iron oxides present in the mechanically mixed wear debris. Similar trend of reducing friction with increasing speed is reported for Al-12Si/B₄C (Hemanth, 2005) and AA6061-B₄C (Monikandan, 2015) composites. However no meaningful correlation is found between friction coefficient and wear rate with varying speed in this experimental study.

Figure 4.16 shows friction profiles obtained at different sliding speeds. Base alloy has displayed large fluctuations in COF at low speed as seen in Figure 4.16(a). Higher adhesion and continuous transfer and back transfer of dislodged material from pin surface due to shearing action can result in such behavior (Ravikiran and Surappa, 1997). With

increasing speed this fluctuation has reduced. This behavior supports the changing wear mechanisms discussed earlier. Composite has shown lower friction coefficients with less fluctuation due to abrasive wear and oxidized debris layer.

4.3.3.2 Influence of distance

As presented earlier, the minimum and maximum wear rates are observed at 0.5 and 1.25 m/s sliding speed respectively. Hence these speeds are selected to further explore the tribological performance of fabricated materials under the influence of varying distance. Although the maximum sliding duration set for both tests is 40 min, they create different sliding distances and hence can't be compared on one to one basis. They are presented below as individual cases

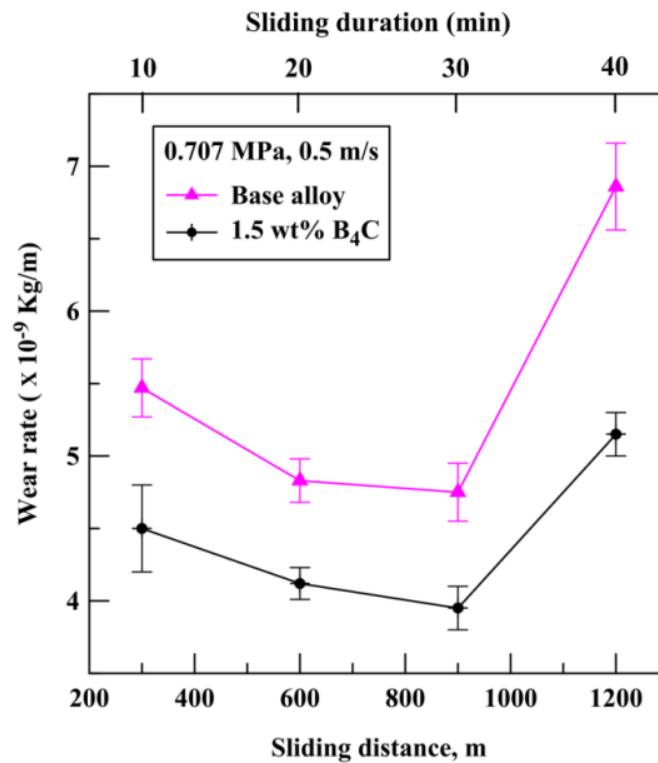


Figure 4.17: Wear rate variation with sliding distance at 0.5 m/s

Figure 4.17 exhibits wear rate variation of both materials with sliding distance for the applied PV factor of 10 Nm/s. It is clearly seen that wear rate of Al-12Si alloy is considerably higher than Al-B₄C composite. Both base alloy and composite pin samples indicated decreasing wear rate with increasing distance up to 900 m. This behavior is

related to 30 minutes of sliding duration. As stated earlier the wear rate is high in the early period of sliding due to more metallic contact and dominant adhesive action. But eventually with further sliding more wear debris are generated and get trapped in the interface. This process continues with sliding and eventually produce mechanically mixed layers on the wearing pin surface. Diminishing metallic contact and tribo layer governed wearing mechanism has therefore exhibited decreasing wear trend. But with further sliding both materials revealed reversed trend showing increase in wear rate. However the composite pin material still has performed better than the base alloy in terms of wear resistance. Plausible explanation to the transition of wear rate observed at 900 m of sliding distance is as follows. Extended sliding duration can increase the thickness of tribo layer due to generation of more and more wear debris. At the same time the process of spalling of critically thickened or loosely compacted tribo layers may coexists. Wear rate has exhibited increasing trend after 900 m possibly because the rate of removal of wear protective tribo layer might have surpassed the rate of its formation.

Worn surface morphologies obtained for both materials at 0.5 m/s and 20, 30, 40 min of sliding duration are displayed in Figure 4.18. These images support the wear rates shown graphically in Figure 4.17. Base alloy has developed delaminated areas, craters and cutting grooves on the surface which are filled with fine debris particles during first 20 min of sliding as shown in Figure 4.18a. The process of formation of these features is close to what has been explained earlier for 500 m sliding distance (Figure 4.14b). But here the worn surface looks relatively smoother while craters and delaminated areas have become smaller and more vivid. This observed difference suggests that debris compaction has progressed during additional 100 m of sliding. The scratch lines and narrow abrasive grooves are then transformed to shallow ploughing grooves and the surface developed tribo layers in the additional 10 min of sliding contact (Figure 4.18b). However after 40 min of dry sliding contact, the wearing surface of base alloy developed large cavities and deformed regions (Figure 4.18c). Close look at the shallow depth of these cavities indicate that they are formed due to removal of thick layer from the sliding surface. It could be a case of sever delamination. However in case of composite, thermal softening of the wearing surface is delayed owing to B₄C reinforcement. Tribo layer is also retained for longer duration as B₄C particles provide thermal stability to the aluminum matrix

(Abdollahi et al., 2014). Abrasive wear mode has remained active for the entire sliding duration as can be witnessed in Figure 4.18 (d, e, and f). Therefore Al-B₄C composite has shown better wear resistance than base alloy for the entire sliding distance.

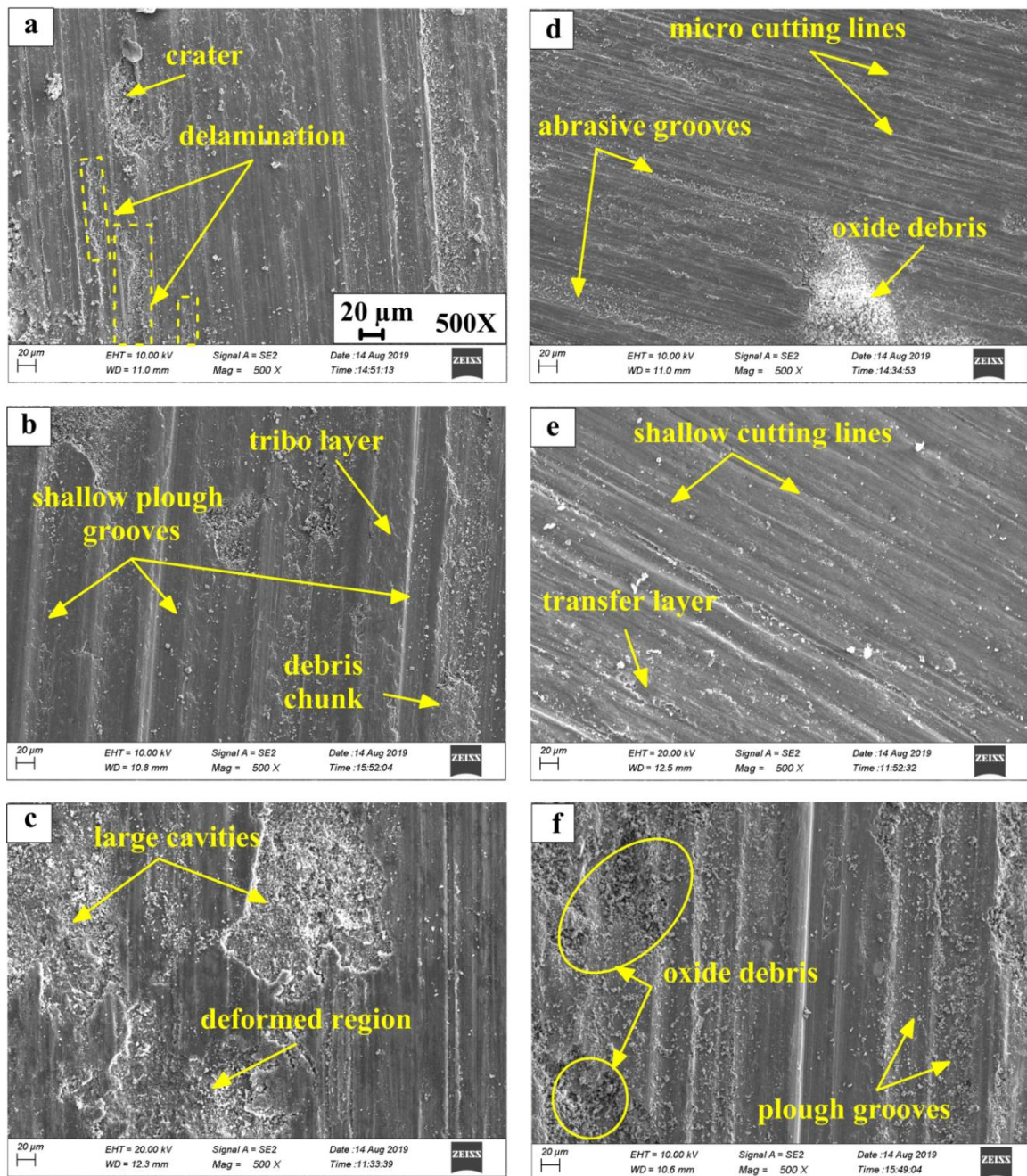
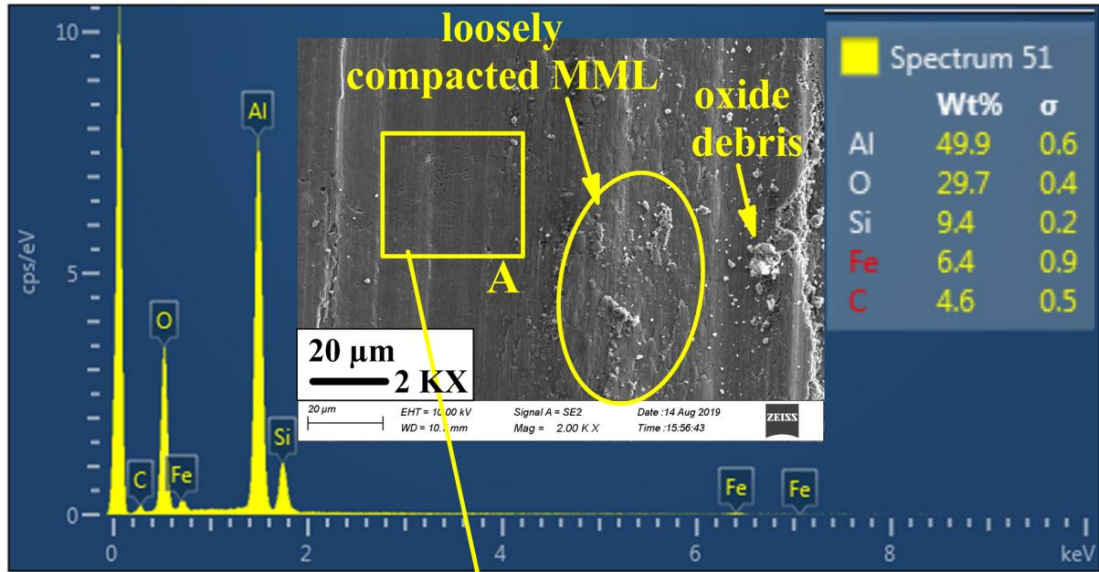


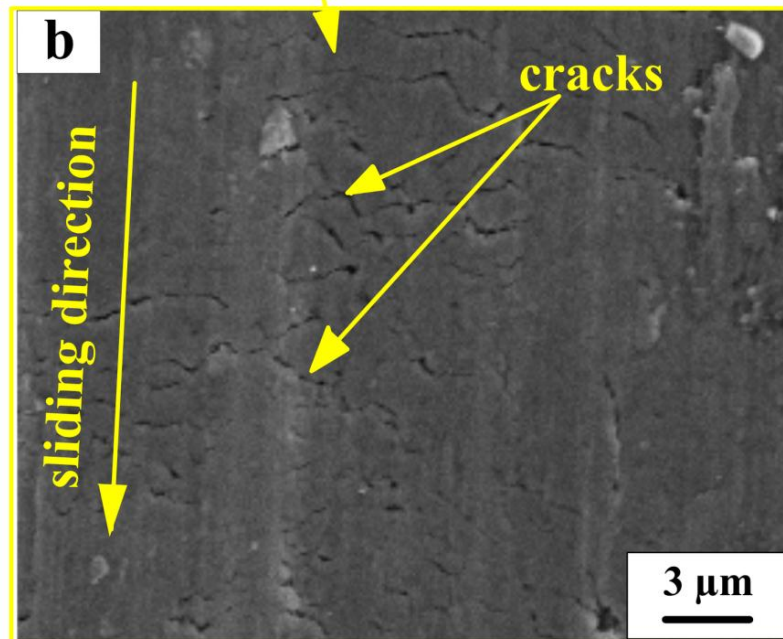
Figure 4.18: Worn surfaces obtained at 0.5 m/s for 20, 30, 40 min of sliding duration (600, 900, 1200 m distance): Base alloy (a, b, c), Al-B₄C composite (d, e, f)

Tribology of Al-B₄C at room temperature

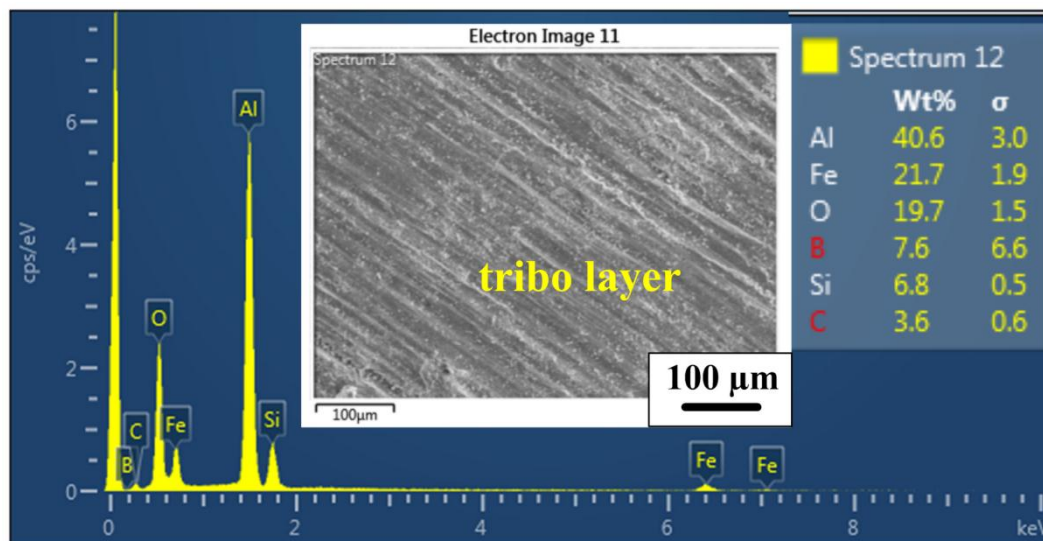
Least wear rate is seen for both materials at 900 m of sliding distance. Hence EDX analysis is done to ascertain the formation of lubricious tribo layer. Magnified micrograph (2000X) and corresponding EDX spectrum of the alloy surface (Figure 4.19a) obtained after 30 min of sliding shows Al, Si, O and Fe. Display of iron and oxygen in the spectrum clearly justifies formation of MML.



(a)



(b)



(c)

Figure 4.19: EDS spectrums obtained at 0.707 MPa, 0.5 m/s, 30 min of sliding: (a) Al-Si alloy (b) magnified view at square 'A' of (a) showing compacted MML with cracks, (c) Al-B₄C composite.

Higher amount of oxygen indicate formation of aluminum and iron oxides under the influence of raised interfacial temperatures. Such oxides are useful to decrease wear rate. The micrograph is showing areas of compacted and less compacted MML along with loose oxidized wear debris. It is interesting to see that compacted layer has developed multiple cracks almost transverse to the sliding direction (Figure 4.19b). Rosenberger et al. (2005) has pointed out that defects like cracks are commonly observed in mechanically mixed layers. These cracks can favour delamination wear due to subsurface shear (Li and Tandon, 1999). Besides, it is said that that MML is continuously replenished. The area marked by ellipse in the figure is showing layered structure which indicates such formation of MML. EDX spectrum of the composite specimen shows Al, Si, B, C and Fe i.e. elements from both the sliding bodies. It is a characteristic feature of MML. Moreover it is observed that under identical tribological conditions, the amount of Fe has increased for the composite sample as shown in Figure 4.19c. Much harder B₄C particles can abrade the counterface transferring more iron to the composite surface which may get oxidized and mixed with debris particles. These particles enter into the grooves and cavities until becoming levelled and flat with the surface to create mechanically mixed layer. Lu et al.

(1999) termed this process of MML formation as ‘debris burial mechanism’. And looking at the micrographs shown in Figure 4.14b, Figure 4.18d and Figure 4.19 it appears that this mechanism is valid.

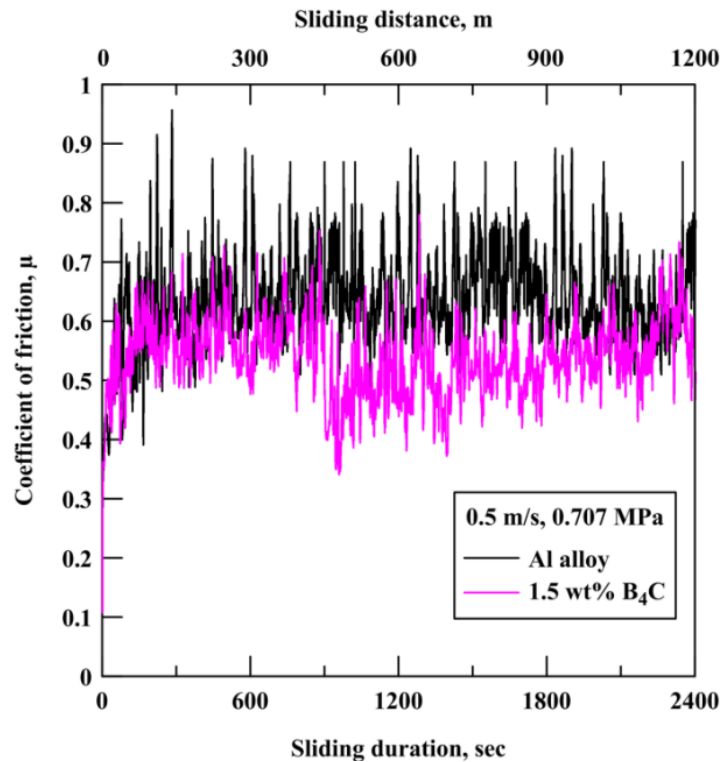


Figure 4.20: Friction profile against sliding duration and/or distance at 0.5 m/s

Figure 4.20 presents friction profiles of alloy and composite material obtained with sliding distance at 0.5 m/s. As can be seen, friction coefficient increased quickly within first 200 m of sliding distance and thereafter became more or less steady for the remaining distance. Contact of smooth surfaces and their adhesive wear during initial phase of sliding could be the reason for this initial spike in friction coefficient. While later on, wear debris generated in the interface which developed almost steady state condition. Average COF values measured for alloy and composite material are 0.63 and 0.54 respectively. Similar observation is reported by Alidokht et al. (2013) for A356-SiC composite. A small drop in COF is observed for the composite matrix somewhere around 450 m of sliding distance which is gradually reduced further. Base matrix also has shown reduction in friction coefficient during 400 to 800 m of sliding distance. It possibly

indicate that compaction of wear debris proceeded for MML formation at that time of sliding.

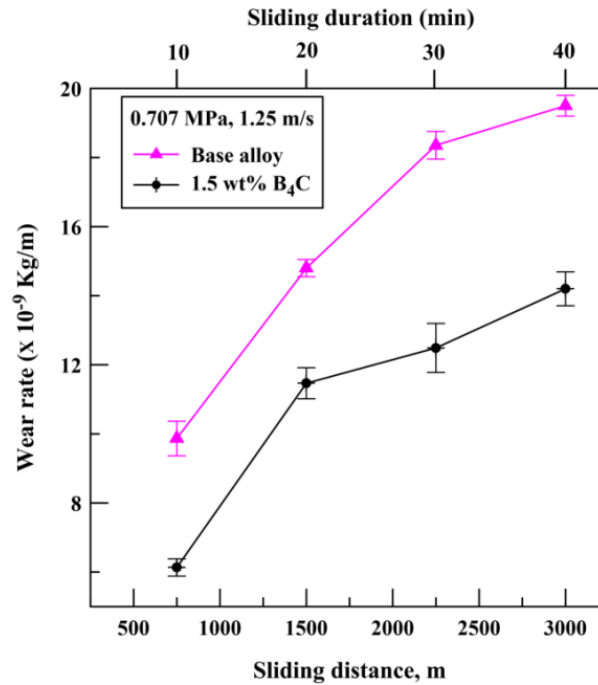


Figure 4.21: Wear rate variation with sliding distance at 1.25 m/s

For higher PV factor of 25 Nm/s, the wear rate trends obtained with varying distance are presented in Figure 4.21. It can be seen that wear rate of Al-Si alloy has increased almost linearly up to the sliding distance of 2250 m. But thereafter the slope of wearing curve has decreased significantly. Al-1.5 wt% B₄C composite specimen also displayed rapid increase in wear rate up to 1500 m of sliding distance. But for further sliding it has reflected only gradual increase in wear. More wear resistance is offered by the composite material. It can be attributed to the strong composite matrix developed on account of the uniformly dispersed ultra-fine B₄C particles. About 30% reduction in the wear rate of alloy is seen over the entire sliding distance due to B₄C reinforcement. Poovazhagan et al. (2016) tested wear behavior of A6061/1.5 wt% B₄C nanocomposite at 20 N and slightly higher speed 1.3 m/s. They found sharp rise in wear loss up to 1000 m of the sliding distance and marginal increase thereafter for further sliding. This finding is in line with our observations. However as expected in general, the volumetric wear loss of aluminum

alloy as well as composite has indicated rising trend with distance as seen in this study and reported elsewhere (Alidokht et al., 2013).

Worn surface morphologies are examined to ascertain the possible wear mechanisms. Figure 4.22 show worn surface morphologies of Al-Si alloy and Al-B₄C composite samples obtained after sliding for 750 m, 2250 m and 3000 m distance. Worn surface of Al-Si alloy as shown in Figure 4.22a provide evidence of heavy delamination wear. Possibility of this wear mechanism is explained as follows. At higher speeds relatively higher temperatures are generated at the interface than bulk matrix in quick times. Dwivedi et al. (2002) measured bulk temperature of Al-Si alloys and found that it quickly reaches to peak temperature within first 10 min of sliding. They measured about 52°C at 1.5 mm depth below the surface under identical conditions. It implies that steep temperature gradient will be created across the sliding surface. This situation might have possibly favoured heavy delamination of the near surface regions during early period of sliding. With extended sliding, bulk temperatures of the sliding bodies will increase due to sharing of the interface temperatures. Generally hardness and shear strength of metal is found to reduce with increasing temperatures. Also subsurface region becomes weaker and deforms easily under the influence of higher temperatures. Therefore both materials have shown increasing deformation with sliding distance as is also evident from the worn surfaces. After sliding at 1.25 m/s for 40 minutes, base alloy suffered heavy and gross surface damage as shown in Figure 4.22c. Composite material on the other hand exhibited long grooves on the worn surface (Figure 4.22d) during initial sliding. It clearly indicates that abrasion acted as a dominant wear mechanism. Small and loose wear debris particles are seen on the surface. Small craters are also formed possibly due to mild adhesion. Uniform spread of dispersoids improves strength and hardness on account of increased boundary area. Such microstructural change retards plastic deformation in the subsurface region (Hemanth, 2005). Hence composite surfaces are deformed less as shown in Figure 4.22(e, f) relative to the base alloy even for the extended sliding duration. B₄C particles are hot hard. Due to fine size they get strongly bonded with matrix by Orowan effect. Also there is a possibility of the formation of boron oxide which is lubricative in nature (Kumaran and Uthayakumar, 2014). As a cumulative effect wear resistance of B₄C composite has significantly improved and it is reflected in the wear rate trends also. Abrasive wear mechanism remained active for composite matrix during the entire sliding

distance. However the formation and oxidation of mechanically mixed transfer debris continued to play important role in the wear behavior. It can be observed from the EDX analysis of worn surfaces of both materials obtained for 10 and 40 min of sliding duration (Figure 4.23).

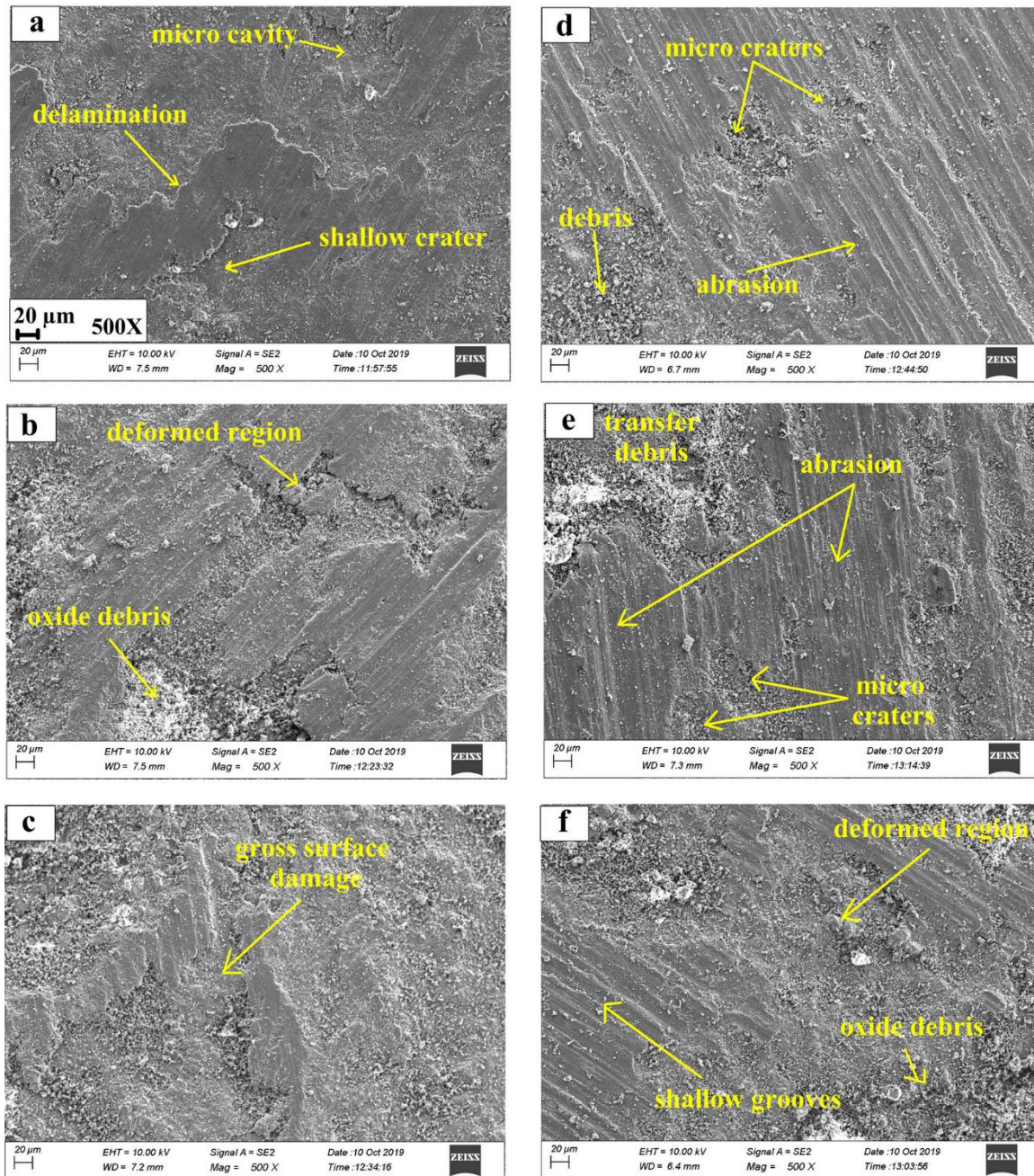


Figure 4.22: Worn surfaces for 750, 2250, 3000 m of sliding distance (10, 30, 40 min duration) obtained at 1.25 m/s: Al alloy (a, b, c), Al-B₄C (d, e, f)

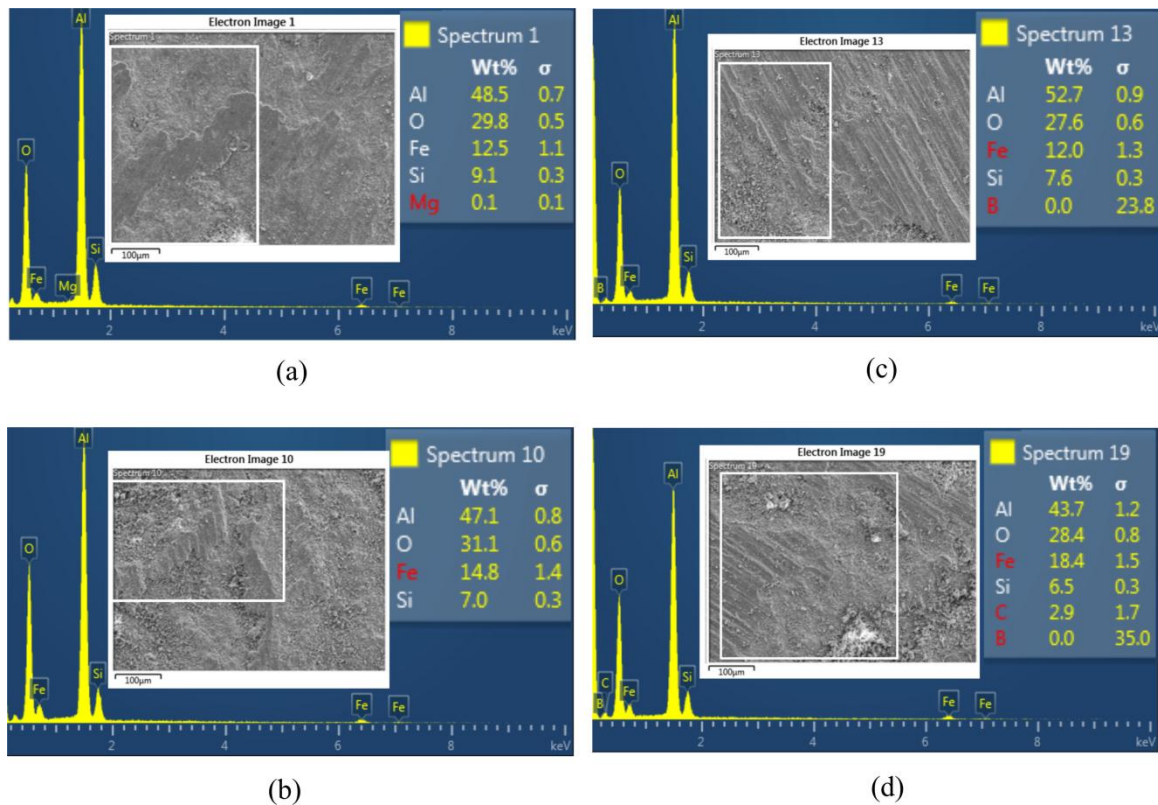


Figure 4.23: EDX analysis of worn surfaces obtained at 1.25 m/s for 10, 40 min of sliding duration: Al alloy (a), (b); Al-B₄C (c), (d)

Profiles in Figure 4.24 shows that friction coefficient of base alloy has fluctuated continuously with high amplitude over the entire sliding distance. While it has varied less for the composite material as can be seen from the relatively smooth curve. These variations probably indicate that continuous deformations have taken place on surface and near surface regions. Because of which the size of actual contact areas varied frequently during entire sliding that resulted in sharp fluctuation of COF. Composite specimen showed marginally lower COF values. Similar results are found elsewhere (Yuvaraj et al., 2015). Looking at the friction profiles (Figure 4.20 and Figure 4.24) obtained for the two cases, it implies that fixed PV factor and instantaneous surface condition decides frictional resistance more than the sliding distance.

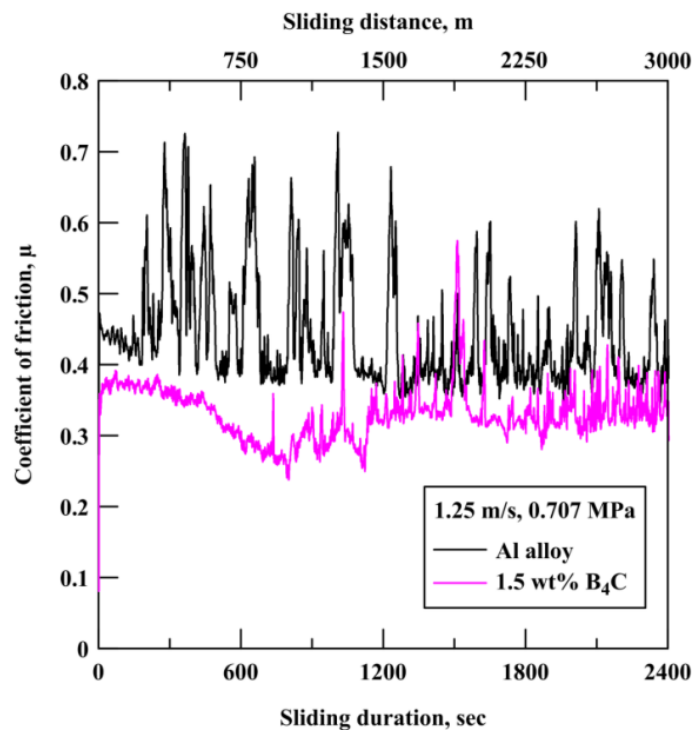


Figure 4.24: Friction profile against sliding duration and/or distance at 1.25 m/s

4.3.4 Wear debris analysis

Figure 4.25a, shows that large size debris particles are generated from the base alloy and EDS spectrum confirms formation of aluminum and iron oxides. Wearing of nanocomposite has created small size debris particles due to uniformly dispersed nanoparticles with less interparticle spacing.

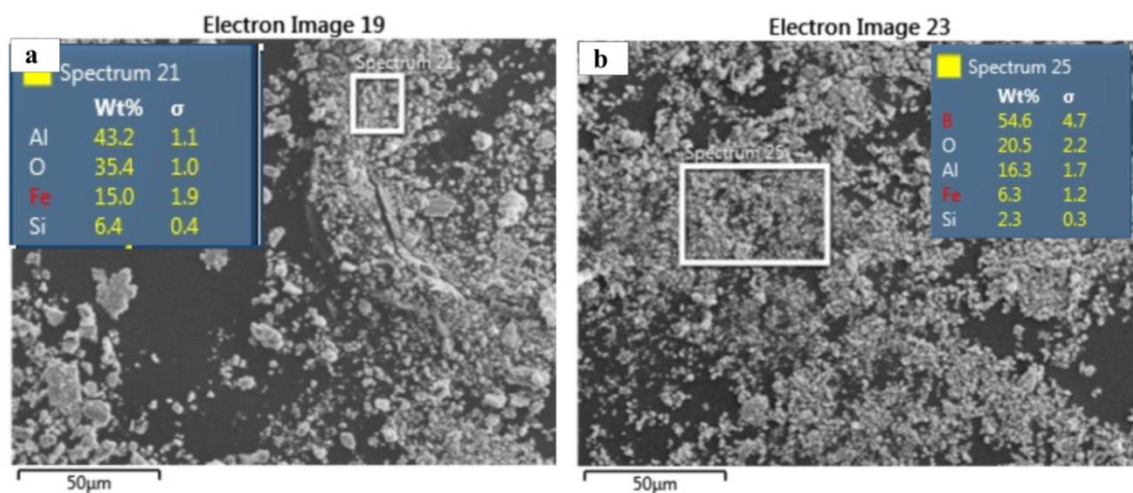


Figure 4.25: Wear debris: **a** base alloy, **b** 2wt% B₄C nanocomposite at 0.354 MPa and 0.66 m/s.

Tribology of Al-B₄C at room temperature

EDS spectrum in Figure 4.25b indicates detection of boron, iron in the wear debris. It implies that after removal of boron particles from Aluminum matrix they become part of lubricative and thermally insulative tribolayer. Such layer is observed to minimize wear rate under intense tribological conditions. At low pressure large and thick debris particles generated from base alloy suggests adhesive-delamination wearing conditions while small, equiaxed debris particles seen for the composite indicate abrasive wear mode. Increased hardness and load bearing capacity of composites could be the reason for reduced debris size. Peaks of elements present in the spectrum confirm that debris is generated due to material loss from both the mating surfaces.

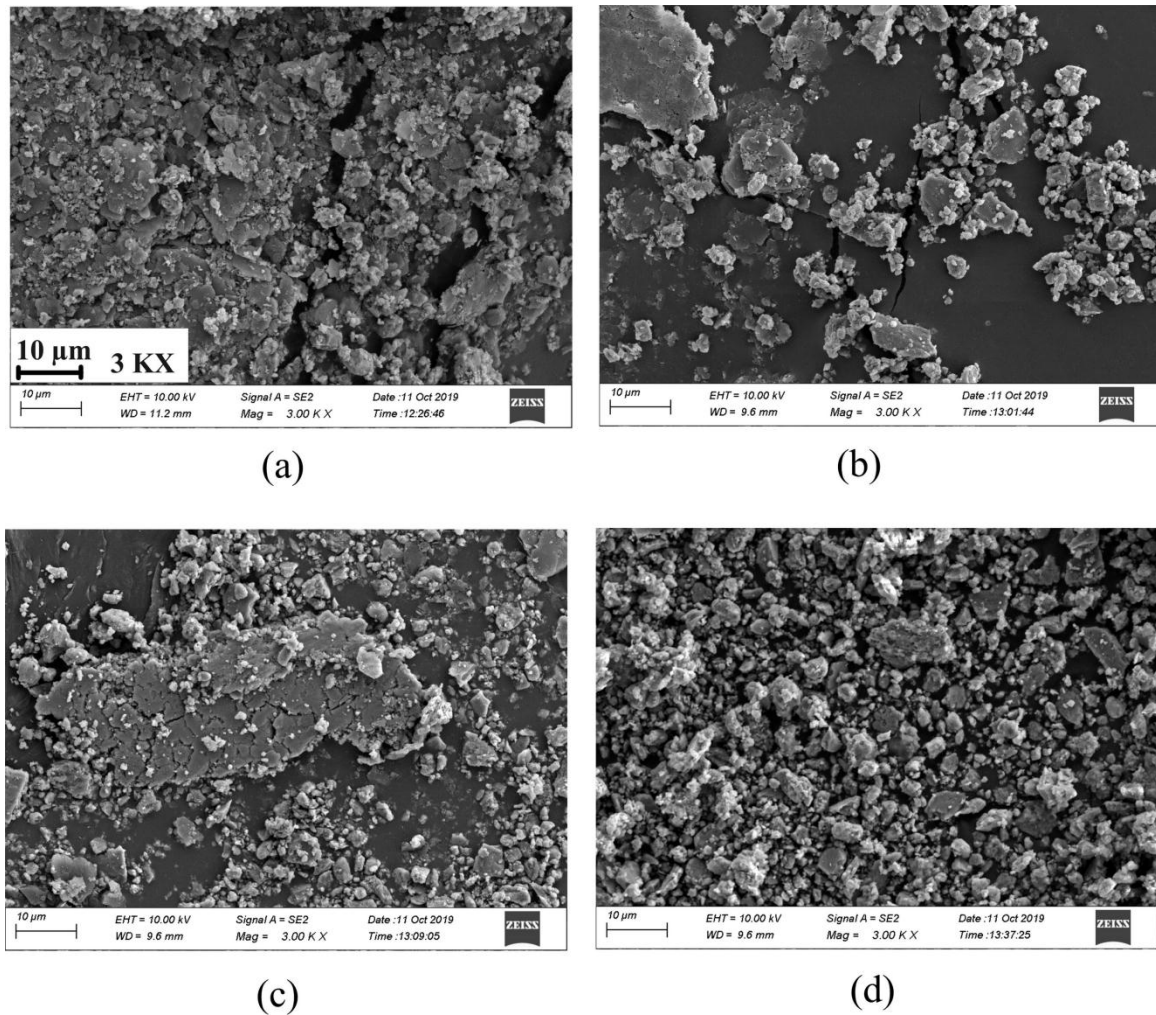


Figure 4.26: Wear debris morphology obtained at 0.49 m/s and 10, 40 min of sliding:

Al alloy (a), (b); Al-1.5 wt% B₄C (c), (d)

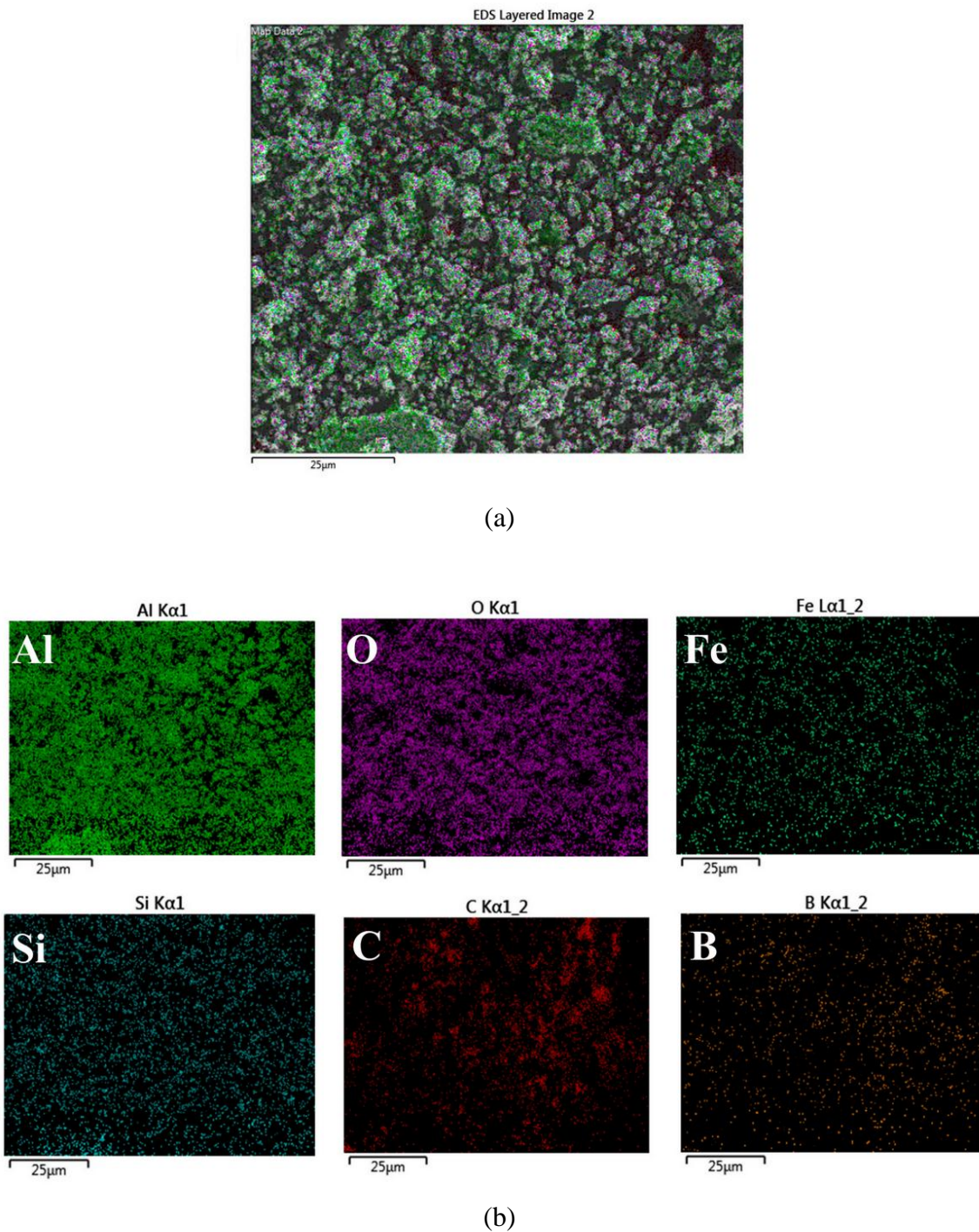


Figure 4.27: (a) wear debris of 1.5 wt% B₄C at 0.49 m/s, 40 min; (b) elemental map

Effect of sliding distance on the formation of wear debris at fixed PV factor is examined for morphology and chemical composition. In general it is found that size of the debris particles are reduced with sliding distance. It could be due to repeated fragmentation and

compaction of debris layers. Morphologies of the wear debris particles generated at 0.5 m/s during 40 min of sliding are shown in Figure 4.26. Large size worn chunks of debris removed from base alloy surface are seen in Figure 4.26(a) which gets reduced to smaller and random size particles with extended sliding as shown in Figure 4.26(b). However the worn particles removed from composite after 10 min sliding appears to be relatively quite small and equiaxed as shown in Figure 4.26(c). One large delaminated wear sheet is also observed in the image and it is interesting to see that it carries multiples cracks on the entire surface. It is possibly due to the dispersed fine particles restricting crack propagation lengths on account of small interparticle spacing. Quantity of small size and more equiaxed particles is found to increase for composite with increasing sliding distance as shown in Figure 4.26(d). The corresponding EDS elemental map (Figure 4.27) shows that it consists of elements from both the sliding bodies. It further confirms that mechanically mixed transfer layer is formed on the wearing surface.

4.4 Closure

In the present chapter the tribological properties of base alloy and the fabricated Al/B₄C composites are discussed by considering different influencing parameters under the room temperature conditions. Reinforcement content (0.5 – 2 wt %), applied pressure (0.354 – 1.412 MPa), speed (0.16 – 0.66 m/s), and distance (400 – 1600 m) are the parametric ranges considered for the tribological investigation. Detailed investigation of the tribological performance of 1.5 wt% B₄C composite is carried out for the extended speeds (0.25 – 1.25 m/s), and sliding distances of (300 – 3000 m) at fixed PV factors of 10 Nm/s and 25 Nm/s. The tests are performed using pin-on-disk apparatus. The results of the tests are elaborated using the microstructural images of worn surfaces and wear debris obtained by the scanning electron microscopes. Wear rate is seen to increase linearly with applied pressure. Critical transition contact pressure appears to exist beyond 1 MPa which accelerated the wearing rate. Worn surface morphology revealed that base alloy is subjected to mild to severe plastic deformation led oxidative wear. Abrasion, oxidation and mild delamination observed to be the wearing mechanisms for Al-B₄C nanocomposites. Formation of oxides and mechanically mixed tribolayer are the key factors to reduce wear rate and friction of fabricated nanocomposites. No evidence of gross metallic wear is seen for the entire load-speed ranges. Wear rate of alloy and

composite reduced initially but after the transition speed of 0.5 m/s, it is increased almost linearly with further rise in speed, becoming twofold at the top speed of 1.25 m/s. Adhesion and delamination wear mechanism is observed for aluminum alloy while abrasion is found dominant for Al-B₄C composite at all speeds. For 10 Nm/s factor, wear rates decreased with increasing distance up to 900 m but thereafter increased for both Al and Al-B₄C material. Optimum condition of least wear is seen for 0.5 m/s and 900 m distance under the applied load of 20 N and it is governed by mechanically mixed transfer layer. For 25 Nm/s, wear rates increased continuously with increasing distance. Delamination wear of base alloy changed to gross plastic deformation with prolonged sliding contact, while composite exhibited combination of abrasion and delamination wear. COF depends on PV factor. For fixed PV factor small variations in average COF over prolonged distance may occur due to the varying contact conditions of the sliding surfaces. Tribological response of Al-B₄C nanocomposite is improved under all the tested experimental conditions.

High temperature tribology of Al-B₄C nanocomposites

5.1 Introduction

With the advancement in technology, the need for tribological component pairs capable of performing effectively at increased loads, higher relative speeds and consequently at high operating temperatures is increasing. Industrial applications such as cutting tools, metal working dies, brake rotors, piston, cylinder liners, cylinder blocks, connecting rods, drive shafts etc. are subjected to wear at high temperature. These components usually operate at temperatures 0.4-0.8 of the melting point of the matrix alloy (Singh and Alpas, 1996). Although Aluminum and its alloys have relatively high strength at ambient temperatures, their mechanical properties get reduced to almost 50% at temperatures close to 200°C which limit their use for high temperature applications (Jerome et al., 2010). Aluminum based particulate reinforced composites have been investigated extensively for their room temperature tribological performance under different operating conditions (Deuis et al., 1997). However limited numbers of research studies have been reported so far about their high temperature tribological behaviour. Complexities involved in the sliding interfaces at high temperatures can lead to premature and sudden failure of components. Accordingly high temperature tribological study of aluminum composites is an important area of research. Ceramic reinforcements have high melting points and so can positively influence or delay the softening of ductile matrix up to certain extent. Among different Aluminum types, Al-Si alloys are better in wear resistance and so are widely used in sliding components. Rajaram et al. (2010) found that wear rate of Al-Si alloy against EN31 counterface decreased with increasing temperature in the range between room temperature and 300°C for the fixed speed of 1.2 m/s and applied load of 20 N. However with similar operating conditions, Martinez et al. (1993) observed that wear rate of Al-Si alloy increases with increasing temperature. The transition temperature between mild abrasive wear and severe adhesive wear was 110°C for Al-20Si alloy and 150°C for Al-7Si/SiC composite respectively. Wear resistance of

composite was better up to 150°C but after 170°C matrix alloy and composite displayed similar behavior. At 200°C wear of both materials was controlled by the matrix exhibiting large plastic deformation. Kumar et al. (2009) studied elevated temperature wear performance of Al-7Si/TiB₂ in-situ micro composites on pin-on disc apparatus employing higher load range of 40-120N and fixed sliding speed of 1 m/s. Temperature of the tests were varied between room temperature (RT) and 300°C. They found characteristic transition of wear from mild to severe mode with increase in load and operating temperature for all materials. Composites were seen to perform exceedingly better than base alloy. The tests carried out on matrix alloy at 40N load and 200°C temperature displayed extrusion and excessive metal flow in the sliding direction indicating severe wear while tests could not be performed on it with further rise in temperature. It has been reported that high temperature wear and friction performance of metallic materials is influenced by change in the bulk properties, reactivity with the environment and tendency of tribolayer formation (Blau, 2010). Pauschitz et al. (2008) presented a detailed overview on the mechanism of sliding wear of metals and alloys at elevated temperature and on the formation of different layers such as transfer layer (TL), mechanically mixed layer (MML) and compacted glazed layer (CL) under different load and speed conditions.

Due to high temperature strength and extreme hardness, boron carbide is an excellent candidate for Al alloys to be used in high temperature tribological applications. It is because boron carbide surface gets oxidized at elevated temperatures to produce a layer of boron oxide (Mahesh et al., 2011). This glassy phase is found to be effective in reducing friction coefficient and wear rate (Uthayakumar et al. 2013). However the explorations of Al/B₄C composites for high temperature wearing conditions are scanty. Recently Canute and Majumder (2018) reported that wear rate of A356/B₄C micro composite increased with increasing B₄C content as well as with load and operating temperature. Whereas wear rate is observed to decrease with increasing speed. The work underlined that decrease in particle size can enhance the tribological performance of A/B₄C composites. Monikandan et al. (2018) also revealed increase in wear and friction of A/B₄C micro composites with increasing temperature.

Detailed literature review indicated that tribological studies of particulate reinforced Aluminum matrix nanocomposites at elevated temperatures are rare to find. In this

scenario, a study reported by Nemati et al. (2016) about the dry sliding wear of Al-Al₁₃Fe₄ nanocomposites at temperatures up to 300°C is interesting and promising. It is stated that 1wt % Al₁₃Fe₄ reinforced and extruded nanocomposite subjected to 250°C and 40 N load exhibited reduced wear rate by 1 order of magnitude compared to non-extruded reinforced sample and 2 orders of magnitude as compared to the unreinforced matrix. Nanostructured and unreinforced Aluminum matrix initially showed decreased wear rate at lower temperatures due to the formation of protective layers. However at 300°C (close to 0.5T_m) the hardness of the compacted tribo layer reduced due to the softening of its Al content which increased the wear rate. Elevated temperature friction and wear study of Al/B₄C nanocomposites produced by ultrasonic stir casting is missing in the literature. So the present work is carried out to bridge this gap and is presented as below.

5.2 Experimental conditions

The procedure and the test equipment employed for the elevated temperature dry sliding tests are discussed earlier in chapter 2, section 2.5.2. The test specimens were of 6 mm diameter and 30 mm length. The counterface disc used was made of AISI SAE 52100 material with hardness of 62 HRC and initial roughness of 0.2 μm. The pin was loaded against the heated disc and slid in contact at fixed speed of 0.66 m/s for the sliding duration of 10 minutes. Pin was not heated to test temperature before the commencement of tribological experiment so as to avoid its possible mass variation on account of oxidation. The sliding distance obtained in each test was almost 400 m. Dry sliding wear tests were carried out by applying two loads (20 and 60 N) at room temperature conditions (35-38°C, RH 40-50%). Temperature was varied in the range of 50-200°C with an interval of 50°C. Contact surface of pin was ground to flat finish with 1200 grit SiC paper and disc cleaned with acetone before each test. The mass loss of the pin was measured with electronic balance (ER 182A, Afcoset) of 0.01 mg resolution. The wear rate was calculated by dividing mass loss (kg) by sliding distance (m). Worn surface of the test pin was characterized by FESEM-EDS to identify wear mechanisms at different loads and operating temperatures. 3D optical microscope was used to obtain roughness values and topography of the worn surfaces for relating with the wear response.

5.3 Results and discussion

5.3.1 Wear behavior

As can be seen in Figure 5.1, the wear rates of alloy as well as composites are decreased with increasing temperature when subjected to dry sliding wear test at low load of 20N (i.e. nominal contact pressure of 0.707 MPa). Mass loss is found to decrease with increasing temperature. This behavior can be attributed to the formation of oxide film, oxide debris particles at low temperatures and then creation of compacted protective glazed layers at further elevated temperatures. It is well known that during sliding of metallic components especially at high ambient temperatures, the surfaces in contact are subjected not only to frictional stresses but they are prone to oxidation. Al and Si are oxidizing elements and the conformal contact between sliding surfaces can trap and retain most of the loose wear debris. Hence the debris eventually formed consists of oxide particles and partially oxidized metallic particles of the constituent metal pairs. The debris which gets retained on the moving surfaces led to the development of layers of particles that diminish direct metal to metal contact and give protection against further wear loss (Stott, 2002).

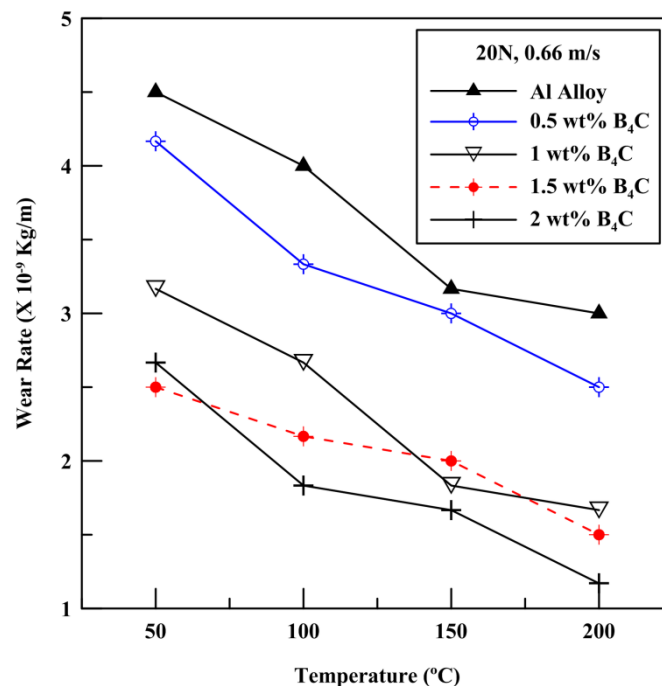


Figure 5.1: Variation of wear rate vs. temperature at 20 N applied load.

High temperature tribology of Al-B₄C nanocomposites

Worn surface SEM micrographs of base alloy obtained at two extreme operating temperatures are shown in Figure 5.2. Shallow ploughing, scratches, few delaminated areas and loose debris particles are observed on the micrograph of the alloy tested at 50°C temperature (Figure 5.2a). Hard silicon phase of the alloy abrades counter disc while at the same time hard asperities of the disc ploughs soft metal matrix to produce wear debris. The temperature of the interface starts oxidizing the worn particles. Thus the dominant wear mechanism in this condition is mostly abrasion while adhesion, delamination and oxidation prevail to limited extent. At this low load and low temperature condition wear protective layer formation is not seen which account to high wear loss. No layer condition of the wearing surface is usually characterized to have abrasive grooves, scratch marks, shallow cavities and most of the surface covered with loose wear debris particles.

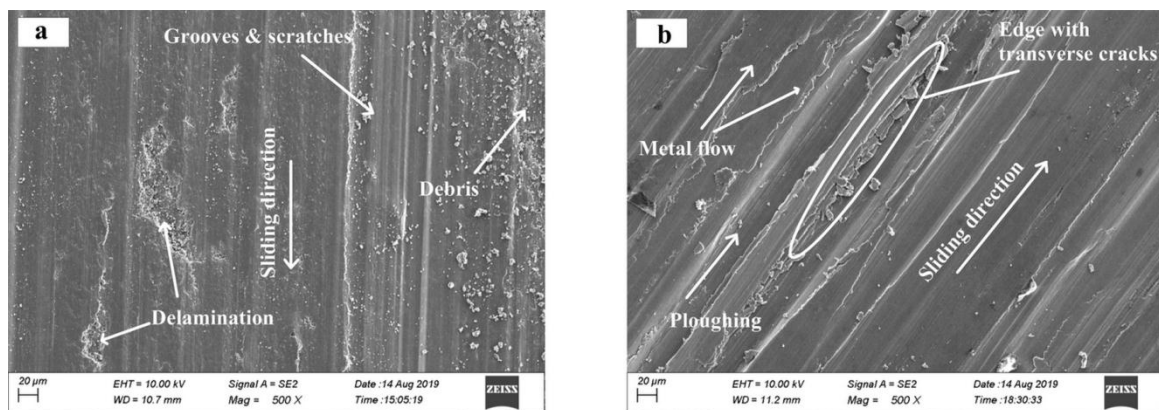


Figure 5.2: Worn out surface FESEM micrographs of AL alloy pin tested at 20 N load and temperature of: **a** 50°C; **b** 200°C

With increasing temperature the sintering rate of loose debris particles increases which led to formation of smoothly burnished hard surface layers called ‘glazes’. These glazed layers protect the sliding surfaces against wear for long times establishing mild wear regime until they break under critical tribological conditions. Sintering of fine particles essentially start at low temperature and glazed layer is typically seen above 150°C (Pauschitz et al. 2008). Worn surface micrograph of base alloy obtained at operating temperature of 200°C clearly shows metal flow (Fig. 5.2b) with shallow and wide ploughing in the sliding direction. Almost negligible amount of loose wear debris is seen

on the wearing surface. Layers of plastically flown material are observed to have edges with transverse cracks indicating the start of fragmentation to produce small particles. The surface otherwise appears relatively smooth with hard and solid compacted layers. Such layers containing compacted oxides become hard (on account of high oxygen) and load bearing as is observed by several researchers in the past while working on different metals and alloys (Pauschitz et al. 2008; Stott, 2002). Oxidative wear mechanism is seen dominant for Al alloy tested at high temperature. Composition of CL is stated to lie in between compositions of both sliding surfaces and characterized by presence of high amount of oxygen. Energy dispersive spectroscopy (EDS) analysis of the worn surface of alloy obtained at 20 N, 200°C is shown in Table 5.1 which justifies the formation of hard, smooth glaze layers. Being hard it lowers wear rate but brittleness and weak bonding can lead to its detachment from substrate. Composites are seen to exhibit similar wear mechanisms but indicate higher wear resistance than that of base alloy. It is possibly due to the increased hardness and thermal stability provided to the matrix by B₄C reinforcement. Besides, mechanically mixed layer formed in the interface act as thermal insulation diminishing metal to metal contact. MML is found to be three to five times harder than base alloy and hence reduces wear rate significantly (Rosenberger et al. 2005).

TABLE 5.1: Constituents obtained in EDS spectrums of the whole area of worn surfaces shown in FESEM micrographs

Elements	Weight %			
	Figure 5.2b	Figure 5.4b	Figure 5.6d	Figure 5.7
Al	67.5	68.4	54.8	46.8
O	15.2	15.7	22.6	25.6
Si	12.0	11.4	7.3	8.8
B	-	-	11.8	6.4
C	5.4	4.5	3.5	2.1
Fe				10.3
Total	100.00	100.00	100.00	100.00

Figure 5.3 displays the wear rate as a function of operating temperatures for alloy and composites with different wt% of B₄C at applied normal load of 60 N (1.412 MPa). It is

High temperature tribology of Al-B₄C nanocomposites

observed that wear rate of base alloy increases with increasing temperature. It is clearly visible that wear rate of base alloy has increased rapidly relative to that of composites above 100°C temperature. Wear rate of composites remains similar to base alloy up to 100°C, then reduces and remains almost constant till 150°C and steadily rises further for operating temperature of 200°C. However it is evident from Figure 4.3 that for all the four temperatures the wear rate of composites is lower than base alloy. Also for composites the wear rate is decreased considerably with increasing wt% B₄C incorporation in the composite matrix.

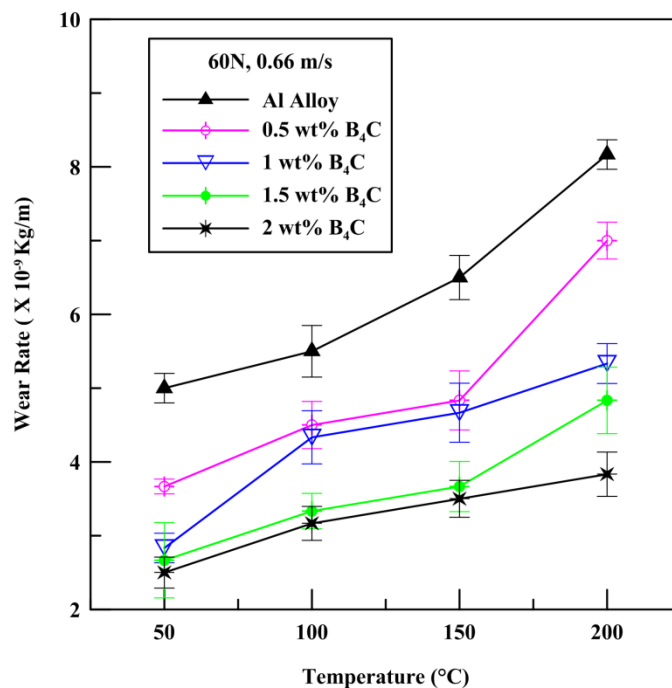


Figure 5.3: Variation of wear rate vs. temperature at 60 N applied load.

At this point it is interesting to see that wear behavior of fabricated materials is completely reversed to that when those were subjected to 20 N load. At low load the tribological behavior was mostly restricted to surface and very near surface areas of the bulk material. It is evident from the shallow delaminated portions of the worn surface. Under the action of increased contact pressure the depth of deformation zone of the alloy increases which led to the nucleation and propagation of subsurface cracks. These subsurface cracks join and at critical length led to shear removal of material between surface and crack in the form of sheet like debris. This delamination theory proposed by Suh (1973) is widely accepted. Besides producing thick delaminated sheets, large amount

of wear debris particles get generated in the interface which act as abrasives to increase wear rate of sliding surfaces. Hence although the wear mechanism still remaining delamination and abrasive in nature the rate of material removal increased significantly even at low temperature of 50°C. It is indicated by the worn surface (Figure 5.4a) having delaminated areas, oxide particles and long deep groove filled with debris. Under increased contact pressure the influence of rising temperature became even more significant to increase the wear rate. It is well known that at critical transition temperature (0.4 times the melting temperature in kelvin), alloy becomes soft and thermally activated deformation process increases wear rate. Soft metal gets penetrated easily by hard asperities of counterface causing more material removal. Mild delamination wear mode of base alloy was changed to severe at 100°C while severe metallic wear started around 150°C temperature which aggravated with further rise in temperature. The hard metallic glazed layer which was effective at low load of 20 N for wear protection (shown in Figure 5.2b) could not sustain the contact pressure at 60 N. The worn surface (Figure 5.4b) indicates heavy damage to the otherwise smooth, hard and oxidized layer obtained at 200°C. Transverse cracks are seen in the work hardened layer in the same micrograph possibly developed due to the lateral force acting on the sliding surface. These cracks eventually lead to the peeling of compacted layer from substrate.

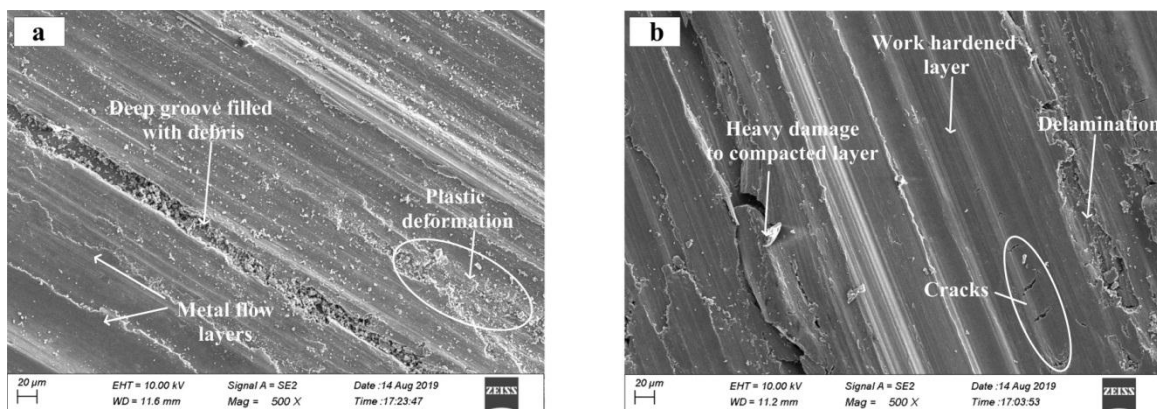


Figure 5.4: Worn out surface FESEM micrographs of AL alloy pin tested at 60N load and temperature of: **a** 50°C; **b** 200°C

Table 5.1 shows EDS analysis of Al alloy at 200°C when subjected to 60 N load. The elemental composition of worn surface is almost same as that obtained at 20 N load but SEM image exhibited severe surface damage. Thus it is evident that layer formed at 20 N

load get damaged at higher load. The process of fragmentation of glazed layer into oxide particles, their reduction in size and further sintering into the reformation of new oxide layer elsewhere on the surface is said to be cyclic and continuous (Pauschitz et al. 2008). But in the process heavy loss of material from contact zone results in the increased wear rate. Another observation recorded is that no wear transition was seen for fabricated materials at 20 N load except the fact that composites were more wear resistant. But at 60 N applied load, wear lines of base alloy and composites deviated at 100°C which marked the transition in wear behavior. The difference is much more evident in between alloy and 2 wt% composite. Wear of alloy increased rapidly. Worn surfaces of alloy and 1 wt% B₄C composites shown in Figure 5.5 are presented to reveal this difference in wear behavior

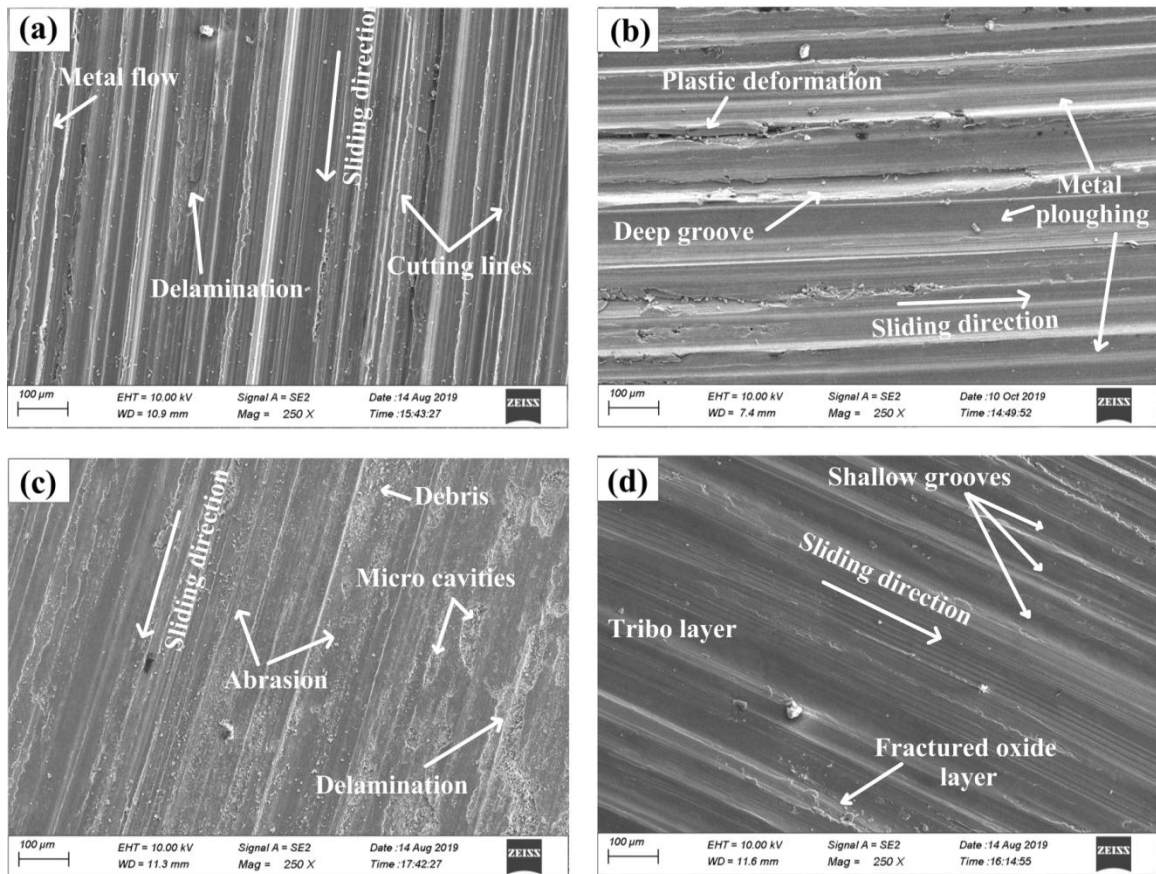


Figure 5.5: Worn out surfaces at 60N: (a) 100°C (b) 150°C (alloy); (c) 100°C (d) 150°C (1.0 wt% composite)

At 100°C, base alloy displayed metal flow with distinct metal cutting lines and delamination whereas abrasion still prevailed as the dominant wear mechanism for composite with lot of loose debris particles on the surface. Heavy plastic deformation and grooves created due to metal ploughing are seen for base alloy at 150°C operating temperature. Composite however displayed only shallow ploughing marks and the entire test surface is seen covered with wear protective tribo layer.

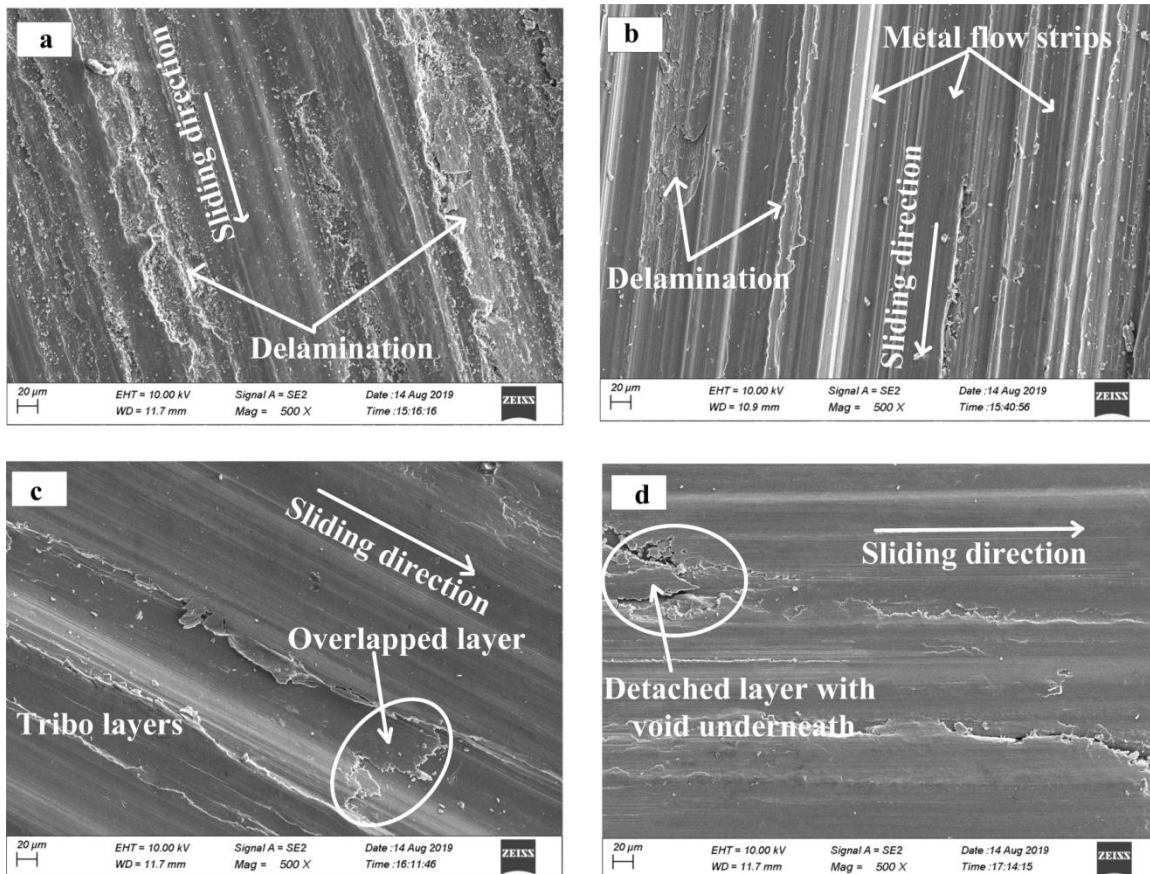


Figure 5.6: Worn out surface FESEM micrographs of Al-2wt% B_4C nanocomposite pin tested at 60N load and temperature of: **a** 50°C; **b** 100°C; **c** 150°C; **d** 200°C

Wear behavior of 2 wt% B_4C nanocomposite at 60N load and at different operating temperatures is illustrated by worn surfaces as shown in Figure 5.6 (a)-(d). The aggressiveness of delamination is seen with shallow and elongated craters at 50°C temperature. Deep grooves and cavities are missing in the surface which can be due to enhanced hardness of composite material. Long wide strips of metal flow with mild

High temperature tribology of Al-B₄C nanocomposites

delamination are observed for the operating temperature of 100°C. For further rise in temperatures, relatively smooth and hard solid surfaces are obtained which indicates why the rate of wear is decreased for the composite material. Oxidized wear debris are compacted to produce relatively smooth surface composed of tribo layers which may get overlapped as seen in Figure 5.6(c)-(d). Its further evidence can be observed in Figure 5.6(d) that a layer is found detached at one place revealing clear void underneath. Most of the surface however looks smooth while its EDS analysis (Table 5.1) shows peaks of Al, B, Si, C and high amount of O confirming the formation of compact layer. For composites the transition temperature shift from mild to severe oxidative wear is observed and it reaches to around 150°C. Especially for 2wt% nanocomposite, it can be seen from Figure 5.3 & Figure 5.6(d) that severe metallic wear has not yet started even at temperature of 200°C.

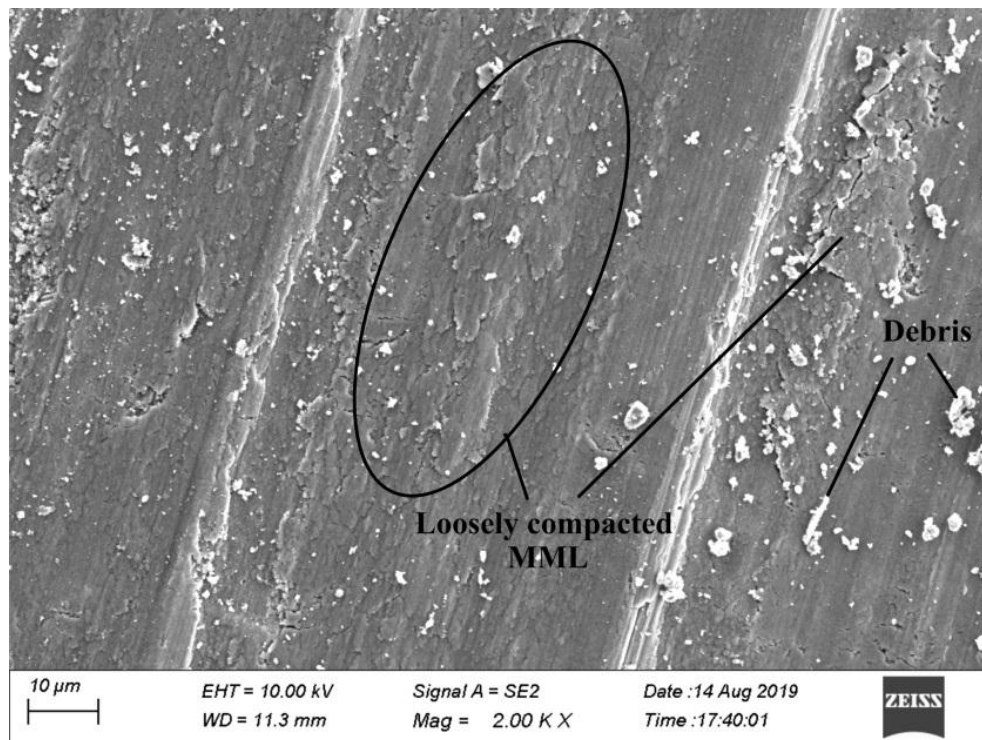


Figure 5.7: FESEM image of MML obtained at 2000X magnification for 0.5 wt% composite at 20 N, 100°C.

It is found that before the formation of compact layers relatively less compact mechanically mixed layers are developed on the wearing surface. MML composition is

characterized by elements from both the sliding surfaces. Hard silicon (1450 HV) and B_4C (3700 HV) phases present in the strong composite matrix can abrade iron from the steel counterface (900 HV) even at low load of 20 N. Magnified view of MML is shown in Figure 5.7 while elements of its EDS spectrum are enlisted in Table 5.1. EDS analysis confirming MML formation at different test conditions is shown in Figure 5.8. Presence of iron oxide is a prominent feature of MML formed on the worn surface of Aluminum slid against steel. Iron oxide is lubricative in nature. Besides boron oxide is also lubricious and can reduce wear (Lashgari et al., 2010). MML formed on the wearing surface diminished direct metal to metal contact. Hence Al/ B_4C composites performed exceedingly better than alloy to resist wear under all the tested experimental conditions. Further it can be seen from Figure 5.8 that applied load is significant to damage the wear protective MML layer formed at lower load.

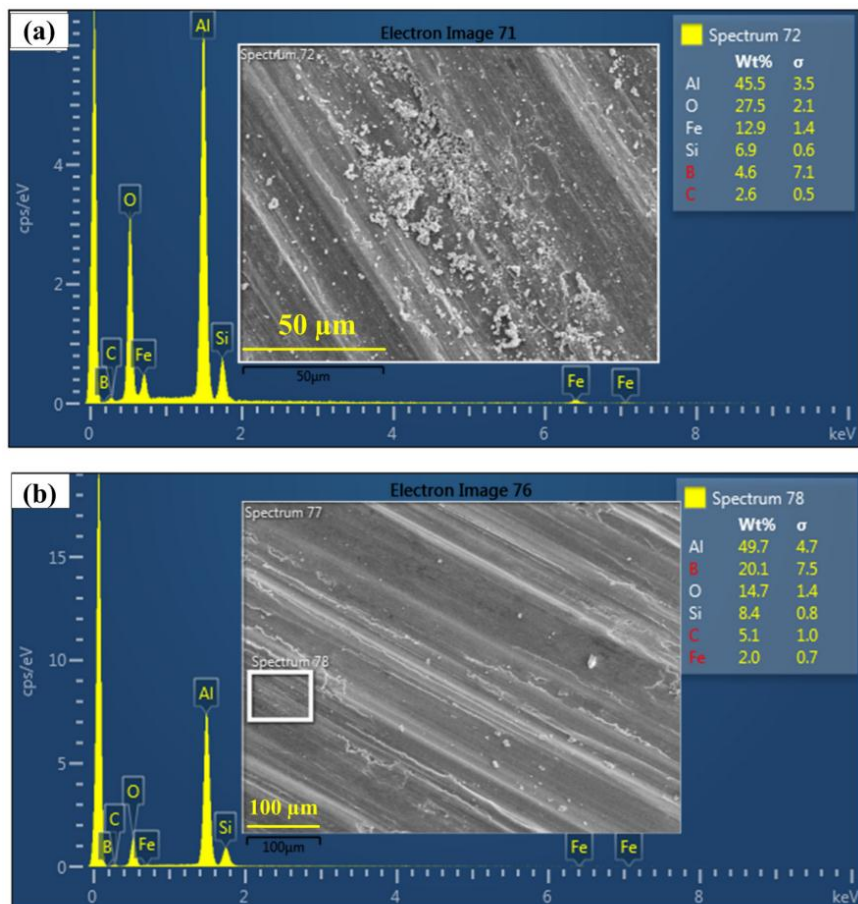


Figure 5.8: FESEM image of MML obtained at different test conditions: (a) 1 wt% composite, 60 N, 50°C (b) 2 wt% composite, 20 N, 150°C.

High temperature tribology of Al-B₄C nanocomposites

Worn surface profiles of base alloy and 2 wt% composite obtained by using 3D optical profilometer are shown in Figure 5.9 whereas the corresponding roughness values are enlisted in Table 5.2. It is observed that Ra values increased with increasing temperatures for both alloy as well as composite material. However roughness values of composite material are lesser than corresponding values of base alloy. This indicates formation of relatively smooth surface of composite material possibly on account of higher hardness. Grooves are clearly visible in all the 3D surface micrographs. Composite materials however exhibited less surface damage while base alloy displayed relatively wide and deeper grooves. Base alloy is observed to be severely ploughed and subjected to higher plastic deformation due to its thermal softening at elevated temperatures. The topographical features are in correlation with the wear rate trends observed in this investigation.

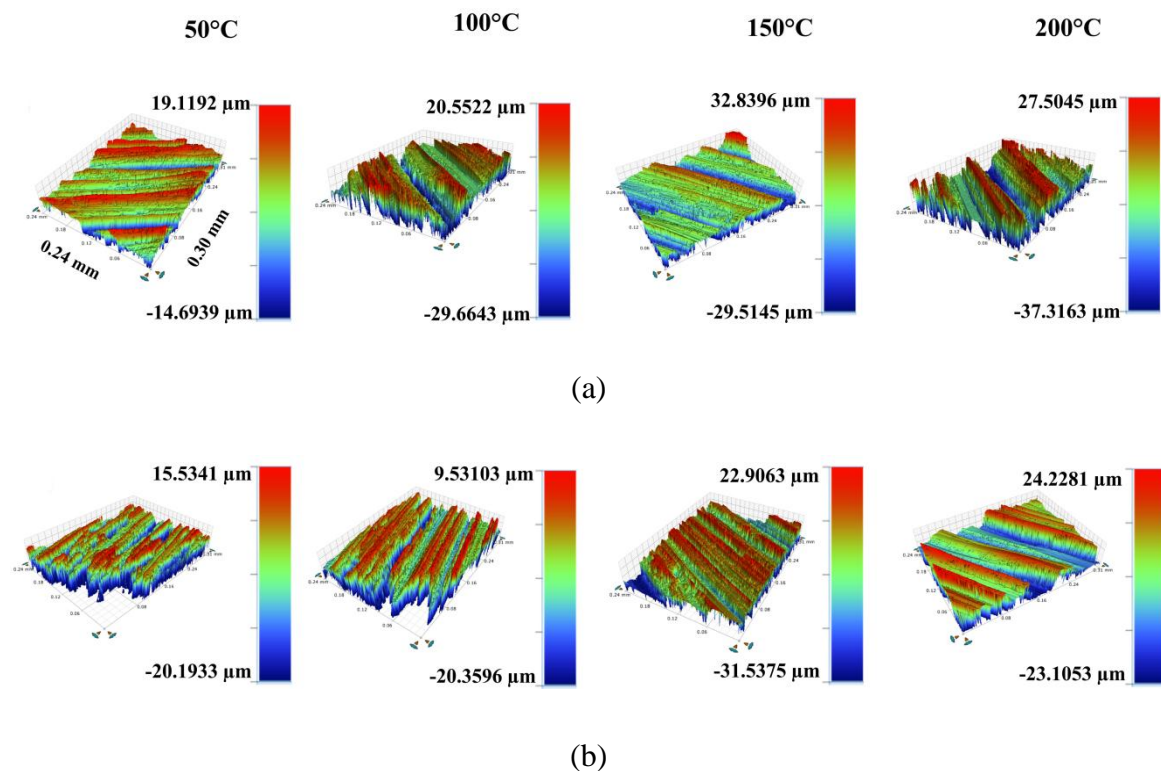


Figure 5.9: 3D topography and roughness of worn out surfaces obtained at different operating temperatures (50-200 °C) and 60 N load: (a) Base alloy (b) 2 wt% B₄C nanocomposite

TABLE 5.2

Surface profile roughness (Ra) values of worn surfaces obtained at different operating temperatures, loads and measured in 3D optical profilometer.

Temperature (°C)	Surface roughness, Ra (μm)			
	Base alloy		2 wt% composite	
	20 N	60 N	20 N	60 N
50	2.497	3.585	1.361	2.68
100	2.955	6.876	2.023	2.908
150	4.941	8.382	3.613	5.256
200	6.245	11.013	5.602	8.907

It was seen from Figure 5.1 and Figure 5.3 that for composites wear rate decreases as a function of B_4C weight percentage. Increased wear resistance with higher incorporation of B_4C particles is attributed to the enhanced strength, hardness and refined microstructure of the composite on account of increased dislocation density (Kumar et al., 2017). Also due to difference in the coefficient of thermal expansion between matrix and particles, strain fields are created around particles during solidification process. These fields give rise to number of dislocations in the process of accommodating thermal strains which eventually improves the strength of material through dislocation strengthening mechanism (Malaki et al., 2019). Dislocations restrict propagation of subsurface cracks generated under the influence of applied pressure during sliding eventually diminishing the wear rate. Besides previously Kumar et al. (2013) have observed that at higher temperature expanding matrix creates tightening effect around particles which strengthens the material and improves its wear resistance. It could be because due to CTE mismatch Aluminum matrix expands relatively more than B_4C particle straining the particle–matrix interface. It may result in the generation of additional dislocations and/or movement of existing ones which probably can hold the particle tightly in the matrix. Strength is always found to improve wear resistance due to enhanced load bearing ability which diminishes crack initiation and propagation (Srivastava and Chaudhari, 2018). Good interfacial bonding and clear interface between particle and matrix reduce wear rate.

High temperature tribology of Al-B₄C nanocomposites

Strong bonding (mechanical and/or chemical) is essential for sharing and transfer of load between matrix and reinforcement which essentially take place through interface. Ideal interface promote wettability and bond the matrix with reinforcement to desired degree (Chawla, 2006). Strongly bonded particles are not easily detached from the matrix and in turn protect the soft matrix from wearing away when slid against hard counterface. Lashgari et al. (2010) have reported that B₄C developed strong interfacial bonding with Aluminum when processed at 750°C by stir casting route and exhibited improved wear resistance. Ceramic nanoparticles due to their sizes in the range of surface roughness do not disintegrate further into small sizes under crushing stress and easily gets occupied in the hard layers formed by oxidization process. Thermal stability offered by these particles prolongs the existence of wear protective oxide layers formed on the wearing surface. Hence the transition temperature of composites from mild to severe metallic wear is pushed to higher temperature values. Additionally the influence of mechanically mixed layer which increase with reinforcement content is always influential in improving wear resistance.

Figure 5.10 (a)-(e) presents the worn surface of base alloy and those of composites with varying weight percentage reinforcement, all obtained at 60N load and 150°C operating temperature. Heavy plastic deformation and metal flow is observed (Figure 5.10a) for base alloy. Relatively smoother surface and less damaged area is exhibited by 0.5 wt% B₄C nanocomposite for identical sliding conditions. Worn surface of 1 wt% B₄C nanocomposite (Figure 5.10c) do not show delamination, grooves or cavities formed. Instead flattening and adherence of small patches of oxide debris are seen on the surface. It suggests initial phase in the formation of hard and wear protective oxide layers. Worn surfaces of 1.5 wt% and 2wt% nanocomposites hardly show loose debris particles spread around wear tracks. Surface looks smoother which is essentially covered with compacted tribo layers responsible for the reduced wear rate of composites. Wear debris particles with nanoparticles experience severe stress at high load that ceases their three-body wear contribution and instead get compacted forming load bearing layers at higher temperatures. Such observations are reported by another researcher (Nemati et al., 2016) for Aluminum reinforced with nanosized Al₁₃Fe₄ particles. Improvement in the wear performance of Aluminum composites can be attributed to better dimensional stability offered by hot hard ceramic reinforcement particles to the composite matrix with

increasing content. Such beneficial effect is observed for elevated temperature dry sliding studies conducted by other researchers for other reinforcements such as SiC, TiB₂, Al₂O₃, ZrO₂ etc (Wilson S., Alpas, 1996; Tan et al., 2018; Poria et al., 2018).

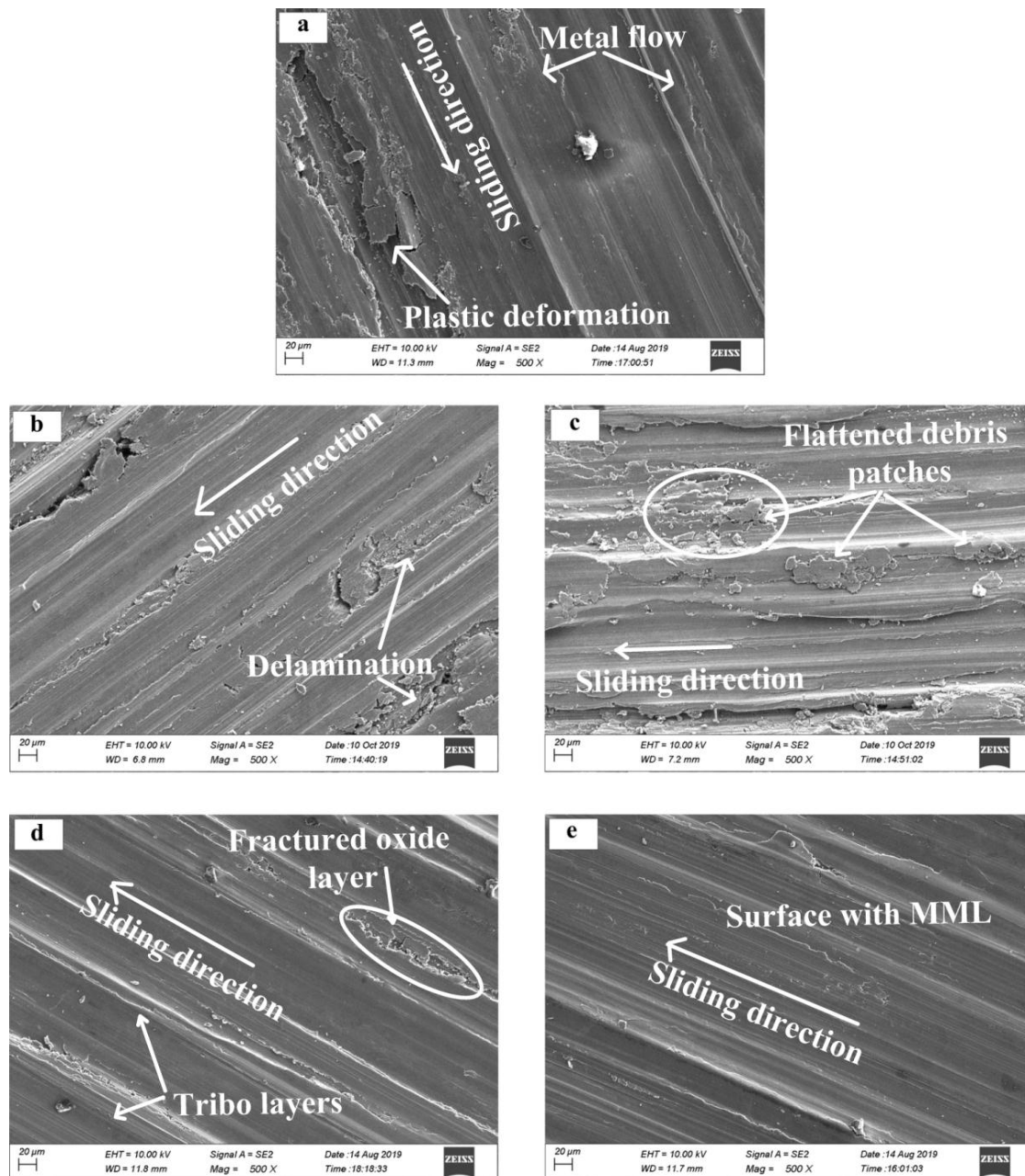


Figure 5.10: FESEM images of wear tracks obtained at 60N and temperature of 150°C for: **a** Al alloy, **b** 0.5 wt% B₄C, **c** 1.0 wt% B₄C, **d** 1.5 wt% B₄C, **e** 2.0 wt% B₄C

5.3.2 Friction behavior

Figure 5.11 shows variation of friction coefficient of alloy and composites with increasing operating temperatures at 20 N applied load. Friction coefficient value of Al alloy is higher which decreased up to 150° but increased for further rise in temperature. At low load-temperature conditions adhesion-delamination was dominant for the alloy. Besides abrading action of hard silicon phase and steel asperities resulted in the higher friction in the interface. With increasing temperature thermal softening of alloy eased its shallow ploughing which possibly reduced the sliding friction. Reduction of loose debris and metal flow occurred beyond 150°C. Formation of such work hardened layers increased frictional resistance for further rise in temperature. Composites displayed lower friction coefficient due to the thermal stability offered by hard B₄C particles and formation of lubricative iron oxide in the interface. This is in line with the earlier reported observation (Kumar et al. 2009).

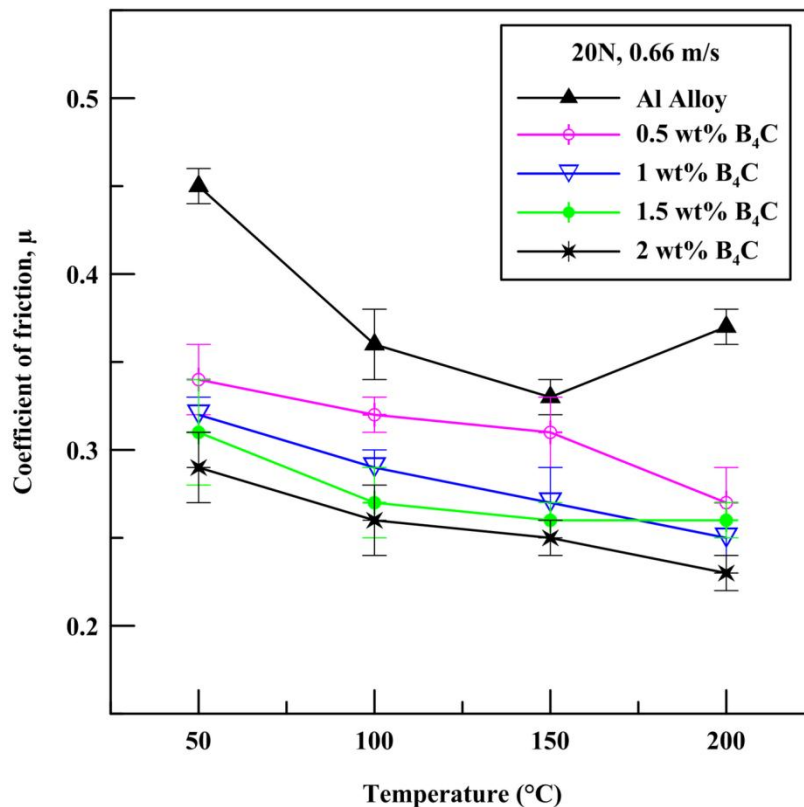


Figure 5.11 Variation of friction coefficient vs. temperature at 20 N applied load

However at higher applied load of 60 N composites exhibited higher friction coefficients than base alloy as shown in Figure 5.12. For temperatures between 100 and 200°C the friction coefficient values of composites were found to be marginally higher. But at temperature of 50°C, composite material exhibited considerably higher (0.42) friction coefficient than that of the base alloy (0.15). Increased hardness of composites not only reduces adhesion but deeper ploughing of the matrix is also diminished. However abrasive wear mode creates lot of loose wear debris in the interface. Increased real area of contact developed at high load increases abrasion due to loose debris and exposed hard B_4C particles. This could be the reason for the increased friction of composites initially at low temperatures which decreased rapidly and became stable for further rise in temperature. Increased COF on account of increased abrasion is reported earlier by Liu et al. (2004) for Al-12Si/ Al_2O_3 composites.

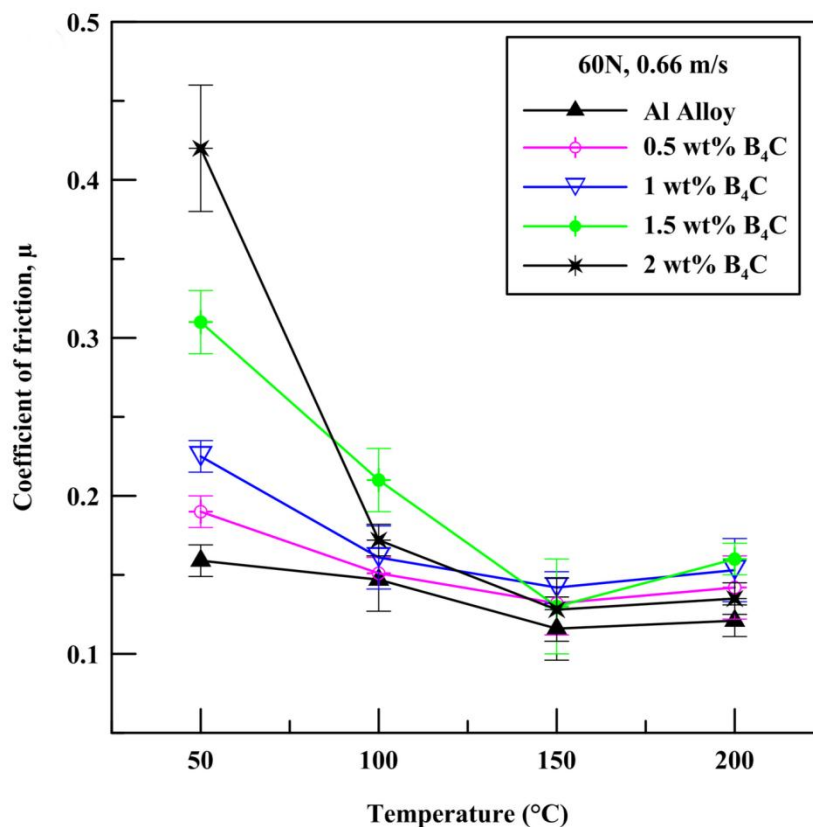


Figure 5.12 Variation of friction coefficient vs. temperature at 60 N applied load

Friction behavior of base alloy at 60 N applied load and four different operating temperatures 50°C, 100°C, 150°C, 200°C is depicted in Figure 5.13. It is seen that friction

High temperature tribology of Al-B₄C nanocomposites

coefficients show strong fluctuation during the entire sliding duration of 600 sec for all the test temperatures. Moreover friction coefficient value is found to decrease with increasing temperature up to 150°C but for 200°C it is increased by a marginal value. Fluctuation in the value can be due to the increased plastic deformation as well as tearing of oxide layer and formation of the same. Al-2 wt% B₄C nanocomposite material however do not show fluctuation in the friction coefficient values as can be seen from Figure 5.14 for all the test temperatures. Particle induced restriction to the removal of oxide scales from sliding surface could have played crucial role in minimizing fluctuation of the frictional force. It is because presence of hot hard B₄C particles restricts plastic deformation of matrix resulting in the more stable oxide film on relatively smooth substrate.

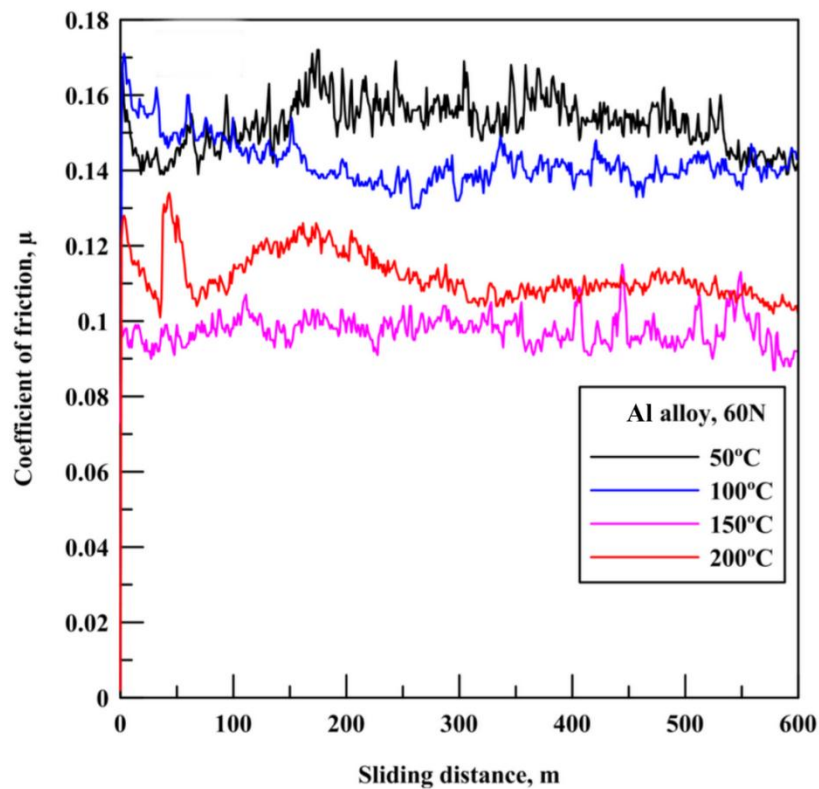


Figure 5.13: COF of base alloy during entire sliding duration at 60 N

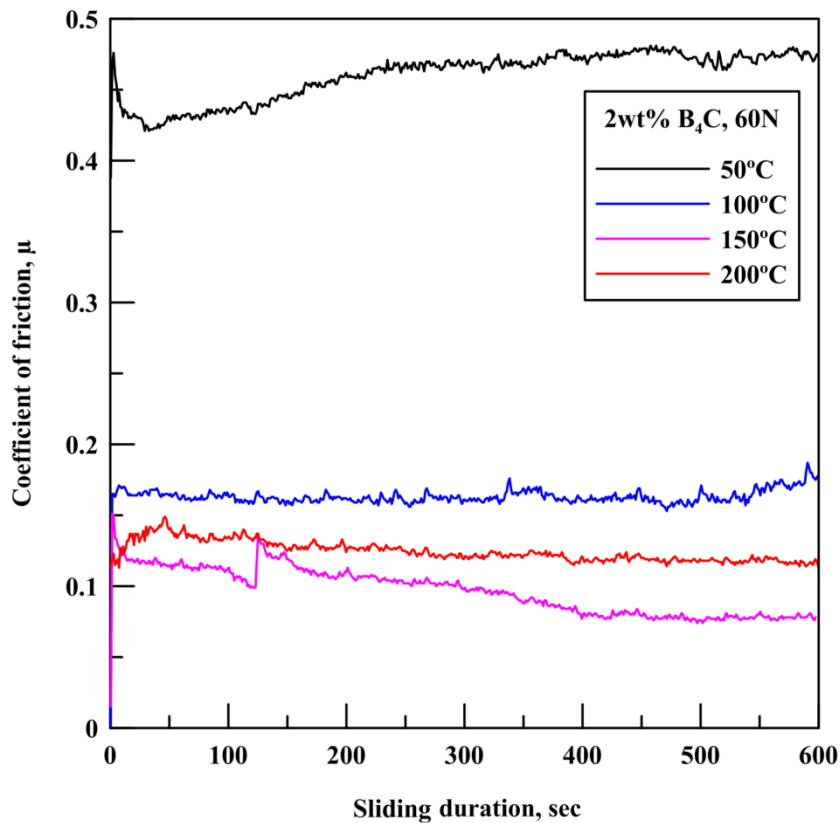


Figure 5.14: COF of 2 wt% B₄C composite during entire sliding duration at 60 N

Wear rate of base alloy at 60N load varied between 5×10^{-9} Kg/m to 8.7×10^{-9} Kg/m with increasing temperature. Corresponding values for 2wt% composite were found to vary between 2.5×10^{-9} Kg/m to 3.83×10^{-9} Kg/m, lower by almost a factor of 2. This difference did not reflect in the frictional behavior of these materials. Friction coefficient was seen to be influenced a lot by rising temperature but we do not see it to be related to the wear rates. It is stated that coefficient of friction depend upon the fraction of frictional energy being partitioned and dissipated into pin and disc. Also it depends on the micro-interactions of varying contact asperities that take place during the entire test duration (Akbari et al., 2015). It has been reported earlier that the attempts of correlating wear and friction behavior have rarely yielded a good correlation (Prasad and Rohatgi, 1987).

5.4 Closure

In the present chapter the tribological properties of base alloy and the fabricated Al/B₄C composites are discussed under a range (50 - 200°C) of elevated operating temperatures.

High temperature tribology of Al-B₄C nanocomposites

Sliding speed is kept constant while the high temperature tribological response is studied at different applied pressures using pin-on-disk apparatus. The results of the tests are elaborated using the microstructural images of the worn surfaces along with their chemical compositions and 3D surface topographies. At 20 N applied load the wear resistance of alloy and composites increased with increasing temperatures. This behavior was due to the retained glaze layers which formed more rapidly at elevated temperatures. These layers played the role of wear protection by minimizing direct metal to metal contact during sliding. But at higher load of 60 N the wear resistance of alloy and composites decreased with increasing temperature. It was because, increased contact pressure coupled with softened metal matrix led to the increased deformation and accelerated wearing of protective oxide scales from the sliding surface. Synergistic influence of applied load and temperature decided the wear behavior of Aluminum alloy and its composites. However nanocomposites were found more wear resistant under all the test conditions due to increased hardness and strengthening effect offered by uniformly distributed and well bonded particles. Transition temperature of the Aluminum matrix from mild oxidative to metallic was found to be pushed by about 50-80°C with increasing reinforcement. Friction coefficients were found to be influenced by varying temperature. COF of composites were lower than alloy at 20 N applied load. However wear rates and friction coefficient values were not seen related at 60 N load and composites displayed increased friction. Friction coefficients were observed to decrease with rising temperatures for all the tested specimens.

“This page is left intentionally blank”

Nanoindentation, scratch, and corrosion behavior of Al/B₄C nanocomposites

6.1 Introduction

Composite properties are governed largely by the properties of the constituent elements, but particle-matrix interfaces also significantly influence its overall macro-scale behavior (Mussert et al., 2002). As such, the determination of mechanical properties at the micro/nanoscale can predict and extend the useful life of composite structures. In this respect, nanoindentation is an effective technique for characterizing the mechanical response of materials at small volumes (Mukhopadhyay and Paufler, 2006). Usually, nanoindentation is applied to determine hardness and elastic modulus. But it is also employed to measure properties like fracture toughness, yield strength, strain hardening exponent, the adhesion strength of coatings, residual stresses, etc. Tarralbo JM et al. (2002) put Ni₃Al intermetallic in Al 2014 matrix through powder metallurgy; heat treated the composite and studied its nanoindentation response. It was found that the hardness of the interphases increased, but their elastic modulus remained unchanged, as compared to the original intermetallic. Another research group revealed that both hardness and elastic modulus of Al-15% SiC micro composite varied between particle, matrix, and interface (Zhanwei et al., 2014). Olivas et al. (2006) reported the development of residual stresses between SiC particles and Al matrix due to the thermal mismatch effect. Through nanoindentation, they observed that these stresses increased with increasing SiC content. Shen et al. (2001) did not find unique relation between tensile strength and hardness of MMC matrix but stated that hardness of composites increased with increasing particle concentration. Thus the literature suggests that it is possible to see the gradient of property change between matrix and the incorporations for micro composites. However, for submicron or nano-size particles, it may not be easy to individually penetrate the particles and the interfaces through indentation due to the ultra-fine sizes and the difficulty in obtaining test surfaces with near-zero roughness. Few reported studies on

nanoindentation revealed tremendous improvement in the hardness and elastic modulus of the Al matrix, even for a very small fraction of nanoparticles (Fale et al., 2014; Wagih and Fathy, 2016; Mazaheri et al., 2010). Secondly, due to far better performance over micro counterparts, nanocomposites may find practical applications soon. Therefore in this context, exploration of nanoindentation for investigating small volume response of composites reinforced by different ultra-fine ceramic particulates would be fruitful.

Scratch resistance is another micro-scale property of significance that governs the machinability behavior of materials. Composites being multi-phase materials have negatively influenced material removal and the surface integrity in machining processes. The scratch test is practical to understand the material removal mechanism at the micro level because it is similar to the abrasive wear process. Recently Zheng et al. (2018) performed a deep cut scratch test on Al-SiC (45% vol.) composites and found no ductile-brittle transition in the material response despite high reinforcement. But SiC particles were found to influence friction coefficients significantly during the scratch process. They observed that practical applications of Al/SiC composites are less due to poor machinability and high machining cost. This concern was projected earlier by Yan and Zhang, 1995, and appears to remain as a challenge even today despite the popularity of composite materials. Using a single point scratch test, they suggested that a higher depth of cut is necessary for machining MMCs with minimum machining energy. Feng et al. (2014) conducted a traditional scratch test, and on observing the rough and uneven scratch topography, concluded that SiC particles were dislodged and deformed in the scratch zone. But in the ultrasonic vibration-assisted scratch test, the width and depth of grooves reduced with a reduction in the size of broken chips. Scratch tests are also effectively utilized to study the adhesion and scratch resistance of micro/nanoparticle reinforced coatings on Al alloy (Vitry et al., 2008; Barletta et al., 2013; Narasimman et al., 2012).

Corrosion studies of Al nanocomposites are necessary because in the near future nanocomposites may start replacing their micro counterparts to satisfy energy demands for high-performance applications. But the area appears to be very much in the introductory or fancy stage. Loto and Babalola, (2018) recently found that decreasing alumina particle size from 500 nm to 80 nm increases the corrosion resistance of Al 1070

alloy in chloride/sulfate solution. Another promising result is by Mosleh-Shirazi et al., (2015) who found an increase in corrosion resistance of 6061 alloy incorporated with SiC (1-3 wt. %) nanoparticles in NaCl and H₂SO₄ solutions. Bharati M. et al., (2019) indicated that sites of agglomerated nanoparticles were prone to corrosion in Al6061/SiO₂ nanocomposite obtained by FSP process. Mahmoud et al., (2012) observed improved corrosion resistance of Al/SiC and Al/alumina nanocomposites over pure matrix in NaCl solution. Further, they reported drop in corrosion resistance with increase in particle size and also particle content above 3 vol% citing the possibility of particle agglomeration. Al/B₄C composites perform quite better than the base matrix alloy under dry tribological conditions in room and elevated temperatures. Hence in order to expand application areas it is necessary to explore the corrosion resistance of Al/B₄C composite. Detailed literature review shows only a few articles on the corrosion behavior of Al/B₄C micro composites, which have reported degradation of Al alloy in NaCl solution (Katkar et al., 2011; Han and Chen, 2015; Dikici et a., 2009). Ding and Hihara, (2005) observed localized corrosion around B₄C microparticles in 0.5M Na₂SO₄ solution due to the possible galvanic coupling effect between B₄C and Al6092 matrix. In K₂SO₄ solution AA1100-16% B₄C microcomposite displayed great corrosion resistance but in 3.5% NaCl solution the composites revealed pitting corrosion at Al/B₄C interfaces (Han Y. et al. 2011).

Detailed literature review indicated that the publications on the nanoindentation response of bulk Al nanocomposites are scanty. Also a very few studies on the scratch behavior of bulk composites are available, while those on submicron or nanoparticle reinforced bulk Al composites are missing. Further, the effect of submicron/nano B₄C particles on corrosion behavior of Al matrix is not found in the existing literature. The present study is carried out to fill this literature gap. It involves the fabrication of Al/B₄C nanocomposites, investigation of micro scale mechanical and tribological behavior by nanoindentation and scratch study respectively. Also the corrosion behavior of Al/B₄C nanocomposites is studied and presented in this chapter.

6.2 Experimental details

For nanoindentation study specimens used were of 5 mm thickness and 10 X 10 mm cross-section size. Test surfaces were prepared as explained earlier in chapter 2, section

2.6. Indentations were made with a three-sided pyramidal indenter of 350 nm tip radius and 50 mN applied load. Loading/unloading rate of 20 mN/min and peak load pause of 5 sec was used in this high load test. Samples were mounted on a steel stub using adhesive gum. 15 indents (5 in each row) spaced by 30 μm from each other in the form of an array were used for repeatability. The average values of test output parameters are reported. The area for indentation was selected randomly on the surface. Values of indentation hardness and elastic modulus of the fabricated materials were obtained directly from the TriboIndenter. A dedicated in-built software package was used for the automatic acquisition of nanoindentation data required for plotting load-displacement profiles. The procedure and equipment used for nanoindentation are detailed in chapter 2, section 2.6.

For the scratch test, composite and base alloy specimens of 10 mm X 10 mm X 4 mm size were prepared. The test surface of each specimen was polished to a mirror finish so that the indenter traverses smoothly without skipping or catching in a pocket. All tests were performed on dry specimen surfaces at room temperature conditions. Different loads were applied through constant mode. Parameters used for the scratch test are listed in Table 6.1. During the test, the indenter moved into the material until an applied load was reached and then moved tangentially to the surface to cover the input stroke length. The indenter was cleaned with acetone before each test to remove adhered wear particles. For repeatability, three test runs were performed at each experimental setting and reported the mean value. Scratch width was measured from the image captured by an inbuilt camera fixed to the indenter machine. Five measurements were taken at different places along the scratch length to obtain the mean value of the scratch width. Scratch hardness, wear volume and friction coefficients are determined as explained earlier in section 2.7.

Table 6.1: Scratch test parameters

Parameter	Value
Applied load	5, 10, 15, 20 N
Load type	Constant
Scratch velocity	0.1 mm/sec
Stroke length	5 mm
Scratch offset	1 mm

Corrosion tests were performed at ambient conditions (36°C, RH 50 %) using 3.5% NaCl as electrolyte, a corrosive media equivalent to seawater. Three electrodes were used wherein the test sample was taken as a working electrode. For providing stable potential, a saturated calomel electrode (SCE) was used as a reference electrode and the applied voltage was determined against it. A platinum electrode was selected as an auxiliary electrode since it provides an alternate path for the applied current into the solution medium. All three electrodes were inserted into the glass cylinder filled with an electrolyte solution. An opening of 1 cm² area of the cylinder was closed tightly against the test surface of the sample thus exposing only that much area to the NaCl solution. After the electrodes were dipped into the solution, a settling time of 15 min was allowed for stabilizing the open circuit potential. The potentiostat was connected to a computer and operated through dedicated software. Corrosion test was performed by polarizing the sample from the settled potential to ± 250 mv at a scan rate of 1 mV/sec. Output data of the test was stored in the computer and the polarization curves were plotted through installed software. Corrosion potential (E_{corr}) and corrosion current (I_{corr}) were obtained by extrapolating cathodic and anodic branches of the Tafel plot. Corrosion parameters like charge transfer resistance (R_{ct}), double layer capacitance (C_{dl}), solution resistance (R_{s}) were extracted from the Nyquist plot by semicircle fitting technique using the installed software. During these tests, the applied frequency was varied from 10 kHz to 0.01 Hz. Corrosion rate (mm/year) and corrosion resistance (Ω/m^2) were calculated using formulae given in chapter 2. Also, the corrosion test equipment is detailed in section 2.7.

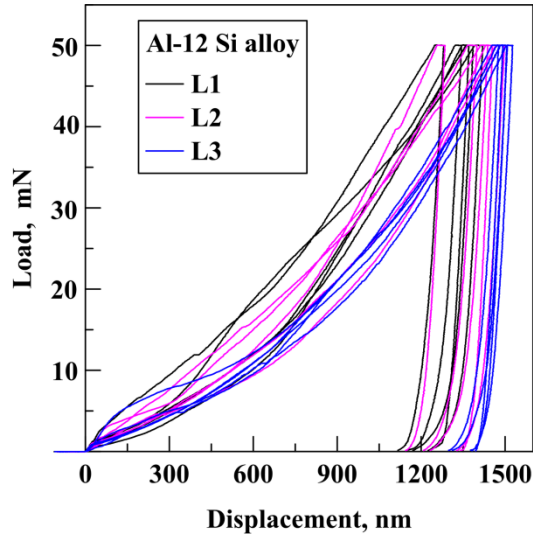
6.3 Results and discussion

6.3.1 Nanohardness and elastic modulus

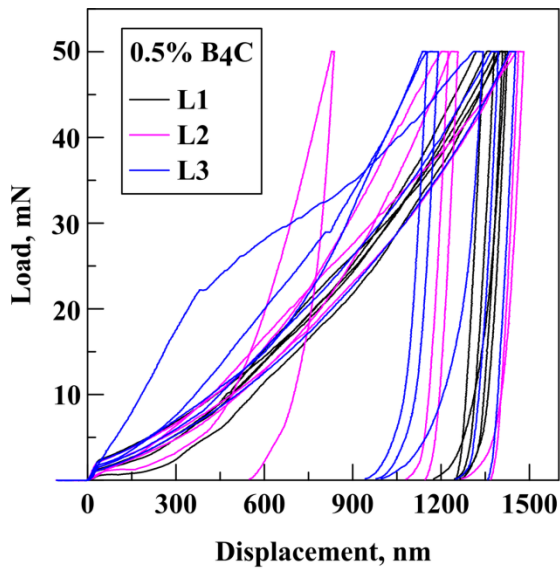
Figure 6.1 shows load-displacement profiles generated for the fabricated alloy and Al/B₄C composites. Penetration depth has been reduced for composite specimens than the base matrix. This indicates that the hardness of alloy is improved with increasing B₄C reinforcement. The plausible explanation for this behavior is that the indenter moving into the composite material encounters more resistance to its travel due to dislocation interactions. Dislocations get created in the material matrix due to fine reinforcement particles. Indenter movement creates additional dislocations, which offer restriction to the

plastic deformation initiated by the indenter under the applied load. As such, composites containing a higher amount of hard particles are likely to present more resistance to the indenter movement due to dislocation strengthened matrix. It is reflected from the experimental data presented in Table 6.2. Mazaheri et al., (2011) have also observed that particle strengthened matrix is responsible for reducing penetration depths of composite materials. Table 6.2 shows averages of different parameters obtained from the nanoindentation set-up following the Oliver and Pharr method. Nano hardness of Al alloy is increased by almost 22% for just 2.0 wt% B_4C content. This significant improvement in hardness could be due to the work-hardened area or the accumulation of more hard phases in the matrix. Hardness increment is reflected in the slopes of the loading curves also. During the initial phase of loading (200 nm depth), all materials have shown similar displacement behavior (as reflected by similar slopes in the loading curves). But as indentation continues further, loading curves of composites exhibited more steepness indicating higher resistance to penetration. It can be understood from the boxes marked in the magnified partial views of loading curves shown in Figure 6.2 Another observation is that many of the loading curves for all samples have shown pop-in behavior indicating displacement discontinuity. It can be due to dislocation nucleation, hard phases, or phase transformations induced by pressure. Such discontinuities are observed commonly in the case of Al-Si alloys due to dislocation mobility (Chen et al., 2009). However, unloading curves are much smoother (missing pop-outs), suggesting no sudden material expansion during indenter withdrawal. Further, it can be seen for all composites that the indentation depth values along or across the indentation rows (L1, L2, L3) are showing random variation. Such isotropic behavior can be due to the uniform dispersion of the hard reinforcing phase in the soft matrix. The scatter of hardness values is more for composites up to 1.5 wt% incorporations when compared to the base alloy. However, for 2.0 wt% composite material, the spread is reduced and looks similar to the base alloy, although the reported hardness values are relatively higher. A possible indication is that 2.0 wt% reinforcement particles have reached the entire volume of the base matrix with uniform dispersion. The slope of the initial part of the unloading curve (stiffness) is used to determine the elastic modulus of the test material. Yield strength and elastic modulus increase with increasing hardness of homogeneous, isotropic metallic materials (Lan and

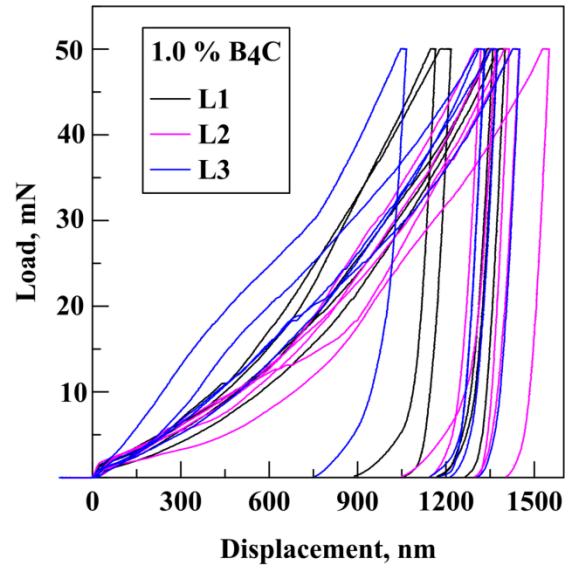
Venkatesh, 2014). Reddy et al., (2017) linked improved modulus of composites with efficient load transfer across the metal-ceramic interface.



(a)



(b)



(c)

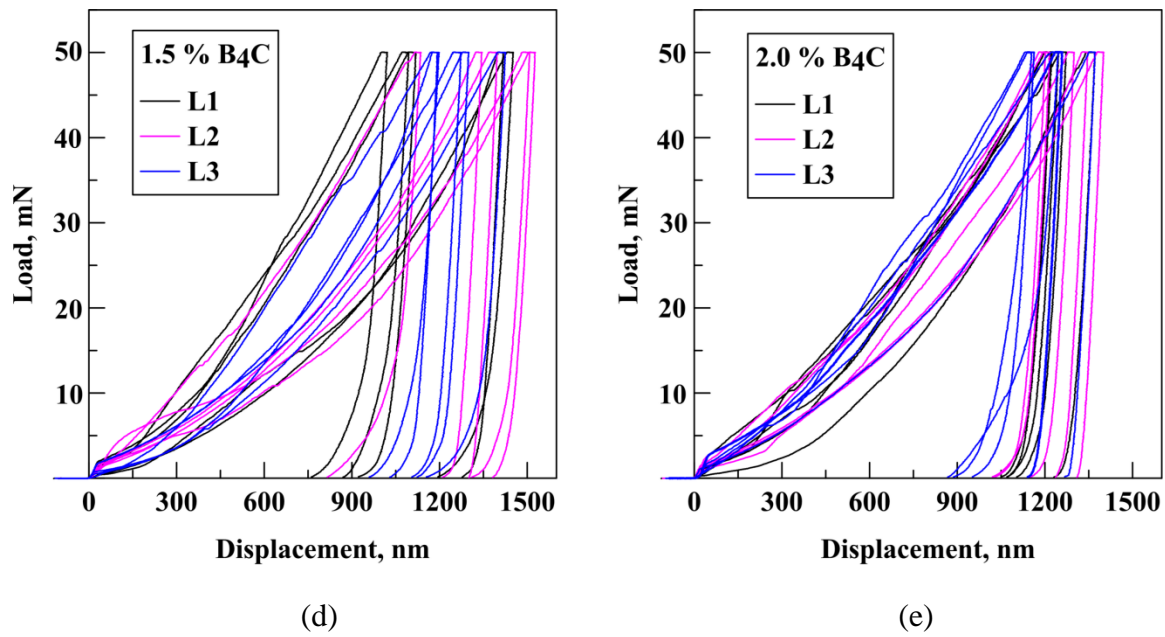


Figure 6.1: Nanoindentation load-displacement profiles: (a) AlSi alloy, (b) 0.5 wt% B₄C, (c) 1.0 wt% B₄C, (d) 1.5 wt% B₄C, (e) 2.0 wt% B₄C

Table 6.2: Average values of 15 indents each for Al alloy and Al/B₄C composites.

Sr. no.	Material	h_{\max} (nm)	h_f (nm)	h_c (nm)	A (μm^2)	S ($\mu\text{N}/\text{nm}$)	Nano hardness (GPa)	Elastic modulus (GPa)
1	Al alloy	1426.79	1292.99	1378.50	53.716	800.31	0.94	97.14
2	0.5% B ₄ C	1360.38	1217.24	1310.17	48.994	769.88	1.04	98.18
3	1.0 % B ₄ C	1345.55	1205.58	1295.68	48.089	775.85	1.07	99.69
4	1.5 % B ₄ C	1294.85	1129.84	1242.83	44.800	738.18	1.18	99.33
5	2.0 % B ₄ C	1267.05	1123.20	1214.37	42.499	746.40	1.19	101.48

It indicates that better particle-matrix bonding is essential for higher modulus and strength of composites. A simultaneous increase in elastic modulus and nanoindentation hardness is also reported by Fale et al., (2014) for AlN/Al nanocomposites with increasing reinforcement. In the present study, the elastic modulus of the aluminum alloy increased from 97.14 GPa to 101.48 GPa for 2.0 wt% B₄C reinforcement content. Similar improvement in hardness and elastic modulus is reported by Mula S. et al., (2009) in the nanoindentation experiment performed on Al-2% Al₂O₃ nanocomposite. They identified

two reasons for this positive change: first, the grain-refined microstructure by ultrasonic casting, and second, the incorporation of hard reinforcement particles. Load-displacement curves shown in Figure 6.1 indicate that displacements are mostly plastic in nature with relatively small elastic recovery. Again, the areas under the curves reveal that composites are less deformed plastically relative to the base alloy. Moreover, the average % elastic recovery of composites $\{(h_{\max} - h_f) \cdot 100 / h_{\max}\}$ is relatively higher and varies between 10.4 - 12.7 % as compared to 9.3 % of the base alloy. Thus it is further confirmed that composites are stronger than base alloy as elastic displacement is related to the strength of the matrix.

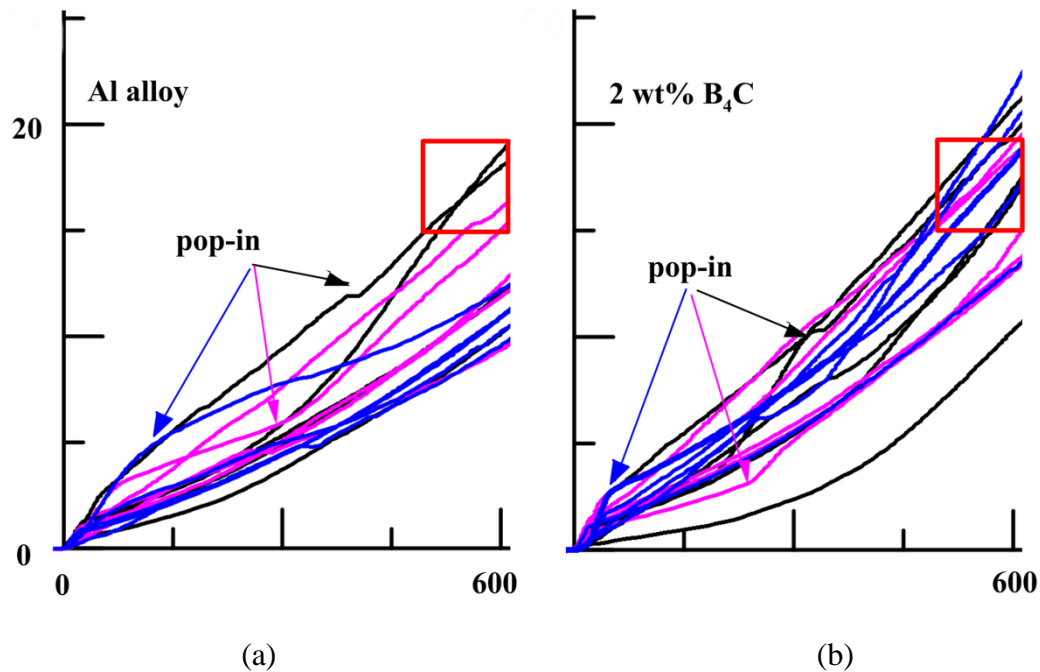


Figure 6.2: Magnified partial views of loading curves showing difference in slopes:
(a) Base alloy, (b) 2 wt% composite

Traditional Al composites show improvement in hardness and strength for a suitable amount of ceramic reinforcements but usually at reduced ductility. Literature suggests that microparticles form clusters causing the weaker interfacial bonds between particles and metal matrix. Unsound interfaces act as preferred sites for crack propagation and so ductility of micro composite is reduced. However, nanocomposites are better than micro composites for they maintain ductility while improving the strength of the matrix. Literature survey indicates that strength, hardness, and % elongation of metallic alloys

improve tremendously even for a small amount of nano-sized ceramic particles. Different strengthening mechanisms identified for this positive change include load-bearing effect, Orowan effect (restriction to dislocation movement), Hall-Petch effect (grain refinement), and dislocations effect (mismatch in thermal expansion and elastic modulus) (Massoud et al., 2019; Ceschini et al., 2017). B_4C particles used here are smaller than the micrometer size and the optical or SEM micrographs do not reveal any evidence of particle clusters. So the notable improvement in indentation hardness and elastic modulus due to submicron B_4C reinforcement can be linked to two aspects: first, dispersion of particles in Al matrix caused by mechanical and ultrasonic stirring action; second, grain refinement and matrix strengthening caused by small size hard B_4C particles. The results of this study are in line with earlier nanoindentation studies of aluminum nanocomposites (Wagih and Fathy, 2016; Mazaheri Y. et al., 2010; Khodabakshi F. et al., 2019).

6.3.2 Wear resistance under scratch loads

The dependence of scratch width on applied load for all the tested materials is shown graphically in Figure 6.3. An almost linear increase in the scratch width is seen with the applied load. Secondly, at any particular loads, the scratch width is decreased with increasing wt % of B_4C content.

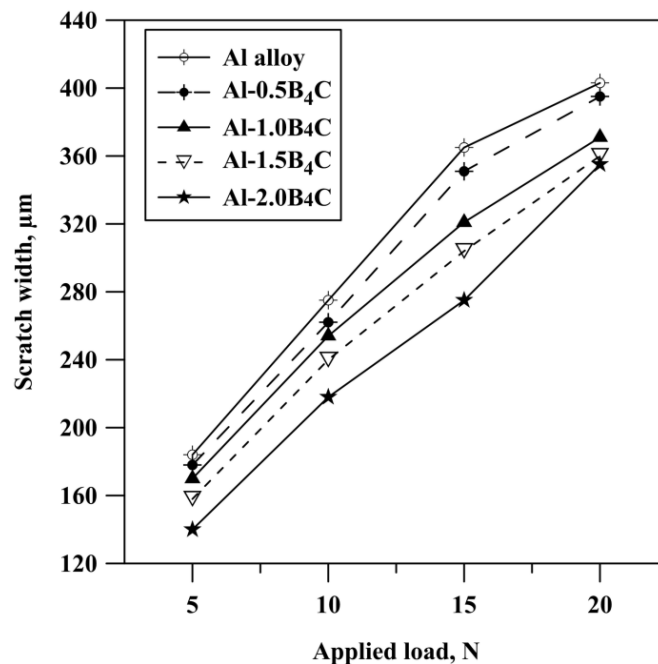


Figure 6.3: Variation of scratch width against applied load

It is also evident from the macroscopic (Figure 6.4) image shown for base alloy and 2.0 wt% B₄C composite material. Decrease in scratch width can be linked to the increase in the hardness of the composite material on account of increasing reinforcement. These trends of scratch width variation at fixed load are comparable to the microhardness results of the fabricated alloy and composites. Microhardness of Al-Si alloy is increased by about 25% due to homogeneous dispersion of just 2.0 wt% B₄C particles. For 2 wt% B₄C content, the scratch width is decreased by 22% to 30% over the load range of 05 – 20 N. It is because the incorporation of micro/ultra-fine B₄C particles enhances the hardness of Al matrix due to better particle-matrix interface, Hall-Petch effect, and Orowan strengthening (Isfahani et al, 2019).

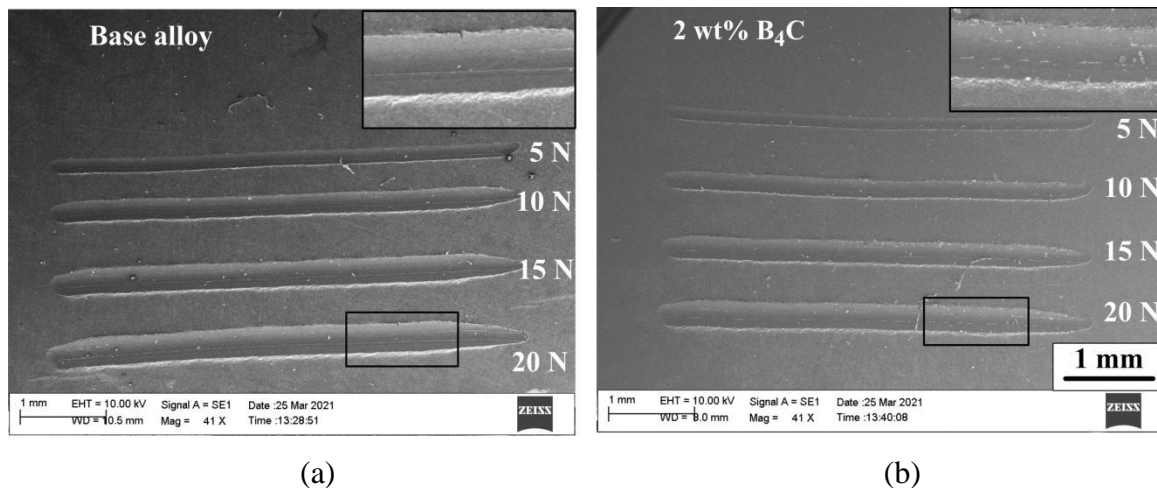


Figure 6.4: Macroscopic image showing load dependence on scratch width

Figure 6.5 reports the effect of B₄C reinforcement on the scratch volumes displaced from grooves at different applied loads. In this scratch test, wear volume is determined as the product of the groove cross-section and the scratch length. While doing so, it is assumed that the surfaces of the triangular groove are smooth, and the groove depth is constant throughout. This method of finding scratch volume is followed by other researches in the past (Yan and Zhang, 1995; Narasimman et al, 2012) also. Wear volumes have decreased with increasing wt% of B₄C for all the applied loads. These trends confirm that the scratch resistance of Al-B₄C composites has enhanced over the base alloy. The strengthening of the Al matrix through B₄C particles is responsible for this behavioral change.

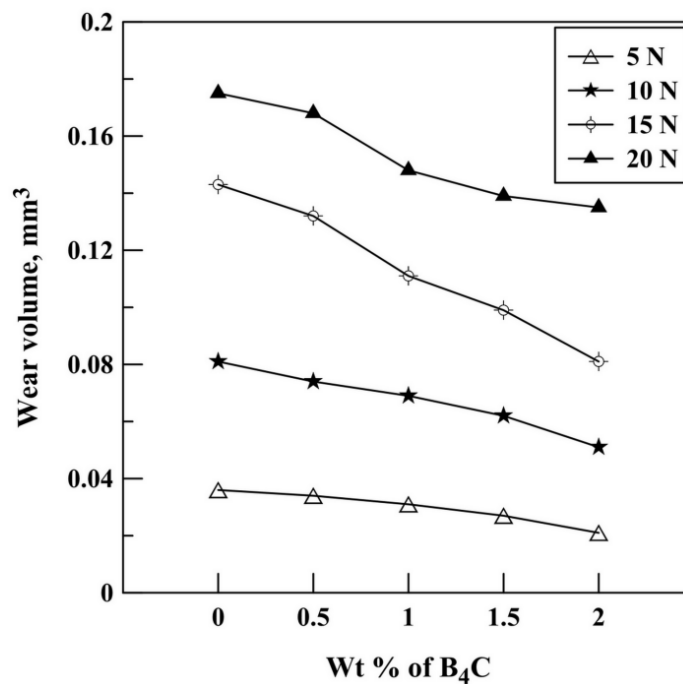


Figure 6.5: Variation of wear volume against wt% of B₄C

6.3.3 Scratch hardness

Table 6.3 displays the scratch hardness values of Al alloy and composites at different loads. Scratch hardness increased with increasing wt% of B₄C reinforcement at all the applied loads. These trends are in line with the microhardness results. It further confirms that the surface properties of Al alloy improved by using submicron B₄C particles. Just 2 wt% B₄C content has improved the scratch resistance of Al alloy by about 73 % and 29 % at 5 N and 20 N respective loads. Another observation is that the scratch hardness of all the tested materials decreased with increasing loads.

Table 6.3: Scratch hardness values of fabricated materials

Material	Scratch hardness (GPa)			
	5 N	10 N	15 N	20 N
Al alloy	0.369	0.330	0.281	0.308
Al-0.5% B ₄ C	0.394	0.364	0.304	0.320
Al-1.0% B ₄ C	0.432	0.387	0.364	0.363
Al-1.5% B ₄ C	0.500	0.434	0.405	0.385
Al-2.0% B ₄ C	0.637	0.526	0.495	0.396

Tabulated data indicate considerable load dependence on scratch hardness. At lowest load (5N), 2.0 wt% B₄C composite (being hardest) has reflected the smallest groove size and highest scratch resistance. However, at a higher load of 20 N, its wear resistance has dropped significantly. It is possible because, at higher depths, a significant amount of material having embedded particles get removed by plastic cutting. In such a situation, the effectiveness of reinforcement against scratch resistance can diminish due to the bulk loss of particles.

6.3.4 Friction characteristics

The average COF values of the fabricated materials at different loads are presented in Table 6.4. Friction coefficients of base alloy and composite materials increased with increasing loads. From the scratch width results, it is obvious that the indenter has moved to greater depths at higher loads. A consequent larger volume of the material was available in front of the moving indenter with every increment of loads. Deformation and displacement of the higher volume of the material require more effort. Thus at higher depth, scratch force (tangential force of traction) has increased with an increased coefficient of friction (Zheng et al., 2018). A similar effect of the load is reported by Dolata et al., (2020) for AlSi12/SiC composite material. It is also observed that an increase in wt% of B₄C has decreased COF values at any particular load. In general, a reduction in COF means a reduction in scratch force. The scratch force of composite material is decreased due to smaller grooves created on account of increased scratch resistance. This behavior can be visualized from the friction profiles plotted for base alloy and 2.0 wt% B₄C composite as shown in Figure 6.6(a)-(b). Friction behavior at the beginning of the scratch test is shown by the magnified inserts indicated by the arrow. COF of the base alloy increased abruptly to 0.1 and after a short dwell increased gradually further. It is because the indenter is pushed inside the bulk of the material matrix to the load-determined depth before its horizontal travel. The composite material, in comparison, has shown lower COF (around 0.05) during indenter penetration due to less material displaced. Thus friction profiles have indicated clear load dependence of COF during the entire scratch event. After an initial gradual increase, the friction coefficient remained almost constant for most of the sliding duration. However, COF has shown local fluctuations. It is because the scratching process is characterized by stick-slip

phenomena (Chatterjee et al., 2015). A scratch groove gets formed due to the displacement of material from the wear track. During the scratch process, the piled-up material facing the moving indenter is shear deformed by fracture or microcracks. Slip occurs in such regions due to an eventual drop in the scratch force. While the fresh undeformed material placed ahead builds up scratch force again, resulting in COF fluctuation. Composite material has reflected less COF fluctuation relative to the base alloy.

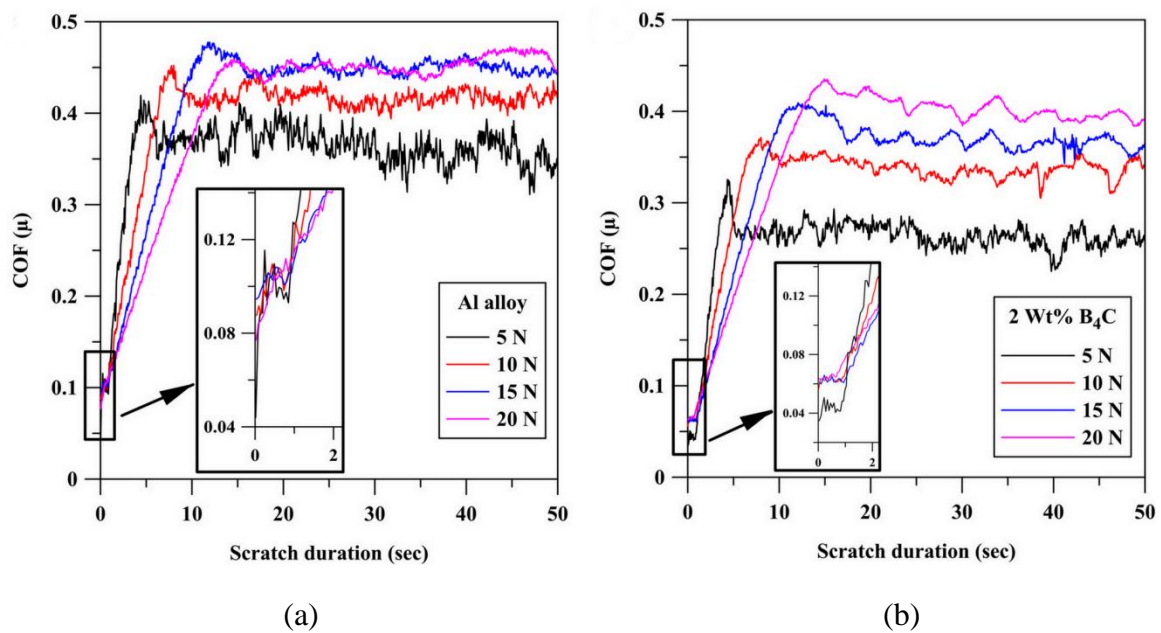


Figure 6.6: Profile of friction coefficient with scratch duration: (a) Al alloy (b) Al-2wt% B₄C composite

Table 6.4: Average friction coefficients at different applied loads in scratch test.

Load, N	Avg. COF, μ				
	Al alloy	0.5% B ₄ C	1.0% B ₄ C	1.5% B ₄ C	2.0% B ₄ C
5	0.355	0.341	0.278	0.260	0.257
10	0.396	0.360	0.344	0.338	0.320
15	0.415	0.390	0.368	0.359	0.342
20	0.406	0.405	0.378	0.360	0.361

6.3.5 Morphology of scratch grooves

Scratches are observed under a scanning electron microscope to understand the micro-mechanisms governing material removal. Macroscopic image and the scratch data presented earlier show that loads and wt% of reinforcement have produced a linear effect on scratch profiles. Hence for having a maximum difference, SEM images of base alloy and 2.0 wt% composite material, obtained at 5N and 20N loads are presented for discussion as Figure 6.7 and Figure 6.8 respectively. Scratch topography of Al alloy obtained at 5 N applied load (Figure 6.7a) shows smooth track surface and distinct ridges.

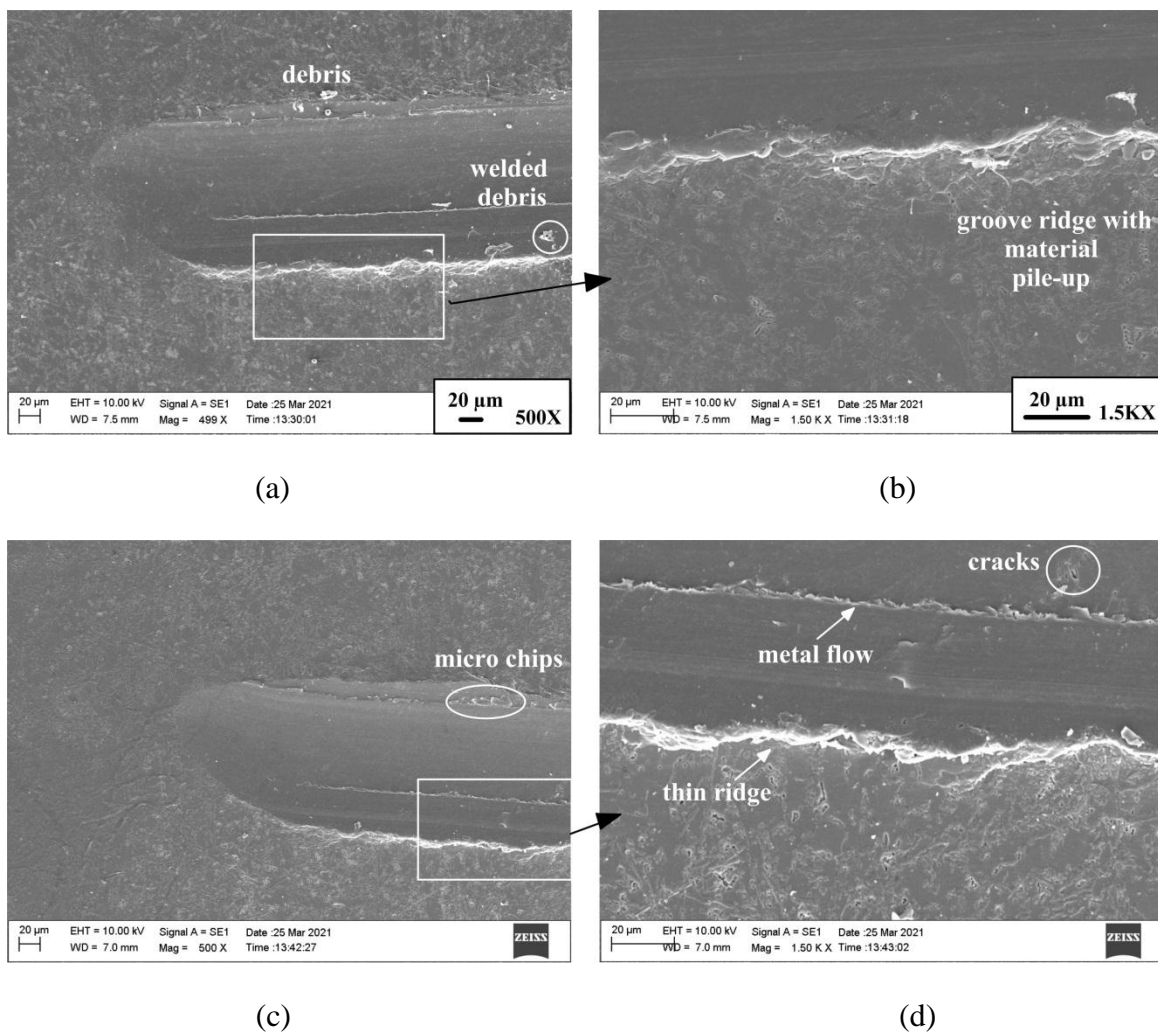


Figure 6.7: Groove topography and magnified ridges at 5 N: (a), (b) Al alloy; (c), (d) Al/2wt% B₄C

Further, the magnified image (Figure 6.7b, 1.5 KX) of the ridge suggests that it has formed by piling material layers. It indicates that the groove is formed by plowing action.

Earlier studies of scratching metals found that the formation of grooves and ridges takes place as a result of the rubbing, plowing, or cutting process (Zheng et al., 2018; Yan and Zhang, 1995; Pohl et al., 2016). Normally rubbing is characterized by small depth and the rough surface formed due to chipping off the material from wear track. Plowing is identified by a higher depth and smooth surface. Therefore observed groove profile here evidently signifies that scratched volume facing the indenter is pushed and then plowed to the sides of the track. It means the micro plowing mechanism was active. Under the same applied load, 2 wt% composite developed a thin ridge (Figure 6.7d), indicating small volume displacement. The surface appears smooth with no debris particles. It suggests that ultra-fine particles have maintained the integrity of the matrix. However, crack formation is detected in the groove surface, which is visible in the magnified view. Crack can form due to tensile stress developed in the surface behind the moving indenter. Microchips are visible at the side of the track and might have formed due to shearing weaker material by the passing indenter.

An increased number of debris particles are visible on the groove surface of Al alloy obtained at 20 N load (Figure 6.8a). Two parallel metal flow lines seen at the groove center are due to the lower end of the indenter. Magnified ridge (Figure 6.8b) shows a broad and layered structure indicating a massive material pile-up. These features suggest that deep plastic cutting has occurred. Deep cutting and more accumulation of material require greater tangential force, which justifies the friction coefficient trends presented earlier. The scratch groove (Figure 6.8c) of the composite appears relatively smoother with small debris particles but is formed essentially by the same cutting action. Irregular and rough ridge area shows displaced material. Careful observation of the groove surface revealed only two places of micro-voids. Ceramic particles on interaction with the indenter can get fractured or pulled out of the matrix creating micro-voids or micro-cracks (Zheng et al., 2018; C. Yan and Zhang, 1995). However, particle pull-out is found less severe for nanocomposites (Narasimman et al., 2012). Alloy and composites are thus scratch deformed mainly by the plowing and plastic cutting mechanisms, while the particle fracture mechanism may exist with a negligible scale.

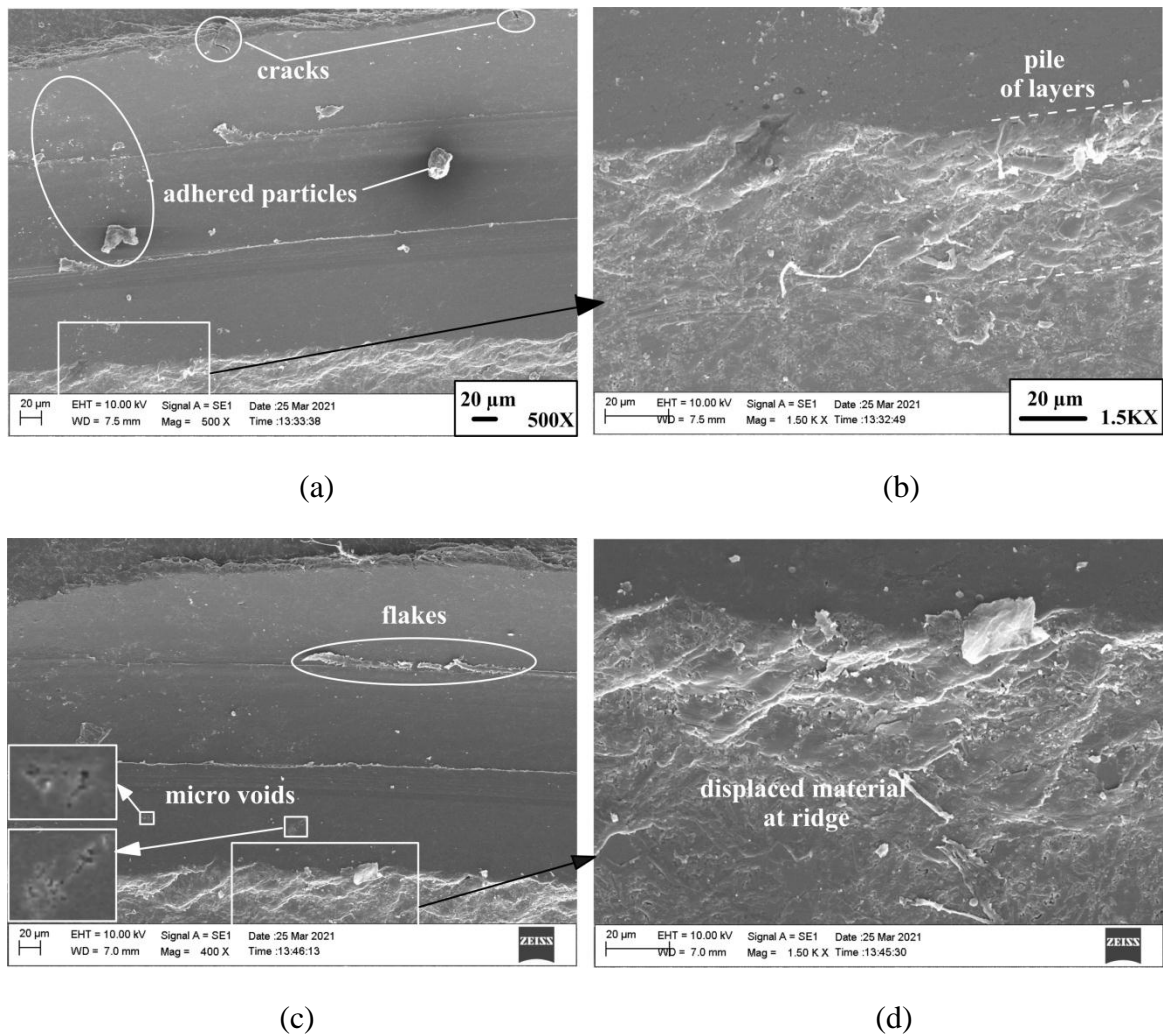


Figure 6.8: Groove topography and magnified ridges at 20 N: (a), (b) Al alloy; (c), (d) Al/2wt% B₄C

6.3.6 Potentiodynamic polarization study

The influence of B₄C content on the corrosion behavior of Al-Si alloy is investigated at room temperature, open to air condition through potentiodynamic polarization technique. PDP curves of all the fabricated test materials are shown in Figure 6.9. The corrosion current density (I_{corr}) values are determined by extrapolating polarization branches back to the open circuit potential (E_{corr}) line. It can be seen that the cathodic branches are showing linear and better-defined Tafel regions for over 200 mV potential. Hence according to McCafferty (2005), the extrapolating line is fitted to the most linear part of the cathode branch to get the intersection point with the E_{corr} line. The slope of the anodic branch is

then determined through that point. Anodic branches of base alloy and 0.5 - 1.5 wt% B₄C composites displayed a gradual increase in current density signifying active polarization with progressive oxidation of Al matrix. But for 2.0 wt% composite, I_{corr} increased rapidly, even for small over potential ascribing severe corrosive reactions. Steep cathodic branches indicated a tendency of concentration polarization with strong reduction reactions at the cathode sites. But, on the whole, the polarization curves of base alloy and composite samples look similar, indicating the occurrence of similar reactions.

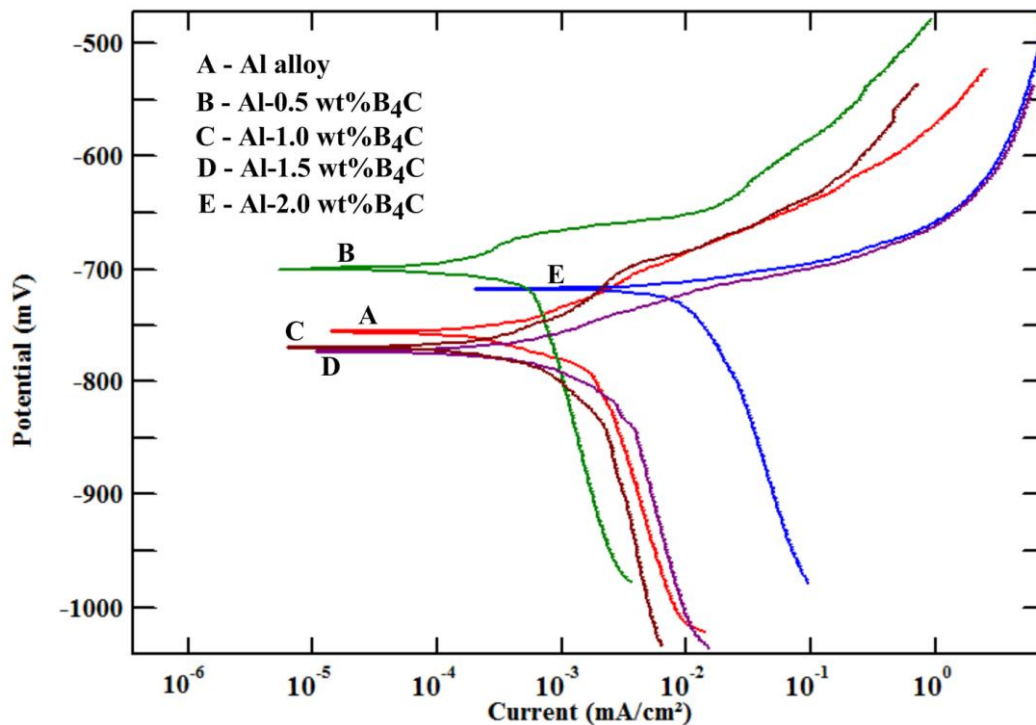


Figure 6.9: PDP curves for Al alloy and Al/B₄C composites

Table 6.5 shows different electrochemical parameters obtained from the Tafel curves. Incorporation of B₄C particles varied corrosion potential in the range from -700 to -774 mV, which is below one order of magnitude concerning base alloy (-755 mV). It generally signifies that the corrosion resistance of the base alloy is not influenced severely by submicron B₄C particles. However, the trend of increasing corrosion with increasing B₄C content is observed, which is obvious from the increasing I_{corr} values of composites. Al-0.5wt% B₄C composite has exhibited the least current density, least corrosion rate, and highest polarization resistance. As per the literature, higher corrosion

potential (nobler) and lower current density means better corrosion resistance. Accordingly, it implies from the tabulated results that 0.5 wt% B₄C composite is the most wear resistant material. The corrosion rate of 1.0 wt% composite is just better than the base alloy. Agglomeration-free dispersion of nano particles and the refined microstructure can be attributed to the improvement in corrosion resistance as observed by Barati M et al. (2019) for Al6061/SiO₂ nanocomposite. After 0.5 wt% B₄C, the corrosion potential was expected to shift to a more noble direction, but it did not happen. Probably more discontinuities occurred in the protective oxide layer on account of increasing B₄C fraction content beyond 1wt%, which led to the deterioration of corrosion performance. However, it is worth noting that the corrosion rates of the tested base alloy (0.0188) and B₄C composites (0.0065-0.1605) typically fall in the excellent to good ranges when related to the ferrous and nickel-based alloys (Fontana, 1986).

Table 6.5: Electrochemical parameters obtained from Tafel plot

Material	Corrosion potential E_{corr} (mV)	Corrosion current density I_{corr} (mA/cm ²)	Anode slope β_a (mV)	Cathode slope β_c (mV)	Corrosion rate (mm/year)	Polarization resistance R_p (Ω/m^2)
Al-Si alloy	- 755	0.00173	64.35	387.03	0.0188	1.3859
0.5% B ₄ C	- 700	0.00060	37.13	433.10	0.0065	2.4829
1.0 % B ₄ C	- 769	0.00157	72.84	445.87	0.0171	1.7327
1.5 % B ₄ C	- 774	0.00260	42.16	422.00	0.0284	0.6387
2.0 % B ₄ C	- 717	0.01473	25.01	352.46	0.1605	0.0689

6.3.7 Electrochemical impedance spectroscopy study

Electrochemical impedance spectroscopy is carried out to confirm the PDP data obtained for base alloy and composites in NaCl solution. The impedance results are shown in the form of Nyquist plots as shown in Figure 6.10. The base alloy shows identical capacitive semicircles in the high and low-frequency range. High frequency semicircle denotes the interface characteristic between the oxide layer and the electrolyte, while the capacitive semicircle at low frequency is attributed to the charge transfer between the metal surface and electrolyte (Katkar et al., 2011).

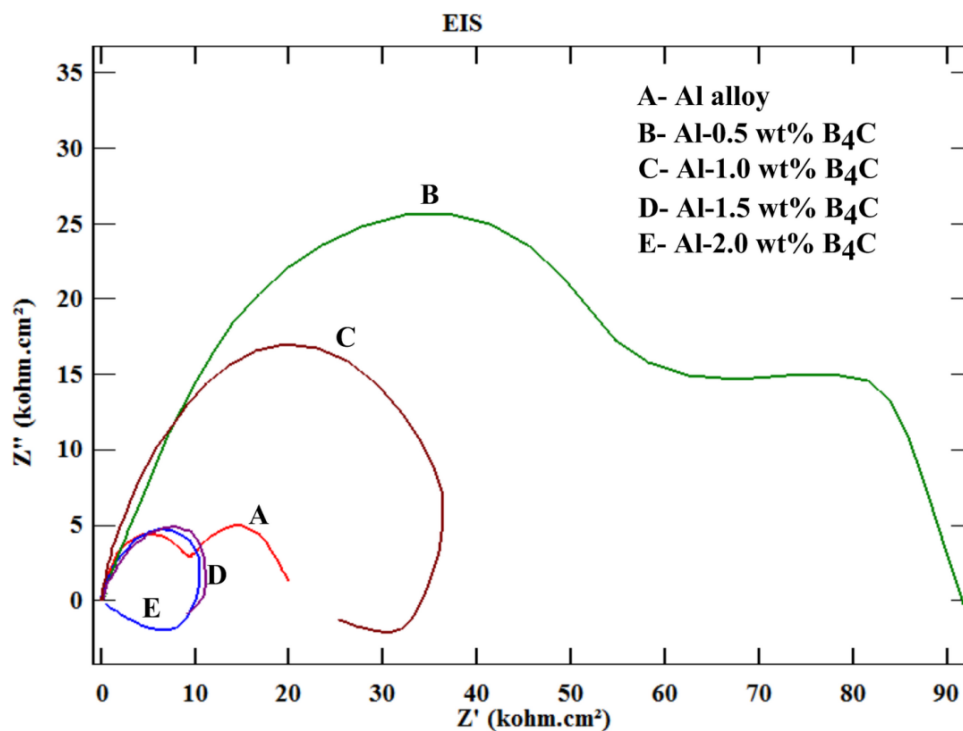


Figure 6.10: Nyquist plots of Al alloy and Al-B₄C composites

In general larger diameter implies higher corrosion resistance. In Figure 6.10, the biggest capacitive semicircles are seen for 0.5 wt% B₄C composite which implies the highest corrosion resistance. The diameters of semicircles are found to decrease with increasing B₄C reinforcement. Composites with 1 wt% B₄C onwards have shown a single capacitive semicircle at high frequency and inductive curve at low frequency range. An inductive loop of 2 wt% B₄C is prominent. It indicates that the matrix surface is either partially or totally active (Katkar et al., 2011). EIS outputs such as solution resistance (R_s), charge transfer resistance (R_{ct}), double layer capacitance (C_{dl}) are determined by circle fitting in the Nyquist plots. The obtained data are presented in Table 6.6. Impedance testing can detect layer formation on the exposed area of the test surface. The formation of such protective oxide layer is known to increase the charge transfer resistance and decrease the double layer capacitance. Increasing incorporation of B₄C particles decreased R_{ct} and R_s values from 65 to 12.72 k Ω cm² and 58.18 to 28.96 Ω cm² respectively, which indicates increasing corrosion rate. The highest values of solution resistance and charge transfer resistance are observed for 0.5 wt% composite which signifies its highest corrosion resistance among all the tested samples. These results are in line with the polarization

results obtained from PDP tests. Similar trends are found elsewhere for Al-B₄C micro composites (Han and Chen, 2015).

Table 6.6: Electrochemical parameters obtained from EIS plots through circle fitting method

Material	Solution resistance R_s ($\Omega \text{ cm}^2$)	Charge transfer resistance R_{ct} ($\text{k}\Omega \text{ cm}^2$)	Double layer capacitance C_{dl} ($\mu\text{F cm}^{-2}$)
Al alloy	35.09	10.4	4.75
0.5% B ₄ C	58.18	65	6.85
1.0 % B ₄ C	46.73	38.95	3.97
1.5 % B ₄ C	37.66	12.10	4.3
2.0 % B ₄ C	28.96	12.72	8.97

6.3.8 Corroded surfaces and degradation mechanisms

Corroded specimen surfaces are observed under the scanning electron microscope to further understand the corrosion process. It is observed that the surface of Al alloy (Figure 6.11a) has developed a small amount of randomly distributed corrosion products and pits on exposure to the NaCl electrolyte. The surface otherwise appears smooth and well protected by an oxide layer under the applied corrosion attack. A magnified view of the corrosion product is shown in the inset of Figure 6.11a. It appears like a white gel with blisters. The area adjacent to it has developed cracks and a cavity suggesting dissolution of Al matrix. Figure 6.11b shows circular and shallow micro pits nearby the intact Si particles. The alloy has Si as a majorly second phase element, which is cathodic to the Al matrix. But as silicon is highly polarized, the risk of galvanic coupling is low, and it is known to least affect the corrosion resistance of the Al matrix. However, there can be precipitation of intermetallic particles like Al₃Fe, Al₁₂Fe₃Si₂, etc., which are cathodic to the Al matrix. Hence localized dissolution of Al alloy can take place through the formation of micro galvanic cells. Intermetallics are discontinuities in the oxide layer, which can promote localized corrosion forming corrosion pits.

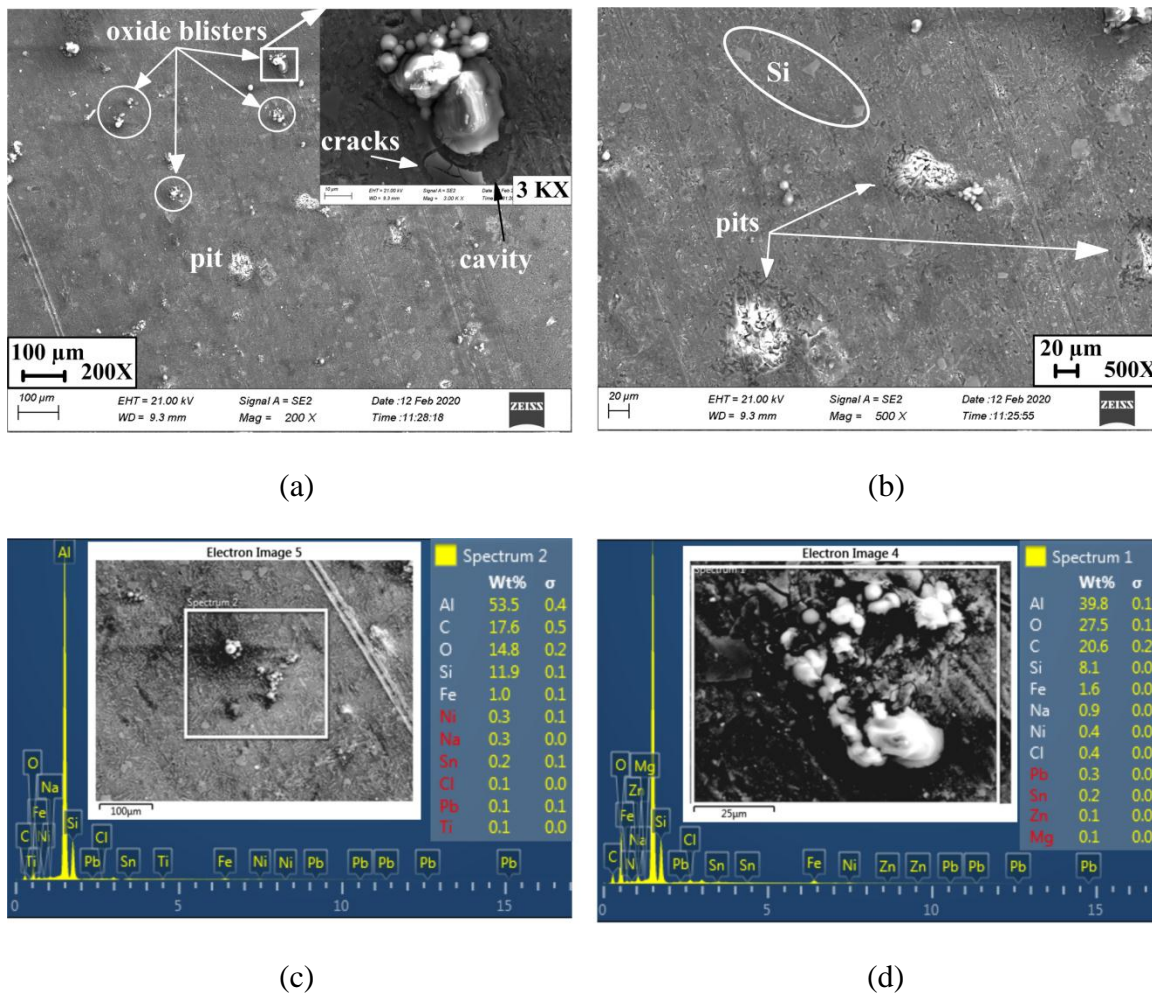
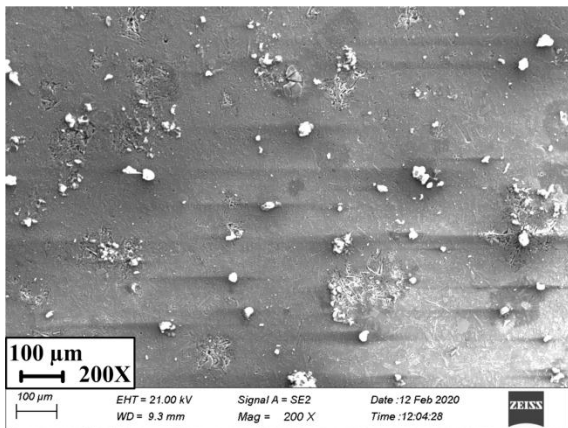


Figure 6.11: Al-Si alloy: (a), (b) Micrographs of corroded surface at different magnifications; (c) EDX analysis; (d) Oxide product at high magnification (3 KX) with EDX spectrum

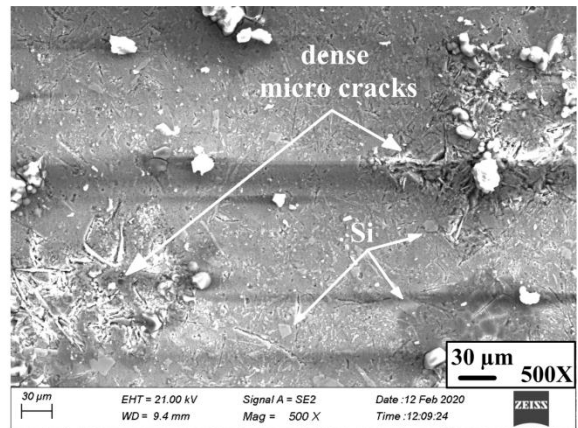
EDX analysis of the corroded alloy surface is presented in Figure 6.11c. It shows peaks of Al, O, Si, Fe, etc., which justify the formation of aluminum oxide in general and oxygen-rich corrosion products due to intermetallics, as mentioned earlier. Mostly the room temperature corrosion products are bayerite and aluminum trihydroxide which forms through the following reactions with water,



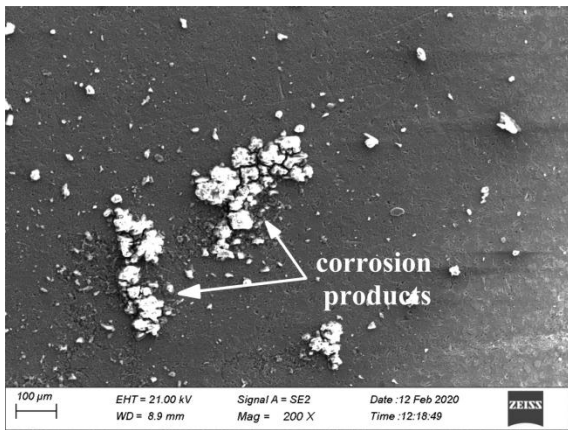
EDX spectrum of the corrosion product shown in Figure 6.11d, with strong peaks of Al and O, justifies the above reactions. A higher amount of Na and Cl signifies corrosion intensity. The trace amount of Mg indicates possible corrosion of anodic Mg₂Si to form oxides of Si and Mg. The morphologies of the corroded surfaces of Al-B₄C composites are shown in Figure 6.12. Similar to base alloy, 0.5 wt% B₄C composite surface show sporadic corrosion products while surface cracks segregated at few places. It signifies that pitting corrosion is active. But the cracks (Figure 6.12b) are not deep which indicates that matrix dissolution is less than that of the base alloy. The surface of 1.0 wt% B₄C composite shows two distinct features; first, relatively smooth area without cracks, and second, corrosion products sitting proudly on the surface. It is interesting to see that the cracks are diminished, suggesting further suppression of the pitting process. However, a magnified view (Figure 6.12d) of the composite surface shows tiny dents (micro pores) developed by mild pitting action. With the further addition of B₄C particles, the pitting process is seen to have diminished as can be seen from Figure 6.12e. The surface is devoid of cracks and micro pores whereas corrosion products have spread over a larger area. Under the same magnification, the surface of 2.0 wt% B₄C composite is seen fully corroded with evidence of metal flow. A mud-flow pattern visible in the SEM image justifies heavy dissolution of the Al matrix under NaCl attack. Thus morphologies of composite surfaces seen in Figure 6.12 indicate a shift in corrosion tendency from pitting to galvanic type with increasing B₄C content. A plausible explanation for this corrosion behavior is as follows. Considering the composite processing temperature of 750°C, it is possible that reaction precipitates such as AlB₂, Al₃BC are present in the microstructure (Viala et al., 1997). These precipitates are cathodic and can cause Al dissolution in the vicinity to form a hydroxyl group of ions. The solution around these intermetallics becomes acidic and the oxidation of Al results in the formation of AlO₂ and Al (OH)₃. Being insoluble in neutral solution, these materials can accumulate at the metal–electrolyte interface in the form of corrosion products. Secondly, boron carbide has low resistivity (1 Ωm) and hence can act as a micro cathodic site to the Al matrix for promoting galvanic corrosion (Ding and Hihara, 2005). Acidification of microvolume solution can lead to the formation of micro crevices or micro-cracks near B₄C particles. But 0.5 wt% content is relatively low. Hence the number of reaction intermetallics and the number of micro galvanic cells would also be less.



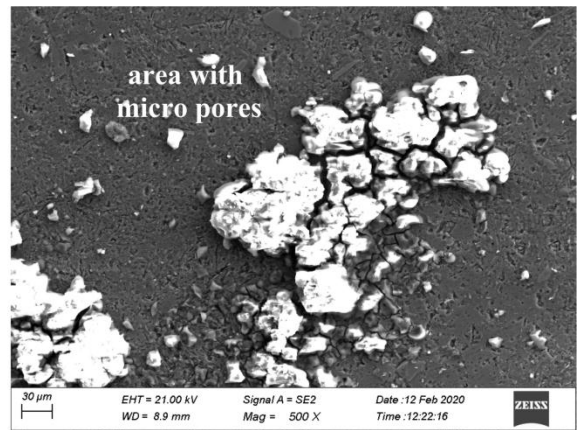
(a)



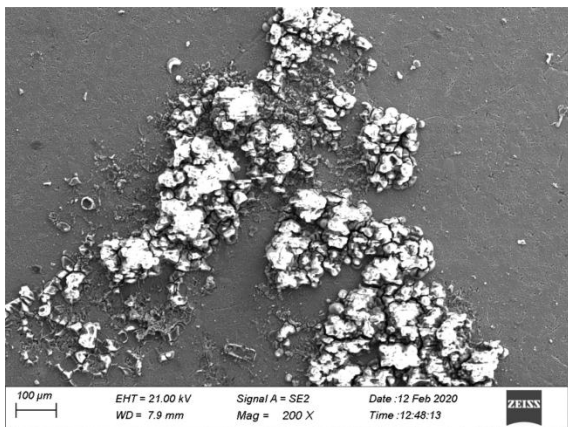
(b)



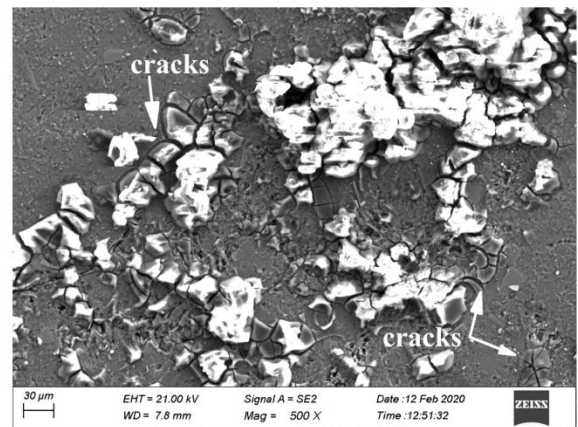
(c)



(d)



(e)



(f)

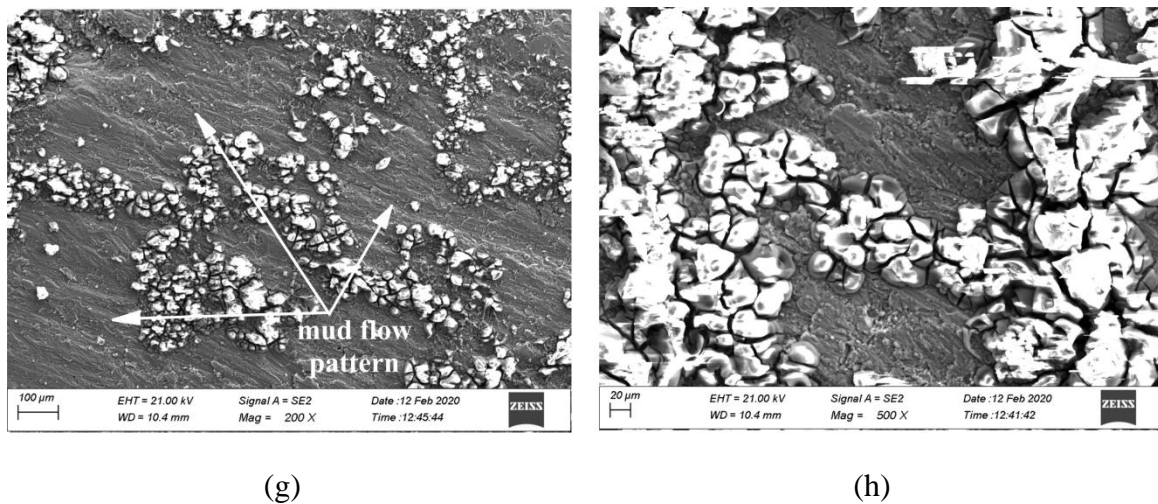
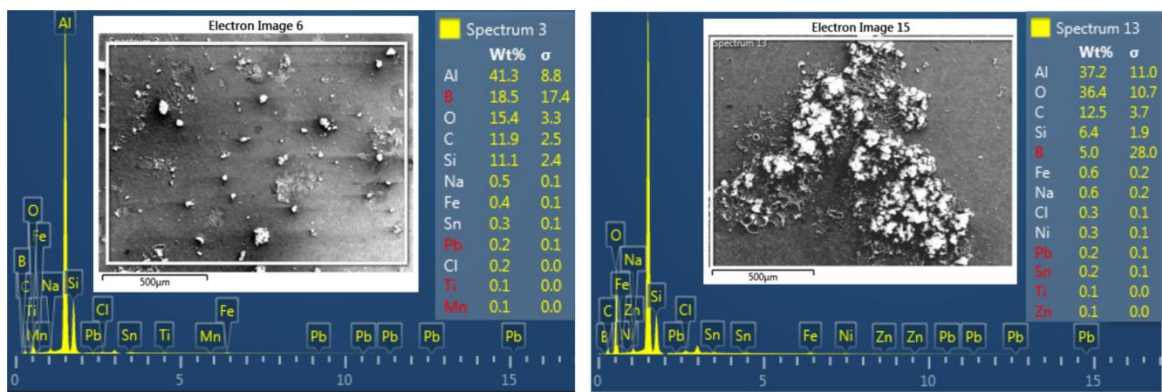


Figure 6.12: SEM images of corroded composites: (a), (b) 0.5 wt% B₄C; (c), (d) 1.0 wt% B₄C; (e), (f) 1.5 wt% B₄C; (g), (h) 2.0 wt% B₄C

It is, therefore, only a few loosely adhered and scattered corrosion products are seen in the micrograph of 0.5 wt% B₄C composite. Further, cracks of lesser depth are seen, which can be due to the barrier effect imposed by B₄C particles to restrict pit growth (Dikici et al., 2009). Increased strength of matrix on account of submicron B₄C particles can also prevent crack growth towards gravity. Thus limited galvanic corrosion and the restricted pitting have probably improved the corrosion resistance of Al-B₄C composite for 0.5 wt% reinforcement. Uniform dispersion of B₄C particles and strong particle-matrix bonding can be other reasons for the improved corrosion resistance as observed elsewhere (Murthy et al., 2013; Nie et al., 2019; El-Aziz et al., 2015). EDX analysis shown in Figure 6.13a has detected a small amount of chloride content which means less corrosion of the metal surface. It also shows that Al and O are the main constituents of the surface layer, indicating the formation of Al oxides. Thus the observed surface morphology of Al-0.5wt% B₄C composite justifies the highest corrosion resistance, which is in line with the largest capacitive semicircle, and least corrosion current detected in the electrochemical tests. Surprisingly, the surfaces of composites with higher B₄C reinforcement of 1 and 1.5 wt % revealed no micro cracks. It could be due to the enhanced barrier effect offered by the increasing reinforcement content. However, at the same time, it is seen that corrosion products occupied an increasing area of the composite surface with increasing B₄C wt%, indicating higher corrosion. It suggests that the increased content of B₄C particles has

increased micro galvanic corrosion sites by a large number. Because the number of B_4C particles per unit area of Al matrix increases with increasing reinforcement. So the accelerated corrosion has occurred at several small places simultaneously to generate a large volume of corrosion products by dissolving a greater amount of Al matrix. The situation is found aggravated for 2.0 wt% B_4C composite as cathodic to anodic area ratio (A^c/A^a) increased further. Material flow patterns observed on the corroded surface present it as a case of severe corrosion.

EDX spectrum shown in Figure 6.13c also confirms high corrosion as higher values of O, B, Cl, and Na are detected. Image of the corroded area captured at high magnification (3 KX) is presented in Figure 6.13d along with its EDX analysis. Larger cracks in the oxide layer are visible. Such cracks allow aggressive Cl ions to infiltrate and corrode the metal surface. Cracks are also known to occur due to the dehydration effect in atmospheric conditions. Small pits and irregular cavities appearing in the oxide layer suggest that it is also getting dissolved. Dikici et al., (2009) have expressed the possibility of the dissolution of the oxide layer by repetitive reaction with chlorine ions. A higher amount of B_4C is detected in the EDX spectrum because boron carbide does not corrode and remains in relief in the corroded matrix. Observations of surface morphologies align well with the PDP and EIS test results presented earlier. Thus, on the whole, it is observed that corrosion resistance of AlSi alloy decreases rapidly when the reinforcement of B_4C particles is increased beyond 1.0 wt%.



(a)

(b)

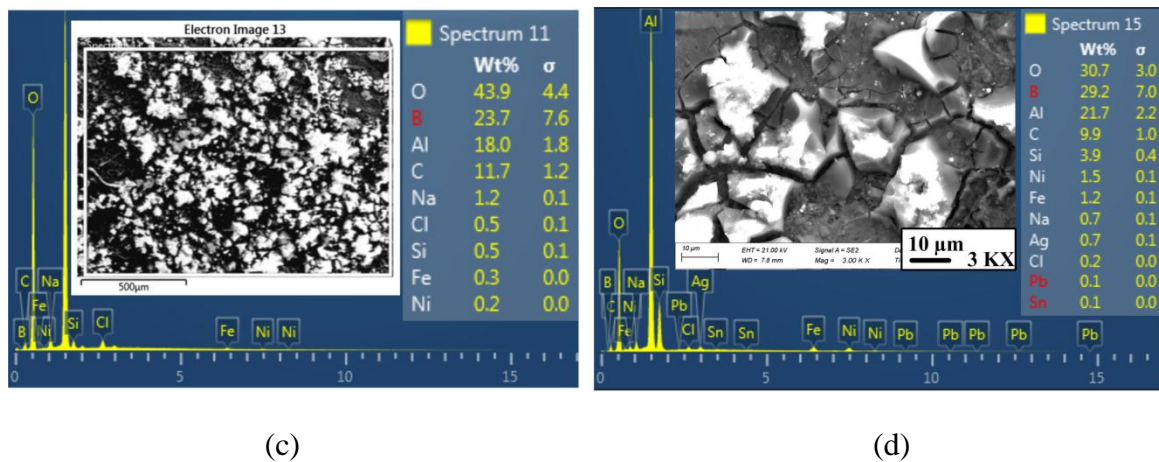


Figure 6.13: EDX analysis of the corroded surfaces at 200X magnification: (a) 0.5 wt% B₄C, (b) 1.5 wt% B₄C, (c) 2.0 wt% B₄C, (d) 2.0 wt% B₄C at 3000X magnification

6.4 Closure

In this chapter, determination of nanohardness and elastic modulus of the fabricated composites and base alloy is discussed using an indentation-depth sensing technique. Nanohardness and elastic modulus of alloy is found to increase with increasing reinforcement content. Dispersion of hard particles strengthened the alloy matrix and caused these notable improvements. Then a micro scale tribological test is presented to evaluate the scratch hardness, wear behavior and frictional response of the test specimens. Examination of scratch morphologies is used to support the discussion. Groove topographies indicated that Al alloy is scratched by plowing and plastic cutting mechanisms. Despite hard dispersoids, the same material removal mechanisms are observed for Al-B₄C nanocomposites. From a machinability viewpoint, it is promising for composites to see only minor traces of particle fracture/pull-out events. Tremendous improvement in the scratch hardness is seen especially at the applied low load. Friction coefficients of all the fabricated materials increased with increasing loads. After the initial increasing trend, the average COF remained constant over the scratch length. More local fluctuations in COF are observed for base alloy than composites. Finally, the corrosion response of the nanocomposites in 3.5% NaCl solution is presented and compared it with that of the base alloy. Electrochemical tests such as potentiodynamic polarization and electrochemical impedance spectroscopy are employed for the purpose. Morphologies of

the corroded surfaces and their EDX analysis done by FESEM-EDS are used to evaluate the corrosion performance. Significant improvement in the corrosion resistance is observed for 0.5 wt% B₄C reinforcement. It is due to the increased strength of matrix, barrier effect imposed by B₄C particles to pit growth, and the low galvanic effect on account of small B₄C content. But higher amount of reinforcement degraded the corrosion response. It is because higher B₄C content increased micro galvanic sites by a large number which accelerated galvanic corrosion. Mud flow pattern on the corroded surface and the development of cracks on it observed at high magnification indicate dissolution of oxide layers.

Final remarks

7.1 Conclusions

In this research work Al/B₄C nanocomposites are fabricated by liquid processing route and investigated for their tribological and corrosion behavior. The important findings of this study are given below.

Ultrasonic stir casting is successfully employed to produce Al-B₄C composites with no cast defects. Porosity of 1.413% is observed for the highest reinforcement content which is quite marginal. Nanoparticles are uniformly distributed in the base alloy matrix which improved the hardness of nanocomposites. Microhardness of the fabricated nanocomposite increased from 68 HV_{0.1} to 87 HV_{0.1} (27% rise) by incorporating just 2 wt% nano boron carbide particles.

Room temperature tribological study revealed that B₄C particle incorporation in LM6 alloy matrix significantly improved its wear resistance. Wear rate is observed to increase almost linearly with increasing contact pressure. Due to B₄C reinforcement, about 25% reduction in wear rate is observed over the speed range of 0.25 to 1.25 m/s. In general, compacted debris and the wear protective transfer layers developed on account of B₄C particles played decisive role in improving wear performance of composite matrix. Oxidation of wear debris is found as a common feature for both materials at all the experimental conditions. Coefficient of friction decreased with increasing speeds. But, friction coefficients and wear rates are not meaningfully correlated with the variation of speed. Sliding distance has no marked influence on the friction coefficient as discernible trend is not observed. Friction coefficient largely depends on PV factor.

Wear rate of alloy and composites decreased with increasing temperatures at the applied load of 20 N while the reverse took place at 60 N. However nanocomposites were found more wear resistant than base alloy. Thermal stability offered by hot hard B₄C, refined microstructure due to nanosized particles, and matrix strengthening due to increased

dislocation density were all decisive in the improved wear performance of composites. Transition in the wear behavior of Al alloy from mild to severe oxidation was seen at 100°C temperature. Metallic wear was dominant at 150°C that aggravated further at 200°C. Al-B₄C nanocomposites exhibited metallic wear at 200°C while at lower temperatures the wear mode displayed was combination of abrasion, oxidation and delamination. Overall the tribological response of Al-B₄C nanocomposite at elevated temperatures is enhanced and appears a suitable tribo material under the tested experimental conditions

With just 2.0 wt% B₄C particle incorporation, nanoindentation hardness and elastic modulus of AlSi alloy are increased by 26.59% and 4.46% respectively. Scratch width of alloy and composites increased linearly with increasing applied loads. At any load, scratch groove size decreased with increasing wt% of B₄C particles. Excellent improvement (73 %) in scratch hardness is seen at low load (5 N), while at the higher load of 20 N, it is enhanced by 29 %. COF trends are observed to fall in line with the scratch volume trends. The corrosion resistance of Al-Si alloy increases significantly for the incorporation of 0.5 wt% B₄C particles. Corrosion increased with increasing B₄C reinforcement content as galvanic corrosion accelerated with increasing cathodic to anodic area ratio. Severe corrosion is observed for 2.0 wt% B₄C composite in 3.5 % NaCl solution.

7.2 Future scope

Learning is a continuous process and every research study carried out is a small contribution in the whole world of possibilities. A research work is never complete in itself and some issues are always left to be explored, so does are here. Efforts can be taken up to modify the ultrasonic stir casting method for its industrial scalability. More advanced tools and techniques can be used for the indepth characterization of the fabricated materials. Tribological pairs are subjected to sudden, intermittent or continuous stresses due to mechanical loading. So evaluation of their mechanical properties is essential and can be carried out, which is not taken up in this study due to cost constraints. Optimization of the test parameters used for the tribological study can be done for suggesting the best operating conditions. Composites can be fabricated with same base matrix but different reinforcements and their comparative study can be carried

out for the general or specific tribological applications. Similarly suitability of B_4C as reinforcement in other light elements like Mg, Ti etc can be tested. Corrosion of Al/ B_4C composites can be studied in other corrosive media like HCL, H_2SO_4 , NaOH etc. Their wear and friction behavior can also be tested in cryogenic environments. Tribocorrosion is an advanced area of research that combines tribology and corrosion. Materials are subjected to wear in corrosive environments also and therefore it is essential to evaluate their tribocorrosion behavior for developing suitable properties. In this study Al/ B_4C composites are tested separately for tribological and corrosion behavior. These composites can be evaluated for their tribocorrosion response.

"This page is left intentionally blank"

Bibliography

- Abbass M.K., Fouad M.J. (2014). *J. Eng. Techol.*, **32A** (7), 1720-1732.
- Abdollahi A., Alizadeh A., Baharvandi H.R. (2014). *Materials and Design*, **55**, 471-481.
- Ahamed H., Senthilkumar V. (2011). *Mater. Charact.*, **62**, 1235-1249.
- Akbari M.K., Baharvandi H.R., Shirvanimoghaddam K. (2015). *Materials and Design*, **66**, 150-161.
- Akbari M.K., Baharvandi H.R., Mirzaee O. (2013). *Composites: Part B*, **52**, 262-268.
- Akbari M.K., Rajabi S., Shirvanimoghaddam K., Baharvandi H.R. (2015). *J. Compos. Mater.*, **49**(29), 3665-3681.
- Alidokht S.A., Abdollah A., Assadi H. (2013). *Wear*, **305**, 291-298.
- Alipour M., Eslami-Farsani R. (2017). *Mater. Sci. Eng. A.*, **6**, 71-82.
- Alizadeh A., Maleki M., Abdollahi A. (2017). *Adv. Powder Technol.*, **28**, 3274-3287.
- Alizadeh M., Paydar M.H. (2010). *J. Alloy Compd.*, **492**, 231-235.
- Alizadeh A., Taheri-Nassaj E. (2011). *Tribol. Lett.*, **44**, 59-66.
- Alizadeh A., Taheri-Nassaj E. (2012). *Mater. Charact.*, **67**, 119-128.
- Allison J.E., Cole G.S. (1993). *JOM*, 19-24.
- Al-Qutub A.M. (2009). *Arab J. Sci. Eng.*, **34**(1B), 205-215.
- Al-Qutub A.M., Allam I.M., Qureshi T.W. (2006). *J. Mater. Process. Tech.*, **172**, 327-331.
- Amarnath G., Sharma K.V. (2013). *IJMET*, **4**(2), 178-188.
- Ambigai R., Prabhu S. (2017). *T. Nonferr. Metal Soc.*, **27**, 986-997.
- Arora H. S., Singh H. Dhindaw B. K. (2012). *Int. J. Adv. Manuf. Technol.*, **61**, 1043-1055.
- Baker I., Sun Y., Kennedy F.E., Munroe P.R. (2010). *J. Mater. Sci.*, **45**, 969-978.

- Barati M., Abbasi M., Abedini M. (2019). *J. Manuf. Process.*, **45**, 491-497.
- Barletta M., Tagliaferri V., Gisario A., Venettacci S. (2013). *Tribol. Int.*, **64**, 39-52.
- Bathula S., Anandani R.C., Dhar A. (2012). *Mater. Sci. Eng. A*, **545**, 97- 102.
- Bathula S., Saravanan M., Dhar A. (2012). *J. Mater. Sci. Technol.*, **28**(11), 969-975.
- Bhoi N.K., Singh H., Pratap S. (2020). *J. Compos. Mater.*, **54**(6), 813-833.
- Blau P.J., (2010). *Tribol. Int.*, **43**, 1203-1208.
- Canute X., Majumder M.C. (2018). *Mechanics and Mechanical Engineering*, **22**(4), 1031-1046.
- Cavalierea P., Jahantigh F., Shabanic A. (2018). *Composites Part B*, **146**, 60-68.
- Ceschini L., Dahle A., Gupta M., Jarfors A.E.W., Jayalakshmi S., Morri A., Rotundo F., Toschi S., Arvind Singh R. (2017). *Aluminum and magnesium metal matrix nanocomposites* (Springer Nature Singapore Pte Ltd.
- Changjun C., Min Z., Qing-Ming C. et al., (2008). *Lasers Eng.*, **18**, 85-94.
- Chatterjee S., Chabri S., Chakraborty H., Sinha A. (2015). *JMEPEG*, **24**, 3407-3418.
- Chawla N., Chawla K.K. (2006) *Metal matrix composites* (Springer Science + Business Media, Inc., USA.
- Chen C.L., Richter A., Thomson R.C. (2009). *Intermetallics*, **17**, 634-641.
- Clarke J., Sarkar A.D. (1979). *Wear*, **54**, 7-16.
- Darmiani E., Danaee I., Golozar M.A. et al., (2013). *Materials and Design*, **50**, 497-502
- Dash k., Chaira D., Ray B.C. (2013). *Mater. Res. Bull.*, **48**, 2535-2542.
- Daouda A., Abou-Elkhair M.T., Rohatgi P. (2004). *Compos. Sci. Technol.*, **64**, 1029-1040
- Dehnavi M.R., Niroumand B., Ashrafizadeh F. (2014). *Mater. Sci. Eng. A*, **617**, 73-83.
- Deuis R.L., Subramanian C., Yellup J.M. (1997). *Compos. Sci. Technol.*, **57**, 415-435.
- Dikici B., Bedir F., Gavgali M.T., Kiyak (2009). *Kovove Mater.*, **47**, 317-323.
- Dinesh Kumar S., Ravichandran M., Jeevika A., Stalin B., Kailasanathan C., Karthick A. (2021). *Ceram. Int.*, **47**(9), 12951-12962.

- Ding H., Hihara L.H., (2005). *J. Electrochem. Soc.*, **152**(4), B161-B167
- Dolata A.J., Mroz M., Dyzia M., Magdalena J. (2020). *Materials*, **13**, 1685
- Donthamsetty S., Babu P.S. (2017). *International Journal of Automotive and Mechanical Engineering*, **14**(4), 4589- 4602
- Durai T.G., Das K., Das S. (2007). *Mat. Sci. Eng. A*, **471**, 88-94.
- Dutkiewicz J., Litynska L., Maziarz W. (2009). *Cryst. Res. Technol.*, **44** (10), 1163-1169.
- Dwivedi D.K. (2010). *Materials and design*, **31**, 2517-2531.
- Dwivedi D.K., Sharma A., Rajan T.V. (2002). *Mater. Trans.*, **43**(9), 2256-2261.
- Ekka K.K., Chauhan S.R., Varun (2015). *Arab. J. Sci. Eng.*, **40**, 571-581.
- El-Aziz K.A., Saber D., Sallam H.E.D.M. (2015). *J. Bio. Tribo. Corros.*, 1:5
- El-Daly A.A., Abdelhammed M., Hashish M. (2013). *Mater. Sci. Eng. A*, **559**, 384–393.
- El-Mahallawi I., Abdelkader H., Yousef L. (2012). *Mater. Sci. Eng. A*, **556**, 76-87.
- Estruga M., Chen L., Choi H. (2013). *Materials and Interfaces*, **5**, 8813-8819.
- Fale S., Likhite A., Bhatt J. (2014). *J. Alloy Compd.*, **615**, 392-396.
- Fale S., Likhite A., Bhatt J. (2015). *J. Compos. Mater.*, **49**(16), 1917-1928.
- Fallahdoost H., Nouri A., Azimi A. (2016). *J. Phys. Chem. Solids*, **93**, 137-144.
- Feng P., Liang G., Zhang J. (2014). *Ceram. Int.*, **40**, 10817-10823.
- Ferguson J.B., Aguirre I., Lopez H. (2014). *Mater. Sci. Eng. A*, **611**, 326–332.
- Fischer-Cripps A. C. (2011) *Nanoindentation, Mechanical engineering series*, Springer
- Fontana M.G. (1986) *Corrosion Engineering*, McGraw-Hill
- Fyzik A.J., Beaman D.R. (1995). *J. Am. Cerum. Soc.*, **78**(2), 305-312.
- Geng L., Zhang X.N., Wang G. (2006). *T. Nonferr. Metal Soc.*, **16**, 387-391.
- Gurrappa I., Bhanu Prasad V.V. (2006). *Mater. Sci. Tech.*, **22**(1), 115-122.
- Hamedan A., Shahmiri M. (2012). *Mater. Sci. Eng. A*, **556**, 921-926.

- Han Q., Geng Y., Setchi R. (2017). *Composites Part B*, **127**, 26-35.
- Han Y., Chen X. (2015). *Materials*, **8**, 6455-6470.
- Han Y., Gallant D., Chen X. G. (2011). Corrosion science section, *Corrosion*, **67**(11), 115005:1-11
- Harichandran R., Selvakumar N. (2016). *Arch. Civ. Mech. Eng.*, **16**, 147-158.
- Hashim J. L., Looney J. L., Hashmi M. (1999). *J. Mater. Process. Tech.*, **92-93**, 1-7.
- Hemanth J. (2005). *Wear*, **258**, 1732-1744.
- Hemanth J. (2009). *Mater. Sci. Eng. A*, **507**, 110-113.
- Hirsch J. (2014). *T. Nonferr. Metal Soc.*, **24**, 1995-2002.
- Hosseini N., Karimzadeh F., Abbasi M.H., Enayati M.H. (2010). *Materials and Design* **31**, 4777-4785.
- Hosseini N., Karimzadeh F., Abbasi M.H., Enayati M.H. (2012). *Tribol. Int.*, **54**, 58-67.
- Hoziefa W., Toschi S., Ahmed M. (2016). *Materials and Design*, **106**, 273–284.
- Hsu C.J., Chang, C.Y., Kao P.W. (2006). *Acta Materialia*, **54**, 5241-5249.
- Isfahani M.J.N., Payami F., Asadabad M.A., Shokri A.S. (2019). *J. Alloys Compd.*, **797**, 1348-1358.
- Jerome S., Ravisankar B., Mahato P., Natarajan S. (2010). *Tribol. Int.*, **43**, 2029-2036.
- Jeyasimman D., Narayanasamy R., Ponalagusamy R., et al. (2014). *Materials and Design* **64**, 783-793.
- Jiang J., Wang Y. (2015). *Materials and Design*, **79**, 32-41.
- Jiang J., Xiao G., Che C., Wang Y (2018). *Metals*, **8**, 460
- Jia S., Zhang D., Xuan Y., Nastac L. (2016). *Appl. Acoust.*, **103**, 226-231.
- Kalashnikov I.E., Bolotova L.K., Kobeleva L.I., et al., (2015). *Russ. Metall-Metall.*, **4**, 285-289.
- Kallip K., Babu N.K., Alogab K.A. (2017). *J. Alloy Compd.*, **714**, 133-143.
- Kandemir S., Atkinson H. V., Weston, D.P. Hainsworth S.V. (2014). *Metall. Mater. Trans. A*, **45**, 5785-5798.

- Kang Y. C., Chan S. L. (2004). *Mater. Chem. Phys.*, **85**, 438-443.
- Kannan C., Ramanujam R., Venkatesan K. et al. (2018). *Mater Today-Proc.*, **5**, 12837-12847.
- Katkar V.A., Gunasekaran G., Rao A.G., Koli P.M. (2011). *Corros. Sci.*, **53**, 2700-2712.
- Khodabakshi F., Gerlich A.P., Verma D., Haghshenas M. (2019). *Mater. Sci. Eng. A*, **744**, 120-136.
- Kiourtsidis G., Skolianos S.M. (1998). *Mater. Sci. Eng. A*, **248**, 165-172.
- Kubota M., Kaneko J. Sugamata M. (2008). *Mater. Sci. Eng. A*, **475**, 96-100.
- Kumar A., Pal K., Mula S. (2017). *J. Manuf. Process.*, **30**, 1-13.
- Kumar N., Gautam G., Gautam R., Mohan A., Mohan S. (2017). *ASME J. Tribol.*, **139**, 011601-1-12.
- Kumar S., Panwar R.S., Pandey O.P. (2013). *Ceram. Int.*, **39**, 6333-6342.
- Kumar S., Subramanaya V., Sarma, Murty B.S. (2009). *Metall. Mater. Trans A.*, **40**, 223-231.
- Kumaran S.T., Uthayakumar M. (2014). *Proc. IMechE Part J: J. Engineering Tribology* **228**(3), 332-338.
- Lan H., Venkatesh T.A. (2014). *Philos. Mag.*, **94**(1), 35-55.
- Lashgari H.R., Sufizadeh A.R., Emamy M. (2010). *Materials and Design*, **31**, 2187-2195.
- Lashgari H.R., Zangeneh Sh., Shahmir H., Saghafi M., Emamy M. (2010). *Materials and Design*, **31**, 4414-4422.
- Lekatou A., Karantzalis A.E., Evangelou A. et al. (2015). *Materials and Design*, **65**, 1121-1135.
- Li G., Wang H., Yuan X. (2013). *Mater. Lett.*, **99**, 50-53.
- Li J., Lü S., Wu S., Gao Q. (2018). *Ultrason. Sonochem.*, **42**, 814-822.
- Li X., Yang Y. Cheng X. (2004). *J. Mater. Sci.*, **39**, 3211-3212.
- Li X.Y., Tandon K.N. (1999). *Wear*, **225-229**, 640-648.
- Litz L.M., Mercuri R.A. (1963). *J. Electrochem. Soc.*, **110**(8), 921-925.
- Liu X., Jia S., Nastac L. (2014). *Int. J. Metalcast.*, **8**(3), 51-58.

- Liu Y., Du J., Yu S., Wang W. (2004). *Wear*, **256**(3-4), 275-285
- Liu Y., Han Z., Cong H. (2010). *Wear*, **268**, 976-983.
- Loto R.T., Babalola P. (2018). *Results Phys.*, **10**,731-737.
- Loto R.T., Babalola P. (2019). *T. Mater. Res. Technol.*, **8**(3), 2517-2527.
- Lu D., Gu M., Shi Z. (1999). *Tribol. Lett.*, **6**, 57-61.
- Ma L., Chen F., Shu G. (1995). *J. Mater. Sci. Lett.*, **14**, 649-650.
- Ma Z., Li Y., Liang Y. (1996). *Mater. Sci. Eng. A*, **219**, 229-231
- Maa S.M., Zhang P., Ji G. (2014). *J. Alloy Compd.*, **616**, 128-136.
- Ma K., Lavernia E.J., Schoenung J.M. (2017). *Rev. Adv. Mater. Sci.*, **48**(2), 91-104.
- Mahesh V.P., Nair P. S., Rajan T.P.D., Pai B.C., Hubli, R.C. (2011). *J. Compos. Mater.* **45**(23) 2371-2378.
- Mahmoud T.S., El-Kady E.Y., Al-Shihri A. (2012). *Corros. Eng. Sci. Technol.*, **47**, 45-53.
- Malaki M., Xu W., Kasar A.K., Menezes P.L., Dieringa H., Varma R.S., Gupta M. (2019). *Metals*, **9**, 330
- Manivannan I., Ranganathan S., Gopalakannan S., Suresh S., Nagakarthikan K., Jubendradass R. (2017). *Surfaces and Interface*, **8**, 127-136.
- Martinez M.A., Martin A., LLorca J. (1993). *Scripta. Metall. Mater.*, **28**, 207-212.
- Masanta M., Ganesh P., Kaul R. (2009). *Mater. Sci. Eng. A*, **508**, 134-140.
- Massoud M., Xu W., Kasar A.K, Menezes P.L., Dieringa H., Varma R.S., Gupta M (2019). *Metals*, **9**, 330
- Mattli M.R., Matli P.R., Shakoor A. (2019). *Ceramics*, **2**, 126-134.
- Mazaheri Y., Karimzadeh F., Enayati M. (2010). *Materials Sciences and Applications*, **1**, 217-222
- Mazaheri Y., Karimzadeh F., Enayati M.H (2011). *J. Mater. Process. Tech.*, **211**, 1614-1619
- McCafferty E. (2005). *Corros. Sci.*, **47**, 3202-3215.

- Moghadam A.D., Omrani E., Menezes P.L., Rohatgi P.K. (2016). *Tribol. Lett.*, **62**, 25
- Monikandan V.V., Joseph M.A., Rajendrakumar P.K. (2018). *Metallography, Microstructure, and Analysis*, **7**, 735–745
- Monikandan V.V., Joseph M.A., Rajendrakumar P.K., Sreejith M. (2015). *Mater. Res. Express*, **2**, 016507.
- Mosleh-Shirazi S., Akhlaghi F., Li D. (2016). *T. Nonferr. Metal. Soc.*, **26**, 1801-1808.
- Mosleh-Shirazi S., Hua G., Akhlaghi F., Yan X., Li D. (2015). *Sci. Rep.*, **5**, 18154.
- Moazami-Goudarzi M., Akhlaghi F. (2016). *Tribol Int.*, **102**, 28-37.
- Mukhopadhyay N.K., Paufler P. (2006). *Int. Mater. Rev.*, **51**(4), 209-245.
- Mula S., Padhi P., Panigrahi S.C., Ghosh S. (2009). *Mater. Res. Bull.*, **44**, 1154-1160.
- Mula S., Pabi S.K., Koch C.C. (2012). *Mater. Sci. Eng. A*, **558**, 485-491
- Muley A.V., Aravindan S., Singh I.P. (2015). *Manuf. Rev.*, **2**, 26-34.
- Murthy H.C.A., Raju V.B., Shivakumara C. (2013). *Bull. Mater. Sci.*, **36**(6), 1057-1066.
- Murthy V., Reddy A.P., Selvaraj N., et al. (2016). *IOP Conf. Series: Materials Science and Engineering*, **149**, 012106.
- Mussert K.M, Vellinga W.P, Bakker A.S, Zwaag S. (2002). *J. Mater. Sci.*, **37**, 789-794.
- Najimi A.A., Shahverdi H.R. (2017). *Mater. Charact.*, **133**, 44-53.
- Narasimman P., Pushpavanam M., Periasamy V.M. (2012). *Wear*, **292-293**, 197-206.
- Nassar A.E., Nassar E.E. (2017). *Journal of King Saud University-Engineering Sciences* **29**, 295-299.
- Nemati N., Emany M., Penkov O.V., Kim J., Kim D. (2016). *Materials and Design*, **90**, 532-544.
- Nemati N., Khosroshahi R., Emany M., Zolriasatein A. (2011). *Materials and Design*, **32**, 3718-3729.
- Nie J., Wang F., Chen Y., Mao Q., Wang H., Song Z., Liu X., Zhao Y. (2019). *Results Phys.*, **14**, 102471
- Nieto A., Yang H., Jiang L. et al. (2017). *Wear*, **390-391**, 228-235.

- Olivas E.R., Swadener J.G., Shen Y.L. (2006). *Scripta. Mater.* **54**, 263-268.
- Oliver W. C., Pharr G. M. (2004). *J. Mater. Res.*, **19**(1), 3-20.
- Pal A., Poria S., Sutradhar G., Sahoo P. (2018). *Mater. Res. Express*, **5**, 036521
- Pauschitz A., Roy M., Franek F. (2008). *Tribol. Int.*, **41**, 584-602.
- Pohl F., Hardes C., Theisen W. (2016). *AIMS Materials Science*, **3**(2), 390-403.
- Poria S., Sutradhar G., Sahoo P. (2018). *Mater. Res. Express.*, **5**, 076519
- Poria S., Sutradhar G., Sahoo P. (2018). *Surf. Rev. Lett.*, **1850122**, 1-18.
- Poirier D., Drewb R., Trudeau M.L. (2010). *Mater. Sci. Eng. A*, **527**, 7605-7614.
- Poovazhagan L., Kalaichelvan K., Rajadurai A. (2014). *Trans. Indian. Inst. Met.*, **67**(2), 229-237
- Poovazhagan L., Kalaichelvan K., Sornakumar T. (2016). *Mater. Manuf. Process.* **31**, 1275-1285.
- Prabhu B., Suryanarayana C., Ana, L. (2006). *Mater. Sci. Eng. A*, **425**, 192-200.
- Prasada S.V., Asthana R. (2004). *Tribol. Lett.* **17**(3), 445-453.
- Prasad S.V., Rohatgi P.K. (1987). *JOM*, **39**(11), 22-26.
- Qu J., Xu H., Feng Z., et al., (2011). *Wear*, **271**, 1940-1945.
- Raj R., Thakur D.G., (2016). *Arch. Civ. Mech. Eng.*, **16**, 949-960.
- Rajaram G., Kumaran S., Srinivasa Rao T. (2010). *Mater. Sci. Eng. A*, **528**, 247-253
- Ramachandra M., Abhishek A., Siddeshwar P et al. (2015). *Proc. Mat. Sci.*, **10**, 212-219.
- Ravikiran A., Surappa M.K. (1997). *Scripta Mater.*, **36**(1), 95-98.
- Ravindran P., Manisekar K., Vinoth Kumar S., Rathika P. (2013). *Materials and Design* **51**, 448-456
- Reddy A.P., Krishna P.V., Rao R.N. (2019). *Silicon*, Epub ahead of print, DOI: 10.1007/s12633-019-0072-9.
- Reddy M.P., Shakoor R.A., Parande G., Manakari V., Ubaid F., Mohamed A.M.A., Gupta M. (2017). *Prog. Nat. Sci.*, **27**, 606-614.

- Rohatgi P.K., Xiang C., Gupta N (2018) *Comprehensive composite materials II, Vol. 4.* ed. by P.W.R. Beaumont, C.H. Zweben pp. 287-312, Elsevier
- Rosenberger M.R., Schvezov C.E., Forlerer E. (2005). *Wear*, **259**, 590-601
- Sahu K., Rana R.S., Purohit R., et al. (2015). *Mater Today-Proc.*, **2**, 1892-1900.
- Sajjadi S. A., Ezatpour H. R., Beygi H. (2011). *Mater. Sci. Eng. A*, **528**, 8765-8771.
- Salehi A., Babakhani A., Zebarjad S. M. (2015). *Mater. Sci. Eng. A*, **638**, 54-59.
- Sameezadeh M., Emany M., Farhangi H. (2011). *Materials and Design*, **32**, 2157-2164.
- Sannino A.P., Rack H.J. (1995). *Wear*, **189**, 1-19.
- Sarkar A.D., Clarke J. (1980). *Wear*, **61**, 157-167.
- Schultz B. F., Ferguson J. B., Rohatgi P. K. (2011). *Mater. Sci. Eng. A*, **530**, 87-97.
- Sharifi E.M., Karimzadeh F. (2011). *Wear*, **271**, 1072-1079.
- Sharifi E.M., Karimzadeh F., Enayati M.H. (2011). *Material and Design*, **32**, 3263-3271.
- Sharifitabar M., Sarani A., Khorshahian S. (2011). *Materials and Design*, **32**, 4164-4172.
- Sharma R., Singh A.K., Arora A., Pati S., De P.S. (2019). *T. Nonferr. Metal. Soc.*, **29**, 1383-1392.
- Shen Y.L., Williams J.J, Piotrowski G., Chawla N., Guo Y.L. (2001). *Acta. Matter.*, **49**, 3219-3229.
- Siddesh Kumar N.G., Ram Prabhu T., Shiva Shankar G.S., Basavarajappa S. (2016). *Tribology- Materials, Surfaces & Interfaces*, **10**, 138-149.
- Siddesh Kumar N.G., Prabhu T.R., Mishra R.K., et al. (2018). *Measurement*, **128**, 362-376.
- Shubhajit S., Chandrasekaran M., Samanta A., Kayaroganam, Paulo D.J. (2018). *Ind. Lubr. Tribol.*, **71**(1), 83-93.
- Singh J., Alpas A.T. (1996). *Metall. Mater. Trans A*, **27**, 3135-3148.
- Singh N., Haq M.I.U., Raina A., et al. (2018). *Alexandria Engineering Journal*, **57**, 1323-1330
- Sinha S. K., Reddy S. U., Gupta M. (2006). *Tribol. Int.*, **39**, 184-189.

- Simoës S., Viana F., Reis M.A. (2014). *Composite Structures*, **108**, 992-1000.
- Soltania M.A., Jamaati R., Toroghinejad M.R. (2012). *Mater. Sci. Eng. A*, **550**, 367-374.
- Srivastava N., Choudhari G.P., (2016). *Mater. Sci. Eng. A*, **651**, 241-247.
- Srivastava N., Chaudhari G.P (2018). *Mater. Sci. Eng. A*, **724**, 199-207.
- Stott F.H. (2002). *Tribol. Int.*, **35**, 489-495.
- Subramanian C. (1991). *Wear*, **151**, 97-110.
- Suh N.P. (1973). *Wear*, **25**, 111-124.
- Surappa, M. K. (2003). *Sadhana*, **28**, 319-334.
- Tan H., Zhu S., Wang S., Yu Y., Li W., Yang J., Liu W. (2018). *Tribol. T.*, **61**, 1107-1116.
- Tavoosi M., Karimzadeh F., Enayati M.H. (2010). *Mater Sci. Techno.*, **26**(9), 1114-1119.
- Tarn W.H., Walker P. (1991) *Handbook of metal etchants*, CRC press LLC.
- Tazari H., Siadati M. H. (2017). *J. Alloy Compd.*, **729**, 960-969.
- Thevenot F. (1990). *J. Eur.Ceram. Soc.*, **6**, 205-225.
- Thirumalai Kumaran S., Uthayakumar M. (2014). *Proc. IMechE Part J: J. Engineering Tribology*, **228**(3), 332-338
- Toptan F., Kilicarslan A., Kerti I. (2010). *Mater. Sci. Forum.*, **636-637**, 192-197.
- Torrallba J.M., Francisco V., Costa C.E., Vergara I., Caceres D. (2002). *Composites: Part A*, **33**, 427-434
- Tavoosi M., Karimzadeh F. Enayati M.H. (2010). *Mater. Sci. Technol.*, **26**(9), 1114-1119.
- Ubaid F., Matli P.R., Shakoor R.A., Parande G., Manakari V., Mohamed A.M.A., Gupta M. (2017). *Materials*, **10**, 621
- Uozumia H., Kobayashia K., Nakanishia K. (2008). *Mater. Sci. Eng. A*, **495**(1-2), 282-287
- Uthayakumar M., Aravindan S., Rajkumar K. (2013). *Materials and Design*, **47**, 456-464.
- Valibeygloo N., Khosroshahi R. A. Mousavian R. T. (2013). *International Journal of Minerals. Metallurgy and Materials*, **20**(10), 978-985.

- Verma A.S., Sumankant, Suri N.M., Yashpal (2015). *Mater Today: Proc.*, **2**, 2840-2851.
- Viala J.C., Bouix J., Gonzalez G., Esnouf C. (1997). *J. Mater. Res.*, **32**, 4559-4573.
- Vishwanatha H.M, Eravelly J., Kumar C.S., Ghosh S. (2017). *Mater. Sci. Eng. A* **708**, 222-229
- Vitry V., Delaunois F., Dumortier C. (2008). *Surf. Coat. Tech.*, **202**, 3316-3324.
- Wagih A., Fathy A. (2016). *Adv. Powder Technol.*, **27**, 403-410.
- Wagih A., Fathy A., Ibrahim, D. (2018). *J. Alloy Compd.*, **752**, 137-147.
- Wan-li G.U. (2006). *J. Trans. Nonferr. Metal Soc.*, **16**, 398-401.
- Wilson S., Alpas A.T. (1996). *Wear*, **196**, 270-278.
- Xu J., Liu W. (2006). *Wear*, **260**, 486-492.
- Xua H., Jiana X., Meeka T.T., Hanb Q. (2004). *Mater Lett.*, **58**, 3669-3673.
- Xuan Y., Nastac L. (2018). *Ultrasonics*, **83**, 94-102.
- Yan C., Zhang L. (1995). *Appl. Compos. Mater.*, **1**, 431-447.
- Yang Y., Lan J., Li X. (2004). *Mater. Sci. Eng. A*, **380**, 378-383.
- Yazdani A., Salahinejad E. (2011). *Materials and Design*, **32**, 3137-3142.
- Ye J., He J., Schoenun J. M. (2006). *Metall. Mater. Trans. A*, **37**, 3099-3109.
- Yu H. (2010). *Master degree thesis* submitted to Wocester polytechnic institute.
- Yuvaraj N., Aravindan S., Vipin (2015). *J. Mate. Res. Technol.*, **4**(4), 398-410.
- Zhang L., Qiu F., Wang J. (2015). *Mater. Sci. Eng. A*, **626**, 338-341.
- Zhang X., Chen Y., Hu J. (2018). *Prog. Aerosp. Sci.* **97**, 22-34.
- Zhang X., Geng L., Wang G. S. (2006). *J. Mater. Process. Tech.*, **176**, 146-151.
- Zhanwei Y., Fuguo L., Peng Z., Chen B., Fengmei X. (2014). *Chinese J. Aeronaut.*, **27**(2), 397-406.
- Zheng W., Wang Y., Zhou M., Wang Q., Ling L. (2018). *Ceram. Int.*, **44**, 15133-15144.

Zhong M., Jiang D., Zhang H., et al. (2014). *J. Laser Appl.*, **26**(2), **022007**:1-10.

Zhou S., Zhang X., Ding Z. (2007). *Compos. Part A- Appl. S.*, **38**, 301-306.

Zolriasatein A., Khosroshahi R.A., Emamy M. et al. (2013). *Int. J. Min. Met. Mater.*, **20**(3), 290-297.

Publications from the thesis

NANOINDENTATION, SCRATCH, AND CORROSION STUDIES OF ALUMINUM COMPOSITES REINFORCED WITH SUBMICRON B₄C PARTICLES

Deepak M. Shinde and Prasanta Sahoo 

Department of Mechanical Engineering, Jadavpur University, Kolkata 700 032, India

Copyright © 2021 American Foundry Society
<https://doi.org/10.1007/s40962-021-00692-7>

Abstract

The reported study examines the effect of submicron boron carbide particles on nanohardness, scratch resistance, and corrosion response of Al/B₄C composites. Liquid metalurgy involving a combination of mechanical and ultrasonic stirring action is employed to produce composites with varying contents of B₄C (0.5, 1, 1.5, and 2 wt%) particles. Fabricated composites are observed under field emission scanning electron microscopy (FESEM) and examined through energy dispersive X-ray (EDX) for particle incorporation and microstructural features. Nanoindentation hardness of alloy increased by 26.59% with just 2.0 wt% B₄C and increased with increasing reinforcement. Scratch resistance increased, while wear volume decreased with higher reinforcement content. Scratch hardness is improved by 73% and 29% at 5 N and

20 N applied respective loads. Composites revealed an increase in friction coefficients with increasing applied scratch load. Potentiodynamic polarization and electrochemical impedance spectroscopy tests examined the corrosion properties of composites and base alloy. Surfaces corroded are characterized using the FESEM-EDX tool to understand the corrosion behavior. The incorporation of 0.5 wt% B₄C significantly improved the corrosion resistance of Al–Si alloy. But further addition of submicron particles degraded the corrosion response.

Keywords: Al/B₄C, ultrasonic casting, nanoindentation, scratch resistance, corrosion behavior, electrochemical test

Introduction

Metal matrix composites present the opportunity to develop materials with desired properties required in high-performance applications. Aluminum composites, in particular, are under continuous research due to many desirable properties of Al such as low density, better strength, and factors like gross availability, processing ease, etc. They are in huge demand and are extensively applied for various applications for aerospace and automotive industries. Different oxides and carbides such as Al₂O₃, CuO, MgO, SiO₂, TiO₂, ZrO₂, B₄C, CrC, SiC, TaC, TiC, and WC are used as reinforcements for the Al matrix, among which alumina and SiC are prominent. Boron carbide possesses excellent properties like low density, high hardness (30 GPa), modulus (460 GPa), melting point (2450 °C), low expansion coefficient, thermal/chemical stability, neutron absorption ability, etc. But it is not yet fully

explored for making Al composites, possibly due to the cost factor. Different solid- and liquid-state processing methods are used, for fabricating Al composites, out of which stir casting is preferred for low cost and simplicity. In traditional stir casting, it is difficult to prevent the formation of particle clusters which hampers the mechanical properties of composites. It is observed recently that ultrasonic stirring action improves the dispersion of particles, enhances wettability, and produces sound castings with refined microstructure. Microstructural enhancement on account of the well-dispersed particles causes significant improvement in the mechanical properties like strength, elongation, impact energy, etc. Accordingly, ultrasonic vibration stir casting is made use of for fabricating composites in the presented study.

Composite properties are governed largely by the properties of the constituent elements, but particle–matrix interfaces also significantly influence its overall macroscale behavior. As such, the determination of mechanical properties at the micro/nanoscale can predict and extend

Received: 09 July 2021 / Accepted: 02 September 2021
 Published online: 27 September 2021

INFLUENCE OF SPEED AND SLIDING DISTANCE ON THE TRIBOLOGICAL PERFORMANCE OF SUBMICRON PARTICULATE REINFORCED Al-12Si /1.5 WT% B₄C COMPOSITE

Deepak M Shinde¹ and Prasanta Sahoo¹

Department of Mechanical Engineering, Jadavpur University, Kolkata 700032, India

Copyright © 2021 American Foundry Society
<https://doi.org/10.1007/s40962-021-00636-1>

Abstract

The paper reports wear and friction performance of Al-12Si aluminum alloy reinforced with 1.5 wt% submicron boron carbide (B₄C) particles. Composite material is fabricated by ultrasonic stir casting process. Microstructural examination is carried out using optical microscopy and field emission scanning electron microscopy (FESEM). Incorporation and agglomeration-free dispersion of B₄C particles is detected in the aluminum matrix. Pin-on-disc tribotester is used to evaluate tribological performance of fabricated composite and base alloy under room temperature dry conditions. Nominal contact pressure of 0.707 MPa is applied against EN31 steel counterface, and sliding speeds are varied between 0.25 and 1.25 m/s. Influence of sliding distance is investigated by varying sliding durations from 10 to 40 min at two fixed load-speed (PV) factors of 10 and 25 Nm/s. Worn pin surfaces and collected wear debris are analyzed using FESEM and

energy-dispersive spectroscopy to reveal undergoing wear mechanisms. After initial decrease, wear rate increased almost linearly with speed and became twofold at the top speed. Wear rate transition is seen at 0.5 m/s with sliding distance for the applied pressure. Friction coefficient is not influenced significantly with sliding distance for the fixed PV condition. Adhesion and delamination governed the wear mechanism of base alloy while mechanically mixed layer played key role in the wear performance of composite matrix. Improved wear resistance of aluminum matrix is observed due to incorporation of small amount of B₄C particulates making the composite better suited for wear-resistant applications than base alloy.

Keywords: Al-B₄C composite, worn surface, wear debris, mechanically mixed layer, speed, distance

Introduction

Automotive and aerospace industries are facing the challenges of pollution norms, fuel economy and increased safety. Besides, more advanced features of comfort and luxury are desired by passengers at competitive cost. Hence, there is continuous research on developing novel light-weight materials with desired and tailored properties. Aluminum alloys have become popular pick due to properties like low weight, good strength, corrosion resistance, near infinite recyclability, casting ease and low-cost availability. Despite this, broader use of aluminum is somewhat restricted due to poorer tribological performance as compared to other material options^{1,2}. The properties of aluminum alloys can be further improved by reinforcing with ceramic phase to produce materials called metal matrix composites (MMCs). Metal matrix and ceramics differ a lot in their physical, thermal and mechanical

properties making it possible to obtain tailored property combinations. MMCs are now commercially available and used on increasing scale in automotive, aerospace, electronics sector with major contribution from particle reinforced Al composites.^{3,4} Various micro-/nano-scale particulates like TiB₂, SiC, TaC, TiC, SiO₂, TiO₂, Si₃N₄, TiN, Al₂O₃, B₄C are utilized to fabricate metal matrix composites through different solid- and liquid-state processing routes.⁵

Stir casting is preferred for composite fabrication due to simplicity and industrial scalability, but it can't avoid formation of particle clusters. Nanocomposite fabrication is even more complex due to difficulty in handling and uniform dispersion of nanoparticles into composite matrix. Ultrasonic treatment in casting process is, however, found to be very effective for the fabrication of ceramic reinforced aluminum nanocomposites.⁶ Nonlinear events like

Published online: 15 June 2021

Deepak M. Shinde,¹ Suswagata Poria,² and Prasanta Sahoo³

High Temperature Tribology of A413/B₄C Nanocomposites under Dry Sliding Contact

Reference

D. M. Shinde, S. Poria, and P. Sahoo, "High Temperature Tribology of A413/B₄C Nanocomposites under Dry Sliding Contact," *Materials Performance and Characterization* 9, no. 1 (2020): 477–496. <https://doi.org/10.1520/MPC20200008>

ABSTRACT

In this work, boron carbide (B₄C) particulate (0.5, 1.0, 1.5, and 2.0 weight %) reinforced A413 alloy nanocomposites were fabricated by ultrasonic stir casting method. The prepared aluminum matrix nanocomposites were characterized using optical microscopy and field emission scanning electron microscopy to observe particle dispersion and quantify microstructural features. A high temperature pin-on-disk tribo-tester was employed to investigate the dry sliding tribological behavior of fabricated nanocomposites and unreinforced alloy at a constant speed (0.66 m/s) and different loads (20, 60 N) over the temperature range of 50°C–200°C. Specimens were slid against an AISI SAE 52100 counterface for the fixed duration of 10 minutes. Worn surfaces were examined under the scanning electron microscopy, and energy dispersive spectroscopy analysis was carried out to understand the wear mechanisms. It was revealed that the wear resistance of the alloy improved because of increasing B₄C content. The wear rate of all specimens was found to increase with increased load and operating temperatures. A shift in the mild oxidative to severe metallic wear of an unreinforced alloy was seen increased by about 50°C–80°C because of particulate reinforcement. The mild abrasive wear mechanism of the base alloy at low temperature was changed to adhesion with heavy plastic deformation at elevated temperature. Increased thermal stability offered by boron carbide particles and oxides and a mechanically mixed transfer layer were key factors enhancing the wear resistance of the nanocomposites. Under the tested experimental conditions A413/B₄C nanocomposite was found suitable and better than the base alloy for use in wear resistance applications.

Keywords

aluminum nanocomposite, boron carbide, ultrasonic stir casting, microstructure, sliding wear, worn surface, elevated temperature

Manuscript received January 28, 2020; accepted for publication July 6, 2020; published online August 18, 2020. Issue published August 18, 2020.

¹ Department of Mechanical Engineering, Jadavpur University, Raja S C Mullik Rd., Kolkata, West Bengal 700032, India, <https://orcid.org/0000-0001-5469-7796>

² Department of Mechanical Engineering, Heritage Institute of Technology, East Kolkata Township, West Bengal 700107, India, <https://orcid.org/0000-0002-9225-7238>

³ Department of Mechanical Engineering, Jadavpur University, Raja S C Mullik Rd., Kolkata, West Bengal 700032, India (Corresponding author), e-mail: psjume@gmail.com, <https://orcid.org/0000-0002-1538-0646>

Surface Topography: Metrology and Properties



PAPER

Dry sliding wear behavior of ultrasonic stir cast boron carbide reinforced aluminium nanocomposites

Deepak M Shinde¹, Suswagata Poria² and Prasanta Sahoo^{1,3} 

¹ Department of Mechanical Engineering, Jadavpur University Kolkata-700 032, India

² Department of Mechanical Engineering, Heritage Institute of Technology, Kolkata 700 107, India

³ Author to whom any correspondence should be addressed.

E-mail: dmsinde1975@gmail.com, suswagataporia@gmail.com, psjume@gmail.com and prasanta.sahoo@jadavpuruniversity.in

Keywords: nB₄C, ultrasonic stir casting, nanocomposite, worn surface, wear debris, tribolayer

Abstract

In the present work ultrasonic stir casting method is used to fabricate aluminium metal matrix nanocomposites reinforced with nano boron carbide (nB₄C) particles with varying (0.5, 1, 1.5 and 2) weight percentages. Microhardness and nanoindentation hardness of the nanocomposite is found to increase with increasing reinforcement content. Pin on disk apparatus is used to study the room temperature dry sliding wear behavior of fabricated composites and base alloy. Nominal contact pressures of 0.354–1.412 MPa and sliding speeds of 0.16–0.66 m s⁻¹ are employed. Each test run is conducted for the fixed contact period of 15 min. Field emission scanning electron microscopy (FESEM) equipped with energy dispersive spectroscopy (EDS) is used to observe worn surface and wear debris to understand the undergoing wear mechanisms. It is observed that base alloy underwent mild to severe plastic deformation led oxidative delamination wear. Nanocomposites are subjected to combination of oxidative, abrasive and mild delamination wear. Nanocomposites display less mass loss and wear rate as compared to base alloy due to the protective tribolayer formed in the contact interface. Part of the mechanically mixed transfer layer is found to adhere firmly to the composite surface under higher load-speed condition. Extremely hard nB₄C particle reinforcement is found beneficial for improving the wear resistance of aluminium alloy at varying combinations of load and speed.

1. Introduction

Aluminium based composites with tailored properties are on widespread usage in automotive and aerospace industries in the pursuit to produce energy efficient vehicles. Aluminium composites hold maximum share of the commercial metallic composites produced and utilized on mass basis. Aluminium is popular since it has attractive properties like light weight, good strength, corrosion resistance, casting ease and is available in abundance with near infinite recyclability. Even then the use of aluminium and its alloys is limited to some extent due to their poor resistance to wear, seizure and galling [1–4]. Component surfaces in sliding or rolling contact is common feature in every engineering system. It is not always possible to lubricate such tribological pairs due to system constraints. Hence the dry contact wear behavior of these components is significant for their extended life with

reliable performance. As heavy iron parts are being replaced by lightweight materials like aluminium, their friction and wear behavior is required to be enhanced and so has become an area of major research focus. Researchers are continuously trying to incorporate different types of ceramics into variety of the aluminium alloys in the pursuit to improve their wear resistance. Efforts are also directed towards developing self-lubricating aluminium composites. It is observed that wear and friction behavior of aluminium composites depend upon several intrinsic and extrinsic parameters [5]. Extrinsic factors include applied load, sliding speed, operating temperature, environment etc. Intrinsic factors include reinforcement (content, type, and size), microstructure, processing method and heat treatment. Micro particles are stated to act as load bearing elements thereby protect the soft alloy matrix against wear loss. But under high loads these micro particles get crushed to smaller size fragments

Tribological characterization of particulate-reinforced aluminum metal matrix nanocomposites: A review

Deepak M Shinde¹, Prasanta Sahoo¹  and J Paulo Davim²

Advanced Composites Letters

Volume 29: 1–28

© The Author(s) 2020

Article reuse guidelines:

sagepub.com/journals-permissions

DOI: 10.1177/2633366X20921403

journals.sagepub.com/home/acm



Abstract

Aluminum (Al)-based composites are on increasing usage in sectors like ground transportation, aerospace, sports, and infrastructure because of the improved properties such as high strength to weight ratio, corrosion, fatigue, and wear resistance. Several applications involving dynamic contact stresses require excellent wear and frictional performance for improved life. Nanocomposites are found to perform exceedingly better than microcomposites and alloys in several lab scale tribological investigations carried out so far in the last decade. In this article, an attempt is made to review those published reports about dry sliding tribological behavior of particulate-reinforced Al nanocomposites. Wear and friction being system properties are found to get influenced by intrinsic factors such as reinforcement, fabrication method, microstructure; extrinsic parameters like load, speed, contact conditions and the system generated in situ tribolayer all being interrelated.

Keywords

aluminum matrix nanocomposites, pin-on-disk, worn surface, wear debris, scanning electron microscopy and energy dispersive spectroscopy, tribolayer, wear mechanism

Introduction

Attractive characteristics like light weight, good corrosion resistance, low expansion coefficient, high strength, near-infinite recyclability, flame retarding properties, casting ease for mass production, and low cost availability make aluminum (Al) a popular material choice for automotive and aerospace sector. It is more so in the scenario when the transportation field is facing the challenges of fuel economy, reduced vehicle emissions, and increased vehicle safety at competitive cost. However, the use of Al and its alloys is restricted due to poor resistance to wear, seizure, and galling.^{1,2} European automotive industry is using new design concepts like body in white and super light car which focus on producing lightweight vehicles for space and fuel economy. Al alloys of 2xxx, 5xxx, 6xxx, and 7xxx series designation are in large usage due to high strength formability, damage tolerance, fatigue resistance, energy absorption, and excellent crash characteristics. Typical automotive applications include power train components, chassis and suspension, and body parts like doors, bumpers, and interiors.³ The need of different property combinations

such as high specific strength and ductility for aerospace and automobile field, low coefficient of thermal expansion (CTE) and high thermal stability for elevated temperature applications, high wear resistance, high specific stiffness, and corrosion resistance for defense sector can be fulfilled by metal matrix composites (MMCs). It is because metals and ceramics have vastly different physical, thermal, electrical, and mechanical properties. Due to possible tailored property combinations, MMCs are now being commercially made available and used on increasing scale. Especially, particulate-reinforced Al-based MMCs are of

¹ Department of Mechanical Engineering, Jadavpur University, Kolkata, West Bengal, India

² Department of Mechanical Engineering, University of Aveiro, Aveiro, Portugal

Date received: 28 August 2019; accepted: 25 February 2020

Corresponding author:

Prasanta Sahoo, Department of Mechanical Engineering, Jadavpur University, Kolkata, West Bengal 700032, India.

Emails: psjume@gmail.com; prasanta.sahoo@jadavpuruniversity.in



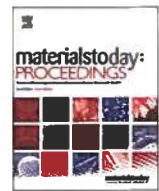
Creative Commons Non Commercial CC BY-NC: This article is distributed under the terms of the Creative Commons Attribution-NonCommercial 4.0 License (<https://creativecommons.org/licenses/by-nc/4.0/>) which permits non-commercial

use, reproduction and distribution of the work without further permission provided the original work is attributed as specified on the SAGE and Open Access pages (<https://us.sagepub.com/en-us/nam/open-access-at-sage>).



Contents lists available at ScienceDirect

Materials Today: Proceedings

journal homepage: www.elsevier.com/locate/matpr

Synthesis and characterization of Al-B₄C nano composites

Deepak M. Shinde*, Suswagata Poria, Prasanta Sahoo

Department of Mechanical Engineering, Jadavpur University, Kolkata 700 032, India

ARTICLE INFO

Article history:

Received 30 May 2019

Accepted 7 June 2019

Available online 15 July 2019

Keywords:

LM6

nB₄C

Ultrasonic stir casting

FESEM-EDS

Nanocomposite

ABSTRACT

In the present study, effect of incorporation of varying weight percentages (0.5, 1, 1.5, and 2) of boron carbide nanoparticles in aluminum-silicon alloy LM6 is investigated. Nanocomposites are fabricated using ultrasonic vibration assisted stir casting process. Field emission scanning electron microscopy (FESEM) and Energy Dispersive spectroscopy images are used to characterize the base alloy and fabricated composites. Nanoparticles are seen to be homogeneously incorporated in the alloy matrix. Refinement in the microstructure is seen effecting improvement in the hardness and density of composites. Hardness values of as cast composites are obtained using Vickers microhardness tester which are found to be higher than the base alloy.

© 2019 Elsevier Ltd. All rights reserved.

Selection and peer-review under responsibility of the scientific committee of the 1st International Conference on Manufacturing, Material Science and Engineering.

1. Introduction

Nanocomposites are the kind of composites in which at least one of the involved phases either matrix or reinforcements do have dimensions in the nanometer scale. Depending on the matrix phase nanocomposites are classified into three types: metal matrix nanocomposites (MMNCs), polymer matrix composite (PMNCs) and ceramic matrix nanocomposites (CMNCs). Reinforcement phase can be nanoparticle, nanoplatelet or nanofibre and so accordingly nanocomposites are named as: nanoparticle reinforced nanocomposites, nanoplatelet reinforced nanocomposites and nanofibre reinforced nanocomposites. Metal matrix nanocomposite is defined as a composite system in which metal or its alloy is incorporated with nanosized metallic or nonmetallic reinforcements. The development of MMNC is still in its infancy [1]. Nanocomposites have become one of the rapidly growing areas of material research due to the parallel progress in nanotechnology. Till year 2005 there were about 300 publications reported on metal matrix nanocomposites in the web of science which grew to the same number of publication on an average per year during 2010 to 2017 [2]. The properties which are targeted to improve in case of nanoscale reinforcements are: tensile and compressive behaviour, ductility, fatigue, creep behaviour, high temperature mechanical properties, thermal shock resistance, wear resistance including scratch resistance, thermal expansion coefficient,

machining, and corrosion resistance. Judicious selection of matrix, reinforcement and careful processing is found to effect exciting improvement in the properties of metal matrix composites. Light weight metals such as Mg, Al, Cu, Zn, Ti, Ni, Zn and their alloys are popular choices for matrix materials out of which aluminium is the mostly targeted one. Nanoparticle-reinforced aluminium matrix composites due to their isotropic nature of improved properties such as high strength, stiffness, ductility, good corrosion and wear resistance are strongly investigated for use in the fields of transportation, defense, aviation, electronics and sports industries. Metallic materials reinforced with nanoscale particles typically are borides (TiB₂, ZrB₂, MoB, CrB, and WB), carbides (B₄C, CrC, SiC, TaC, TiC, WC, ZrC), nitrides (AlN, BN, CrN, Si₃N₄, TiN, WN, ZrN) and oxides (Al₂O₃, B₂O₃, CuO, Fe₃O₄, MgO, SiO₂, TiO₂, WO₃, Y₂O₃, ZnO, ZrO₂). Silicon carbide (SiC) and Aluminium oxide (Al₂O₃) are the two most often used reinforcements for research studies undertaken in the area of metal matrix composites. Wide availability of nanoscale aluminium oxide has motivated its use but poor wettability with molten metals and alloys restricted its incorporation up to 4 vol% in order to avoid clustering. On the other hand TiB₂ and TiC shows good wettability and stability with molten aluminium and so often selected as reinforcement phases in aluminium metal matrix nanocomposites [3]. Among different nano particle reinforced composites, despite promising, B₄C reinforced aluminium nanocomposites are quite scanty due to high cost of B₄C nano powder. B₄C is an appropriate reinforcing particle for producing aluminium matrix nanocomposites due superior properties like high melting point (2450 °C), low thermal conductivity

* Corresponding author.

E-mail address: dmshinde1975@gmail.com (D.M. Shinde).

Chapter 5

Fabrication of Aluminium Metal Matrix Nanocomposites: An Overview



Deepak M. Shinde and Prasanta Sahoo

1 Introduction

Improved fuel economy, reduced vehicle emission, increased safety, attractive styling options and better features of comfort and luxury to passengers at competitive cost are the challenges being faced by automotive and aerospace industries these days. This has prompted continuous research on developing light-weight materials with desired and tailored properties. Aluminium and its alloys have become obvious choice due to low cost availability, low density, better strength, corrosion resistance, near-infinite recyclability and casting ease. Aluminium composites in particular have attracted researchers due to properties like high strength and stiffness, increased resistance to wear and corrosion and improved high-temperature performance [6, 74]. Successful automotive applications of Al include transmission components, brake elements, structural parts like chassis, suspension, body parts including bumpers, doors and interiors [36, 79]. Improvement in properties of aluminium is affected by reinforcing with ceramic phase to produce so-called aluminium metal matrix composites (AMMCs). It is because aluminium and ceramics have vastly different properties making it possible to obtain desired property combinations. Large number of MMCs are now commercially being produced and used with major contribution of particulate-reinforced Al composites on mass basis [111]. Different micro/nano-scale particles such as TiB_2 , SiC, TaC, TiC, SiO_2 , TiO_2 , Si_3N_4 , TiN, Al_2O_3 and B_4C are used to produce metal matrix composites via different solid- and liquid-state fabrication routes.

Aluminium-based microcomposites have been successfully utilized in different sectors like ground transportation, aerospace, electronics, recreational goods industries for structural and wear resistance applications. It is also clearly demonstrated

D. M. Shinde (✉) · P. Sahoo
Jadavpur University, Kolkata, India
e-mail: dmshinde1975@gmail.com

© The Author(s), under exclusive license to Springer Nature Singapore Pte Ltd. 2021
S. Sahoo (ed.), *Recent Advances in Layered Materials and Structures*,
Materials Horizons: From Nature to Nanomaterials,
https://doi.org/10.1007/978-981-33-4550-8_5

107

15/07/2022